

# **Single-site supported metal catalysts for aqueous phase conversion of methane to oxygenates**

A dissertation submitted by

Mengwei Li

in partial fulfillment of the requirements for the degree of

Doctor of Philosophy

in

Chemical Engineering

Tufts University

May 2019

Advisor:

Prof. Maria Flytzani-Stephanopoulos, Ph.D.

# Abstract

Throughout history, natural gas has been both one of the primary sources of energy and the raw material for chemicals production in the industry. Aside from being used as a fuel for power generation, transportation and heating, natural gas can also be converted to syngas, which is widely used in industrial processes including production of ammonia, methanol, dimethyl ether and diesel. The need to convert natural gas to syngas as an intermediate step poses a particular economical challenge as the process is energy intensive and typically operates at temperatures above 800°C. Such a process is only economical at large scale and difficult to implement for gas sources that are associated with oil or located at remote areas. An efficient oxidative route to convert natural gas to other chemicals in one step at low temperature is thus highly desirable.

Methane is the main component of natural gas and has four symmetric C-H bonds with bond energy of 104 kcal/mol. Direct functionalization of methane offers a potential alternative to the energy demanding syngas route. A one-step oxidative conversion of methane to oxygenates like methanol and acetic acid is of particular interest since methanol is both a fuel with high energy density and a feedstock for other chemicals like dimethyl ether, acetic acid and formaldehyde. Acetic acid, on the other hand, is a high value chemical in large demand. Its largest use is in the production vinyl acetate followed by solvent use in terephthalic acid production.

This thesis aims to design novel heterogeneous catalysts for selective oxidation methane to methanol and acetic acid in one-step, with particular emphasis on the role of supported single atom species for activating and functionalizing the C-H bonds of methane at low temperatures. Rhodium single atom supported on zeolites was first investigated for the selective oxidation of methane to methanol and acetic acid. A parametric study on the catalyst was conducted to improve conversion and selectivity. A low partial pressure of O<sub>2</sub> was found to be favorable for the selective oxidation of methane to acetic acid and the catalyst is catalytic, with turnover number over 300 in a single batch reaction. The active site of the

catalyst was elucidated by characterization of the catalyst using advanced microscopy and spectroscopy methods and identified as isolated rhodium cation in intermediate oxidation state anchored inside the micropores of the zeolite.

Furthermore, mechanistic investigations of the reaction pathway found that single atom of rhodium can activate methane and generate a Rh-CH<sub>3</sub> complex, while subsequent functionalization follows two parallel pathways: Carbonylation of the complex yields acetic acid while direct hydroxylation leads to methanol formation. The coordination environment of the support was found to affect product selectivity. Supports with Brønsted acidity favors the formation of acetic acid, while non-acidic supports favor the formation of methanol.

Next, iridium-based catalysts were also studied for this reaction. The monometallic iridium catalyst shows a relatively low activity due to its tendency to form small clusters and nanoparticles. However, the addition of a second metal, namely palladium or copper, significantly promotes both the activity and selectivity of the catalyst, leading to high methanol yield. The promoter itself has a negligible activity and there is clearly a synergistic effect between iridium and the second metal. Detailed studies on the role of each promoter were performed and the underlying mechanism was presented.

Finally, the role of carbon monoxide in this reaction system is discussed. The presence of CO serves two roles. First, it stabilizes rhodium and iridium species in their mononuclear state at reaction conditions, forming Rh(I)(CO)<sub>2</sub> and Ir(I)(CO)<sub>2</sub> as characterized by CO-DRIFTS. The ability of CO to fracture Rh and Ir into single atoms from metallic state can be followed by CO-DRIFTS. Second, CO molecule serves as the two-electron donor for reductive activation of molecular oxygen and the generation of peroxo species. The generation of peroxo species and their release into the aqueous phase can be monitored at temperatures as low as 50°C but methane oxidation does not light off at temperatures below 100°C. Low temperature production of H<sub>2</sub>O<sub>2</sub> can be utilized by introducing iron sites into the zeolite pores and conducting the reaction in acidic media.

# Acknowledgements

I would like to express my sincere gratitude for all the family members, friends, colleagues and my Ph.D. advisor for their continuous support and help along my Ph.D. study. I could not have completed this long journey without their encouragement, urge and understanding.

First and foremost, I would like to thank my Ph.D. advisor, Prof. Maria Flytzani-Stephanopoulos for her unwavering support and dedicated mentorship. I would not have been able to complete this thesis without her insightful suggestions in my time of struggle for directions. The joy and excitement of pioneering a new direction in the group is very rewarding and I am grateful to have had this experience because of her. I would also like to thank my thesis committee members, Prof. Hyunmin Yi, Prof. Terry Haas, Prof. Prashant Deshlahra and Prof. Yuri Román-Leshkov for their helpful suggestions and critical evaluations. My thoughts and prayers go to Prof. Elena Rybak-Akimova as she continued to evaluate my thesis during her battle against cancer. Her dedication to research and teaching will always be an inspiration for me. May her soul rest in peace. To all the faculty members of ChBE department, I have learned a lot from the rich course materials covered in class and I am grateful to be a member of this great program. I'd like to offer special thanks to Prof. Jerry Meldon, who although no longer with us, continues to inspire me.

I would like to also offer my special thanks to Dr. Junjun Shan, who has been a close partner in jump-starting this research project. I have learned a lot from his hard-work, academic curiosity and rich experience. To all the previous and current group members of the Nano Catalysis and Energy Lab, Dr. Ioannis Valsamakis, Dr. Nan Yi, Dr. Branko Zugic, Dr. Matthew Boucher, Matthew Rutter, George Cladaras, Dr. Ming Yang and Dr. Chongyang Wang for their tutoring in my early days of study, Dr. Jilei Liu, Sufeng Cao, Georgios Giannakakis, Dr. Antonios Trimbali and Ouyang Mengyao for their kind help and thoughtful discussions. Many thanks to all the staff members of Department of Chemical and

Biological Engineering, Beth Frasso, Margaret DeChiaro, Maura Tierney and Emily Edwards as well as Dr. David Wilbur in Department of Chemistry. It has been a great experience working with you.

Finally, I would like to express my profound affection and gratitude to my wife, Xi Wang, who has been my greatest supporter and fan for the past few years. Her upbeat spirit and wonderful cooking skills have carried me through the difficult time of research. I would also like to express my sincere thanks to my parents and parents-in-law. Their understanding and support have given me strength and courage to overcome all the difficulties in research and life.

The financial support of my project by Advanced Research Projects Agency – Energy (ARPA-E), U.S. Department of Energy (grant number SU0433) is gratefully acknowledged. I would also like to thank for the support of the U. S. Department of Energy, Office of Science, Office of Basic Energy Sciences for use of the Advanced Photon Source at Argonne National Laboratory under Contract No. DE-AC02-06CH11357.

# Table of Contents

Abstract.....	ii
Acknowledgements.....	iv
List of Abbreviations .....	1
List of Figures .....	2
List of Tables .....	7
Chapter 1 Introduction .....	8
1.1 Supported single atom catalysts.....	8
1.2 Direct conversion of methane to oxygenates .....	9
1.3 Methane activation review .....	12
1.3.1 Activation of methane in strongly acidic media .....	13
1.3.2 Activation of methane in aqueous media.....	17
1.3.3. Activation of methane in the gas phase.....	20
1.3.4. Strategies for molecular oxygen activation.....	23
1.4 Single site catalysts for C-H bond activation.....	24
1.5 Thesis objectives.....	25
1.6 References.....	27
Chapter 2 Experimental Methods and Procedures.....	38
2.1 Catalyst synthesis.....	38
2.1.1 Materials and chemicals.....	38
2.1.2 Preparation methods.....	38
2.2 Catalyst characterization.....	40
2.3 Catalytic testing .....	43
2.4 References.....	50
Chapter 3 Selective conversion of methane to methanol and acetic acid over RhZSM-5 single site catalyst .....	51
3.1 Introduction.....	51
3.2 Experimental Methods .....	53
3.3 Results and Discussion .....	55
3.3.1 Catalytic activity of RhZSM-5 and parametric study .....	55
3.3.2 Experimenting with different reactor setup for improved acetic acid concentration .....	63

3.3.3 Catalyst Characterization .....	65
3.4 Conclusions.....	84
3.5 References.....	86
Chapter 4 Mechanistic study of the selective oxidation of methane using rhodium-based catalysts .....	89
4.1 Introduction.....	89
4.2 Experimental Methods .....	90
4.2.1 Catalyst synthesis.....	90
4.2.2 Catalytic testing .....	91
4.2.3 Catalyst characterization .....	93
4.3 Results and Discussion .....	94
4.3.1 Identification of a two-pathway functionalization mechanism .....	94
4.3.2 Exploration of methane activation mechanism .....	106
4.3.3 Understanding the efficiency of CO .....	114
4.3.4 Design of bimetallic FeRhZSM-5 catalyst for selective C1 formation.....	120
4.4 Conclusions.....	128
4.5 References.....	130
Chapter 5 Selective conversion of methane to methanol over Ir- based catalysts.....	135
5.1 Introduction.....	135
5.2 Experimental Methods .....	136
5.2.1 Catalyst synthesis.....	136
5.2.2 Catalyst evaluation.....	137
5.2.3 Catalyst characterization .....	139
5.3 Results and discussion .....	140
5.3.1 Catalytic activity of IrZSM-5 promoted by copper and palladium.....	140
5.3.2 Elucidating the role of metal promoters.....	146
5.3.3 Characterization of iridium- based catalysts .....	152
5.4 Conclusions.....	163
5.5 References.....	164
Chapter 6 Conclusions and Recommendations.....	169
6.1 Conclusions.....	169
6.2 Recommendations.....	171
6.3 References.....	174

## List of Abbreviations

<b>GC</b>	Gas Chromatography
<b>TCD</b>	Thermal Conductivity Detector
<b>BET</b>	Brunauer-Emmett-Teller Theory
<b>ICP-AES</b>	Inductive Coupled Plasma – Atomic Emission Spectroscopy
<b>XRD</b>	X-Ray Diffraction
<b>XPS</b>	X-ray Photoemission Spectroscopy
<b>ac HAADF-STEM</b>	Aberration Corrected High Angle Annular Dark Field – Scanning Transmission Electron Microscopy
<b>UV-Vis</b>	Ultraviolet – Visible Spectroscopy
<b>DRIFTS</b>	Diffuse Reflectance Infrared Fourier Transform Spectroscopy
<b>EPR</b>	Electron Paramagnetic Resonance
<b>NMR</b>	Nuclear Magnetic Resonance
<b>XAS</b>	X-ray Absorption Spectroscopy
<b>XANES</b>	X-ray Absorption Near Edge Spectroscopy
<b>EXAFS</b>	Extended X-ray Absorption Fine Structure
<b>TPO</b>	Temperature Programmed Oxidation
<b>DP</b>	Deposition Precipitation
<b>IWI</b>	Incipient Wetness Impregnation
<b>RT</b>	Room Temperature
<b>TOF</b>	Turnover Frequency
<b>CN</b>	Coordination Number
<b>LCF</b>	Linear Combination Fitting

# List of Figures

Figure 1.1 U.S. natural gas gross withdrawals (2000-2016).....	9
Figure 1.2 Schematic of a typical electrophilic methane oxidation catalytic cycle (adapted from 18-21) .	14
Figure 1.3 Ligand protonation by acids. <sup>22</sup> .....	15
Figure 1.4 Generation of active center on Fe-ZSM-5. <sup>45</sup> .....	18
Figure 1.5 Methane to methanol reaction scheme on Cu-ZSM-5. <sup>59-61, 63</sup> .....	21
Figure 2.1 Solubility trends of O <sub>2</sub> , CO, CH <sub>4</sub> and CO <sub>2</sub> in water at different temperatures, solubilities calculated from empirical equations published in literature. <sup>2-5</sup> .....	44
Figure 2.2 Two-way gas sampling system with a Tedlar gas bag.....	45
Figure 2.3 A typical chromatogram obtained for the product gas from GC-TCD test. ....	46
Figure 2.4 A typical H-NMR spectrum of liquid oxygenates obtained after reaction. ....	47
Figure 2.5 Calibration curves for formic acid, methanol and acetic acid obtained by H-NMR measurement. ....	49
Figure 3.1 Catalytic activity of RhZSM-5 catalysts with different loadings as well as synthesized with different heat treatment. Conditions: 20mg catalyst, 4bar O <sub>2</sub> , 5bar CO, 20bar CH <sub>4</sub> , 150°C, 1h.....	56
Figure 3.2 Product formation on 0.5wt% RhZSM-5 at different temperatures. Conditions: 4bar O <sub>2</sub> , 5bar CO, 20bar CH <sub>4</sub> , 20mg catalyst, 20mL DI water, 1h. ....	58
Figure 3.3 Product formation on 0.5wt% RhZSM-5 at different batch time. Conditions: 4bar O <sub>2</sub> , 5bar CO, 20bar CH <sub>4</sub> , 150°C, 20mg catalyst, 20mL DI water. ....	59
Figure 3.4 Methane oxidation product formation on 0.5wt% RhZSM-5 with different pO <sub>2</sub> ; Conditions: 20 mg catalyst, 20 mL DI water, 5 bar CO, 20 bar CH <sub>4</sub> , 150 °C. ....	60
Figure 3.5 Methane oxidation product formation (a) and gas phase composition (b) on 0.5wt% RhZSM-5 with different reaction time at pO <sub>2</sub> =2bar; Conditions: 20 mg catalyst, 20 mL DI water, 2 bar O <sub>2</sub> , 5 bar CO, 20 bar CH <sub>4</sub> , 150 °C.....	61
Figure 3.6 Product formation on 0.5wt% RhZSM-5 with same O <sub>2</sub> /CO ratio. Conditions: 20mg catalyst, 20mL DI water, 20bar CH <sub>4</sub> , 150°C, 3h. ....	62
Figure 3.7 (a) Comparison of product formation using single-batch and fed-batch operation and (b) comparison of product formation using fed-batch operation and feed gas mixture with and without CH <sub>4</sub> ; Conditions: 10~100 mg catalyst, 10~20 mL DI water, 2 bar O <sub>2</sub> , 5 bar CO, 20 bar CH <sub>4</sub> , 150 °C. ....	63
Figure 3.8 (a) aqueous phase product concentration and (b) gas phase composition at different time on stream monitored during semi-batch operation; Conditions: 400mg catalyst, 80 mL DI water, O <sub>2</sub> :CO:CH <sub>4</sub> =2:5:20, P=560 psig, 150 °C, 14 mL/min.....	64
Figure 3.9 Comparison of catalytic activity of aqueous phase rhodium ions and RhZSM-5. Conditions: 0.9μmol Rh, 20mL DI water, 2bar O <sub>2</sub> , 5bar CO, 20bar CH <sub>4</sub> , 150°C, 3h. ....	68
Figure 3.10 X-ray Diffraction Patterns of parent ZSM-5, as-synthesized and used 0.5wt% RhZSM-5.....	69

Figure 3.11 Photoemission features of Rh 3d (A) and Si 2p (B) of as-synthesized 0.5wt% RhZSM-5 before and after Ar <sup>+</sup> sputtering. ....	70
Figure 3.12 HAADF and BF STEM image pairs, acquired simultaneously, of as-synthesized 0.5wt% RhZSM-5 (a and b), 0.5wt% RhZSM-5 after use in the reaction (c and d), and 0.5wt% RhZSM-5_washed (e and f). ....	71
Figure 3.13 (a) and (b) ac-HAADF STEM images of as-synthesized 0.5wt% RhZSM-5 showing (a) isolated rhodium single cations on thin edge of the flake of catalyst and (b) nanoparticles of rhodium at same magnification (rhodium species circled in white). ....	72
Figure 3.14 CO-DRIFTS of (a) RhZSM-5 samples with different loadings prepared by H <sub>2</sub> reduction and (b) 0.5wt% RhZSM-5 samples prepared with different heat treatment. ....	73
Figure 3.15 CO-DRIFTS of 0.5wt% RhZSM-5 with 10% CO treated at different temperature. Prior to experiment the catalyst was intentionally sintered with H <sub>2</sub> at 250°C for 1h. ....	74
Figure 3.16 Normalized Rh K-edge XANES spectra of different RhZSM-5 catalysts and rhodium standards. Spectra of RhZSM-5 samples were collected ex-situ in the gas phase in fluorescence mode. For 0.5wt% RhZSM-5_washed, aqueous suspension of the sample was also analyzed in fluorescence mode. Spectra for the four standards were collected in transmission mode. ....	76
Figure 3.17 Linear combination fitting (LCF) of first order derivative XANES spectra for (a) 0.5wt% RhZSM-5_washed, (b) 0.5wt% RhZSM-5_washed after reaction and (c) 0.5wt% RhZSM-5. ....	78
Figure 3.18 Rh K-edge EXAFS data of (a) 0.5wt% RhZSM-5_washed, (b) 0.5wt% RhZSM-5_washed after reaction and (c) 0.5wt% RhZSM-5 plotted in Fourier Transform space. ....	80
Figure 3.19 (a) Normalized Rh K-edge XANES spectra of 0.5wt% RhZSM-5_washed sample before reduction, reduced at 250-550°C, exposed to air at RT after reduction and rhodium foil (b) Corresponding white line intensities of the four samples. ....	81
Figure 3.20 (a) TPO profile of used 0.5wt% RhZSM-5 catalyst (b) CO pulsed chemisorption on 0.5wt% RhZSM-5 catalyst at 150°C. ....	83
Figure 3.21 CO-DRIFTS spectra of 0.5wt% RhZSM-5 used for semi-batch reaction. ....	84
Figure 4.1 Product formation using methanol as reactant on 0.5wt% RhZSM-5. Conditions: 20mg catalyst, 3mM CH <sub>3</sub> OH solution, 2bar O <sub>2</sub> , 5bar CO, 20bar CH <sub>4</sub> , 150°C, 1h. ....	94
Figure 4.2 <sup>13</sup> C-NMR spectrum of the aqueous solution after reaction with <sup>13</sup> CO. Conditions: 100mg 0.5wt% RhZSM-5, 2bar O <sub>2</sub> , 5bar <sup>13</sup> CO, 20bar CH <sub>4</sub> , 150°C, 3h. ....	96
Figure 4.3 Arrhenius-type plot of the initial rate of reaction on 0.5wt% RhZSM-5. Conditions: 2bar O <sub>2</sub> , 5bar CO, 20bar CH <sub>4</sub> , 130-170°C, 30min, 9-83mg catalyst. ....	98
Figure 4.4 CO-DRIFT spectra of RhTiO <sub>2</sub> catalysts of different loadings prepared by DP method. ....	99
Figure 4.5 Amount of leachable rhodium after UV irradiation of RhTiO <sub>2</sub> in ethanol solution for different lengths of time. ....	100
Figure 4.6 X-band EPR spectra of different TiO <sub>2</sub> samples recorded at 120K. ....	101
Figure 4.7 Ti 2p XP spectra of the fresh and used 0.6wt% RhTiO <sub>2</sub> . ....	102

Figure 4.8 XANES and EXAFS spectra of 0.6wt% RhTiO <sub>2</sub> prepared by UV-assisted deposition. EXAFS fitting parameters are summarized here: Rh-O: CN 6.6±1.4, R(Å) 2.10±0.02, σ <sup>2</sup> (Å <sup>2</sup> ) 0.003±0.0028; Rh-Rh: 0.....	103
Figure 4.9 Linear Combination Fitting (LCF) of XANES spectrum for 0.6wt% RhTiO <sub>2</sub> prepared by UV-assisted deposition. ....	104
Figure 4.10 Catalytic activity of different rhodium catalysts with single atom dispersion. Conditions: 20mg catalyst, 20mL DI water, 2bar O <sub>2</sub> , 5bar CO, 20bar CH <sub>4</sub> , 150°C, 3h. ....	105
Figure 4.11 CO-DRIFT spectra of rhodium species anchored on different supports. ....	106
Figure 4.12 Mass spectrometry analysis of gas phase products after reaction with <sup>18</sup> O <sub>2</sub> . Conditions: 100mg 0.5wt% RhZSM-5, 2bar <sup>18</sup> O <sub>2</sub> , 5bar CO, 20bar CH <sub>4</sub> , 150°C, 3h. Channels: C <sup>16</sup> O <sub>2</sub> (m/z=44), C <sup>16</sup> O <sup>18</sup> O (m/z=46), C <sup>18</sup> O <sub>2</sub> (m/z=48), <sup>16</sup> O <sub>2</sub> (m/z=32), <sup>16</sup> O <sup>18</sup> O (m/z=34) and <sup>18</sup> O <sub>2</sub> (m/z=36).....	107
Figure 4.13 Mass spectrometry, H-NMR and <sup>13</sup> C-NMR analysis of the aqueous phase product after reaction with <sup>18</sup> O <sub>2</sub> . (a) H <sub>2</sub> O analysis in control experiments without <sup>18</sup> O <sub>2</sub> ; (b) H <sub>2</sub> O analysis of aqueous phase in labeling experiment; (c) H-NMR analysis of aqueous phase from both labeling and control experiment; (d) <sup>13</sup> C-NMR analysis of aqueous phase product of <sup>18</sup> O <sub>2</sub> experiment and control experiment. Conditions: 100mg 0.5wt% RhZSM-5, 2bar <sup>18</sup> O <sub>2</sub> , 5bar CO, 20bar CH <sub>4</sub> , 150°C, 3h. Channels: H <sub>2</sub> <sup>16</sup> O (m/z=18), H <sub>2</sub> <sup>18</sup> O (m/z=20). ....	108
Figure 4.14 Effect of solvent on the catalytic activity of 0.5wt% RhZSM-5. Conditions: 20mg catalyst, 20mL DI water, 4bar O <sub>2</sub> , 5bar CO, 20bar CH <sub>4</sub> , 150°C, 1h. ....	110
Figure 4.15 (a) UV-Vis spectra and (b) picture of the product liquid showing H <sub>2</sub> O <sub>2</sub> production on 0.5wt% RhZSM-5 determined by colorimetric method. Conditions: 560mg catalyst, 20mL aqueous solution containing 0.1mol/L H <sub>2</sub> SO <sub>4</sub> and 0.1mol/L TiOSO <sub>4</sub> , 5bar O <sub>2</sub> , 5bar CO, 50°C. ....	111
Figure 4.16 CO efficiency on 0.5wt% RhZSM-5 at different reaction time. Conditions: 20mg catalyst, 20mL DI water, 2bar O <sub>2</sub> , 5bar CO, 20bar CH <sub>4</sub> , 150°C. ....	115
Figure 4.17 (a) Catalytic activity and (b) CO efficiency of 0.5wt% RhZSM-5 with different methane partial pressure. Conditions: 100mg catalyst, 20mL DI water, 2bar O <sub>2</sub> , 5bar CO, 150°C, 3h.....	116
Figure 4.18 (a) Catalytic activity and (b) CO efficiency of 0.5wt% RhZSM-5 at different reaction temperature. Conditions: 10-300mg catalyst, 20mL DI water, 2bar O <sub>2</sub> , 5bar CO, 20bar CH <sub>4</sub> , 3h. ....	117
Figure 4.19 Arrhenius-type plot of initial rate of both CO consumption and CH <sub>4</sub> oxidation on 0.5wt% RhZSM-5. Conditions: 20mL DI water, 2bar O <sub>2</sub> , 5bar CO, 20bar CH <sub>4</sub> , 0.5h, 130-170°C. ....	118
Figure 4.20 (a) Product formation and (b) CO efficiency on 0.5wt% RhZSM-5 and 0.5wt% RhZSM-5_washed at full O <sub>2</sub> conversion. Conditions: 100mg 0.5wt% RhZSM-5 (or 500mg 0.5wt% RhZSM-5_washed), 2bar O <sub>2</sub> , 5bar CO, 20bar CH <sub>4</sub> , 150°C, 3h.....	119
Figure 4.21 (a) UV-Vis spectra and (b) picture of the product liquid showing no H <sub>2</sub> O <sub>2</sub> production on 0.5wt% FeZSM-5 determined by colorimetric method. Conditions: 560mg catalyst, 20mL aqueous solution containing 0.1mol/L H <sub>2</sub> SO <sub>4</sub> and 0.1mol/L TiOSO <sub>4</sub> , 5bar O <sub>2</sub> , 5bar CO, 50°C.....	123
Figure 4.22 CO-DRIFT spectra of (a) 0.1wt% FeZSM-5 with CO desorption at room temperature at different time and (b) 0.1wt% FeZSM-5 and 0.1Fe0.5RhZSM-5 after desorption of 5min at room temperature. ....	124

Figure 4.23 Fe K-edge XANES spectra of fresh, used and in-situ FeRhZSM-5 catalyst along with Fe foil and Fe <sub>2</sub> O <sub>3</sub> used as standards.....	125
Figure 4.24 Arrhenius-type plot using 0.1Fe0.5RhZSM-5 in the temperature range of 24-60°C. Conditions: 5bar O <sub>2</sub> , 5bar CO, 30bar CH <sub>4</sub> , 357mg catalyst, 20mL 0.1mol/L H <sub>2</sub> SO <sub>4</sub> , 30min.....	126
Figure 4.25 Fe K-edge EXAFS data of fresh, used and in-situ FeRhZSM-5 catalyst plotted in Fourier Transform space along with Fe foil and Fe <sub>2</sub> O <sub>3</sub> as standards.....	127
Figure 4.26 Cyclic stability of 0.1Fe0.5RhZSM-5 catalyst. Conditions: 5bar O <sub>2</sub> , 5bar CO, 30bar CH <sub>4</sub> , 560mg catalyst, 50°C, 20mL 0.1mol/L H <sub>2</sub> SO <sub>4</sub> .....	128
Figure 5.1 Oxidation of methanol over iridium-based catalysts. Conditions: 4bar O <sub>2</sub> , 5bar CO, 20bar He, 20mL 3mM methanol, 150°C, 1h.....	141
Figure 5.2 <sup>13</sup> C-NMR spectrum of the aqueous solution after reaction with <sup>13</sup> CO. Conditions: 100mg 1.39wt% Ir <sub>1</sub> Cu <sub>1</sub> Pd <sub>0.1</sub> ZSM-5, 4bar O <sub>2</sub> , 5bar <sup>13</sup> CO, 20bar CH <sub>4</sub> , 150°C, 3h. ....	142
Figure 5.3 Product formation and methanol selectivity on copper and palladium promoted 1.0wt% IrZSM-5. Reaction conditions: 30mg catalyst (40mg for IrCuPdZSM-5), 4bar O <sub>2</sub> , 5bar CO, 20bar CH <sub>4</sub> , 20mL water, 150°C, 1h .....	143
Figure 5.4 Product formation and methanol selectivity (over both liquid and gaseous oxygenates) on 1.33wt% Ir <sub>1</sub> Cu <sub>1</sub> ZSM-5 at (a) different temperatures and (b) different reaction times. Reaction conditions: 30mg catalyst, 4bar O <sub>2</sub> , 5bar CO, 20bar CH <sub>4</sub> , 20mL water, 110-170°C, 0.5-3h.....	144
Figure 5.5 Catalyst stability as shown in (a) Methanol formation of 1.33wt% Ir <sub>1</sub> Cu <sub>1</sub> ZSM-5 catalyst after multiple reaction cycles and (b) XRD patterns of parent ZSM-5, 1.0wt% IrZSM-5 and 1.33wt% Ir <sub>1</sub> Cu <sub>1</sub> ZSM-5 after reaction.....	145
Figure 5.6 Product formation and methanol selectivity on 1.39wt% Ir <sub>1</sub> Cu <sub>1</sub> Pd <sub>0.1</sub> ZSM-5 at different reaction times. Reaction conditions: 40mg catalyst, 4bar O <sub>2</sub> , 5bar CO, 20bar CH <sub>4</sub> , 20mL water, 150°C.....	146
Figure 5.7 Promotional effect of Cu on 1.0wt% IrZSM-5 and 1.06wt% Ir <sub>1</sub> Pd <sub>0.1</sub> ZSM-5 as either heterogeneous metal species or aqueous Cu <sup>2+</sup> ions. Conditions: 4bar O <sub>2</sub> , 5bar CO, 20bar CH <sub>4</sub> , 150°C, 1h, 20mL DI water or aqueous solution of Cu(NO <sub>3</sub> ) <sub>2</sub> .....	147
Figure 5.8 Arrhenius-type plot of 1.0wt% IrZSM-5, 1.33wt% Ir <sub>1</sub> Cu <sub>1</sub> ZSM-5 and 1.06wt% Ir <sub>1</sub> Pd <sub>0.1</sub> ZSM-5. Conditions: 4bar O <sub>2</sub> , 5bar CO, 20bar CH <sub>4</sub> , 20mL DI water, 30min. ....	148
Figure 5.9 UV-Vis spectra of liquid product after H <sub>2</sub> O <sub>2</sub> synthesis reaction with 1.0wt% IrZSM-5 and 1.33wt% Ir <sub>1</sub> Cu <sub>1</sub> ZSM-5. Conditions: 300mg catalyst, 20mL 0.1mol/L H <sub>2</sub> SO <sub>4</sub> , 0.1mol/L TiOSO <sub>4</sub> , 5bar O <sub>2</sub> , 5bar CO, 50°C, 3h. Absorption band centered at 400nm clearly indicated formation of H <sub>2</sub> O <sub>2</sub> on both IrZSM-5 and IrCuZSM-5. The higher intensity on IrCuZSM-5 confirms the promoted formation of H <sub>2</sub> O <sub>2</sub> due to addition of copper. ....	150
Figure 5.10 Normalized Pd K edge XANES spectra of 1.06wt% Ir <sub>1</sub> Pd <sub>0.1</sub> ZSM-5 and Pd foil. The higher absorption edge position and white line intensity clearly demonstrate the presence of cationic Pd species. ....	152
Figure 5.11 Pd K edge EXAFS data and fitting of 1.06wt% Ir <sub>1</sub> Pd <sub>0.1</sub> ZSM-5. Detailed fitting parameters Pd-O: CN 3.02±1.08, R(Å) 2.00±0.02, σ <sup>2</sup> (Å <sup>2</sup> ) 0.008±0.006; Pd-Pd: CN 4.92±1.19, R(Å) 2.76±0.01, σ <sup>2</sup> (Å <sup>2</sup> ) 0.007±0.002 .....	153

Figure 5.12 Ir 4f, Cu 2p and Pd 3d XPS spectra of catalyst 1.0wt% IrZSM-5, 1.33wt% Ir <sub>1</sub> Cu <sub>1</sub> ZSM-5 and 1.06wt% Ir <sub>1</sub> Pd <sub>0.1</sub> ZSM-5. ....	154
Figure 5.13 CO-DRIFTS spectra of (a) 1.0wt% IrZSM-5, 1.33wt% Ir <sub>1</sub> Cu <sub>1</sub> ZSM-5 and 1.06wt% Ir <sub>1</sub> Pd <sub>0.1</sub> ZSM-5 exposed to CO at room temperature and (b) 1.0wt% IrZSM-5 exposed to CO at 25-250°C. ....	155
Figure 5.14 CO-DRIFTS spectra of (a) 1.0wt% IrZSM-5 and (b) 1.33wt% Ir <sub>1</sub> Cu <sub>1</sub> ZSM-5 catalyst after reaction exposed to CO at RT and after 10% CO reduction at 150°C .....	156
Figure 5.15 HAADF and BF image pairs of as-prepared 1.0wt% IrZSM-5 from STEM imaging. Nanoparticles of size up to 2nm are clearly visible on the external surface of zeolite. ....	157
Figure 5.16 Normalized XANES spectra of 1.0wt% IrZSM-5, 1.33wt% Ir <sub>1</sub> Cu <sub>1</sub> ZSM-5 and 1.06wt% Ir <sub>1</sub> Pd <sub>0.1</sub> ZSM-5 with Ir foil and IrO <sub>2</sub> -ZSM-5 at Ir LIII edge .....	158
Figure 5.17 EXAFS fitting of 1.0wt% IrZSM-5, 1.33wt% Ir <sub>1</sub> Cu <sub>1</sub> ZSM-5 and 1.06wt% Ir <sub>1</sub> Pd <sub>0.1</sub> ZSM-5 plotted in R space. XAS spectra were recorded at Ir LIII edge ex-situ in fluorescence mode. ....	160
Figure 5.18 DRIFT spectra of IrZSM-5 in (a) C-H stretching region and (b) CO stretching region after activation with reaction gas (black) followed by H <sub>2</sub> O vapor treatment (red) at 150°C .....	161
Figure 5.19 (a) Product formation rate of 1.0wt% IrZSM-5 and 0.05wt% IrZSM-5, conditions: 4bar O <sub>2</sub> , 5bar CO, 20bar CH <sub>4</sub> , 150°C, 1.6μmol Ir, 20mL DI water, 1h; (b) EXAFS data of 1.0wt% IrZSM-5, 0.05wt% IrZSM-5 and Ir foil in R space. ....	162
Figure 5.20 EXAFS fitting of 0.05wt% IrZSM-5 plotted in R space. XAS spectra were recorded at the Ir LIII edge ex-situ in fluorescence mode. Detailed fitting parameters Ir-O: CN 6.00±0.7, R(Å) 1.97±0.01, σ <sup>2</sup> (Å <sup>2</sup> ) 0.002±0.001; Ir-Ir: 0. ....	163

## List of Tables

Table 1.1 Standard heat of combustion of C1 species .....	11
Table 3.1 Calculated CH <sub>4</sub> conversion at different reaction time.....	61
Table 3.2 Physicochemical properties of ZSM-5 supported Rh catalysts.....	65
Table 3.3 Rhodium leaching during methane oxidation reaction at conditions.....	66
Table 3.4 Fraction of cationic and metallic rhodium species from LCF of Rh K-edge XANES spectra ...	78
Table 3.5 EXAFS fitting parameters for RhZSM-5 catalysts at Rh K-edge.....	80
Table 4.1 Notations, preparation methods and metal species dispersion of the catalysts tested.....	91
Table 4.2 Metal-oxo structures proposed after oxidation with peroxide species for C-H bond activation .....	112
Table 4.3 Catalytic activity of rhodium-based catalyst at 50°C in different solvents .....	121
Table 5.1 Product formation on 0.06wt% PdZSM-5 and 1.06wt% Ir <sub>1</sub> Pd <sub>0.1</sub> ZSM-5 catalyst with different oxidants.....	150
Table 5.2 Product formation on IrPdZSM-5 catalyst with different atomic ratio.....	151
Table 5.3 Product formation on IrCuZSM-5 catalyst with different atomic ratio .....	151
Table 5.4 EXAFS fitting parameters for iridium catalysts at Ir LIII edge .....	160

# Chapter 1 Introduction

## 1.1 Supported single atom catalysts

Supported single atom catalysts represent a unique family of catalysts where each metal atom forms a mononuclear species and coordinates only with ligands supplied by catalyst support or secondary promoters. Similarities can be drawn from homogeneous catalysts where the metal center coordinates with ligands in the liquid phase. Heterogeneous catalysts are widely used in the petrochemical industry, responsible for the efficient production of major industrial commodities like petroleum, diesel, syngas, ammonia, sulfuric acid. environmental technology. They tend to have higher catalytic activities due to under-coordinate sites at kinks, steps and edges. However, the supported metal sites easily form mixed structures, with nature of site ranging from metal cations, oxide to metallic and sizes from sub-nano meter to tens of nanometers. Homogeneous catalysts, on the other hand, offer well-defined and uniform structures. Supported single atom catalysts bridges these two catalyst families in the sense that the metal species are mononuclear and uniform as in molecular catalysts, but are still under-coordinated like other supported catalysts.

The chance to achieve maximum metal efficiency, which means all active sites are exposed and accessible by reactants as compared to clusters and nanoparticles, is another important property of single atom catalyst. This is particularly important for noble metal active species, for which we want to achieve the highest activity with a given loading. A number of single-site catalysts, with noble metals from Pt<sup>1,2</sup>, Au<sup>3,4</sup>, Pd<sup>5</sup> and Rh<sup>6</sup> supported on oxides or zeolites have been reported to be highly active for a range of reactions. Zeolites are highly crystalline aluminosilicates with well-defined framework structure and micropore channels. The cation exchange sites on the zeolite framework can accommodate and stabilize low valence metal ions (+1 to +3 ions) through electrostatic interaction. Pt<sup>2</sup>, Au<sup>4</sup> and Fe<sup>7</sup> catalysts supported on zeolite with atomic dispersion of ions have been successfully synthesized, respectively, by ion exchange, direct impregnation of metal cluster or chemical vapor impregnation. Whereas such

catalysts are under study in reactions like the water gas shift and CO oxidation, the direct conversion of methane to oxygenates is a relatively unexplored area.

## 1.2 Direct conversion of methane to oxygenates

The recent breakthrough in hydraulic fracturing has ushered in a new age of cheap and abundant natural gas supply. The yearly market production of natural gas in US has reached 33,000,000 million cubic feet in 2018<sup>8</sup> and shale gas constitutes more than 50% of the gas withdrawal. The abundant supply of natural gas has drawn renewed interest in alternative method of valorization, and gas-to-liquid technology is currently under heated discussion.



Figure 1.1 U.S. natural gas gross withdrawals (2000-2016).<sup>8</sup>

The energy-efficient utilization of methane has long been a major topic of study for the chemical and energy industries. As the main component of natural gas the problem lies in the fact that: 1) methane is the most inert molecule in all hydrocarbons, with four symmetrical C-H bonds and a bond energy of 104 kcal/mol, high ionization potential and low electron affinity<sup>9</sup>; 2) The high bond energy means that activation of methane is usually achieved by using harsh conditions or highly energetic species, while the

desired product, namely C1-2 oxygenates and aromatics can be easily oxidized to CO<sub>2</sub> at these conditions;

3) The global methane reserves are inconveniently located in remote areas of the world, like Alaska, Siberia and deep oceans. Currently, methane extracted as associated gas together with oil is flared directly to avoid emitting this potent greenhouse gas in the atmosphere. The World Bank estimates around 5 trillion cubic feet of natural gas is flared annually worldwide. Still, flared natural gas is ultimately converted to CO<sub>2</sub> which accounts for 1.2% of global CO<sub>2</sub> emission<sup>10</sup>. Methane from large natural gas reserves is either transported through the pipeline network or condensed to liquefied natural gas (LNG) for shipping. Both of these two methods require high capital investment in infrastructure. Although oil price is experiencing a dip, the dwindling oil reserves still call for an alternative source of fuel that is relatively cheap, with low carbon emission intensity and can be readily incorporated into the current chemical industry to provide chemical feedstock. Methane has long been used both as a fuel and as the raw material to produce syngas, hydrogen, methanol, dimethyl ether and hydrocarbons. Methane steam reforming has been the source of hydrogen and syngas from the 1930s and it is current at an affordable price: 2.5 dollars per 1000 cf. if imported via pipeline (as disclosed by US Energy Information Administration). An alternative to the current transportation of methane, either via LNG tanks or through pipelines, is to convert methane to liquid fuel. For the gas reserves at remote locations, it is desirable to convert methane into its liquid oxygenates (which has a higher energy density) in a low footprint process and ship it to customers cheaply through containers similar to the refined petroleum products of today<sup>11</sup>. Stranded gas which used to be flared directly can also be utilized should a low-profile methane-to-liquid process be available.

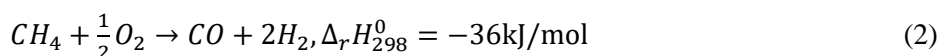
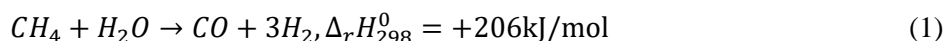
As more oxygen is incorporated, methane is first converted to methanol and then to its deep oxidation products. The reduction in chemical energy as we go from methanol to formic acid means that quenching the oxidation process in the methanol stage is the most desirable in an energy sense. Methanol can be directly used in methanol fuel cells to produce electricity or serve as a source of hydrogen through methanol steam reforming.

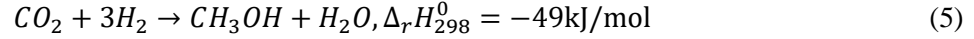
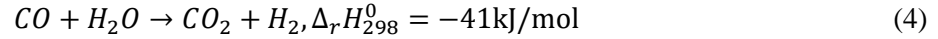
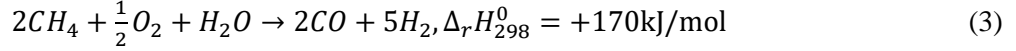
Table 1.1 Standard heat of combustion of C1 species<sup>12</sup>

C1 species	$-\Delta_c H^0$ (kcal/mol)
CH <sub>4</sub>	212.79
CH <sub>3</sub> OH	173.64
HCHO	136.42
HCOOH	60.86
CO	67.64
CO <sub>2</sub>	0

Besides, methanol can undergo a number of processes like partial oxidation, carbonylation, methanol-to-olefin (MTO) or coupling reactions to produce formaldehyde, acetic acid, olefins, methylformate and dimethyl ether. In 2012, about 56 million metric tons of methanol were consumed around the world, and the demand is projected to reach 104 million metric tons by 2022, with a growth rate exceeding 6% per year. China is responsible for 80% of this growth and is projected to consume 63 million metric tons of methanol by 2022<sup>13</sup>. Therefore, the combination of this big market demand with the abundant source of natural gas worldwide (especially with the shale gas now available) leads to renewed interest for the direct methane-to-methanol process both in academia and in industry.

The conventional methanol synthesis process consists of two energy intensive steps: First, conversion of methane to syngas at high temperature (typically over 800°C) takes place through steam reforming in most part (rxn 1), but also through partial oxidation or autothermal reforming reactions<sup>14</sup>, rxns 2 and 3. Second, after the water gas shift (WGS) reaction is used to adjust the CO: H<sub>2</sub> ratio, rxn 4, the syngas is passed over a Cu/Zn/Al<sub>2</sub>O<sub>3</sub> catalyst at 35-55 bar, 200-300°C to yield methanol<sup>15</sup>, rxn 5:





This process is energy intensive and only when carried out in large scale can it be economically viable.

To make better use of the stranded natural gas and remote natural gas reserves, a direct, highly selective one-step conversion of methane to methanol is the most attractive.

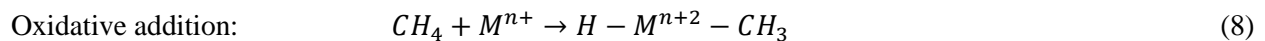


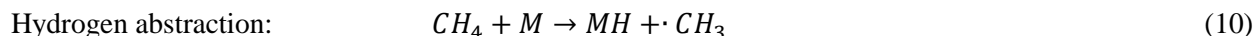
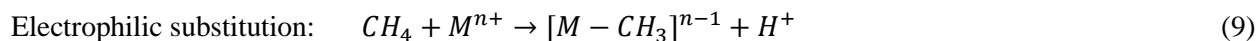
Besides, other value-added products can be obtained from methane through oxidative coupling, carboxylation and aromatization reactions. Acetic acid is a major chemical feedstock and is used to produce vinyl acetate monomer (VAM), which is the precursor for PVA plastics. Production of terephthalic acid (PTA) also uses acetic acid as a solvent and PTA is further used to produce polyethylene terephthalate (PET). The global acetic acid market was valued at 14,234 kilotons in 2017 and is expected to reach 18,296 kilotons by 2023, showing an annual growth rate of 4.9%. The direct carboxylation of methane to acetic acid with oxygen is another attractive goal of methane upgrading as the current technology of its production also relies on the multi-step methanol synthesis followed by carbonylation of methanol.



### 1.3 Methane activation review

A key step in the functionalization of methane is the activation of the inert C-H bond. Over the years, different mechanisms of methane activation have been identified and are listed below:



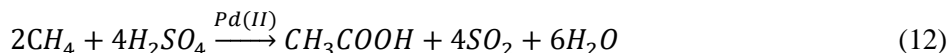
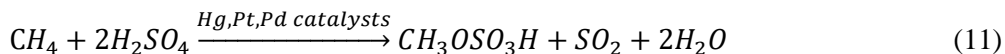


Oxidative addition of methane was first demonstrated on  $(\eta^5-C_5Me_5)Ir(CO)_2$  complex in 1983<sup>16</sup>. After the complex was thermally or photochemically activated in the presence of methane, its methyliridium hydride derivative was formed and well characterized. Although the yield of the activation product can reach 20% after 6 h of irradiation, subsequent functionalization of the methyl species was not reported. In 1969, Shilov et al discovered the “Shilov system”, in which methane can be converted to a mixture of methanol and methyl chloride in aqueous solutions of  $[PtCl_4]^{2-}$  and  $[PtCl_6]^{2-}$ <sup>17</sup>. Following research revealed that the reaction proceeds through the activation of methane on  $[PtCl_4]^{2-}$  and the square planar  $[PtCl_3CH_3]^{2-}$  structure formed can be oxidized by  $[PtCl_6]^{2-}$ . The use of prohibitively expensive  $[PtCl_6]^{2-}$  as oxidant limited its potential to be a realistic catalytic system, and the exact mechanism of activation is still under debate. Still, this inspired great interest in the research on electrophilic activation of methane in the years that followed. In this section, the more recent catalytic systems that activate methane and catalyze its functionalization are reviewed, with their main features, merits and drawbacks highlighted.

### 1.3.1 Activation of methane in strongly acidic media

The most effective low-temperature conversion of methane to oxygenates is achieved on electrophilic metal cations or complexes in strongly acidic media. The reaction features high conversion of methane and good selectivity to oxygenates at temperatures around 200°C. These electrophilic metal cations can remove electrons from the bonding orbitals of methane, leading to heterolytic cleavage of the C-H bond. The work by Periana’s group has covered a wide range of homogeneous catalysts, including  $Hg(II)$ <sup>18</sup>,  $(bpym)PtCl_2$ <sup>19</sup>,  $Pd(II)$ <sup>18, 20</sup> and  $Au(III/I)$ <sup>21</sup> in concentrated sulfuric acid.  $H_2SO_4$  serves as both oxidant and solvent and methyl ester is the primary oxidation product of methane. For  $Au(III/I)$ , only stoichiometric conversion of methane to methanol derivatives is observed in 98%  $H_2SO_4$  and cationic Au is reduced to

Au(0). Addition of selenic acid can oxidize Au(0) back to cationic state but it is unclear whether it is in the Au(III) or Au(I) state. On Pd(II), the formation of acetic acid is also observed<sup>20</sup>.



The general reaction mechanism can be broken down into three steps: methane activation through electrophilic displacement by the acid counter anion, reductive elimination of the metal methyl complex to generate the methyl ester product and the reduced metal catalyst, and the re-oxidation of the catalyst to its original state (see Fig. 1). In the case of (bpym)PtCl<sub>2</sub> the oxidation step precedes the functionalization step that gives first a oxidized Pt(IV)-CH<sub>3</sub> species followed by reductive elimination to re-generate Pt(II) catalyst<sup>19</sup>.

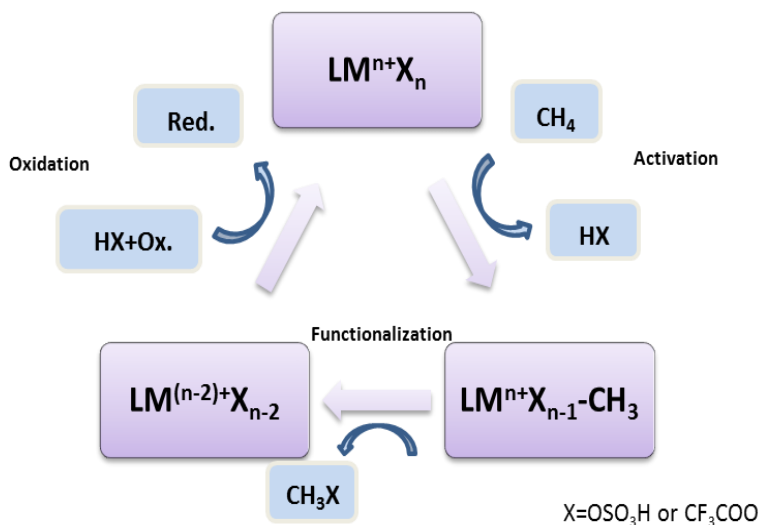
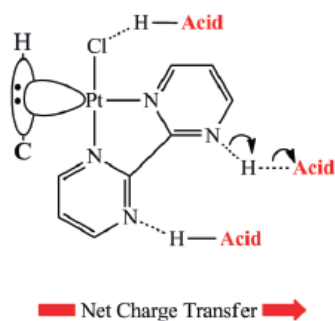


Figure 1.2 Schematic of a typical electrophilic methane oxidation catalytic cycle (adapted from 18-21)

The presence of concentrated acid is essential for this system. First, the counter anion of a strong acid



(written as X<sup>-</sup>) is a weak base and it binds weakly to the electrophilic metal center. The incoming methane molecule can easily displace X<sup>-</sup> and coordinate with the metal center. Second, the product of methane oxidation is formed directly as the ester of methanol. The acid counter anion, which is an electron drawing ligand, can retard the

participation of C-H bonds of the methyl ester in further electrophilic reactions<sup>18</sup>. Other methanol molecules will be present as protonated methanol (CH<sub>3</sub>OH<sub>2</sub><sup>+</sup>). Indeed, a lower rate of oxidation of methyl ester compared to methane has been observed on a number of catalysts<sup>18, 19</sup>. Finally, in the case of H<sub>2</sub>SO<sub>4</sub> acting as an oxidant, it is sufficiently strong to oxidize reduced metal species back to higher oxidation state. Recently, a non-catalytic system using H<sub>2</sub>O<sub>2</sub> as initiator and fuming sulfuric acid to convert methane to methyl sulfonic acid with high conversion was reported. The H<sub>2</sub>O<sub>2</sub> only initiates the reaction to form a CH<sub>3</sub><sup>+</sup> radical that react with SO<sub>3</sub>. The reaction does not generate SO<sub>2</sub> as a byproduct.<sup>22</sup>

Both the Sen's and Moiseev's groups have shown that in trifluoroacetic acid (TFA), Pd(II) can also activate methane and perform stoichiometric oxidation to give methyl ester and palladium black at above 80°C<sup>24, 25</sup>. The reaction becomes catalytic if H<sub>2</sub>O<sub>2</sub> is added<sup>26</sup>.

Based on the positive results obtained with homogeneous catalysts, their heterogeneous analogs that operate in acidic media are also investigated. Sen's group showed that using 5%Pd/C and a mixture of H<sub>2</sub> and O<sub>2</sub>, methane and ethane can be converted to their corresponding carboxylic acids in nitromethane/TFA mixture. The H<sub>2</sub> and O<sub>2</sub> can generate H<sub>2</sub>O<sub>2</sub> in situ and the reaction occurred only under acidic conditions<sup>27</sup>. However, the high selectivity to formic acid makes the system less attractive for methane conversion. A similar system that uses 5%Pd/C and copper chloride as catalyst is shown to oxidize methane to methanol derivatives with oxygen and carbon monoxide in a 3:1 volume mixture of

TFA and water<sup>28</sup>. Here CO and O<sub>2</sub> still serve as in situ generator of H<sub>2</sub>O<sub>2</sub>, but under this circumstance, water is necessary to complete this reaction:



Furthermore, the addition of copper chloride can shift the selectivity mainly to methanol and its ester. The heterogeneous Pt catalysts were investigated by Schuth's group. Since the 2,2'-bypyrimidine group is essential to stabilize the Pt(II) species as a bidentate ligand and prevents it from precipitating, their strategy focused on designing heterogeneous analog of this ligand as a solid support. A series of solid supports, including a covalent triazine-based framework (CTF), a polybenzimidazole (PBI) network and a nitrogen-doped carbon from the skeleton of lobster were synthesized that contain numerous nitrogen coordination sites and Pt(II) can be readily deposited onto them<sup>29-31</sup>. Reaction was carried out under similar conditions as Periana's work, i.e. 215°C, 102% H<sub>2</sub>SO<sub>4</sub> and the catalyst was found to be reusable. In addition, barium sulfate supported Pt(SO<sub>4</sub>)<sub>2</sub>, HgSO<sub>4</sub>, Ce(SO<sub>4</sub>)<sub>2</sub> and Pb(SO<sub>4</sub>)<sub>2</sub> treated in 100% sulfuric acid can convert methane to methanol in the gas phase<sup>32</sup>. Oxygen is claimed to be the terminal oxidant by conducting SO<sub>2</sub> oxidation to SO<sub>3</sub> in-situ but the validity of this claim is questionable.

Apart from C1 oxygenates, several reports have shown that methane can also undergo direct carboxylation reactions to yield acetic acid. Early work on Pd(II)/Cu(II) in TFA demonstrates carboxylation of methane with CO using K<sub>2</sub>S<sub>2</sub>O<sub>8</sub> as oxidant<sup>33</sup>. Low yield of 0.4% based on methane is achieved. Although the author claims in the presence of Pd(II) the reaction proceeds by the electrophilic activation, radical pathways cannot be ruled out as decomposition of TFA generates CF<sub>3</sub>·. The fact that carboxylation can also be observed in CO<sub>2</sub> instead of CO provides additional evidence<sup>34</sup>. In concentrated sulfuric acid, Pd(II) can catalyze direct condensation of methane to acetic acid where both of the two carbon atoms originate from methane. A CO intermediate from overoxidation of methane is believed to be the carbonylation agent and the total yield of methanol and acetic acid is 12% after 4 h at 180°C<sup>20</sup>. During the process, Pd(0) is formed due to the low oxidation rate of Pd(0) to Pd(II) by H<sub>2</sub>SO<sub>4</sub>. This re-oxidation step can be facilitated by adding CuCl<sub>2</sub> and O<sub>2</sub>, thereby extending catalyst stability<sup>35</sup>.

The reports reviewed so far mainly pertain to the electrophilic activation of methane in protic media. Although radicals are known to activate methane at high temperatures<sup>36</sup>, the selectivity is difficult to control as high energy radicals readily induce deep oxidation. Interestingly, the work by Fujiwara and Pombeiro's group shows that vanadium catalysts, such as VO(acac)<sub>2</sub>, amavadinone and vanadium containing heteropolyacids can convert methane and CO to acetic acid by using a radical initiator K<sub>2</sub>S<sub>2</sub>O<sub>8</sub> in TFA<sup>37-39</sup>. Contrary to what one might assume for radical reactions, which leads to mainly complete oxidation, a yield of 14%-50% for acetic acid based on methane can be achieved under only 5atm of methane (20 h, 80°C). The authors proposed that methyl radical (CH<sub>3</sub>·) is generated by hydrogen abstraction either directly from a SO<sub>4</sub>· radical (generated by S<sub>2</sub>O<sub>8</sub><sup>2-</sup>) or from a high valence vanadium species (V<sup>V</sup>-oxo or V<sup>V</sup>-peroxo). CO can further combine with CH<sub>3</sub>· and abstract an oxygen from the catalyst generating CH<sub>3</sub>COO·. The cycle is completely by hydrogen abstraction from methane to CH<sub>3</sub>COO· and form CH<sub>3</sub>COOH and CH<sub>3</sub>·.

In summary, methane activation in strongly acidic media is an effective method to achieve methane conversion. The electrophilic activation of methane gives high rate of conversion and the protection of methanol by forming esters and protonated CH<sub>3</sub>OH<sub>2</sub><sup>+</sup> guarantees high selectivity. Still, the process is limited by a number of factors. The ester formed requires further hydrolysis and then re-concentration of acids. Oxidants required to oxidize the reduced metal, namely selenic acid or K<sub>2</sub>S<sub>2</sub>O<sub>8</sub>, are too expensive. The most active system so far, the Periana system, is prone to inhibition of water formed through over-oxidation during the reaction<sup>19</sup>. Finally, the corrosive nature of this system and formation of SO<sub>2</sub> when H<sub>2</sub>SO<sub>4</sub> is the oxidant draws environmental and safety concerns.

### 1.3.2 Activation of methane in aqueous media

Compared to the acidic media, water is the most environmentally benign solvent and caters to the concept of green chemistry. Several groups have sought to design catalysts that can convert methane to

oxygenates in water solutions. Greener oxidants, mainly  $\text{H}_2\text{O}_2$  solutions or  $\text{O}_2$  with a reductive promoter, are used in the aim of generating a pollution-free process. Using aqueous solutions of  $\text{H}_2\text{O}_2$  (0.35M), methane can be oxidized to a mixture of methanol, methyl hydroperoxide and formic acid on a phthalocyanine (Pc)-based Fe catalyst,  $(\text{FePc}^t\text{Bu}_4)_2\text{-SiO}_2$ <sup>40, 41</sup>. After 20 h at 60°C, 0.04% of methane is converted and the reaction shows poor selectivity to methanol. Also, the catalyst supported on silica suffers from intense iron leaching into the liquid phase and is not reusable. Several water-soluble metal chloride salts are also investigated<sup>42</sup>. Among the group VIII and group 1B metal salts,  $\text{OsCl}_3$  and  $\text{HAuCl}_4$  show the highest turnover frequency for C1 oxygenates. Study with radical inhibitors suggests that formation of hydroxyl radicals through the interaction of  $\text{H}_2\text{O}_2$  with the catalyst is responsible for the reaction. Similar radical mechanism has also been observed on a palladium-gold nanoparticle alloy supported on  $\text{TiO}_2$  ( $\text{PdAu/TiO}_2$ ) and methanol can be formed with selectivity of 50~70% but at very low conversions (conversion <0.01% after 1h)<sup>43</sup>. In a more recent report, PdAu colloidal nanoparticles are found to catalyze this reaction more efficiently than  $\text{PdAu/TiO}_2$  using  $\text{O}_2$  as terminal oxidant and  $\text{H}_2\text{O}_2$  as initiator. A sub-stoichiometric amount of  $\text{H}_2\text{O}_2$  is consumed for product formation<sup>44</sup>. The most promising result in an aqueous  $\text{H}_2\text{O}_2$  system is reported by Hammond et al. On CuFe-ZSM-5 prepared by solid state ion exchange, methane can be oxidized at high turnover frequency ( $\text{TOF} > 14000 \text{ hr}^{-1}$ ) and conversion can reach 10% at 70°C within 1h. Selectivity of methanol can be improved by loading Cu onto the Fe-ZSM-5 catalyst and suppressing the further oxidation of methanol by hydroxyl radicals<sup>45, 46</sup>. The activation of methane is achieved by a di-iron species anchored on the ZSM-5 framework and its interaction with  $\text{H}_2\text{O}_2$  generates a  $\text{Fe}^{2+}/\text{Fe}^{4+}$  dimer.

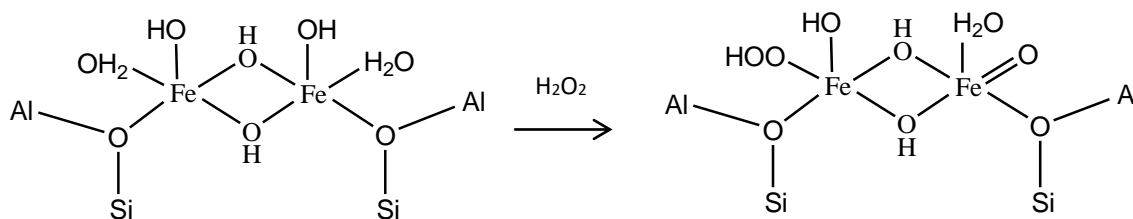
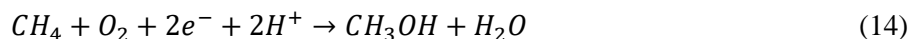


Figure 1.4 Generation of active center on Fe-ZSM-5.<sup>45</sup>

Following this work, a number of other isolated metal atoms or clusters immobilized inside microporous or mesoporous matrix have also been reported to catalyze methane oxidation to methanol or formic acid using H<sub>2</sub>O<sub>2</sub> as oxidant. Pd<sub>1</sub>O<sub>4</sub> moiety anchored inside ZSM-5 micropores achieved similar level of conversion (12.3%) with 0.01wt% Pd loading and the selectivity to methanol is also improved through impregnation of CuO<sup>47</sup>. A ligand stabilized tricopper complex immobilized in MCM-41 catalyzes the oxidation of methane with H<sub>2</sub>O<sub>2</sub> at RT<sup>48</sup>. Finally, catalytic activity using isolated iron species anchored on MOF (Al-MIL-53) was also demonstrated. However, due to the stability of the material, the reaction was limited to temperatures below 60°C<sup>49</sup>. On open support, atomically dispersed iron stabilized by graphene cavity<sup>50</sup> or rhodium supported on ZrO<sub>2</sub><sup>51</sup> were also reported, suggesting that micropores are not the pre-requisite to construct active catalytic center.

The in-situ generation of H<sub>2</sub>O<sub>2</sub> is another method frequently employed in aqueous batch reaction systems. O<sub>2</sub> can be activated by a reductive promoter to generate H<sub>2</sub>O<sub>2</sub> on the catalyst surface and oxidize methane at low temperatures. This highly resembles the oxidation of methane carried out by soluble or particulate methane monooxygenases where the 2-electron promoter is NADH.

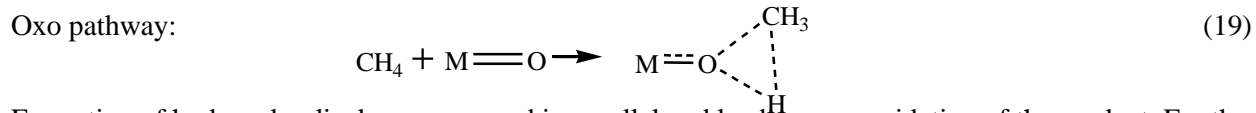
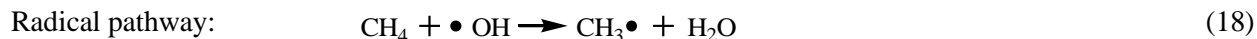


Pd is known to catalyze H<sub>2</sub>O<sub>2</sub> formation from O<sub>2</sub> and H<sub>2</sub>, thus catalysts based on Pd have been investigated in a mixture of H<sub>2</sub>, O<sub>2</sub> and methane. Palladium gold alloy nanoparticles<sup>43</sup> and Pd/C<sup>27</sup> suspended in aqueous phase either gives low methane conversion at mild conditions or high selectivity to formic acid and CO<sub>2</sub> if conversion is pushed higher, indicating a trade-off between selectivity and conversion is inevitable if the methanol product is not properly protected from overoxidation. In water solution, direct carboxylation of methane with O<sub>2</sub> and CO can also be performed to yield acetic acid. The homogeneous RhCl<sub>3</sub>-NaCl-HI catalyst system reported by Lin and Sen<sup>52</sup> catalyzes this reaction at a low TOF (0.07 h<sup>-1</sup> at 420 h). Mechanistic study shows that a Rh-oxo center formed from either interaction with reactive intermediate (HIO or H<sub>2</sub>O<sub>2</sub>) or direct interaction of O<sub>2</sub> with Rh carbonyl species can activate methane into formyl species<sup>53</sup>. Subsequent research in a H<sub>2</sub>O:C<sub>3</sub>F<sub>7</sub>COOH=6:1<sup>54</sup> or D<sub>2</sub>O:CD<sub>3</sub>COOD=4:1<sup>55</sup>

solvent mixture shows a five to six times increase in acetic acid yield. The role of I<sup>-</sup> was proposed to be the catalyst to activate O<sub>2</sub> through a set of redox reactions<sup>53</sup>:



It can be generalized that in aqueous solutions, catalyst interaction with peroxide type oxidant mainly results in two pathways to activate methane. First is the generation of hydroxyl radicals via a Fenton-type chemistry and it further abstracts one hydrogen from methane, as evidenced by O-FeN<sub>4</sub>-O on graphene, Pd/C and AuPd/TiO<sub>2</sub> catalysts (However, Pd may behave in a different way in a concentrated acid by forming Pd<sup>2+</sup>/Pd<sup>0</sup> redox couple<sup>22, 29</sup>). Second is the oxidation of metal catalysts to a metal-oxo or peroxo structure that can oxidize methane directly in water, as seen on Fe-ZSM-5, Fe-MIL-53, Pd-ZSM-5, (FePc<sup>t</sup>Bu<sub>4</sub>)<sub>2</sub>-SiO<sub>2</sub> and RhCl<sub>3</sub>-NaCl-HI catalysts.



Formation of hydroxyl radicals may proceed in parallel and lead to over-oxidation of the product. For the first pathway, selectivity is difficult to maintain at high methane conversions. Mild conditions and short contact time are necessary to give methanol as primary product and the overall methanol yield will be low. The second pathway offers more control over the selectivity as the further oxidation of methanol to deep oxidation products can be suppressed by adding copper<sup>45</sup>, giving high selectivity to methanol.

### 1.3.3. Activation of methane in the gas phase

The activation of methane by oxo compounds formed through high temperature treatment of catalyst with oxidant was first demonstrated by Panov in 1990<sup>56</sup>. Fe-ZSM-5 was found to decompose N<sub>2</sub>O at

250°C and gave off N<sub>2</sub>, along with depositing an α-oxygen species on the iron center. This α-oxygen species can selectively convert methane to methanol at room temperature<sup>57</sup>. The active center for this conversion is thought to be octahedral and tetrahedral Fe<sup>2+</sup> formed through self-reduction of Fe<sup>3+</sup> during high temperature calcination in vacuum or in steam<sup>58</sup>. Later, Smeets et al showed that copper ion exchanged ZSM-5 and MOR can demonstrate similar reactions<sup>59</sup>. In this case, Cu-ZSM-5 is activated in O<sub>2</sub> at 450°C, which gives rise to a mono(μ-oxo) dicopper(II) core that can abstract one hydrogen from methane and form a methoxy species through a rebound mechanism<sup>60, 61</sup>. After that several other metals were investigated in a similar fashion, namely cobalt and nickel<sup>62, 63</sup>. Co-ZSM-5 can convert methane to a mixture of methanol and formaldehyde using a 550°C activation step in flowing air and 150°C methane reaction step. Cobalt oxide is believed to be responsible for the formation of methanol while Co cation leads to the formation of formaldehyde. Ni-ZSM-5 on the other hand forms the similar mono(μ-oxo) dinickel structure but the product is a mixture of methanol, formic acid and ethylene glycol. Furthermore, the dicopper center is not the only active site that carries out the reaction. Tricopper site and copper oxide clusters were also found to be active<sup>64-66</sup>. The matrix that stabilize the active copper site is further extended to SSZ, SAPO-34, MOF and even SiO<sub>2</sub>.

The major drawback of this system is that it is non-catalytic in nature. First, the oxygenate formed after reaction is strongly adsorbed at the metal site inside the zeolite micropore channel and an additional ex-situ extraction by protic solvent (water or acetonitrile) is needed to close the catalytic cycle. Heating the catalyst would result in the further oxidation of methoxy species to CO<sub>x</sub> before they can desorb.

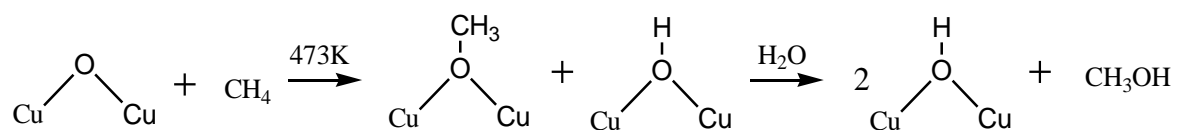


Figure 1.5 Methane to methanol reaction scheme on Cu-ZSM-5.<sup>59-61, 63</sup>

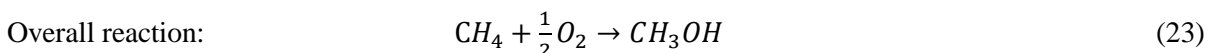
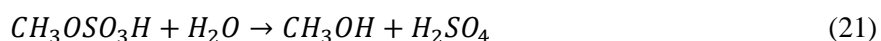
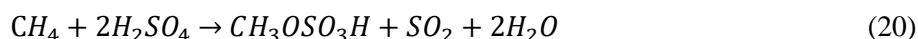
Alayon et al proposed an in-situ extraction process that use water vapor saturated helium to desorb methanol. By combining this extraction with oxygen activation and methane activation steps, they can

form a closed catalytic cycle in-situ<sup>68</sup>. Still, the extraction step takes up to 5 hours of purging to fully desorb the product, which makes the whole process highly inefficient. Furthermore, the activation of the catalyst by oxidant needs to be carried out at high temperature which forms the oxo complex needed for methane activation, while the methane activation step is performed in a stream 200°C lower. This cyclic operation is necessary due to poor selectivity to methanol if methane reacts with the activated catalyst at the same temperature as the oxidant activation step. Recently, efforts have been made to conduct this reaction isothermally and catalytically on both Fe-ZSM-5 and Cu-ZSM-5<sup>69, 70</sup>. On Fe-ZSM-5, N<sub>2</sub>O and methane were reacted with a 1:1 volume ratio at 160°C and a maximum TON of around 3 was achieved without desorbing the product. The authors postulate that spillover of methoxy species can liberate active sites for further deposition of  $\alpha$ -oxygen. For Cu-ZSM-5, NO is used to activate the catalyst at 150°C and methane is passed over the catalyst at the same temperature. An isothermal and catalytic process for this reaction is challenging, as the water extraction step cannot be incorporated into the reaction step. Water readily destroys the active oxo complex before it reacts with methane (considering the much weaker bond of H-O in water compared to C-H bond in methane). Recently, catalytic turnover on CuZSM-5 was demonstrated by Narsimhan et al. by cofeeding CH<sub>4</sub>, O<sub>2</sub> and H<sub>2</sub>O vapor. However, the reaction rate is too low to be economically viable (1.81  $\mu$ mol/g/h) and methanol selectivity decreases to 70% due to over-oxidation<sup>71</sup>. Apart from oxidation to methanol, several other types of chemistry were demonstrated on the copper oxo structure. Further functionalization of methoxy specie to acetic acid was catalyzed by the Brønsted acid site of zeolite<sup>72</sup>. Sushkevich et al. showed that cyclic operation with water as oxidant is also plausible, yielding an anaerobic process the produces hydrogen and methanol<sup>73</sup>.

Although the merit of high selectivity to oxygenates is well recognized for this system, the challenges illustrated above have limited its realistic application. Besides, the problem of low product yield needs to be addressed before we can consider it as a viable candidate for future methane conversion. The highest product yield reported so far is on the level of <200  $\mu$ mol/g for methane oxidation and 60.9  $\mu$ mol/g for oxidative methane carbonylation<sup>72</sup>.

### 1.3.4. Strategies for molecular oxygen activation

Molecular oxygen or more preferably, air, is considered as the most economic and environmentally friendly oxidant. From the various catalytic systems reviewed in section 3.1, the use of O<sub>2</sub> as a terminal oxidant has been an important aspect of research for methane conversion. The ground-state triplet oxygen cannot interact directly with CH<sub>4</sub> at low temperatures. Several strategies are proposed that utilize O<sub>2</sub> either in-situ or ex-situ as oxidant. One method requires the use of an oxidant to convert methane that is readily regenerable by aerobic oxidation. In this case the oxidant serves as an oxygen carrier to perform methane oxidation. For example, an ex-situ process that includes hydrolysis of methyl ester and oxidation of SO<sub>2</sub> to SO<sub>3</sub> is proposed in the Periana system:



Aerobic oxidation of methane using oxygen mediators has also been reported. Bao et al.<sup>74</sup> designed an electron-transfer chain system that uses benzoquinone and NO<sub>2</sub> as oxygen mediator and Pd(II) as methane oxidation catalyst in TFA. However, only 6.9 turnovers can be achieved after 10 h at 80°C. Bar-Nahum et al.<sup>75</sup> found that polyoxometalate (H<sub>5</sub>PV<sub>2</sub>Mo<sub>10</sub>O<sub>40</sub>) can mediate the aerobic oxidation of methane when it is ion exchanged with [MebpymPtCl<sub>2</sub>]<sup>+</sup> and loaded onto silica. TON of 6 can be achieved in water at 50°C after 4 h.

Finally, the use of reductive promoters to induce two electron activation of O<sub>2</sub> is the most common method. The reducing agents reported include (but are not limited to) hydrogen<sup>27, 28, 43</sup>, carbon monoxide<sup>29, 52, 53</sup>, aldehydes<sup>76, 77</sup> and zinc powder<sup>78</sup>. The activation of O<sub>2</sub> does not necessarily induce observable H<sub>2</sub>O<sub>2</sub>

as it is considered short-lived at high temperatures and the reductive promoters are sacrificial reagents that are oxidized during the oxygen activation step.

#### 1.4 Single site catalysts for C-H bond activation

The application of single site catalysts for C-H bond activation has been gaining momentum in recent years. The uniform structure of single site catalysts offers unique balance of high activity and high selectivity. Notable examples of their application include nonoxidative alkane and alcohol dehydrogenation<sup>79, 80</sup>, C-C coupling reaction<sup>81</sup>, olefin hydroformylation<sup>82, 83</sup> and selective alkane oxidation<sup>84, 85</sup>. Metal species with atomic dispersion display different electronic state which in turn lead to different binding of the reactant. The weak binding of single atom alloy PtCu to butane leads to only partial dehydrogenation of butane and limits coke formation<sup>79</sup>. In hydroformylation reaction, isolated rhodium species catalyze regio-selective formation of linear aldehyde by kinetically favoring the activation of terminal C-H bond of the alkene<sup>82</sup>. For selective oxidation reactions, single site iron stabilized on zeolite or graphene selectively converts linear alkanes to their corresponding alcohols at close to ambient temperature with H<sub>2</sub>O<sub>2</sub>. The unique property of single atom catalysts has opened up new route in C-H bond activation and the application of this strategy to selective methane oxidation using molecular oxygen is a promising solution to this challenging problem in catalysis. Specifically, single atom catalysts have the potential to catalyze both oxygen activation and methane activation reactions with high activity. These two steps are considered crucial for an effective catalytic process to convert methane to oxygenates using molecular oxygen at low temperature.

## 1.5 Thesis objectives

Based on the literature review above, one concludes that although breakthroughs have been made in homogeneous catalysis for efficient methane conversion, a heterogeneous, environmentally benign and clean catalytic process that uses molecular oxygen and converts methane into oxygenates at high yields at mild conditions has yet to be developed and demonstrated. In aqueous phase, CO has been identified as an effective promoter to activate molecular oxygen and soluble salts of palladium<sup>27</sup>, rhodium<sup>52</sup> and vanadium<sup>86</sup> have been reported to convert methane at a low rate. Their heterogeneous analogs were only studied in a cursory manner, using large metallic particles supported on carbon (5% Pd/C and Rh/C). These catalysts behave rather differently due to a different valence and coordination state of the metallic particles compared to their salts in solution and supported single atom catalysts. What's more, only a small fraction of metal sites is utilized with the limited surface sites available. Therefore, careful consideration of preparation techniques needs to be conducted to synthesize the catalysts with metals dispersed in their single site cationic state and properly stabilized, which would bring their electronic state closer to their counterparts in the homogeneous catalysts, while still maintaining the high activity of a heterogeneous catalyst.

Accordingly, this thesis aims to address the following problems:

- (1) Use literature-guided screening to identify promising heterogeneous catalysts for the selective oxidation of methane to liquid oxygenates at low temperatures using molecular oxygen as the oxidant.
- (2) Optimize the reaction conditions for high yield of liquid oxygenates and consider reaction systems to accumulate oxygenates at high concentrations.
- (3) Explore the mechanism of methane activation and functionalization on candidate catalysts. Elucidate the necessary elementary reactions to activate methane using molecular oxygen.
- (4) Understand how different catalyst structures contribute to the activity for methane oxidation. Can we develop more efficient dual site catalysts? What is the general strategy for catalyst design?

To address these problems, an initial screening of candidate catalysts based on the existing literature is conducted. Rhodium- and iridium- based catalysts are found to be promising and the study focuses on preparing single site rhodium and iridium cations anchored on zeolite supports like ZSM-5 and MOR or metal oxide like TiO<sub>2</sub>. On these materials, the selective conversion of methane to methanol or acetic acid is successfully realized using O<sub>2</sub> in the presence of CO as the oxidant. A parametric study is conducted, and a few reactor systems are evaluated to arrive at improved conditions for high-yield production of liquid oxygenates. The selected catalysts also provide a platform to further investigate the mechanism of the reaction and understand the role of CO. Detailed elementary steps leading to the conversion of methane to final products are identified and how to use CO efficiently is discussed. Finally, the exploration of bimetallic systems for both rhodium- and iridium-based catalysts reveals the catalyst design strategy for highly efficient catalytic systems. The overarching goal of this thesis is to provide important guiding principles for rational selection of catalyst components and reaction conditions for oxidative methane conversion in aqueous solutions using molecular O<sub>2</sub>.

## 1.6 References

- (1) Zhai, Y.; Pierre, D.; Si, R.; Deng, W.; Ferrin, P.; Nilekar, A. U.; Peng, G. Alkali-stabilized Pt-OH<sub>x</sub> species catalyze low-temperature water-gas shift reactions. *Science* **2010**, 239, 1633-1636.
- (2) Kistler, J. D.; Chotigkrai, N.; Xu, P.; Enderle, B.; Praserttham, P.; Chen, C.; Browning, N. D.; Gates, B. C. A single-site platinum CO oxidation catalyst in zeolite KLTL: microscopic and spectroscopic determination of the locations of the platinum atoms. *Angew. Chem. Int. Ed.* **2014**, 53, 8904-8907.
- (3) Yang, M.; Allard, L. F.; Flytzani-Stephanopoulos, M. Atomically dispersed Au-(OH)<sub>x</sub> species bound on Titania catalyze the low-temperature water-gas shift reaction. *J. Am. Chem. Soc.* **2013**, 135, 3768-3771.
- (4) Yang, M.; Li, S.; Wang, Y.; Herron, J. A.; Xu, Y.; Allard, L. F.; Lee, S.; Huang, J.; Mavrikakis, M.; Flytzani-Stephanopoulos, M. Catalytically active Au-O(OH)<sub>x</sub>-species stabilized by alkali ions on zeolites and mesoporous oxides. *Science* **2014**, 346, 1498-1501.
- (5) Kwak, J. H.; Kovarik, L.; Szanyi, J. Heterogeneous catalysis on atomically dispersed supported metals: CO<sub>2</sub> reduction on multifunctional Pd catalysts. *ACS Catal.* **2013**, 3, 2094-2100.
- (6) Duarte, R. B.; Safonova, O. V.; Krumeich, F.; van Bokhoven, J. A. Atomically dispersed rhodium on a support: the influence of a metal precursor and a support. *Phys. Chem. Chem. Phys.* **2014**, 16, 26553-26560.
- (7) Forde, M. M.; Armstrong, R. D.; McVicker, R.; Wells, P. P.; Dimitratos, N.; He, Q.; Lu, L.; Jenkins, R. L.; Hammond, C.; Lopez-Sanchez, J. A.; Kiely, C. J.; Hutchings, G. J. Light alkane oxidation using catalysts prepared by chemical vapor impregnation: tuning alcohol selectivity through catalyst pre-treatment. *Chem. Sci.* **2014**, 5, 3603-3616.
- (8) U.S. Energy Information Administration. U.S. Natural Gas Marketed Production.  
<https://www.eia.gov/dnav/ng/hist/n9050us2a.htm> (accessed March 27, 2019)

- (9) Shilov, A. E.; Shul'pin, G. B. Activation and catalytic reactions of alkanes in solutions of metal complexes. *Russ. Chem. Rev.* **1987**, 56, 442-464.
- (10) World Bank. Global Gas Flaring Reduction Partnership. <http://www.worldbank.org/ggfr> (accessed March 27, 2019)
- (11) Fleisch, T. H.; Sills, R. A.; Briscoe, M. D. 2002 – Emergence of the gas-to-liquid industry: a review of global GTL developments. *J. Nat. Gas Chem.* **2002**, 11, 1-14.
- (12) *CRC handbook of chemistry and physics, Internet Version*; Lide, D. R. ed.; CRC Press: Boca Raton, FL, 2005.
- (13) Tullo, A. H. Methanol for sale. *Chem. Eng. News* **2014**, 92, 12-13.
- (14) Wilhelm, D. J.; Simbeck, D. R.; Karp, A. D.; Dickenson, R. L. Syngas production for gas-to-liquids applications: technologies, issues and outlook. *Fuel Process. Technol.* **2001**, 71, 139-148.
- (15) Tijm, P. J. A.; Waller, F. J.; Brown, D. M. Methanol technology developments for the new millennium. *Appl. Catal. A: Gen.* **2001**, 221, 275-282.
- (16) Hoyano, J. K.; McMaster, A. D.; Graham, W. A. G. Activation of methane by iridium complexes. *J. Am. Chem. Soc.* **1983**, 105, 7190-7191.
- (17) Gol'dshleger, N. F.; Tyabin, M. B.; Shilov, A. E.; Shteinman, A. A. Activation of saturated hydrocarbons - deuterium-hydrogen exchange in solutions of transition metal complexes. *Russ. J. Phys. Chem.* **1969**, 43, 1222-1223
- (18) Periana, R. A.; Taube, D. J.; Evitt, E. R.; Löffler, D. G.; Wentreck, P. R.; Voss, G.; Masuda, T. A mercury-catalyzed, high-yield system for the oxidation of methane to methanol. *Science* **1993**, 259, 340-343.

- (19) Periana, R. A.; Taube, D. J.; Gamble, S.; Taube, H.; Satoh, T.; Fujii, H. Platinum catalysts for the high-yield oxidation of methane to a methanol derivative. *Science* **1998**, 280, 560-564.
- (20) Periana, R. A.; Mironov, O.; Taube, D.; Bhalla, G.; Jones, C. J. Catalytic, oxidative condensation of CH<sub>4</sub> to CH<sub>3</sub>COOH in one step via CH activation. *Science* **2003**, 301, 814-818.
- (21) Jones, C.J.; Taube, D.; Ziatdinov, V. R.; Periana, R. A.; Nielsen, R. J.; Oxgaard, J.; Goddard III, W. A. Selective oxidation of methane to methanol catalyzed, with C-H activation, by homogeneous, cationic gold. *Angew. Chem.* **2004**, 116, 4726-4729.
- (22) Diaz-Urrutia, C.; Ott, T. Activation of methane to CH<sub>3</sub><sup>+</sup>: a selective industrial route to methanesulfonic acid. *Science* **2019**, 363, 1326-1329.
- (23) Hashiguchi, B. G.; Young, K. J. H.; Yousufuddin, M.; Goddard III, W. A.; Periana, R. A. Acceleration of nucleophilic CH activation by strongly basic solvents. *J. Am. Chem. Soc.* **2010**, 132, 12542-12545.
- (24) Gretz, E.; Oliver, T. F.; Sen, A. Carbon-hydrogen bond activation by electrophilic transition-metal compounds. Palladium(II)-mediated oxidation of arenes and alkanes including methane. *J. Am. Chem. Soc.* **1987**, 109, 8109-8111.
- (25) Vargaftik, M. N.; Stolarov, I. P.; Moiseev, I. I. Highly selective partial oxidation of methane to methyl trifluoroacetate. *J. Chem. Soc., Chem. Comm.* **1990**, 1, 1049-1050.
- (26) Kao, L.; Hutson, A. C.; Sen, A. Low-temperature, palladium(II)-catalyzed, solution-phase oxidation of methane to a methanol derivative. *J. Am. Chem. Soc.* **1991**, 113, 700-701.
- (27) Lin, M.; Sen, A. A highly catalytic system for the direct oxidation of lower alkanes by dioxygen in aqueous medium. A formal heterogeneous analog of alkane monooxygenases. *J. Am. Chem. Soc.* **1992**, 114, 7307-7308.

- (28) Lin, M.; Hogan, T.; Sen, A. A highly catalytic bimetallic system for the low-temperature selective oxidation of methane and lower alkanes with dioxygen as the oxidant. *J. Am. Chem. Soc.* **1997**, 119, 6048-6053.
- (29) Palkovits, R.; Antonietti, M.; Kuhn, P.; Thomas, A.; Schüth, F. Solid catalysts for the selective low-temperature oxidation of methane to methanol. *Angew. Chem. Int. Ed.* **2009**, 48, 6909-6912.
- (30) Palkovits, R.; von Malotki, C.; Baumgarten, M.; Müllen, K.; Baltes, C.; Antonietti, M.; Kuhn, P.; Weber, J.; Thomas, A.; Schüth, F. Development of molecular and solid catalysts for the direct low-temperature oxidation of methane to methanol. *ChemSusChem* **2010**, 3, 277-282.
- (31) Soorholtz, M.; White, R. J.; Zimmerman, T.; Titirici, M.; Antonietti, M.; Palkovits, R.; Schüth, F. Direct methane oxidation over Pt-modified nitrogen-doped carbons. *Chem. Comm.* **2013**, 49, 240-242.
- (32) Li, F.; Yuan, G. Low temperature catalytic conversion of methane to methanol by barium sulfate nanotubes supporting sulfates: Pt(SO<sub>4</sub>)<sub>2</sub>, HgSO<sub>4</sub>, Ce(SO<sub>4</sub>)<sub>2</sub> and Pb(SO<sub>4</sub>)<sub>2</sub>. *Chem. Comm.* **2005**, 2238-2240.
- (33) Nakata, K.; Yamaoka, Y.; Miyata, T.; Taniguchi, Y.; Takaki, K.; Fujiwara, Y. Palladium(II) and/or copper(II)-catalyzed carboxylation of small alkanes such as methane and ethane with carbon monoxide. *J. Organomet. Chem.* **1994**, 473, 329-334.
- (34) Kurioka, M.; Nakata, K.; Jintoku, T.; Taniguchi, Y.; Takaki, K.; Fujiwara, Y. Palladium-catalyzed acetic acid synthesis from methane and carbon monoxide or dioxide. *Chem. Lett.* **1995**, 244.
- (35) Zerella, M.; Mukhopadhyay, S.; Bell, A. T. Direct oxidation of methane to acetic acid catalyzed by Pd<sup>2+</sup> and Cu<sup>2+</sup> in the presence of molecular oxygen. *Chem. Comm.* **2004**, 1948-1949.
- (36) Gesser, H. D.; Hunter, N. R. The direct conversion of methane to methanol by controlled oxidation. *Chem. Rev.* **1985**, 85, 235-244.
- (37) Taniguchi, Y.; Hayashida, T.; Shibasaki, H.; Piao, D.; Kitamura, T.; Yamaji, T.; Fujiwara, Y. Highly efficient vanadium-catalyzed transformation of CH<sub>4</sub> and CO to acetic acid. *Organ. Lett.* **1999**, 1, 557-559.

- (38) Reis, P. M.; Silva, J. A. L.; Palavra, A. F.; Fraústo da Silva, J. J. R.; Kitamura, T.; Fujiwara, Y.; Pombeiro, A. J. L. Single-pot conversion of methane into acetic acid in the absence of CO and vanadium catalysts such as amavadine. *Angew. Chem. Int. Ed.* **2003**, 42, 821-823.
- (39) Kirillova, M. V.; da Silva, J. A. L.; Fraústo da Silva, J. J. R.; Pombeiro, A. J. L. Direct and efficient transformation of gaseous alkanes into carboxylic acids catalyzed by vanadium containing heteropolyacids. *App. Catal. A: Gen.* **2007**, 332, 159-165.
- (40) Sorokin, A. B.; Kudrik, E. V.; Alvarez, L. X.; Afanasiev, P.; Millet, J. M. M.; Bouchu, D. Oxidation of methane and ethylene in water at ambient conditions. *Catal. Today* **2010**, 157, 149-154.
- (41) Forde, M. M.; Grazia, B. C.; Armstrong, R.; Jenkins, R. L.; Ab Rahim, M. H.; Carley, A. F.; Dimitratos, N.; Lopez-Sanchez, J. A.; Taylor, S. H.; McKeown, N. B.; Hutchings, G. J. Methane oxidation using silica-supported N-bridged di-iron phthalocyanine catalyst. *J. Catal.* **2012**, 290, 177-185.
- (42) Yuan, Q.; Deng, W.; Zhang, Q.; Wang, Y. Osmium-catalyzed selective oxidation of methane and ethane with hydrogen peroxide in aqueous medium. *Adv. Synth. Catal.* **2007**, 349, 1199-1209.
- (43) Ab Rahim, M. H.; Forde, M. M.; Jenkins, R. L.; Hammond, C.; He, Q.; Dimitratos, N.; Lopez-Sanchez, J. A.; Carley, A. F.; Taylor, S. H.; Willock, D. J.; Murphy, D. M.; Kiely, C. J.; Hutchings, G. J. Oxidation of methane to methanol with hydrogen peroxide using supported gold-palladium alloy nanoparticles. *Angew. Chem. Int. Ed.* **2012**, 51, 1-6.
- (44) Agarwal, N.; Freakley, S. J.; McVicker, R. U.; Althahban, S. M.; Dimitratos, N.; He, Q.; Morgan, D. J.; Jenkins, R. L.; Willock, D. J.; Taylor, S. H.; Kiely, C. J.; Hutchings, G. J. Aqueous Au-Pd colloids catalyze selective CH<sub>4</sub> oxidation to CH<sub>3</sub>OH with O<sub>2</sub> under mild conditions. *Science* **2017**, 358, 223-227.
- (45) Hammond, C.; Forde, M. M.; Ab Rahim, M. H.; Thetford, A.; He, Q.; Jenkins, R. L.; Dimitratos, N.; Lopez-Sanchez, J. A.; Dummer, N. F.; Murphy, D. M.; Carley, A. F.; Taylor, S. H.; Willock, D. J.; Stangland, E. E.; Kang, J.; Hagen, H.; Kiely, C. J.; Hutchings, G. J. Direct catalytic conversion of

methane to methanol in an aqueous medium by using copper-promoted Fe-ZSM-5. *Angew. Chem. Int. Ed.* **2012**, 51, 5129-5133.

(46) Hammond, C.; Jenkins, R. L.; Dimitratos, N.; Lopez-Sanchez, J. A.; Ab Rahim, M. H.; Forde, M. M.; Thetford, A.; Murphy, D. M.; Hagen, H.; Stangland, E. E.; Moulijin, J. M.; Taylor, S. H.; Willock, D. J.; Hutchings, G. J. Catalytic and mechanistic insights of the low-temperature selective oxidation of methane over Cu-promoted Fe-ZSM-5. *Chem. Eu. J.* **2012**, 18, 15735-15745.

(47) Huang, W.; Zhang, S.; Tang, Y.; Li, Y.; Nguyen, L.; Li, Y.; Shan, J.; Xiao, D.; Gagne, R.; Frenkel, A. I.; Tao, F. Low-Temperature Transformation of Methane to Methanol on Pd<sub>1</sub>O<sub>4</sub> Single Sites Anchored on the Internal Surface of Microporous Silicate. *Angew. Chem. Int. Ed.* **2016**, 55, 13441-13445.

(48) Liu, C.-C.; Mou, C.-Y.; Yu, S. S.-F.; Chan, S. I. Heterogeneous formulation of the tricopper complex for efficient catalytic conversion of methane into methanol at ambient temperature and pressure. *Energy Environ. Sci.* **2016**, 9, 1361-1374.

(49) Osadchii, D.; Suarez, A. I. O.; Szécsényi, Á.; Li, G.; Nasalevich, M. A.; Dugulan, A. I.; Serra-Crespo, P.; Hensen, E. J. M.; Veber, S. L.; Fedin, M. V.; Sankar, G.; Pidko, E. A.; Gascon, J. Isolated Fe sites in metal organic framework catalyze the direct conversion of methane to methanol. *ACS Catal.* **2018**, 8, 5542-5548.

(50) Cui, X.; Li, H.; Wang, Y.; Hu, Y.; Hua, L.; Li, H.; Han, X.; Liu, Q.; Yang, F.; He, L.; Chen, X.; Li, Q.; Xiao, J.; Deng, D.; Bao, X. Room-temperature methane conversion by graphene-confined single iron atoms. *Chem.* **2018**, 4, 1902-1910.

(51) Kwon, Y.; Kim, T. Y.; Kwon, G.; Yi, J.; Lee, H. Selective activation of methane on single-atom catalyst of rhodium dispersed on zirconia for direct conversion. *J. Am. Chem. Soc.* **2017**, 139, 17694-17699.

- (52) Lin, M.; Sen, A. Direct catalytic conversion of methane to acetic acid in an aqueous medium. *Nature* **1994**, 368, 613-615.
- (53) Chepaikin, E. G.; Bezruchenko, A. P.; Leshcheva, A. A. Homogeneous rhodium-copper-halide catalytic systems for the oxidation and oxidative carbonylation of methane. *Kinet. Catal.* **2002**, 43, 507-513.
- (54) Lin, M.; Hogan, T. E.; Sen, A. Catalytic carbon-carbon and carbon-hydrogen bond cleavage in lower alkanes. Low-temperature hydroxylations and hydroxycarbonylations with dioxygen as the oxidant. *J. Am. Chem. Soc.* **1996**, 118, 4574-4580.
- (55) Chepaikin, E. G.; Bezruchenko, A. P.; Leshcheva, A. A.; Boyko, G. N.; Kuzmenkov, I. V.; Grigoryan, E. H.; Shilov, A. E. Functionalisation of methane under dioxygen and carbon monoxide catalyzed by rhodium complexes: Oxidation and oxidative carbonylation. *J. Mol. Catal. A: Chem.* **2001**, 169, 89-98.
- (56) Panov, G. I.; Sobolev, V. I.; Kharitonov, A. S. The role of iron in N<sub>2</sub>O decomposition on ZSM-5 zeolite and reactivity of the surface oxygen formed. *J. Mol. Catal.* **1990**, 61, 85-97.
- (57) Sobolev, V. I.; Dubkov, K. A.; Panna, O. V.; Panov, G. I. Selective oxidation of methane to methanol on a FeZSM-5 surface. *Catal. Today.* **1995**, 24, 251-252.
- (58) Dubkov, K. A.; Ovanesyan, N. S.; Shteinman, A. A.; Starokon, E. V.; Panov, G. I. Evolution of iron states and formation of  $\alpha$ -sites upon activation of FeZSM-5 zeolites. *J. Catal.* **2002**, 207, 341-352.
- (59) Smeets, P. J.; Groothaert, M. H.; Schoonheydt, R. A. Cu based zeolites: A UV-vis study of the active site in the selective methane oxidation at low temperatures. *Catal. Today.* **2005**, 110, 303-309.
- (60) Woertink, J. S.; Smeets, P. J.; Groothaert, M. H.; Vance, M. A.; Sels, B. F.; Schoonheydt, R. A.; Solomon, E. I. A [Cu<sub>2</sub>O]<sup>2+</sup> core in Cu-ZSM-5, the active site in the oxidation of methane to methanol. *Proc. Natl. Acad. Sci.* **2009**, 106, 18908-18913.

- (61) Smeets, P. J.; Hadt, R. G.; Woertink, J. S.; Vanelderen, P.; Schoonheydt, R. A.; Sels, B. F.; Solomon, E. I. Oxygen precursor to the reactive intermediate in methanol synthesis by Cu-ZSM-5. *J. Am. Chem. Soc.* **2010**, 132, 14736-14738.
- (62) Bezins, N. V.; Weckhuysen, B. M.; Bitter, J. H. Partial oxidation of methane over Co-ZSM-5: tuning the oxygenate selectivity by altering the preparation route. *Catal. Lett.* **2010**, 136, 52-56.
- (63) Shan, J.; Huang, W.; Nguyen, L.; Yu, Y.; Zhang, S.; Li, Y.; Frenkel, A. I.; Tao, F. Conversion of methane to methanol with a bent mono( $\mu$ -oxo)dinickel anchored on the internal surfaces of micropores. *Langmuir.* **2014**, 30, 8558-8569.
- (64) Grundner, S.; Markovits, M. A.; Li, G.; Tromp, M.; Pidko, E. A.; Hensen, E. J. M.; Jentys, A.; Sanchez-Sanchez, M.; Lercher, J. A. Single-site trinuclear copper oxygen clusters in mordenite for selective conversion of methane to methanol. *Nat. Comm.* **2015**, 6, 7546.
- (65) Wulfers, M. J.; Teketel, S.; Ipek, B.; Lobo, R. F. Conversion of methane to methanol on copper-containing small-pore zeolites and zeotypes. *Chem. Commun.* **2015**, 51, 4447-4450.
- (66) Bozbag, S. E.; Sot, P.; Nachtegaal, M.; Ranocchiari, M.; van Bokhoven, J. A.; Mesters, C. Direct stepwise oxidation of methane to methanol over Cu-SiO<sub>2</sub>.
- (67) Ikuno, T.; Zheng, J.; Vjunov, A.; Sanchez-Sanchez, M.; Ortuño, M. A.; Pahls, D. R.; Fulton, J. L.; Camaioni, D. M.; Li, Z.; Ray, D.; Mehdi, B. L.; Browning, N. D.; Farha, O. F.; Hupp, J. T.; Cramer, C. J.; Gagliardi, L.; Lercher, J. A. Methane oxidation to methanol catalyzed by Cu-oxo clusters stabilized in NU-1000 Metal-Organic Framework. *J. Am. Chem. Soc.* **2017**, 139, 10294-10301.
- (68) Alayon, E. M.; Nachtegaal, M.; Ranocchiari, M.; van Bokhoven, J. A. Catalytic conversion of methane to methanol over Cu-mordenite. *Chem. Comm.* **2012**, 48, 404-406.
- (69) Starokon, E. V.; Parfenov, M. V.; Arzumanov, S. S.; Pirutko, L. V.; Stephanov, A. G.; Panov, G. I. Oxidation of methane to methanol on the surface of FeZSM-5 zeolite. *J. Catal.* **2013**, 300, 47-54.

- (70) Sheppard, T.; Hamill, C. D.; Goguet, A.; Rooney, D. W.; Thompson, J. M. A low temperature, isothermal gas-phase system for conversion of methane to methanol over Cu-ZSM-5. *Chem. Comm.* **2014**, 50, 11053-11055.
- (71) Narsimhan, K.; Iyoki, K.; Dinh, K.; Román-Leshkov, Y. Catalytic oxidation of methane into methanol over copper-exchanged zeolites with oxygen at low temperature. *ACS Cent. Sci.* **2016**, 2, 424-429.
- (72) Narsimhan, K.; Michaelis, V. K.; Mathies, G.; Gunther, W. R.; Griffin, R. G.; Román-Leshkov, Y. Methane to acetic acid over Cu-exchanged zeolites: mechanistic insights from a site-specific carbonylation reaction. *J. Am. Chem. Soc.* **2015**, 137, 1825-1832.
- (73) Sushkevich, V. L.; Palagin, D.; Ranocchiari, M.; van Bokhoven, J. A. Selective anaerobic oxidation of methane enables direct synthesis of methanol. *Science* **2017**, 356, 523-527.
- (74) An, Z.; Pan, X.; Liu, X.; Han, X.; Bao, X. Combined redox couples for catalytic oxidation of methane by dioxygen at low temperatures. *J. Am. Chem. Soc.* **2006**, 128, 16028-16029.
- (75) Bar-Nahum, I.; Khenkin, A. M.; Neumann, R. Mild, aqueous, aerobic, catalytic oxidation of methane to methanol and acetaldehyde catalyzed by a supported bipyrimidinylplatinum-polyoxometalate hybrid compound. *J. Am. Chem. Soc.* **2004**, 126, 10236-10237.
- (76) Rodgers, K. R.; Arafa, I. M.; Goff, H. M. Iron porphyrin catalyzed oxidation of propanal and cyclohexene by molecular oxygen. *J. Chem. Soc., Chem. Comm.* **1990**, 1323-1324.
- (77) Karandikar, P.; Chandwadkar, A. J.; Agashe, M.; Ramgir, N. S.; Sivasanker, S. Liquid phase oxidation of alkanes using Cu/Co-perchlorophthalocyanine immobilized MCM-41 under mild reaction conditions. *App. Catal. A: Gen.* **2006**, 297, 220-230.
- (78) Yamanaka, I.; Soma, M.; Otsuka, K. Oxidation of methane to methanol with oxygen catalyzed by europium trichloride at room temperature. *J. Chem. Soc., Chem. Comm.* **1995**, 2335-2336.

- (79) Marcinkowski, M. D.; Darby, M. T.; Liu, J.; Wimble, J. M.; Lucci, F. R.; Lee, S.; Michaelides, A.; Flytzani-Stephanopoulos, M.; Stamatakis, M.; Sykes, E. C. H. Pt/Cu single-atom alloys as coke-resistant catalyst for efficient C-H activation. *Nat. Chem.* **2018**, 10, 325-332.
- (80) Shan, J.; Lucci, F.; Liu, J.; El-Soda, M.; Marcinkowski, M. D.; Allard, L. F.; Syke, E. C. H.; Flytzani-Stephanopoulos, M. Water co-catalyzed selective dehydrogenation of methanol to formaldehyde and hydrogen. *Surf. Sci.* **2016**, 650, 121-129.
- (81) Zhang, X.; Sun, Z.; Wang, B.; Tang, Y.; Nguyen, L.; Li, Y.; Tao, F. C-C coupling on single-atom-based heterogeneous catalyst. *J. Am. Chem. Soc.* **2018**, 140, 954-962.
- (82) Wang, L.; Zhang, W.; Wang, S.; Gao, Z.; Luo, Z.; Wang, X.; Zeng, R.; Li, A.; Li, H.; Wang, M.; Zheng, X.; Zhu, J.; Zhang, W.; Ma, C.; Si, R.; Zeng, J. Atomic-level insights in optimizing reaction paths for hydroformylation reaction over Rh/CoO single-atom catalyst. *Nat. Comm.* **2016**, 7, doi:10.1038/ncomms14036
- (83) Lang, R.; Li, T.; Matsumura, D.; Miao, S.; Ren, Y.; Cui, Y.-T.; Tan, Y.; Qiao, B.; Li, L.; Wang, A.; Wang, X.; Zhang, T. Hydroformylation of olefins by a rhodium single-atom catalyst with activity comparable to RhCl(PPh)<sub>3</sub>. *Angew. Chem. Int. Ed.* 2016, 55, 16054-16058.
- (84) Deng, D.; Chen, X.; Yu, L.; Wu, X.; Liu, Q.; Liu, Y.; Yang, H.; Tian, H.; Hu Y.; Du, P. A single iron site confined in a graphene matrix for the selective catalytic oxidation of benzene at room temperature. *Sci. Adv.*, **2015**, 1, e1500462.
- (85) Forde, M. M.; Armstrong, R. D.; McVicker, R.; Wells, P. P.; Dimitratos, N.; He, Q.; Lu, L.; Jenkins, R. L.; Hammond, C.; Lopez-Sanchez, J. A.; Kiely, C. J.; Hutchings, G. J. Light alkane oxidation using catalysts prepared by chemical vapor impregnation: tuning alcohol selectivity through catalyst pre-treatment. *Chem. Sci.* **2014**, 5, 3603-3616.

(86) Nizova, G. V.; Suss-Fink, G.; Stanislas, S.; Shul'pin, G. B. Carboxylation of methane with CO or CO<sub>2</sub> in aqueous solution catalyzed by vanadium complexes. *Chem. Comm.* **1998**, 1885-1886.

## Chapter 2 Experimental Methods and Procedures

### 2.1 Catalyst synthesis

#### 2.1.1 Materials and chemicals

For the synthesis of rhodium based catalysts,  $\text{Rh}(\text{NO}_3)_3$  hydrate (36% metal basis, Sigma Aldrich) and  $\text{Fe}(\text{NO}_3)_3 \cdot 9\text{H}_2\text{O}$  (99.99%, Sigma Aldrich) were used as the precursor.  $\text{IrCl}_3$  hydrate (99.8%, Alfa Aesar),  $\text{Pd}(\text{NH}_3)_4\text{Cl}_2 \cdot \text{H}_2\text{O}$  (>99.99%, Aldrich),  $\text{Cu}(\text{NO}_3)_2 \cdot 2.5\text{H}_2\text{O}$  (98%, Alfa Aesar) were used to synthesize IrPd, IrCu bimetallic and IrCuPd trimetallic catalysts.  $\text{NH}_4$  form ZSM-5 zeolite with Si/Al ratio ranging from 15 to 400 (Alfa Aesar) and MOR zeolite (Si/Al=10, Alfa Aesar) were used as catalyst support. For the case of  $\text{RhTiO}_2$  catalyst, commercial  $\text{TiO}_2$  nanoparticles (Millenium G5, Anatase) was used as catalyst support. All materials are used as received unless otherwise noted.

All gases used in this study were purchased from Airgas with Ultra High Purity. Gas mixtures were purchased as customarily mixed and certified by Airgas.

#### 2.1.2 Preparation methods

##### Incipient wetness impregnation

Rhodium and iridium catalysts supported on zeolite were prepared through incipient wetness impregnation method.  $\text{NH}_4$ -ZSM-5 zeolite was first dehydrated at  $120^\circ\text{C}$  in a furnace for 3h to remove moisture inside the zeolite pores. An aqueous solution containing desired amount of  $\text{Rh}(\text{NO}_3)_3$  or  $\text{IrCl}_3$  were prepared by dissolving the corresponding metal precursor in deionized water (0.6mL/g of zeolite). The aqueous solution was impregnated on the dehydrated zeolite and the sample was dried in a vacuum oven at  $60^\circ\text{C}$  overnight. The dried powder was then reduced at  $550^\circ\text{C}$  in 5% $\text{H}_2$ /He for 3h (ramping rate  $3^\circ\text{C}/\text{min}$ ). Alternatively, a different heat treatment protocol was also used on IrZSM-5 catalyst. The dried powder was heat treated at  $450^\circ\text{C}$  in He for 5h.

## Back ion exchange

Back ion exchange of catalyst with sodium ion was conducted by stirring 1g of catalyst in 36mL 2.44M CH<sub>3</sub>COONa solution at 80°C for 12h. The catalyst was then filtered and washed with DI water and dried in vacuum at 60°C overnight. This process is repeated twice for complete back ion exchange.

## UV assisted precipitation deposition

RhTiO<sub>2</sub> catalyst was prepared through UV-assisted precipitation deposition (DP) method. In a typical synthesis, Rh<sub>2</sub>O<sub>3</sub> was first introduced onto TiO<sub>2</sub> support through a DP method. The desired amount of Rh(NO<sub>3</sub>)<sub>3</sub> solution was added dropwise into TiO<sub>2</sub> aqueous suspension maintained at 80°C and pH of 8.5. During the course of addition, 0.1M NaOH solution was used to adjust the pH. The suspension was further aged at 80°C for 3h under constant stirring. Afterwards, the solids were filtered, and the obtained catalyst contains Rh<sub>2</sub>O<sub>3</sub> loosely bound on TiO<sub>2</sub> that can be readily removed with hydrochloric acid.

The dried sample was transferred to an ethanol solution, where the slurry was exposed to UV irradiation with an 8W BL lamp centered at 365nm. During the irradiation process, Rh cations are anchored on certain surface sites of the titania, while excess Rh, weakly bound on the surface can be readily removed by hydrochloric acid leaching. Starting from 2.5wt.% Rh/TiO<sub>2</sub> using the DP method, UV irradiation for 3h can anchor ~0.6wt.% rhodium as single atoms; the rest of Rh species were leached by 3.0 M hydrochloric acid at room temperature. Leaching was conducted typically with 100mg of catalyst suspended in 20mL 3.0 M hydrochloric acid, the suspension was vigorously stirred with a magnetic stirrer bar at room temperature for 3h. Afterwards the solids were filtered and washed until no Cl<sup>-</sup> residue can be detected and dried under vacuum at 60°C overnight. The filtered liquid containing leached rhodium was collected and analyzed by ICP-AES.

## 2.2 Catalyst characterization

### Surface area

The surface area of catalysts was measured using single point N<sub>2</sub> physisorption method on Micromeritics AutoChem II 2920 apparatus. The sample was first degassed in He at 400°C for 60min before adsorption step which is performed at 77K with 30% N<sub>2</sub>/He gas mixture.

### Catalyst composition

Catalyst composition was analyzed on Leeman Labs Prodigy Inductively Coupled Plasma Atomic Emission Spectroscopy (ICP-AES) spectrometer. For RhTiO<sub>2</sub> catalysts, aqueous solutions before and after deposition-precipitation were analyzed by ICP-AES using the radial signal. Calibration curve was constructed using plasma grade standards of 1000ppm RhCl<sub>3</sub>.

### X-ray Diffraction (XRD)

XRD patterns were collected on a PANalytical X'Pert Pro instrument using nickel-filtered Cu K $\alpha$  radiation ( $\lambda = 1.54056 \text{ \AA}$ ). The instrument was operated at 45 kV and 40 mA in a continuous mode and measurements were taken in  $2\theta$  range from 10° to 60°.

### X-ray Photoelectron Spectroscopy (XPS)

XPS data were collected in a PHI VersaProbe II system equipped with a monochromatic Al K $\alpha$  source and a double-focusing hemispherical analyzer. An argon ion sputtering gun was used to sputter the

sample for the depth-profile analysis of the sample. The samples were prepared by loading the catalyst powder onto a Cu foil.

### Scanning Transmission Electron Microscopy (STEM)

Aberration corrected high angle annular dark field (ac HAADF) STEM images of catalysts were obtained with a JEOL 2200FS-AC (S)TEM instrument at Oak Ridge National Laboratory. The instrument is fitted with a CEOS GmbH (Heidelberg, Germany) corrector on the probe-forming lenses and is operated at 200kV for all analyses. The samples for high-resolution imaging were prepared by dispersing the catalyst powder in water and adding a few drops onto copper grids supported on carbon films. Energy-dispersive X-ray analysis data were obtained using a Bruker-AXS 30 mm<sup>2</sup> silicon-drift detector (SDD) system. Trial imaging experiments allowed the determination of the most appropriate beam conditions to minimize loss of the zeolite crystal structure when scanning the sample for the best thin edges of powder support particles to examine. An incident probe with a nominal 14 pA current at a convergence semi-angle of 26.5° was therefore used (i.e. Mag mode 9C on the JEOL 2200FS instrument). In comparison, catalyst samples with more stable support material are typically imaged with beam currents of 41 pA to achieve 0.07 nm resolution for single-atom imaging on stable supports.

### Diffuse Reflectance Infrared Fourier Transform Spectroscopy (DRIFTS)

DRIFTS investigations of the catalyst were conducted on a Thermo Scientific Nicolet iS50 FTIR Spectrometer fitted with a Praying Mantis Diffuse Reflection system including the high temperature reaction chamber (Harrick<sup>TM</sup>). Carbon monoxide was used as a probe molecule to identify surface metal species. The sample was adsorbed with CO at different temperatures followed by helium purge to remove gas phase CO prior to DRIFTS measurements. A gas mixture simulating the reaction atmosphere was also

used to study the change of catalyst structure in DRIFTS mode. DRIFT spectra were taken with  $4\text{cm}^{-1}$  resolution using a DTGS KBr detector. The spectra were processed using the OMNIC Spectra software.

#### Diffuse Reflectance UV-Vis Spectroscopy (DR UV-Vis)

DR UV-Vis spectra were collected on Jasco V-570 UV-Vis Spectrometer fitted with a sphere accessory for solid sampling. A powdered sample was pressed into the sample holder to create a flat surface and spectra were collected in the range of 200-800nm.

#### Electron Paramagnetic Resonance (EPR)

X-band (9GHz) EPR spectra were collected on a Bruker EMX spectrometer to probe the unpaired electrons in the catalyst sample. The powder catalysts were packed in a thin wall quartz EPR tube (Wilmad LabGlass) and cooled to 120K with liquid nitrogen flow. Measurements were conducted with magnetic field from 2000 to 5000 Gauss and g factors were calculated based on the following equation

$$h\nu = g\mu_B B_0$$

where  $h$  is the Planck's constant,  $B_0$  is the applied magnetic field strength and  $\mu_B$  is the Bohr magneton.

#### X-ray Absorption Spectroscopy (XAS)

X-ray Absorption Spectroscopy (XAS) studies were performed at Advanced Photon Source 12-BM at Argonne National Laboratory. The beamline uses a water-cooled, double-crystal, fixed-exit monochromator with Si(111) and Si(311) crystals. A double mirror system (flat and toroidal) focuses the beam in the experimental station to 0.5 mm x 0.5 mm. The beamline is equipped with a Canberra 13-element Ge detector placed perpendicular to the x-ray beam at sample stage. In addition, 3 Ion chambers

were also used to monitor the beam with one before the sample area, one between the sample area and reference foil and one after the reference foil. This setup allows the simultaneous measurement of catalyst sample in both transmission and fluorescence mode.

XAS recording of catalyst samples was carried out either ex-situ or in a capillary cell with different gas atmosphere with at least 5 consecutive scans. Typically, XAS study on catalyst samples was conducted in fluorescence mode to obtain better signal. Spectra of different standards were recorded in transmission mode. XAS data processing was conducted using the Demeter software package<sup>1</sup>.

### Temperature Programmed Oxidation (TPO)

TPO analysis of catalyst material was conducted on Micromeritics AutoChem II 2920 apparatus. Prior to oxidation, the catalyst was heat treated at 350°C for 1h in 10mL/min He to remove surface adsorbed species. After cooling down to room temperature, a stream of 2% O<sub>2</sub> balanced with He at 10mL/min was introduced to the sample and temperature was ramped continuously to 500°C with a ramping rate of 2°C/min. The product stream was monitored by an RGA analyzer.

### 2.3 Catalytic testing

Methane oxidation reaction was conducted in aqueous phase in a 50mL pressurized Parr reactor. The reactor was fitted with a glass liner and a type J thermocouple inserted into the aqueous phase. Powder catalysts were mixed with deionized water in the glass liner and sonicated until a uniform suspension was achieved. In a typical experiment, 20-600mg of catalyst and 20mL of deionized water were used. After placing the liner into the reactor body and sealing the reactor, oxygen, carbon monoxide and methane were pressurized into the reactor in a stepwise fashion to achieve their corresponding partial pressure. The pressurized reactor was heated up using either an oil bath or a band heater made of Monel alloy to the

desired temperature (50-190°C) and a magnetic stirrer bar was used to agitate the suspension. After reaching the specific reaction time the reaction was quenched by placing the reactor in ice water and cooled to 10°C. Carrying out the reaction in the aqueous phase requires first dissolving the reactant gases in the liquid, the solubilities of different gases at different temperatures are calculated based on published empirical equations and plotted in Figure 2.1. The solubility of gases is reported to decrease as temperature increases. However, at close to 100°C the trend starts to reverse and higher temperature leads to higher solubility in the aqueous phase. Therefore, conducting the experiment at 110-170°C does not lead to a condition with significantly lower gas solubility compared to that of temperatures below 100°C.

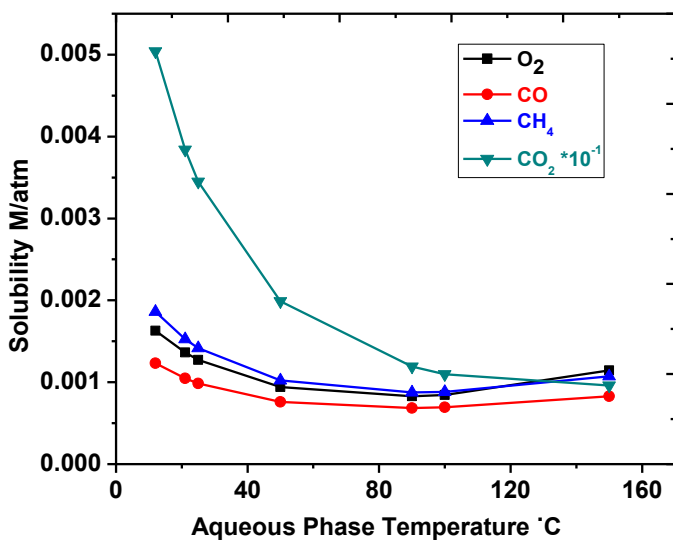


Figure 2.1 Solubility trends of O<sub>2</sub>, CO, CH<sub>4</sub> and CO<sub>2</sub> in water at different temperatures, solubilities calculated from empirical equations published in literature.<sup>2-5</sup>

The product gas was collected using a two-way gas sampling system fitted with a Tedlar gas bag. One end was attached to vacuum and the other was attached to reactor outlet. A picture of the setup is shown in Figure 2.1. Prior to depressurizing the product gas, the system was evacuated for 2min to remove residual air. The vacuum valve was closed, and reactor outlet valve was opened at the same time. The

sampled gas was analyzed either by gas chromatography (GC) using a thermal conductivity detector (TCD) or a Residual Gas Analyzer (RGA) quadrupole mass spectrometer.

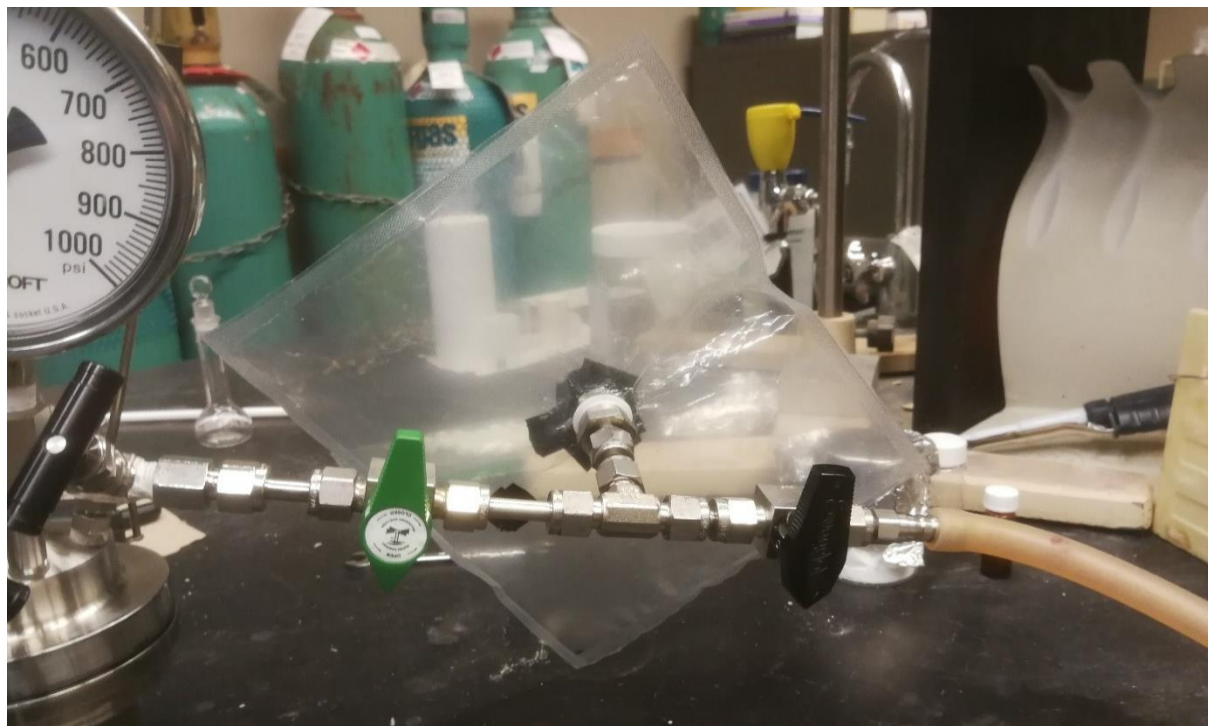


Figure 2.2 Two-way gas sampling system with a Tedlar gas bag.

The GC-TCD test was performed on an SRI model 310 GC fitted with a Carbosphere column. Analysis was conducted by connecting the gas bag to a gas sampling line fitted with an air-actuated six-port valve. A vacuum pump was connected to the end of sampling line and during analysis, the pump was turned on to draw gas flow from the gas bag. A loop injection using the six-port valve was initiated after 0.5min of pumping to flush the whole sampling line with product gas. The temperature program used by the GC is 50°C for 2min, ramping to 110°C with a rate of 3°C/min and then hold at 110°C for 2min. A sample chromatogram is shown in Figure 2.2.

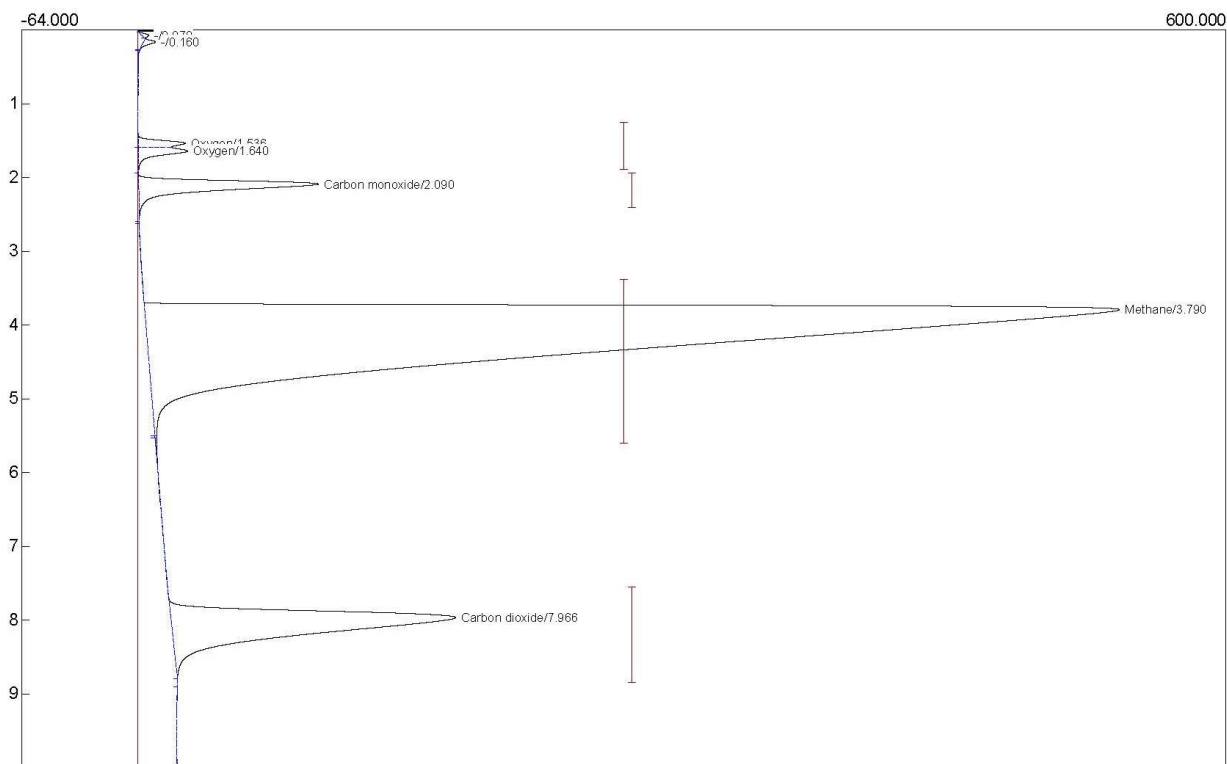


Figure 2.3 A typical chromatogram obtained for the product gas from GC-TCD test.

The product liquid was filtered and collected in a sample vial for H-NMR analysis. To prepare the NMR sample, 0.6mL aqueous sample was mixed with 0.1mL D<sub>2</sub>O (Sigma Aldrich, 99.9% D atom) and placed in a 500MHz thin wall precision NMR sample tube (Wilmad LabGlass), a coaxial insert holding 1%(v/v) TMS/CDCl<sub>3</sub> mixture (Sigma Aldrich, 99.8% D atom) was placed in the sample tube as an internal standard. H-NMR analysis was conducted on a Bruker Avance III 500 NMR spectrometer with a presaturation program to suppress the water peak. 8 scans were recorded for each analysis. Figure 2.3 shows a typical spectrum obtained from the reaction liquid. The identified products in Figure 2.2 were methanol ( $\delta = 3.36$  ppm, singlet), acetic acid ( $\delta = 2.08$  ppm, singlet), and formic acid ( $\delta = 8.33$  ppm, singlet). Additional peaks include chloroform-D ( $\delta = 7.26$ , singlet), trace water dissolved in chloroform ( $\delta = 1.58$ , singlet) and TMS ( $\delta = 0.00$ , singlet).<sup>7</sup>

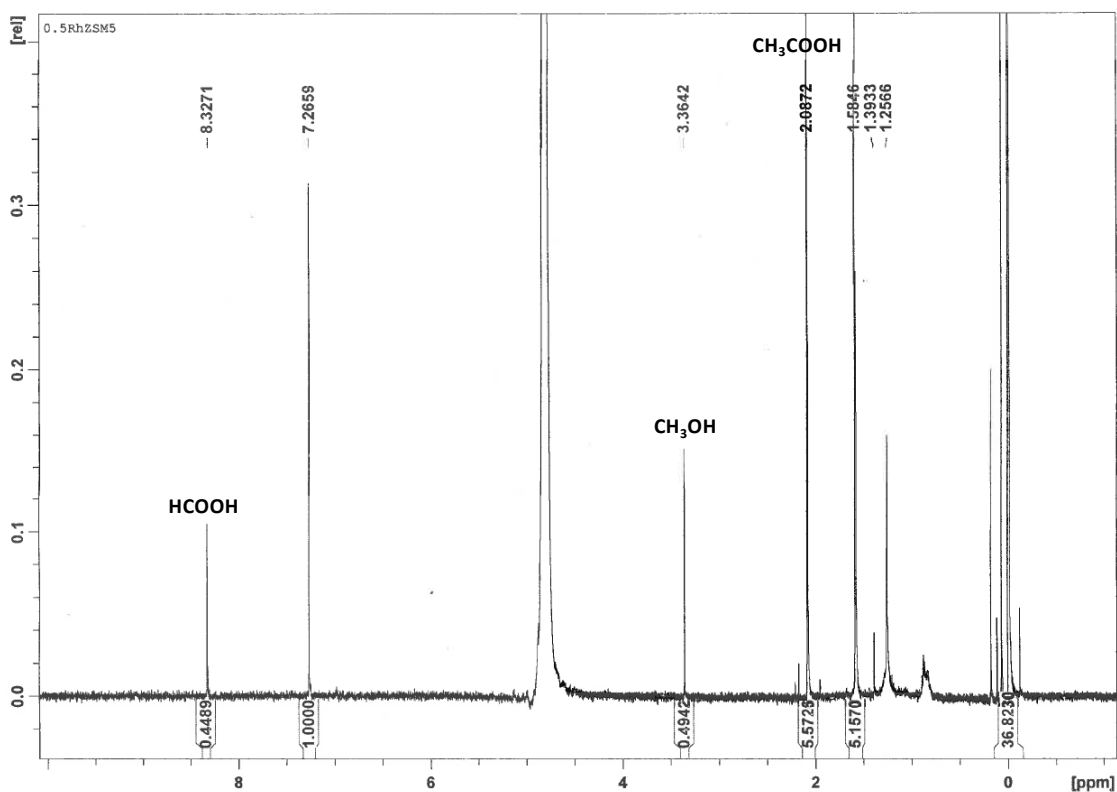


Figure 2.4 A typical  $^1\text{H}$ -NMR spectrum of liquid oxygenates obtained after reaction.

Product concentration was quantified against a set of calibration curves obtained by measuring standard solutions of each liquid oxygenates. The calibration curves were constructed using the peak area of the oxygenates over the peak area of the internal standard (TMS) versus concentration of the standard solutions.

$$\text{Concentration (mM)} \quad v.s. \quad \frac{A_{\text{oxygenate}}}{A_{\text{internal standard}}}$$

The relaxation time of the program was set to 5 sec to ensure sharp peaks and linear correlation between the relative peak area and the product concentration. The calibration curves for all three liquid oxygenates are summarized in Figure 2.4. Liquid phase product formation is reported as  $\mu\text{mol}$  product per gram of catalyst powder used.

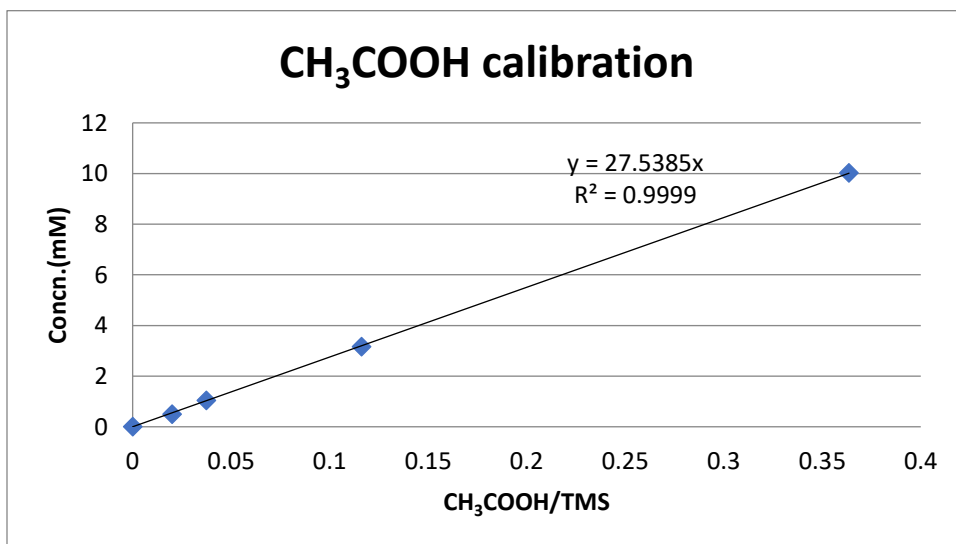
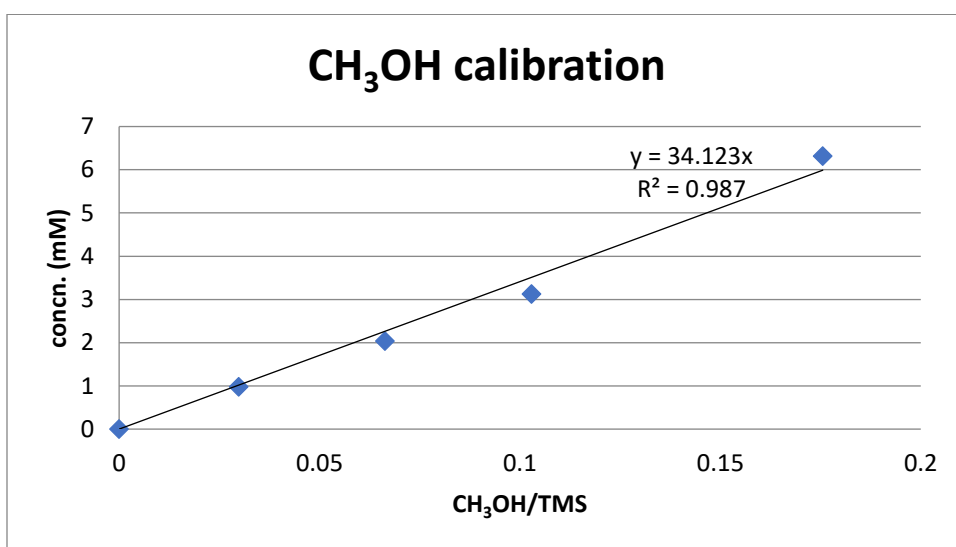
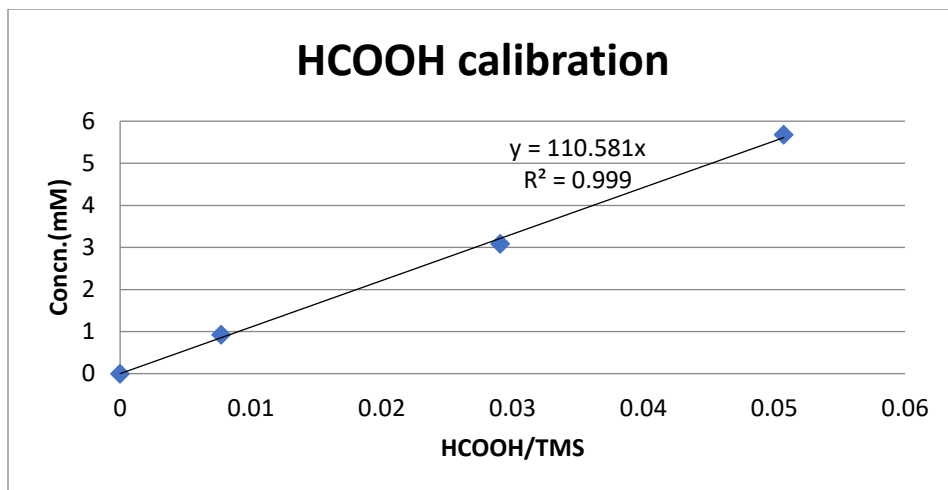


Figure 2.5 Calibration curves for formic acid, methanol and acetic acid obtained by H-NMR measurement.

Initial rate measurements were conducted in a 50mL Parr reactor with specific amount of catalyst at different temperatures to ensure conversion lower than 15%. The typical reaction time used was 0.5h. Rates were calculated as  $\mu\text{mol}$  of product formed per hour normalized by gram of catalyst used. The overall rates include the formation of all products, while specific rates for different pathways only account for the products formed from that pathway. For C1 pathway, the product includes methanol, formic acid and  $\text{CO}_2$  from methane. For C2 pathway, only acetic acid is considered.

## 2.4 References

- (1) Ravel, B.; Newville, M. ATHENA, ARTEMIS, HEPHAESTUS: Data analysis for X-ray absorption spectroscopy using IFEFFIT. *J. Synchrotron Radiat.* **2005**, 12, 537-541.
- (2) *IUPAC solubility data series, volume 7 oxygen and ozone* Battino, R. ed. Pergamon Press Inc.: New York 1981.
- (3) *IUPAC solubility data series, volume 43 carbon monoxide* Cargill, R. W. ed. Pergamon Press Inc.: New York 1990.
- (4) Crovetto, R. Fernandez-Prini, R.; Japas, M. L. Solubilities of inert gases and methane in H<sub>2</sub>O and in D<sub>2</sub>O in the temperature range of 300 to 600 K. *J. Chem. Phys.* **1982**, 76, 1077-1086.
- (5) Clever, H. L.; Han, C. H. The solubility of gases in water from 350-600 K. Thermodynamics of Aqueous Systems with Industrial Applications; Newman, S., et al.; ACS Symposium Series; American Chemical Society: Washington, DC, 1980.
- (6) Gottlieb, H. E.; Kotlyar, V.; Nudelman, A. NMR chemical shifts of common laboratory solvents as trace impurities. *J. Org. Chem.* **1997**, 62, 7512-7515.

# Chapter 3 Selective conversion of methane to methanol and acetic acid over RhZSM-5 single site catalyst

## 3.1 Introduction

Rh metal has long been the subject of study for methane partial oxidation to produce syngas at high temperature<sup>1,2</sup>. More recently, there has been a shift of interest to low-temperature methane functionalization to produce value-added chemicals, for example C1 and C2 oxygenates. Promising candidate for methane activation has been proposed as a cationic Rh center with low oxidation state<sup>3-5</sup> instead of bulk metallic rhodium nanoparticles. These cationic species are either coordinated with organic ligands and used as homogeneous catalyst or supported on metal oxide as heterogeneous catalysts. Lin and Sen reported that rhodium chloride promoted by iodide catalyzes oxidative carboxylation of methane to acetic acid with molecular oxygen at temperature below 200°C in the liquid phase.<sup>3a</sup> Catalytic turnover was achieved without metal precipitation but only TOF of 0.07h<sup>-1</sup> was achieved at 95°C. Follow up study from Chepaikin et al. and Lin et al. demonstrated that catalytic turnover rate and product selectivity can be promoted by switching from dilute aqueous acid solution to concentrated perfluoro acetic or butyric acid, leading to TOF of 2.9h<sup>-1</sup>.<sup>3b-c</sup> However, the homogeneous nature of the catalyst calls for concern of downstream separation of the catalyst component from product stream. Furthermore, rhodium chloride was also reported as a catalyst for methane oxidation using H<sub>2</sub>O<sub>2</sub> as oxidant at 90°C, forming C1 oxygenates of methanol, formaldehyde, methyl hydroperoxide with TOF of 4.6 h<sup>-1</sup>.<sup>4</sup> More recently, Kwon et al. reported methane activation on atomically dispersed rhodium species anchored on ZrO<sub>2</sub>.<sup>5</sup> The primary C-H bond of methane can be activated by rhodium cations at 70°C in a DRIFTS cell and catalytic reaction with H<sub>2</sub>O<sub>2</sub> showed high selectivity towards methanol. The major drawback of the catalyst is its inefficiency in utilizing H<sub>2</sub>O<sub>2</sub>, as majority of H<sub>2</sub>O<sub>2</sub> is decomposed by ZrO<sub>2</sub> support rather than incorporated into methanol. To conclude, although rhodium in ionic state was investigated as a catalyst

for methane activation at low temperature, and interesting results have been reported to demonstrate its potential, there has been no report of a heterogeneous rhodium catalyst that efficiently catalyzes low-temperature methane conversion using molecular oxygen as oxidant.

This chapter reports the successful anchoring of rhodium single cations onto zeolite supports that are highly crystalline and porous. The supported single cation Rh catalysts can catalyze the selective oxidation of methane to methanol or acetic acid in the aqueous phase using oxygen as oxidant and carbon monoxide as a promoter. Catalyst loading and heat treatment protocol to yield the most active catalyst was investigated. Parametric studies discovered the optimum operating condition for the selective oxidation of methane to acetic acid by using low partial pressure of oxygen. A combination of characterization methods including STEM, XPS, XANES/EXAFS and CO-DRIFTS were used to investigate the active rhodium species and isolated rhodium cations anchored inside zeolite pores

### 3.2 Experimental Methods

RhZSM-5 catalysts were synthesized following the incipient wetness impregnation method illustrated in Chapter 2. The loading of rhodium species ranges from 0.1wt% to 1.0wt%. Additionally, to prepare RhZSM-5 catalyst with solely single atom, a washing step is employed before heat treatment to remove nanoparticles on the external surface. Specifically, after impregnation of 0.5wt% Rh onto the ZSM-5 support, the obtained yellow powder was dried under vacuum overnight. The powder was washed with deionized water to remove loosely bound rhodium precursor and the washed catalyst was heat treated in 5% H<sub>2</sub>/He at 550°C for 3h. This catalyst is denoted as 0.5wt% RhZSM-5\_washed. Heat treatment in different atmosphere was also investigated. After impregnation, a portion of 0.5wt% RhZSM-5 was calcined in static air at 550°C for 3h, and the sample is denoted as 0.5wt% RhZSM-5\_O<sub>2</sub>.

The catalytic activity of the Rh catalysts was tested inside a high-pressure batch reactor fitted with a glass liner holding the catalyst suspension. A mixture of O<sub>2</sub>, CO and CH<sub>4</sub> was charged into the reactor to the desired pressure. The partial pressure of CO and CH<sub>4</sub> was fixed at 5 bar and 20 bar respectively, while pO<sub>2</sub> was varied from 0.5 bar to 4 bar. Typically, 20mg of catalyst was suspended in 20mL deionized water. Batch reactions were conducted with constant stirring for 0.5 ~ 6h at temperature of 110~170°C. After reaction was conducted at the reaction temperature for desired amount of time, the reactor was cooled with ice water. The gas phase product was quantified using GC-TCD (Carbosphere column) and mass spectrometer. The liquid phase product was analyzed by H-NMR.

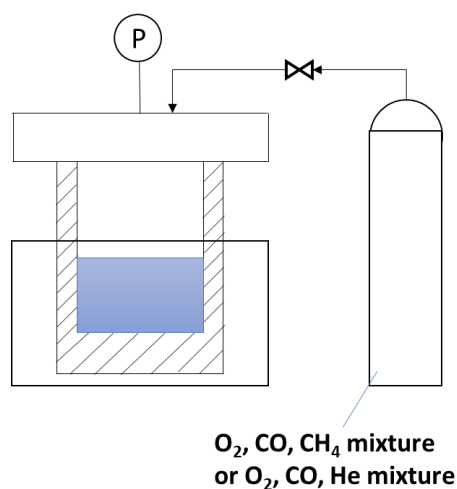
Conversion of methane was calculated by first measuring the headspace volume of the reactor. The total headspace volume, excluding space taken by the glass liner, magnetic stirrer bar and reaction solvent (typically 20mL) was quantified to be 15mL. Conversion is then calculated using the following equation:

$$Conversion = \frac{\text{Total oxidation product from CH}_4 \text{ (including CO}_2\text{)}}{\text{Amount of CH}_4 \text{ charged into the reactor}} \quad (1)$$

The amount of CO<sub>2</sub> formed from CO was determined from a separate experiment using identical reaction conditions but without CH<sub>4</sub>. Thus, the amount of CO<sub>2</sub> originated from CH<sub>4</sub> was calculated by

subtracting the CO<sub>2</sub> produced from CO oxidation from the total amount of CO<sub>2</sub> formed. The carbon balance, including all CH<sub>4</sub> and CO derived products, reaches over 97% for the catalytic tests conducted.

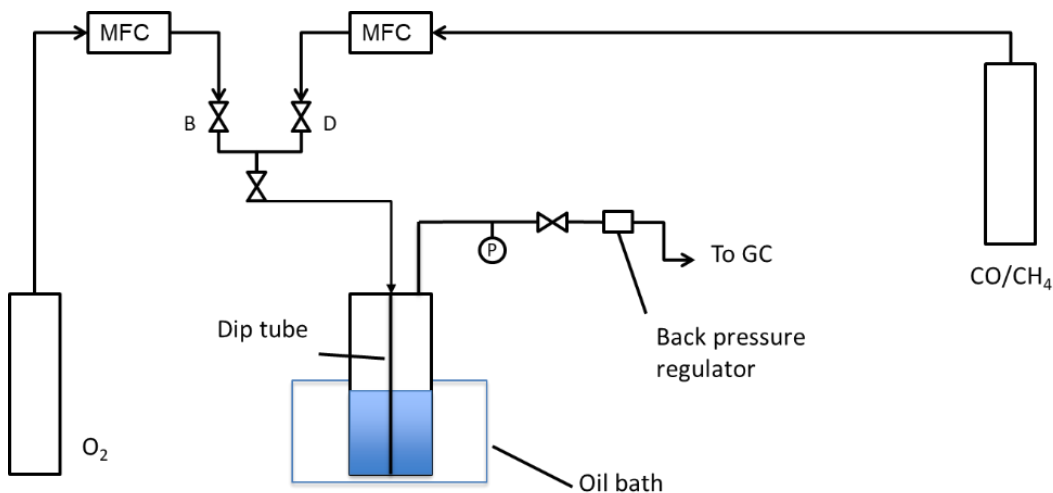
Reaction was also conducted in the fed-batch mode. A separate cylinder with pre-mixed gas consisting the same composition as the reaction mixture (O<sub>2</sub>:CO:CH<sub>4</sub>=2:5:20) is connected to the reactor. By setting the cylinder pressure to the same level of the initial autogenic pressure in the reactor at 150 °C, the reactant gas can be replenished continuously into the reactor as the gas is consumed during experiment. For feed gas containing no CH<sub>4</sub>, same partial pressure of helium was used as balancing gas. The reactor layout is shown in Scheme 3.1



Scheme 3.1 Fed-batch operation with replenishing of reactant gas.

A semi-batch bubbler reactor was set up by continuously flowing gas mixture of O<sub>2</sub>, CO and CH<sub>4</sub> (O<sub>2</sub>:CO:CH<sub>4</sub>=2:5:20) through the reactor at pressure corresponding to autogenic pressure of the mixture at 150°C. The gas mixture was controlled through two mass flow controllers (Brooks model 5850E) and continuously bubbled through the aqueous phase inside the reactor. As reaction happens, acetic acid continuously condensed into the aqueous phase at high pressure and accumulate in concentration. A flow diagram of the setup was shown in Scheme 3.2. The gas phase product was monitored continuously with GC-TCD and the aqueous phase product was sampled periodically by cooling liquid sample down with

ice bath to 10°C. The liquid samples were analyzed by H-NMR following the same procedure as the batch reaction.



Scheme 3.2 Semi-batch bubbler operation with continuous flow of reactant gas.

The catalysts were characterized using N<sub>2</sub>-physisorption, ICP-AES, XRD, XPS, DR UV-Vis, ac-HAADF STEM, CO-DRIFTS and XANES/EXAFS as detailed in Chapter 2.

### 3.3 Results and Discussion

#### 3.3.1 Catalytic activity of RhZSM-5 and parametric study

A key finding of this chapter is the unique activity of RhZSM-5 in activating methane and converting it into a mixture of C1 and C2 oxygenates in the aqueous phase. The first attempt is to identify the optimum loading and synthesis protocol to achieve the most active catalyst. Initial screening of RhZSM-5 with different loadings and different heat treatment was conducted and the results were summarized in Figure 3.1.

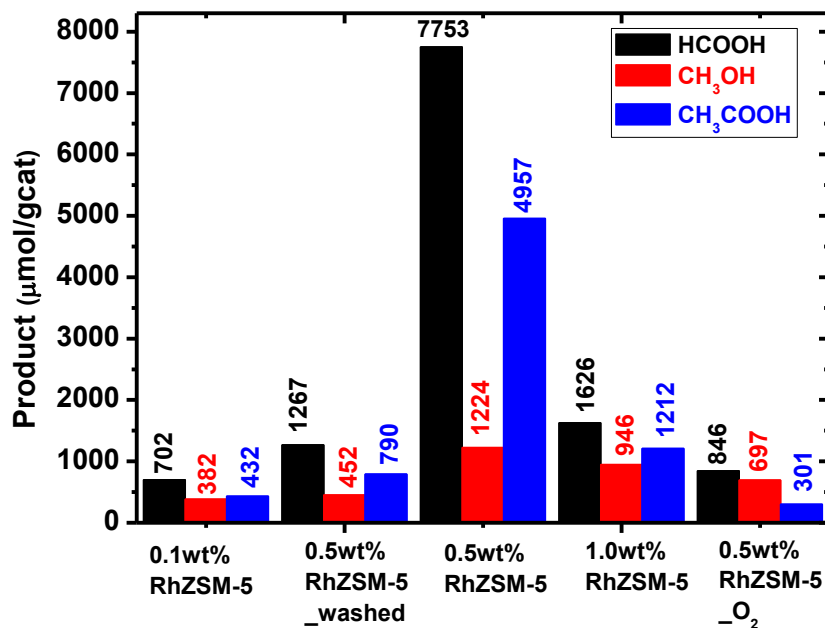


Figure 3.1 Catalytic activity of RhZSM-5 catalysts with different loadings as well as synthesized with different heat treatment. Conditions: 20mg catalyst, 4bar O<sub>2</sub>, 5bar CO, 20bar CH<sub>4</sub>, 150°C, 1h.

Figure 3.1 clearly shows that among the three loadings of samples (0.1wt% RhZSM-5, 0.5wt% RhZSM-5, 1.0wt% RhZSM-5), 0.5wt% RhZSM-5 exhibits the best catalytic performance. Compared to 0.1wt% Rh-ZSM-5, it is likely that 0.5wt% RhZSM-5 has more active sites than the former, hence its superior activity. On the other hand, higher loadings of rhodium on 1.0wt% RhZSM-5 inevitably leads to more rhodium nanoparticles (as will be shown in CO-DRIFTS studies) which not only decreases noble metal atom efficiency, but also may partially block access to the zeolite pores, thus decreasing the activity. Comparing catalyst with 0.5wt% loading obtained by H<sub>2</sub> reduction and air calcination, 0.5wt% RhZSM-5-O<sub>2</sub> also shows inferior activity. Previous studies<sup>6</sup> have shown that air calcination of Rh supported on zeolite at temperatures higher than 500°C leads to the formation of Rh<sub>2</sub>O<sub>3</sub> with limited protonolysis to form rhodium ions. Therefore, it can be concluded that rhodium oxide species is less active compared to

the sites generated through H<sub>2</sub> reduction. The nature of active rhodium species will be further elucidated in section 3.3.3.

The unique catalytic performance of 0.5wt% RhZSM-5 warrants further study to better understand how reaction conditions affect the reaction rate and product distribution. Parametric study on the effect of reaction temperature, batch reaction time and partial pressure of O<sub>2</sub> was conducted using 0.5wt% RhZSM-5.

Product formation at different temperatures on 0.5wt% RhZSM-5 is shown in Figure 3.2. The reaction lights off at temperature above 110°C. The product involves HCOOH, CH<sub>3</sub>OH and CH<sub>3</sub>COOH in the aqueous phase, and CO<sub>2</sub> as over-oxidation product in the gas phase. At 130°C, the reaction is highly selective and formation of CO<sub>2</sub> from methane over-oxidation is negligible. However, the overall amount of product formed is too low and methane conversion is below 0.1%. At 150 °C, the highest amount of aqueous oxygenates can be achieved, as the reaction rate depends exponentially on temperature. However, over-oxidation of liquid product leads to 5800 μmol/gcat CO<sub>2</sub>. As temperature is further increased to 170 °C, deep oxidation of the oxygenates leads to the formation of CO<sub>2</sub> as the primary product.

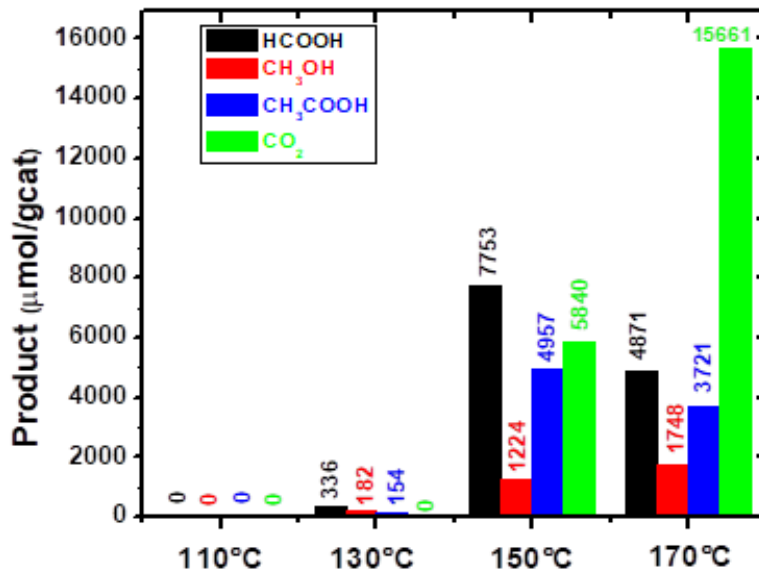


Figure 3.2 Product formation on 0.5wt% RhZSM-5 at different temperatures. Conditions: 4bar O<sub>2</sub>, 5bar CO, 20bar CH<sub>4</sub>, 20mg catalyst, 20mL DI water, 1h.

Similarly, if the temperature is fixed at 150°C and the batch reaction time is extended, the evolution of product at different reaction time with pO<sub>2</sub>=4 bar at 150 °C is shown in Figure 3.3. The formation of C1 liquid oxygenates, namely methanol and formic acid, undergo a maximum as reaction time is varied. The decrease of formic acid and methanol formation at longer reaction time is attributed to oxidation of the product to CO<sub>2</sub>. Acetic acid, on the other hand, continues to increase at long reaction time. These results suggest that under pO<sub>2</sub>=4 bar, over oxidation of C1 oxygenates to CO<sub>2</sub> is facile which eventually reduces selectivity at high CH<sub>4</sub> conversions.

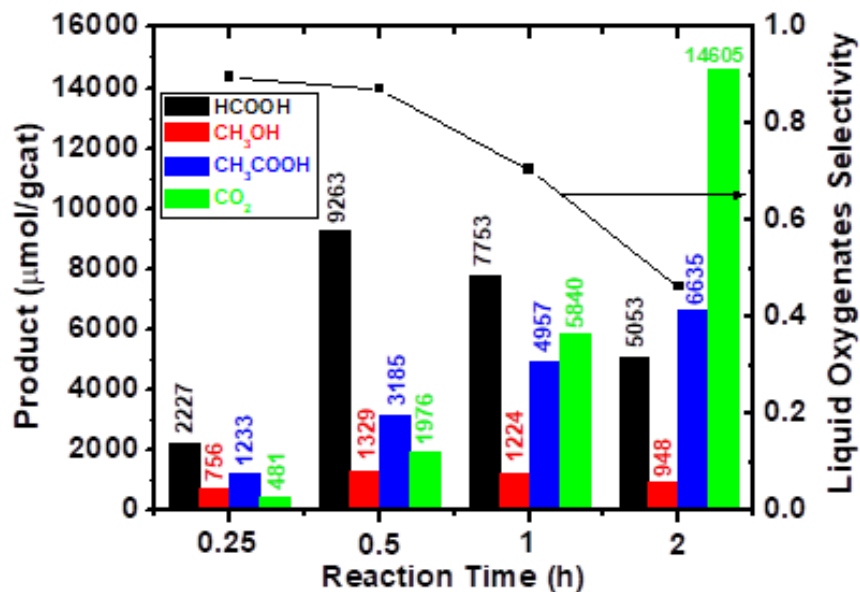


Figure 3.3 Product formation on 0.5wt% RhZSM-5 at different batch time. Conditions: 4bar O<sub>2</sub>, 5bar CO, 20bar CH<sub>4</sub>, 150°C, 20mg catalyst, 20mL DI water.

These results prompted further study on the partial pressure of O<sub>2</sub>, aiming to reduce over oxidation of the liquid oxygenates and increase their yields at high conversion. As shown in Figure 3.4, as partial pressure of O<sub>2</sub> is reduced from 4 bar to 0.5 bar, over-oxidation of liquid oxygenates is significantly suppressed and product selectivity shifts to form CH<sub>3</sub>COOH. The selectivity of acetic acid increases to 56% when pO<sub>2</sub> is reduced to 2 bar. Further reducing pO<sub>2</sub> to 0.5 bar, acetic acid selectivity increases to 87%. However, the rate of oxygenates formation is also significantly reduced, as low pO<sub>2</sub> results in limited O<sub>2</sub> concentration in the aqueous phase. Overall, the formation of acetic acid can be maximized with pO<sub>2</sub>=2 bar with high selectivity. The shift of selectivity to C2 product can be accounted by the relative rate of two competing reaction pathways (discussed in further detail in the mechanistic study). Lower oxygen partial pressure reduces not only the rate of methane activation but also the subsequent oxy functionalization of methane. The competing carbonyl insertion step, on the other hand, depends on carbon monoxide partial pressure and is therefore unaffected. The overall result is a faster C2 product formation compared to C1 product.

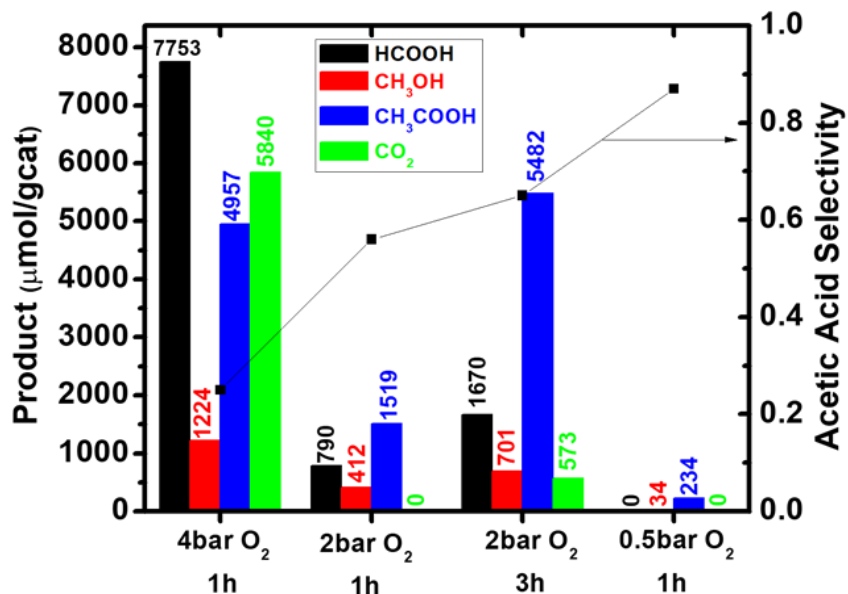


Figure 3.4 Methane oxidation product formation on 0.5wt% RhZSM-5 with different pO<sub>2</sub>; Conditions: 20 mg catalyst, 20 mL DI water, 5 bar CO, 20 bar CH<sub>4</sub>, 150 °C.

The optimized reaction condition for acetic acid production using 2bar O<sub>2</sub>, 5bar CO, 20bar CH<sub>4</sub> at 150°C can be further investigated to push for higher conversion and examine if the conversion – selectivity tradeoff<sup>7</sup> that is typically encountered in oxidative methane conversion applies. Under the optimized condition, the reaction was tested at different batch time (Figure 3.5). Acetic acid can be formed as the primary aqueous phase product throughout the reaction and selectivity to acetic acid is over 55%. At 6 h reaction time, formation of acetic acid is over 13500 µmol/gcat and selectivity can still maintain at 59%. Over oxidation of aqueous oxygenates can be controlled under this condition and acetic acid can be accumulated in the aqueous phase with a rate of 2252 µmol/gcat/h. Conversion of CH<sub>4</sub> is calculated and tabulated in Table 1.1. The final conversion at 6h is 4%. Further extending the reaction

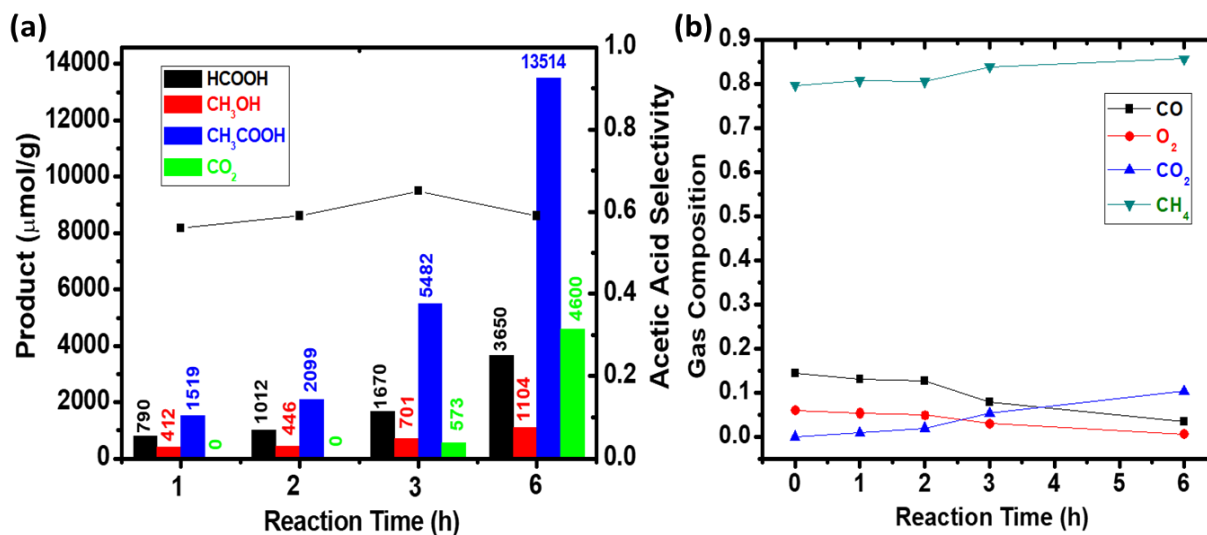


Figure 3.5 Methane oxidation product formation (a) and gas phase composition (b) on 0.5wt% RhZSM-5 with different reaction time at  $p_{O_2}=2\text{bar}$ ; Conditions: 20 mg catalyst, 20 mL DI water, 2 bar  $O_2$ , 5 bar  $CO$ , 20 bar  $CH_4$ , 150 °C.

time to 12h only led to a small increase of acetic acid to 14711 µmol/gcat. Analysis of gas phase composition shows that at 6h the limiting reactant  $O_2$  is almost depleted and therefore further extending reaction time does not lead to significant accumulation of product.

Table 3.1 Calculated  $CH_4$  conversion at different reaction time

Reaction time (h) <sup>#</sup>	1	2	3	6
Total amount of product (µmol)	54	65	168	475
Calculated $CH_4$ conversion (%) <sup>*</sup>	0.4	0.5	1.4	4.0

<sup>#</sup>Reaction conditions: 20mg catalyst, 2bar  $O_2$ , 5bar  $CO$ , 20bar  $CH_4$ , 20mL DI water, 150°C

<sup>\*</sup>The amount of  $CH_4$  charged into the reactor is calculated from 20bar of  $CH_4$  at RT. The volume of gas is 15mL, which corresponds to 12mmol  $CH_4$ .

Considering the significant background consumption of CO and O<sub>2</sub> due to side reactions, one would naturally wonder if the methane conversion can be further increased just by pressurizing more O<sub>2</sub> and CO (since simply increasing O<sub>2</sub> partial pressure would lead to high level of over-oxidation as shown in Figure 3.4). The reaction with different O<sub>2</sub>, CO partial pressure while fixing their ratio was conducted. Figure 3.6 shows that increasing the partial pressure of O<sub>2</sub> and CO can lead to a higher reaction rate, but the activity is notably suppressed if CO partial pressure reaches a certain level. High level of CO likely leads to the reduction of rhodium species into metallic particles, deactivating the otherwise active rhodium cations. Therefore, it is concluded that simply increasing O<sub>2</sub> and CO pressure cannot further increase methane conversion.

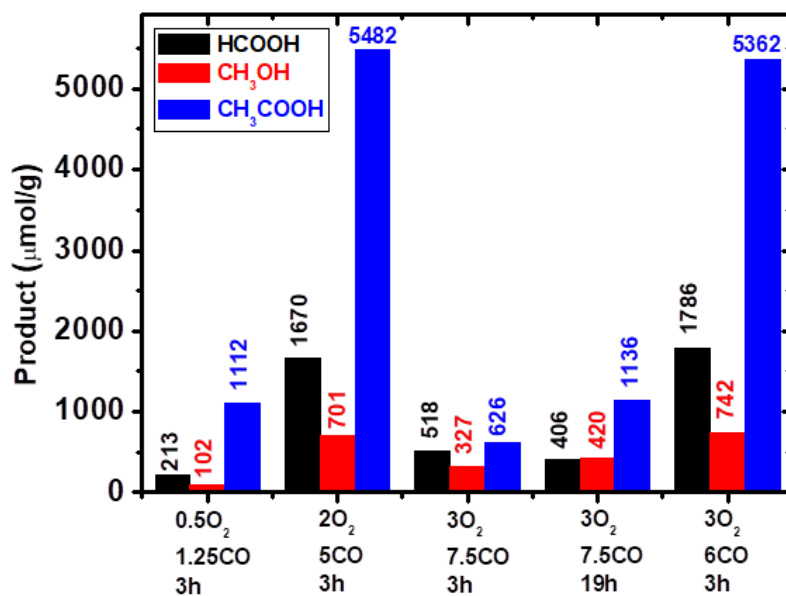


Figure 3.6 Product formation on 0.5wt% RhZSM-5 with same O<sub>2</sub>/CO ratio. Conditions: 20mg catalyst, 20mL DI water, 20bar CH<sub>4</sub>, 150°C, 3h.

### 3.3.2 Experimenting with different reactor setup for improved acetic acid concentration

The potential to further increase acetic acid formation on Rh-ZSM-5 beyond the single batch result was studied first using the fed-batch operation (description and scheme detailed in 3.2 Experimental Methods). The idea is to feed reactant gas into the reactor continuously during reaction to replenish so that the limitation of one-pass operation can be addressed. The feed gas mixture with or without CH<sub>4</sub> was both tested and Figure 3.7 shows the results.

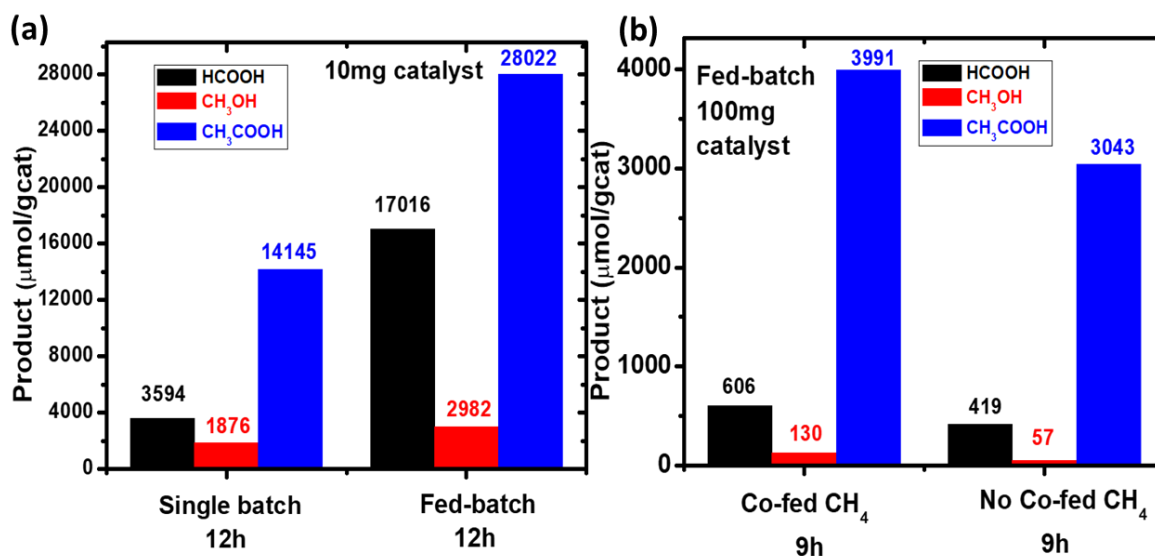


Figure 3.7 (a) Comparison of product formation using single-batch and fed-batch operation and (b) comparison of product formation using fed-batch operation and feed gas mixture with and without CH<sub>4</sub>; Conditions: 10~100 mg catalyst, 10~20 mL DI water, 2 bar O<sub>2</sub>, 5 bar CO, 20 bar CH<sub>4</sub>, 150 °C.

Under fed-batch operation, acetic acid can be produced with yield of 28022  $\mu\text{mol/gcat}$  if reaction time is extended to 12 h while single batch operation conducted for the same reaction time only leads to 14145  $\mu\text{mol/gcat}$ . The average rate of acetic acid formation is 2335  $\mu\text{mol/gcat/h}$  which is comparable to the rate of 2252  $\mu\text{mol/gcat/h}$  at 6 h in single batch operation. It is therefore concluded that the 0.5wt% RhZSM-5 is stable on stream at the current acetic acid concentration. In this case, acetic acid concentration can be increased from 0.8g/L to 1.6g/L. When CH<sub>4</sub> was not co-fed in the reactant gas, there's a 23% decrease in

the acetic acid formation. The decrease indicates that the reaction is still limited by the presence of methane dissolved in the aqueous phase in the fed-batch operation and that higher methane partial pressure benefits the formation of aqueous oxygenates.

Although fed-batch operation demonstrates that acetic acid formation can further continue, the reaction is eventually still limited by accumulation of CO<sub>2</sub> in the gas phase. Without a continuous system that removes CO<sub>2</sub> and replenish reactant simultaneously, the reaction eventually comes to stop due to the lack of reactants. Therefore, a semi-batch bubbler reaction system was further set up by continuously bubbling reactant gas mixture through the catalyst suspension and condense acetic acid into the aqueous phase. The semi-batch operation was conducted at 150°C with total pressure of 560 psig and volumetric flow rate of 14 mL/min (measured at ambient condition). At conditions similar to the batch operation, acetic acid can indeed further accumulate to higher concentrations. With 24 h accumulation, acetic acid concentration reached 2.5 g/L, as shown in Figure 3.6. However, further extending reaction time leads to

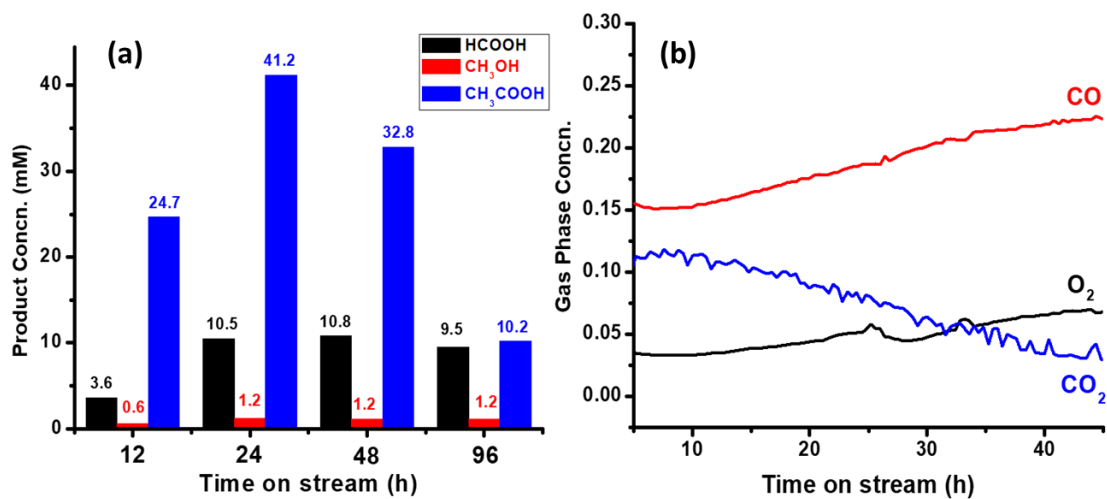


Figure 3.8 (a) aqueous phase product concentration and (b) gas phase composition at different time on stream monitored during semi-batch operation; Conditions: 400mg catalyst, 80 mL DI water, O<sub>2</sub>:CO:CH<sub>4</sub>=2:5:20, P=560 psig, 150 °C, 14 mL/min.

continued decrease of acetic acid concentration. At the same time, gas phase composition showed an increase of O<sub>2</sub> and CO content and decrease in concentration of CO<sub>2</sub>. Combining these observations, it can be concluded that the catalyst is showing deactivation when subjected to long time semi-batch reaction. To confirm this, the used catalyst was collected through filtration, and then washed and dried for further testing. The catalyst becomes completely inactive at this point. To understand the reason behind deactivation, used catalyst was characterized by TPO, CO chemisorption and CO-DRIFTS. The results and analysis are detailed in section 3.3.3. Regeneration of the catalyst is possible and will be discussed in section 3.3.3 as well.

### 3.3.3 Catalyst Characterization

Both the as-synthesized and used RhZSM-5 catalysts were characterized by a combination of different spectroscopic and microscopic technique to understand the properties of the catalyst and nature of the active catalytic center.

#### BET surface area

N<sub>2</sub>-physisorption surface area analysis was conducted on both HZSM-5 and different rhodium incorporated catalysts. Surface area was determined using single-point BET method. The introduction of rhodium species onto the ZSM-5 support does not lead to significant change of both the surface area and pore volume, indicating that no pore blockage happened.

Table 3.2 Physicochemical properties of ZSM-5 supported Rh catalysts

Catalyst	BET surface area (m <sup>2</sup> /g)	Total pore volume (cm <sup>3</sup> /g)
----------	--------------------------------------	--

HZSM-5 (Alfa Aesar, 550°C calcined)	510	0.2568
0.5wt% RhZSM-5	509	0.2562
0.5wt% RhZSM-5_washed	526	0.2650
1.0wt% RhZSM-5	498	0.2553

### ICP-AES analysis

To verify that the reaction happens on the heterogeneous catalyst surface rather than rhodium species leached into the liquid phase, first the leaching of metal species was studied. The reaction filtrate from 0.5wt% RhZSM-5 at different reaction time was collected and analyzed by ICP-AES.

Table 3.3 Rhodium leaching during methane oxidation reaction at conditions

Rxn time (h)	Condition	Rh Conc. (ppm)	wt% Rh Loading Leached	Corresponding carboxylic acid production ( $\mu\text{mol/g-cat}$ )
1	4bar O <sub>2</sub>	0.6	0.06	12720
3	2bar O <sub>2</sub>	n.d.	0	7152
4.5		n.d.	0	10374
6		n.d.	0	17164
12		0.1	0.01	18449

Conditions: 20mg 0.5wt% RhZSM-5, 20mL DI water, 5bar CO, 20bar CH<sub>4</sub>, 150°C

As shown in Table 3.3, rhodium leaching under the condition that selectively converts methane to acetic acid is negligible and only at longer contact time that rhodium leaching can be detected. At a more oxidizing environment (4bar O<sub>2</sub>), rhodium leaching is faster due to the faster accumulation of carboxylic acid. Typically, the pH of the aqueous phase drops to 2.5 after reaction and the acidic environment is the possible reason of rhodium leaching. The leached rhodium species arise from metallic nanoparticles on the external surface of the zeolite, while the isolated cations inside zeolite pore channels are resistant to leaching.<sup>8,9</sup> The faster leaching at a more oxidizing environment also confirms that the metallic rhodium is the leaching source.

The activity of the filtrate from Table 3.3 entry 1 was further tested at the same reaction conditions to double check the activity of leached rhodium species. The leached solution does not show any activity for CH<sub>4</sub> oxidation, only further oxidizing the liquid oxygenates. Additionally, aqueous solutions of both Rh(NO<sub>3</sub>)<sub>3</sub> and RhCl<sub>3</sub> were tested for their activity on methane partial oxidation in the reactor and compared to the heterogeneous catalyst. Same charge of rhodium species (0.9 μmol) was used and the reported value was scaled to a per gram catalyst unit assuming a 0.5wt% loading on solid support, Figure 3.9. Rhodium ions in aqueous solution only shows limited activity, and addition of mineral acid only promotes formation of formic acid and methanol, contrary to what's reported in homogeneous catalysis<sup>3</sup>. Once HZSM-5 is added together with Rh(NO<sub>3</sub>)<sub>3</sub>, formation of acetic acid immediate starts to light-off, and amongst all catalysts, 0.5wt% RhZSM-5 which contains ample rhodium coordinated with zeolite framework shows the highest activity towards acetic acid. This strongly suggests that coordination of rhodium ion onto the zeolite framework is essential to yield an active catalyst and therefore, the observed activity for CH<sub>4</sub> oxidation is predominantly due to heterogeneous Rh species on the ZSM-5 support rather than homogeneous Rh leached out.

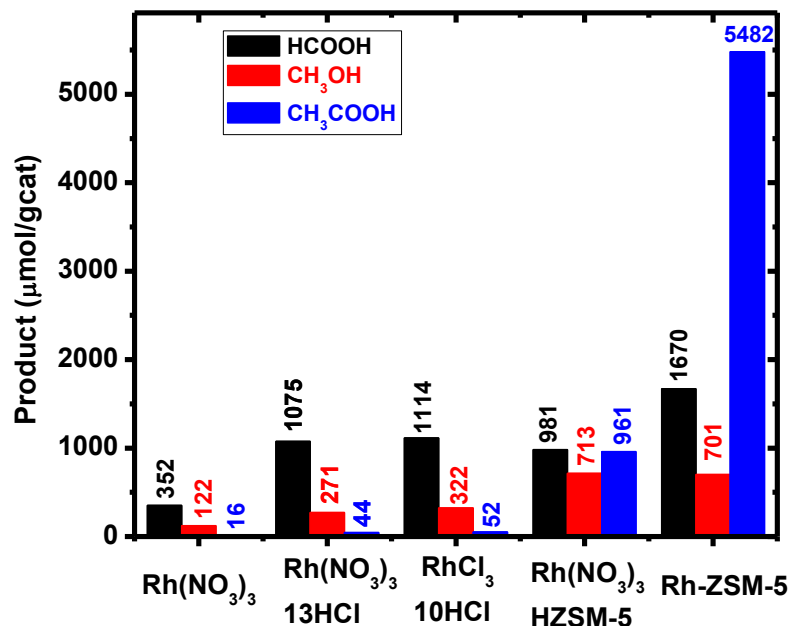


Figure 3.9 Comparison of catalytic activity of aqueous phase rhodium ions and RhZSM-5. Conditions: 0.9 μmol Rh, 20 mL DI water, 2 bar O<sub>2</sub>, 5 bar CO, 20 bar CH<sub>4</sub>, 150 °C, 3 h.

## XRD

The XRD patterns of the parent ZSM-5 support, fresh 0.5 wt% RhZSM-5 and the sample after reaction were recorded. As shown in Figure 3.10, the addition of rhodium into the zeolite does not change the zeolite XRD pattern and no diffraction peaks corresponding to rhodium metal or oxide can be observed, suggesting that the zeolite structure remains intact and the rhodium species are well dispersed. Previous studies on zeolites have indicated that under hydrothermal conditions the framework of certain types of zeolites is prone to dealumination, which leads to the destruction of the framework, for example HY zeolite<sup>10</sup>. Similar observations can also be made when zeolites are treated in hot water<sup>11</sup>. Here it is shown that under the reaction conditions studied the ZSM-5 structure is stable and does not degrade during hot water treatment.

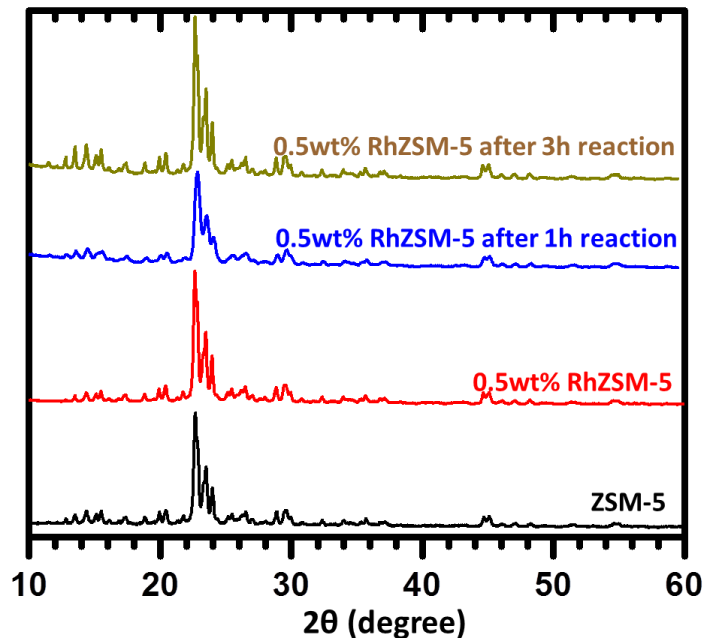


Figure 3.10 X-ray Diffraction Patterns of parent ZSM-5, as-synthesized and used 0.5wt% RhZSM-5.

## XPS

Rh 3d and Si 2p XPS characterization was performed on the as-synthesized 0.5wt% RhZSM-5 (Figure 3.11). The surface scan of the zeolite catalyst shows no Rh photoemission. This indicates that the amount of Rh on the external surface of the zeolite is below the detection limit of XPS<sup>12</sup>. To study the Rh species anchored on the internal wall of the micropores of RhZSM-5, the oxide surface layers of ZSM-5 must be removed. After Ar<sup>+</sup> sputtering for 5 min, enough layers of silica on the external surface of RhZSM-5 were removed, and Rh 3d feature contributed from the Rh species anchored in the internal walls of zeolite was clearly identified in Figure 3.11(a)<sup>13</sup>. On the other hand, the photoemission feature of Si 2p shows no difference before and after Ar<sup>+</sup> sputtering.

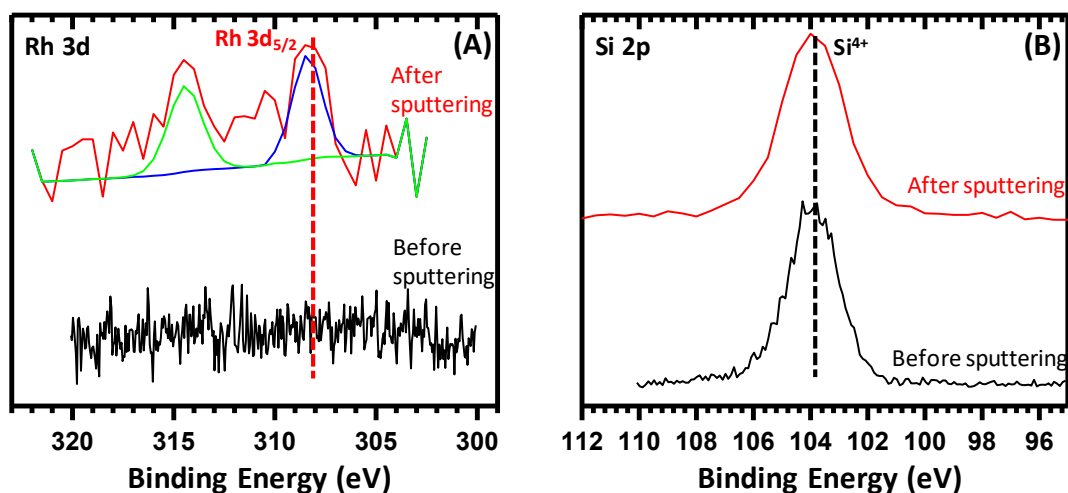


Figure 3.11 Photoemission features of Rh 3d (A) and Si 2p (B) of as-synthesized 0.5wt% RhZSM-5 before and after Ar<sup>+</sup> sputtering.

#### Microscopy characterization

ac-HAADF STEM images were taken for 0.5wt% RhZSM-5 and 0.5wt% RhZSM-5\_washed samples to elucidate rhodium dispersion on the catalyst (imaging study conducted in collaboration with Dr. Lawrence F. Allard, Oak Ridge National Lab). Figure 3.12 shows dark field and bright field images pairs of the samples at lower magnification. There are a few Rh nanoparticles on the external surface of zeolite for 0.5wt% RhZSM-5 both in fresh and used state, whereas for the sample of RhZSM-5\_washed no Rh nanoparticles can be observed.

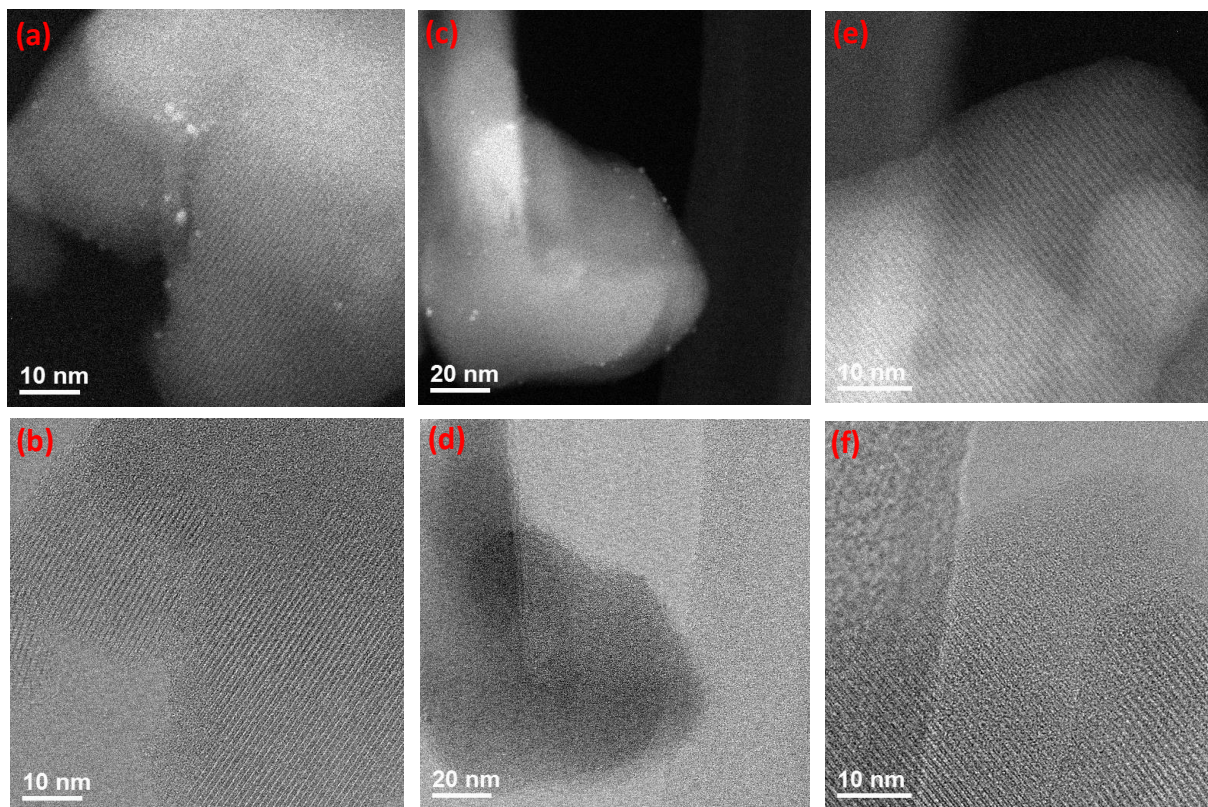


Figure 3.12 HAADF and BF STEM image pairs, acquired simultaneously, of as-synthesized 0.5wt% RhZSM-5 (a and b), 0.5wt% RhZSM-5 after use in the reaction (c and d), and 0.5wt% RhZSM-5\_washed (e and f).

The presence of rhodium nanoparticles on the external surface does not rule out the possibility of rhodium residing inside zeolite pores as single cations. Therefore, further imaging studies were performed on the as-synthesized 0.5wt% RhZSM-5 sample to identify them. Figure 3.13 shows the aberration-corrected HAADF STEM images of a thin edge of as-synthesized 0.5wt% RhZSM-5 flake. The rhodium single atoms (circled in white) are clearly visible as brighter dots due to higher Z number of the atom compared to aluminum, oxygen or silicon. The imaging results strongly suggests the presence of rhodium single atoms in the as-synthesized 0.5wt% RhZSM-5 catalyst, accompanied by nanoparticles on the external surface.

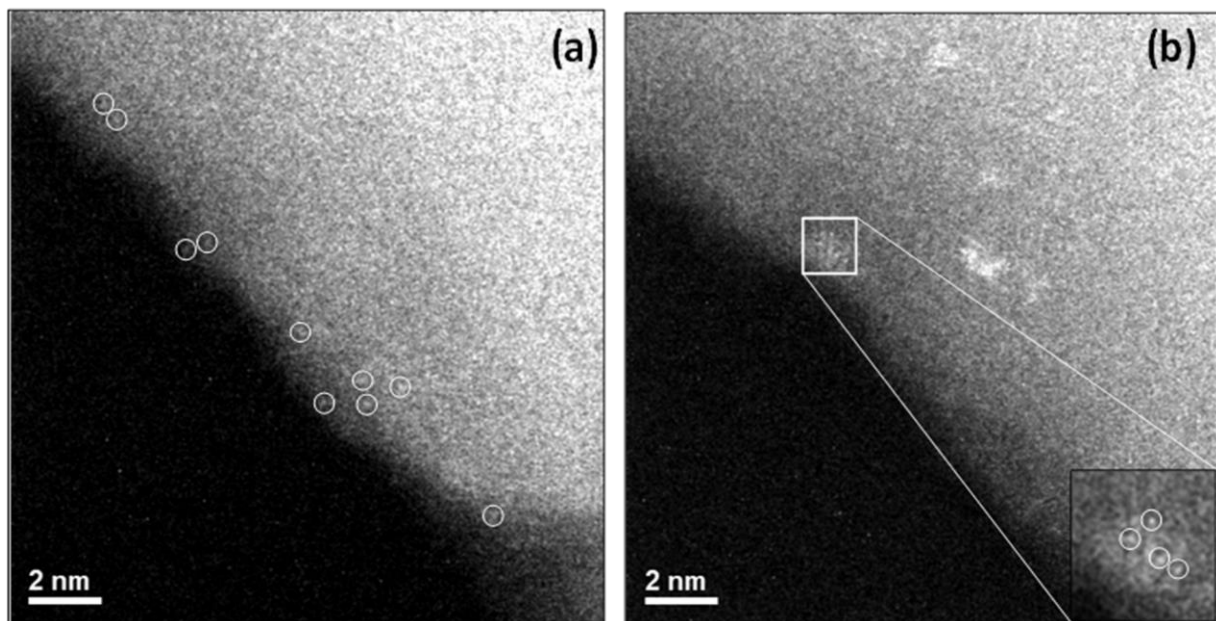


Figure 3.13 (a) and (b) ac-HAADF STEM images of as-synthesized 0.5wt% RhZSM-5 showing (a) isolated rhodium single cations on thin edge of the flake of catalyst and (b) nanoparticles of rhodium at same magnification (rhodium species circled in white).

## CO-DRIFTS

Using CO as a probe molecule, DRIFTS was performed on various active RhZSM-5 catalysts at ambient conditions. Dicarbonyl species are formed on isolated Rh cations, whereas on Rh nanoparticles, CO binds in both atop and bridged configuration<sup>14</sup>. Figure 3.14(a) shows the CO-DRIFT spectra for 1.0wt% RhZSM-5, 0.5wt% RhZSM-5, and 0.5wt% RhZSM-5\_washed. All three binding modes of CO are present on samples of 1.0wt% and 0.5wt% RhZSM-5. The absorption peaks at 2116  $\text{cm}^{-1}$  and 2049  $\text{cm}^{-1}$  are due to the symmetrical and asymmetrical stretching of CO from the isolated mononuclear Rh(I)(CO)<sub>2</sub> species;<sup>14</sup> while the peak at 2082  $\text{cm}^{-1}$  is attributed to either the atop binding of CO on Rh nanoparticles or isolated Rh(I)(CO)<sub>3</sub> species.<sup>14, 15</sup> The broad peak centered at 1885  $\text{cm}^{-1}$  is assigned to bridged binding of CO on Rh nanoparticles.<sup>14</sup> Based on the method described in literatures,<sup>15</sup> the portion

of isolated Rh was estimated at 50%. Moreover, as expected, for 0.5wt% RhZSM-5\_washed, the peaks at 2082 and 1885  $\text{cm}^{-1}$  are almost absent, indicating the preponderance of isolated dicarbonyl  $\text{Rh}^{\text{I}}(\text{CO})_2$  species. Washing is an appropriate method here to check for the presence of the isolated rhodium species and identify the active catalyst sites. As shown in Figure 3.1, the selectivity of the parent and 0.5wt% RhZSM-5\_washed samples are similar, and the activities are also comparable.

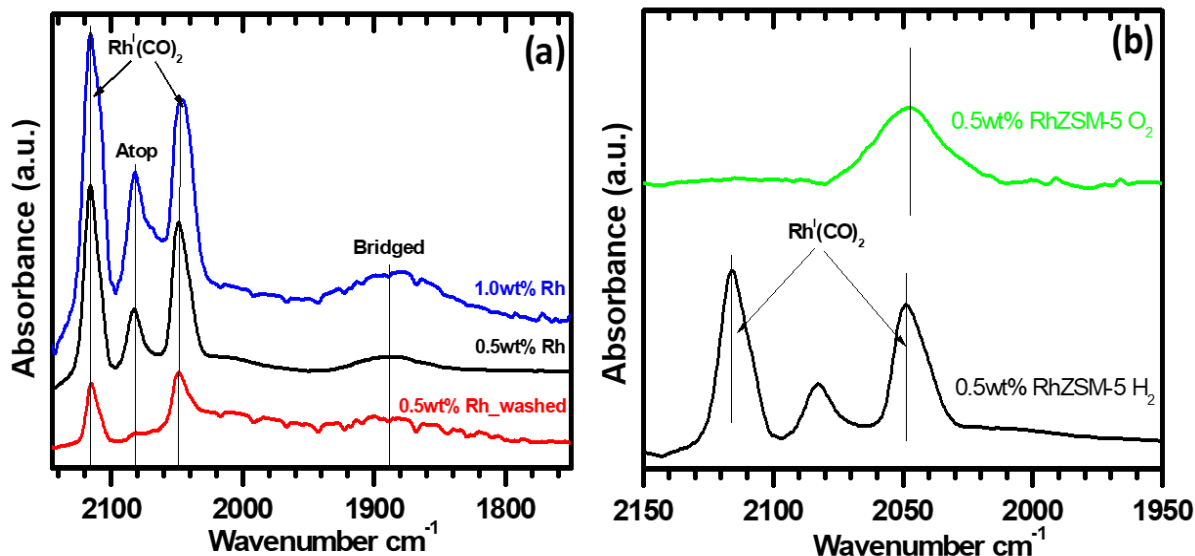


Figure 3.14 CO-DRIFTS of (a) RhZSM-5 samples with different loadings prepared by  $\text{H}_2$  reduction and (b) 0.5wt% RhZSM-5 samples prepared with different heat treatment.

Figure 3.14(b) shows CO-DRIFTS of as-synthesized 0.5wt% RhZSM-5 (bottom trace), and 0.5wt% RhZSM-5 calcined in air (top trace). For the latter, the  $\text{Rh}^{\text{I}}(\text{CO})_2$  peaks are absent, whereas a single broad peak centered at 2045  $\text{cm}^{-1}$  appears. This peak can be assigned to atop binding of CO on Rh/Rh oxide nanoparticles.<sup>16</sup> Since 0.5wt% RhZSM-5 calcined in air has much less activity (Figure 3.1), it can be concluded that the active sites are the isolated rhodium cations in the zeolite formed during  $\text{H}_2$  reduction, not rhodium oxidic particles formed from air calcination.

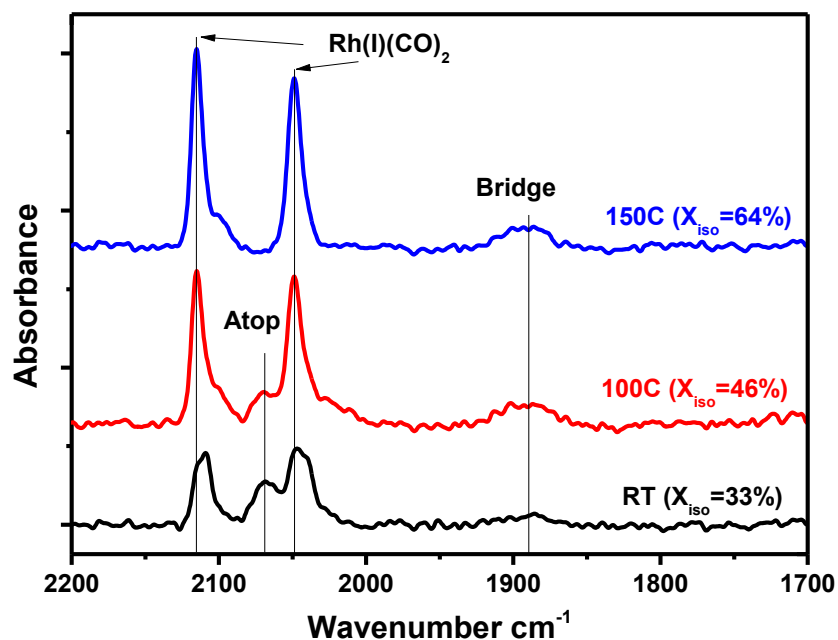


Figure 3.15 CO-DRIFTS of 0.5wt% RhZSM-5 with 10% CO treated at different temperature. Prior to experiment the catalyst was intentionally sintered with H<sub>2</sub> at 250°C for 1h.

Furthermore, CO was found to not only stabilize rhodium single atom in the mononuclear Rh(I)(CO)<sub>2</sub> state, but also re-disperse metallic rhodium species into single atoms. Figure 3.15 shows the CO-DRIFTS spectra of 0.5wt% RhZSM-5 intentionally sintered to generate more metallic rhodium aggregates. Fractions of single atom rhodium was calculated from extinction coefficient of different rhodium carbonyl species.<sup>15</sup> The sintered catalyst adsorbed with CO at room temperature consists of 33% single atom rhodium, while as the adsorption temperature increases from RT to 110°C and 150°C, a decrease of CO binding atop to rhodium coupled with an increase in the Rh(I)(CO)<sub>2</sub> corresponding to rhodium single atom is observed. The fraction of isolated rhodium species increased to 46% at 110°C and further to 64% at 150°C. However, the bridged binding feature at ~1880cm<sup>-1</sup> does not decrease even at 150°C, suggesting that big nanoparticles on the external surface are difficult to re-disperse by CO.

## XAS study

Both the oxidation state and coordination environment of rhodium species was investigated by X-ray Absorption Spectroscopy (XAS) at Rh K-edge. XANES spectra of RhZSM-5 with different loadings and heat treatment can illustrate the oxidation state of the active rhodium species (Figure 3.16). Four rhodium standards, including rhodium foil,  $\text{Rh(I)}_2(\mu\text{-OH})(\text{COD})_2$  ( $\text{Rh}^{1+}$ ),  $\text{Rh(II)}_2(\text{CH}_3\text{COO})_4$  ( $\text{Rh}^{2+}$ ) and  $\text{Rh}_2\text{O}_3$  ( $\text{Rh}^{3+}$ ) were used in the XANES analysis. All RhZSM-5 samples clearly shows absorption edge patterns different from that of rhodium foil and similar to that of cationic rhodium standards, indicating that rhodium species are mostly in cationic state. As a comparison, XANES spectrum of 0.5wt% RhZSM-5\_washed was also recorded in aqueous suspension of the catalyst and compared to the spectrum recorded in the gas phase. The absorption edge does not show any change either in edge position or edge pattern, which indicates that rhodium structure does not undergo significant changes upon interaction with water and that XAS studies conducted in the gas phase can accurately capture the structural information of active rhodium species.

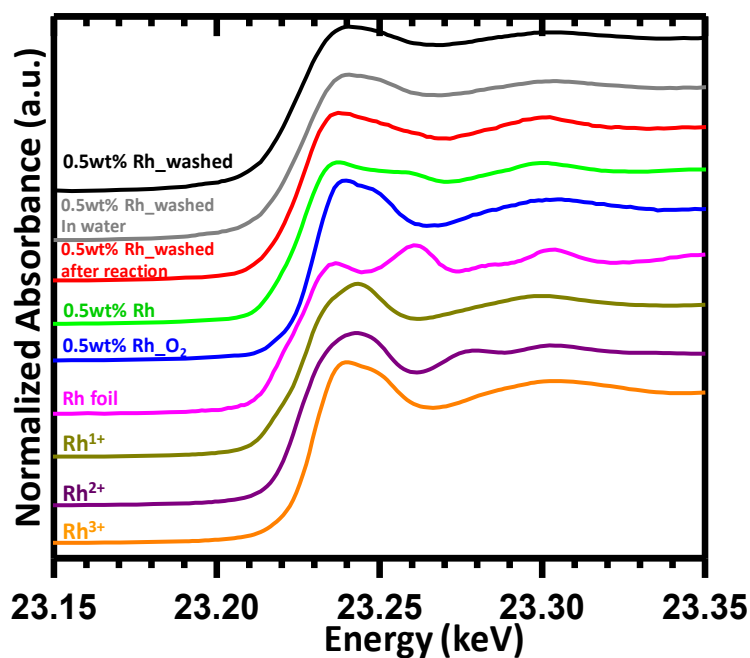


Figure 3.16 Normalized Rh K-edge XANES spectra of different RhZSM-5 catalysts and rhodium standards. Spectra of RhZSM-5 samples were collected ex-situ in the gas phase in fluorescence mode. For 0.5wt% RhZSM-5\_washed, aqueous suspension of the sample was also analyzed in fluorescence mode. Spectra for the four standards were collected in transmission mode.

One cannot fully rule out contributions of metallic rhodium species by just comparing absorption edge patterns from the XANES spectra. Therefore, Linear combination fitting of RhZSM-5 samples were performed using the four standards to elucidate the contribution of different oxidation state. The fitted fraction of cationic and metallic rhodium contributions is summarized in Table 3.4. The fitting results indicated that in the as-synthesized 0.5wt% RhZSM-5\_washed sample, Rh is fully cationic and is most likely in 1+ oxidation state. While the linear combination fitting of 0.5wt% RhZSM-5\_washed after reaction shows 78% of cationic Rh and 22% of metallic Rh. For 0.5wt% RhZSM-5 without washing, the fitting shows that it consists of 53% cationic Rh and 47% metallic Rh. The metallic contribution of 0.5wt% RhZSM-5 most likely arises from nanoparticles on the external surface. Indeed, the ratio of metallic Rh corresponds well with the fraction of rhodium nanoparticles obtained from CO-DRIFTS study. For 0.5wt% RhZSM-5\_washed, the fully cationic state of rhodium also matches CO-DRIFTS result of fully single atom dispersion (Figure 3.14) and the absence of nanoparticles on the external surface from STEM imaging (Figure 3.12).

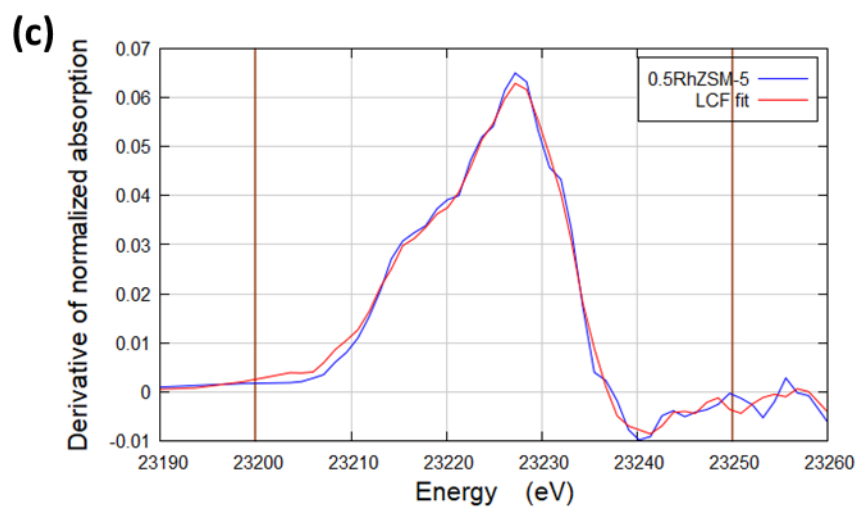
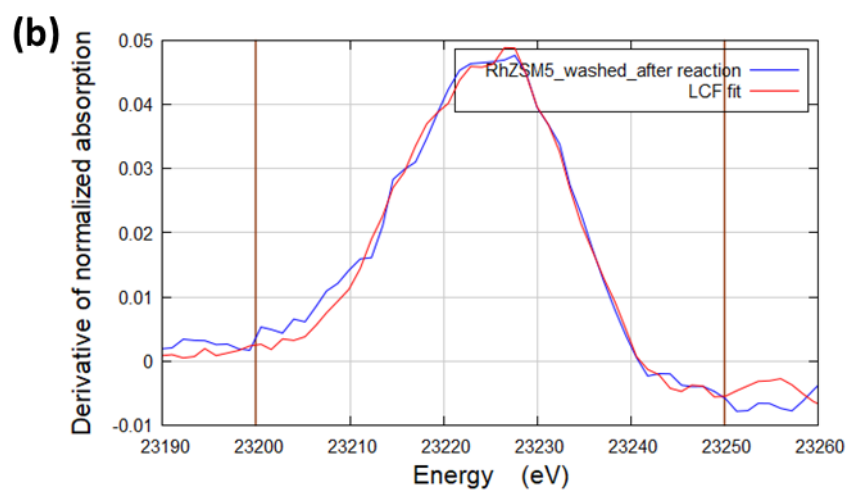
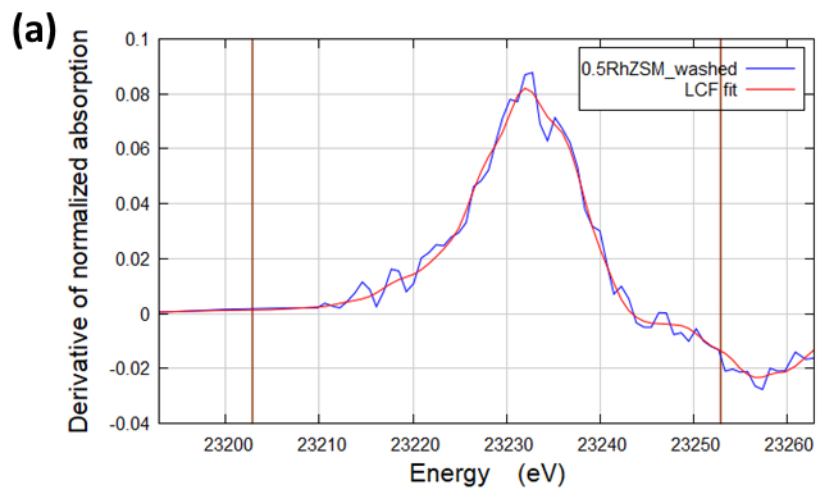


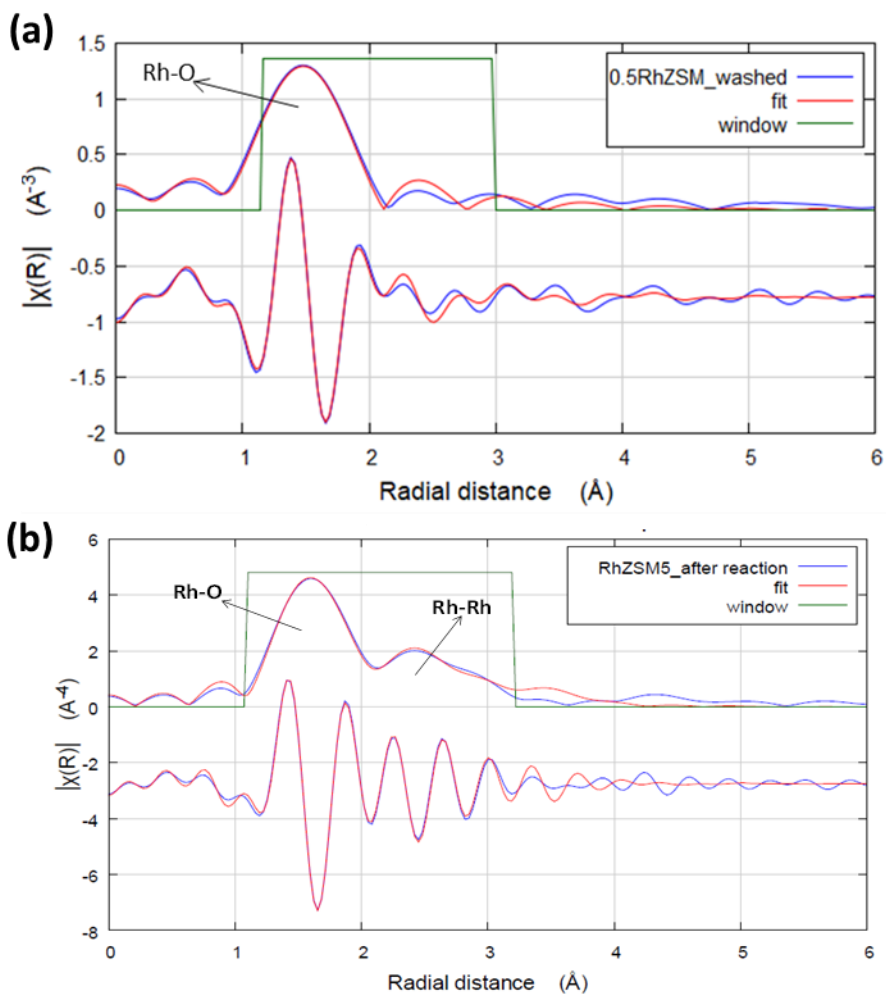
Figure 3.17 Linear combination fitting (LCF) of first order derivative XANES spectra for (a) 0.5wt% RhZSM-5\_washed, (b) 0.5wt% RhZSM-5\_washed after reaction and (c) 0.5wt% RhZSM-5.

Table 3.4 Fraction of cationic and metallic rhodium species from LCF of Rh K-edge XANES spectra

Sample	Cationic Rh	Metallic Rh
0.5wt% RhZSM-5_washed	100%	0
0.5wt% RhZSM-5_washed After reaction	78%	22%
0.5wt% RhZSM-5	53%	47%

EXAFS analysis of different RhZSM-5 samples was conducted to investigate the coordination environment of rhodium. The EXAFS data along with the fit was plotted in Fourier Transformed space in Figure 3.18. The detailed fitting results for different rhodium catalysts are summarized in Table 3.5. While as-synthesized 0.5wt% RhZSM-5 contains both Rh-Rh interaction and Rh-O interaction, confirming the co-existence of both single rhodium cations and metallic nanoparticles, 0.5wt% RhZSM-5\_washed shows no distinct Rh-Rh interaction. Rhodium species are coordinated with oxygen with a coordination number of around 4 and bond length of 1.99Å, Table 3.5. The full dispersion of rhodium in single cations is consistent with both the CO-DRIFTS study and STEM images. At the same time, 0.5wt% RhZSM-5\_washed dispersed in water showed no change of coordination environment, confirming the finding in the XANES spectra that interaction with water does not lead to structural changes of rhodium. When 0.5wt% RhZSM-5\_washed catalyst was used for reaction at 2bar O<sub>2</sub>, 5bar CO, 20bar CH<sub>4</sub> at 150°C for 3h, the used catalyst readily shows development of Rh-Rh bonding as a result of rhodium nanocluster formation, Table 3.5. The formation of nanoclusters is likely due to sintering from

isolated rhodium cations. However, the sintered metallic nanoclusters can be readily re-dispersed by CO at the reaction temperature, as shown in Figure 3.15. The sintering of rhodium single atoms to small nanoclusters therefore do not lead to significant decrease in catalyst activity. Indeed, single batch and fed-batch operation demonstrated that the catalyst is stable on-stream for 12h, Figure 3.5(a) and Figure 3.7(a).



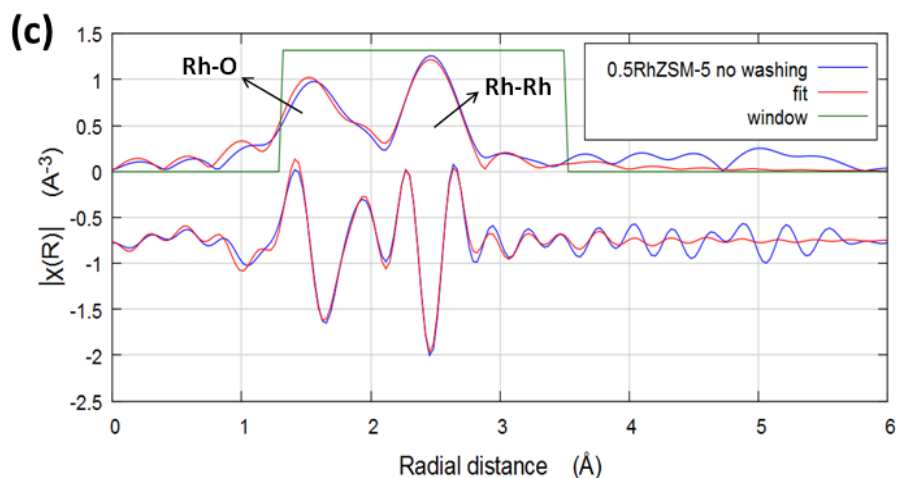


Figure 3.18 Rh K-edge EXAFS data of (a) 0.5wt% RhZSM-5\_washed, (b) 0.5wt% RhZSM-5\_washed after reaction and (c) 0.5wt% RhZSM-5 plotted in Fourier Transform space.

Table 3.5 EXAFS fitting parameters for RhZSM-5 catalysts at Rh K-edge

Sample	Path	CN <sup>[a]</sup>	R(Å) <sup>[b]</sup>	$\sigma^2(\text{Å}^2)$
0.5wt% RhZSM-5_washed	Rh-O	3.6±0.6	1.99±0.03	0.007
	Rh-Rh	-	-	-
0.5wt% RhZSM-5_washed after reaction	Rh-O	2.7±0.6	2.03±0.02	0.003
	Rh-Rh	0.6±0.2	2.70±0.01	0.005
0.5wt% RhZSM-5	Rh-O	3.0±0.7	2.03±0.04	0.005
	Rh-Rh	5.7±1.1	2.69±0.03	0.015

[a] CN, coordination number; [b] R, distance between absorber and backscattered atoms.

The fully cationic state of rhodium species in 0.5wt% RhZSM-5\_washed even after H<sub>2</sub> reduction is rather interesting. One can postulate that either rhodium species in single site dispersion is strongly resistant to reduction, or highly dispersed rhodium can easily coordinate to oxygen once it is in contact with air after reduction. To confirm this, the evolution of rhodium species during synthesis was followed by conducting in-situ XAS measurement on the 0.5wt% RhZSM-5\_washed sample (not subjected to any heat treatment prior to the experiment) after H<sub>2</sub> reduction at different temperatures and then exposed to air at room temperature. Figure 3.19 shows the XANES spectra of 0.5wt% RhZSM-5\_washed before reduction, reduced with 4% H<sub>2</sub>/He at different temperature and then exposed to air at room temperature.

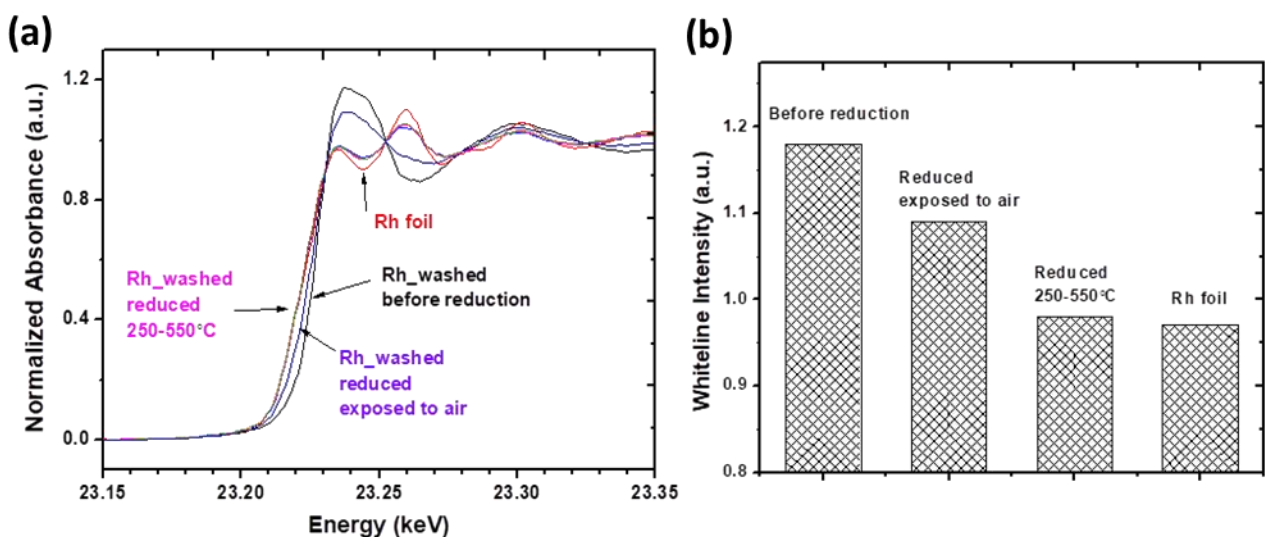


Figure 3.19 (a) Normalized Rh K-edge XANES spectra of 0.5wt% RhZSM-5\_washed sample before reduction, reduced at 250-550°C, exposed to air at RT after reduction and rhodium foil (b) Corresponding white line intensities of the four samples.

XANES spectra clearly demonstrated that the RhZSM-5 before reduction is in +3 state, likely in the form of Rh(NO<sub>3</sub>)<sub>3</sub>. Reduction with H<sub>2</sub> readily happens at temperatures above 250°C and spectra recorded in H<sub>2</sub> atmosphere show absorption edge similar to metallic rhodium. Both the decrease of white line intensity

and shift of absorption edge lower energy confirm that rhodium is indeed reduced to metallic state during synthesis. However, upon exposure to air at room temperature, rhodium species were quickly re-oxidized to cationic state and both the absorption edge energy and white line intensity correspond to an intermediate oxidation state between 0 and +3. During the re-oxidation step rhodium species likely coordinated with the zeolite framework and dispersed as isolated cations.

#### Characterization of deactivated catalyst

The 0.5wt% RhZSM-5 catalyst after testing on stream in the semi-batch reactor for 48hr was found to deactivate significantly. Rhodium leaching is found to be negligible from ICP-AES analysis of the product liquid. To understand the reason behind deactivation, the used catalyst was checked for structural changes after prolonged reaction. Temperature programmed oxidation was first used to check carbon deposition on the catalyst surface. Prior to oxidation, the used catalyst was washed thoroughly with DI water to remove oxygenates. The catalyst was further degassed at 350°C to desorb any CO on the rhodium surface. Figure 3.20(a) shows the TPO profile of the used 0.5wt% RhZSM-5. Carbon is indeed deposited onto the catalyst, with an oxidation peak at 265°C. The origin of carbon is likely due to the exothermic Boudouard reaction:



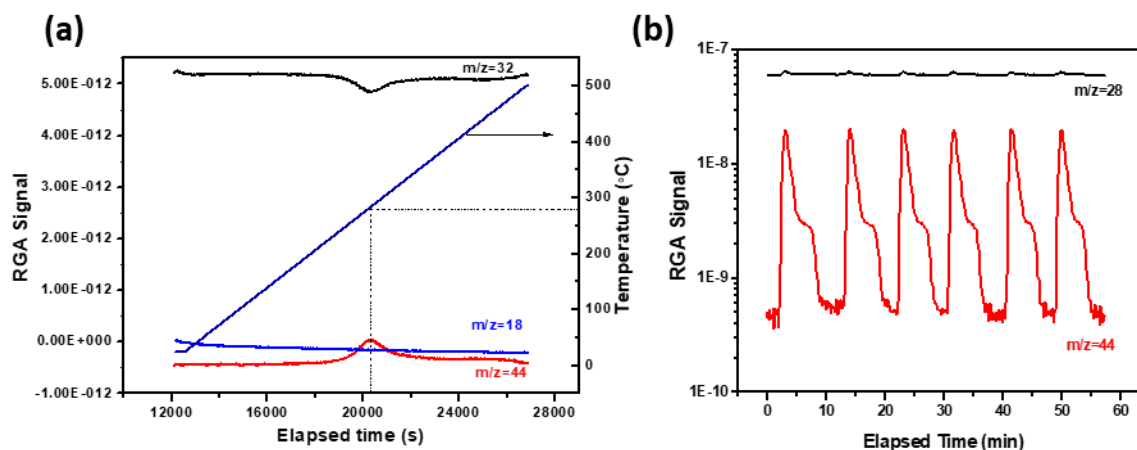


Figure 3.20 (a) TPO profile of used 0.5wt% RhZSM-5 catalyst (b) CO pulsed chemisorption on 0.5wt% RhZSM-5 catalyst at 150°C.

To confirm the deposition of carbon, CO pulsed chemisorption was further performed on 0.5wt% RhZSM-5 at 150°C. Figure 20(b) shows the mass spectrometry signal of CO and CO<sub>2</sub> during the chemisorption experiment. The pulsed CO is converted to CO<sub>2</sub> without forming other product and a TPO after chemisorption experiment confirms deposition of carbon. The type of deposited carbon is graphitic carbon on the metal sites, as indicated by the low carbon burn-off temperature.<sup>17</sup>

Although carbon deposition is confirmed, it does not account for the deactivation of the catalyst. Burning off the carbon at 300°C does not reactivate the catalyst. To understand the true reason behind deactivation, CO-DRIFTS was further used to characterize the used catalyst. Figure 3.21 shows that initially the used catalyst contains strongly bound CO species as Rh(I)(CO)<sub>2</sub>. If 10% CO is adsorbed at RT, the formation of metallic rhodium features is dominant, further increasing adsorption temperature to 150°C only re-disperses rhodium to a limited extent. It is therefore considered that the main reason for catalyst deactivation is formation of stable metallic aggregates that are not active for methane conversion.

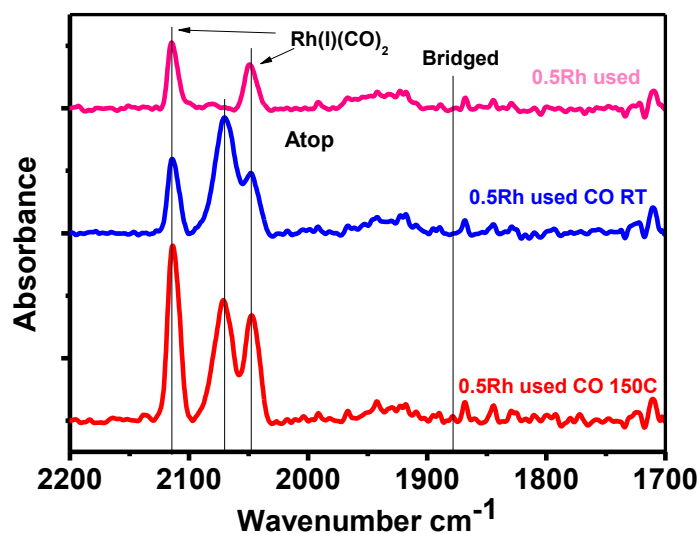


Figure 3.21 CO-DRIFTS spectra of 0.5wt% RhZSM-5 used for semi-batch reaction.

Although these stable metallic species cannot be fully re-dispersed by CO at the reaction temperature, which explains the decrease of activity during semi-batch operation, an ex situ regeneration of the catalyst with CO at even higher temperatures is possible. The ability of CO to re-disperse metallic rhodium into single rhodium cations is clearly affected by temperature, as shown in Figure 3.15. A regeneration step with CO at temperatures above 200°C can break these stable metallic species to single atoms and the catalyst can be reused again in the bubbler reactor.

### 3.4 Conclusions

This chapter reports the discovery of a novel RhZSM-5 catalyst and its high activity towards selective oxidation of methane to methanol and acetic acid. This is the first use of this kind of heterogeneous catalyst to demonstrate its ability to convert methane to oxygenates with O<sub>2</sub> as oxidant and CO as promoter. The effect of rhodium loadings and type of heat treatment on catalyst performance was

correlated with structural information of rhodium through characterization methods including ICP-AES, XRD, XRD, CO-DRIFTS, STEM, XANES and EXAFS.

The most active catalyst is obtained when rhodium species were reduced at high temperature (550°C) with 5% H<sub>2</sub>. Parametric studies on the reaction conditions show that, higher O<sub>2</sub> partial pressure favors the formation of formic acid and methanol, while acetic acid selectivity can be improved by conducting the reaction at low O<sub>2</sub> partial pressure. Extending the reaction time at high pO<sub>2</sub> ultimately leads to strong over-oxidation and low oxygenates selectivity, but at conditions selective to acetic acid, higher conversion of methane can be achieved with longer reaction time. Conversion of methane can reach 4% with selectivity of 59% to acetic acid with 6h batch reaction, and acetic acid formation rate is more than 2200 μmol/gcat/h.

The active rhodium species formed during H<sub>2</sub> reduction was found to be isolated cationic rhodium with oxidation state close to +1 and they are anchored on the internal walls of the zeolite framework. Metallic nanoparticles on the external surface are not likely to be the active phase. On the other hand, these metallic nanoparticles catalyze CO oxidation, which is an undesirable side reaction that consumes the limiting reactant O<sub>2</sub>. How metallic nanoparticles catalyze CO oxidation will be further discussed in Chapter 4.

The stability of RhZSM-5 catalysts was evaluated both in single batch and fed-batch operation. Although EXAFS analysis showed agglomeration of rhodium cations into metallic nanoclusters, the clusters can be re-dispersed to single atom state by CO at the reaction temperature, and the catalyst is stable on-stream in single batch operation. In fed-batch operation, rhodium cations agglomerate into more stable metallic species that are not re-dispersed by CO at the reaction temperature. An ex situ regeneration step with CO at temperatures above 200°C can be proposed to reactivate the catalyst.

### 3.5 References

- (1) Au, C. T.; Wang, H. Y. Mechanistic studies of methane partial oxidation to syngas over SiO<sub>2</sub>-supported rhodium catalysts. *J. Catal.* **1997**, 167, 337-345.
- (2) Ruckenstein, E.; Wang, H. Y. Effect of support on partial oxidation of methane to synthesis gas over supported rhodium catalysts. *J. Catal.* **1999**, 187, 151-159.
- (3) a. Lin, M.; Sen, A. Direct catalytic conversion of methane to acetic acid in an aqueous medium. *Nature* **1994**, 368, 613-615. b. Chepaikin, E. G.; Bezruchenko, A. P.; Leshcheva, A. A.; Boyko, G. N.; Kuzmenkov, I. V.; Grigoryan, E. H.; Shilov, A. E. Functionalisation of methane under dioxygen and carbon monoxide catalyzed by rhodium complexes: oxidation and oxidative carbonylation. *J. Mol. Catal. A: Chem.* **2001**, 169, 89-98. c. Lin, M.; Hogan, T. E.; Sen, A. Catalytic carbon-carbon and carbon-hydrogen bond cleavage in lower alkanes. Low-temperature hydroxylations and hydroxycarbonylations with dioxygen as the oxidant. *J. Am. Chem. Soc.* **1996**, 118, 4574-4580
- (4) Yuan, Q.; Deng, W.; Zhang, Q.; Wang, Y. Osmium-catalyzed selective oxidations of methane and ethane with hydrogen peroxide in aqueous medium. *Adv. Synth. Catal.* **2007**, 349, 1199-1209
- (5) Kwon, Y.; Kim, T. Y. Kwon, G.; Yi, J.; Lee, H. Selective activation of methane on single-atom catalyst of rhodium dispersed on zirconia for direct conversion. *J. Am. Chem. Soc.* **2017**, 139, 17694-17699.
- (6) Schünemann, V.; Adelman, B.; Sachtler, W. M. H. Formation of the rhodium oxides Rh<sub>2</sub>O<sub>3</sub> and RhO<sub>2</sub> in Rh/NaY. *Catal. Lett.* **1994**, 27, 259-265.
- (7) Latimer, A. A.; Kakekhani, A.; Kulkarni, A. R.; Nørskov, J. K. Direct methane to methanol: The selectivity-conversion limit and design strategies. *ACS Catal.* **2018**, 8, 6894-6907.

- (8) Fu, W.; Liu, T.; Fang, Z.; Ma, Y.; Zheng, X.; Wang, W.; Ni, X.; Hu, M.; Tang, T. High activity and stability in the cross-coupling of aryl halides with disulfides over Cu-doped hierarchically porous zeolite ZSM-5. *Chem. Commun.* **2015**, 51, 5890-5893.
- (9) Wang, L.; Zhang, J.; Yi, X.; Zheng, A.; Deng, F.; Chen, C.; Ji, Y.; Liu, F.; Meng, X.; Xiao, F.-S. Mesoporous ZSM-5 zeolite-supported Ru nanoparticles as highly efficient catalysts for upgrading phenolic biomolecules. *ACS Catal.* **2015**, 5, 2727-2734.
- (10) Fleisch, T. H.; Meyers, B. L.; Ray, G. J.; Hall, J. B.; Marshall, C. L. Hydrothermal dealumination of faujasites. *J. Catal.* **1986**, 99, 117-125.
- (11) Ravenelle, R. M.; Schüßler, F.; D'Amico, A.; Danilina, N.; van Bokhoven, J. A.; Lercher, J. A.; Jones, C. W.; Sievers, C. Stability of zeolites in hot liquid water. *J. Phys. Chem. C* **2010**, 114, 19582-19595.
- (12) Shan, J.; Zhu, Y.; Zhang, S.; Zhu, T.; Rouvimov, S.; Tao, F. Catalytic performance and in situ surface chemistry of pure  $\alpha$ -MnO<sub>2</sub> nanorods in selective reduction of NO and N<sub>2</sub>O with CO. *J. Phys. Chem. C* **2013**, 117, 8329-8335.
- (13) Zhu, Y.; Zhang, S.; Shan, J.; Nguyen, L.; Zhan, S.; Gu, X.; Tao, F. In situ surface chemistries and catalytic performances of ceria doped with palladium, platinum, and rhodium in methane partial oxidation for the production of Syngas. *ACS Catal.* **2013**, 3, 2627-2639.
- (14) Matsubu, J. C.; Yang, V. N.; Christopher, P. Isolated metal active site concentration and stability control catalytic CO<sub>2</sub> reduction selectivity. *J. Am. Chem. Soc* **2015**, 137, 3076-3084.
- (15) Ivanova, E.; Hadjiivanov, K. Polycarbonyls of Rh<sup>+</sup> formed after interaction of CO with Rh-MFI: an FTIR spectroscopic study. *Phys. Chem. Chem. Phys.* **2003**, 5, 655-661.

(16) Kroner, A. B.; Newton, M. A.; Tromp, M.; Roscioni, O. M.; Russell, A. E.; Dent, A. J.; Prestipino, C.; Evans, J. Time-resolved, in situ DRIFTS/EDE/MS studies on alumina-supported rhodium catalysts: effects of ceriation and zirconiation on rhodium-CO interactions. *Chemphyschem* **2014**, 15, 3049-3059.

(17) Remiro, A.; Valle, B.; Aramburu, B.; Aguayo, A. T.; Bilbao, J.; Gayubo, A. G. Steam reforming of the bio-oil aqueous fraction in a fluidized bed reactor with in situ CO<sub>2</sub> capture. *Ind. Eng. Chem. Res.* **2013**, 52, 17087-17098.

# Chapter 4 Mechanistic study of the selective oxidation of methane using rhodium-based catalysts

## 4.1 Introduction

In Chapter 3, it is demonstrated that RhZSM-5 prepared by hydrogen reduction is an active catalyst for methane activation in the presence of O<sub>2</sub> and CO and the active site is proposed as atomically dispersed rhodium stabilized by CO. On the reaction side, the unique activity of this catalyst warrants further mechanistic study. The reaction product consists of methanol and formic acid, which is C1 oxygenates, as well as acetic acid which is C2. The pathway to form C1 oxygenates should be very different from C2, as the former only involves scission of C-H bond and formation of C-O bond, while the latter involves also C-C bond formation. In homogeneous catalysts<sup>1</sup>, palladium cations exhibit similar product formation using fuming sulfuric acid as the oxidant, with C1 and C2 products originating from two functionalization routes from the same XPd-CH<sub>3</sub> precursor. In this chapter, experimental results will be presented that depict a similar functionalization pathway on rhodium, starting from a Rh-CH<sub>3</sub> complex. Structural dependence of the two pathways is studied, and the zeolite Brønsted acidity is found necessary for the C2 pathway, while the C1 pathway can proceed on non-acidic supports, including TiO<sub>2</sub> or other open supports.

Furthermore, detailed studies to elucidate the intermediates for both oxygen activation and methane activation that generates the Rh-CH<sub>3</sub> were conducted. Whereas C-H bond activation has been proposed to undergo oxidative addition, hydrogen abstraction or electrophilic substitution mechanisms,<sup>2</sup> the mechanism on rhodium catalysts is more complex. The reaction sequence involves first formation of peroxide intermediate via reaction of CO, O<sub>2</sub> and H<sub>2</sub>O and then oxidation of rhodium(I) to a high valence oxo structure, likely Rh(III)=O. Activation of methane on the oxo structure is different from the rebound

mechanism proposed for cytochrome P450 enzyme in which a methyl radical rebounds to the metal hydroxyl to liberate methanol,<sup>3</sup> as a formal Rh-CH<sub>3</sub> complex is needed for the carbonylation reaction.

The mechanistic understanding helps to construct a general strategy for catalyst design that couples a peroxide synthesis site with a methane activation site. A FeRh bimetallic catalyst was used as a demonstration of this strategy that enabled methane conversion at close to ambient conditions.

## 4.2 Experimental Methods

### 4.2.1 Catalyst synthesis

0.5wt% RhZSM-5 was prepared by incipient wetness impregnation method as detailed in Chapter 3. 0.5wt% RhNaZSM-5 was prepared by back ion exchange method using 0.5wt% RhZSM-5. 1g of RhZSM-5 was ion exchanged with 36mL 2.44M CH<sub>3</sub>COONa solution at 80°C for 12h. The sample was filtered and washed with hot deionized water and dried in vacuum overnight. This process was repeated twice to obtain RhNaZSM-5. Samples prepared from NaZSM-5 (Davison Si/Al=14) directly using the incipient wetness impregnation method detailed in Chapter 2 were also tested and yielded similar activity and product selectivity. RhTiO<sub>2</sub> catalysts were synthesized using a UV-assisted deposition precipitation (DP) method. A 2.5wt% RhTiO<sub>2</sub> catalyst was first synthesized using the DP method and the sample was transferred into ethanol solution and irradiated with UV blacklight lamp centered at 365nm for 3h. The rhodium species not anchored during the irradiation step were leached with 3M HCl aqueous solution at room temperature and the final catalyst contained 0.6wt% RhTiO<sub>2</sub>. FeRhZSM-5 catalysts were prepared by co-impregnation of aqueous solution containing Fe(NO<sub>3</sub>)<sub>3</sub> and Rh(NO<sub>3</sub>)<sub>3</sub> onto dehydrated NH<sub>4</sub>-ZSM-5 (Si/Al=15). The catalysts were reduced with 5% H<sub>2</sub>/He at 550°C for 3h. Loadings of both iron and rhodium species range from 0.1wt% to 0.5wt%. A list of all the catalysts used here including preparation methods and metal dispersion is provided in Table 4.1. The latter was determined from both CO-DRIFTS and EXAFS analysis.

Table 4.1 Sample composition, preparation methods, and metal dispersion

Catalyst	Preparation Method	Metal Dispersion
0.5wt% RhZSM-5	Incipient wetness impregnation; 5% H <sub>2</sub> reduction at 550°C for 3h	~50% isolated Rh cations
0.5wt% RhNaZSM-5	Back ion exchange with sodium acetate using 0.5wt% RhZSM-5 for 3 consecutive times.	~50% isolated Rh cations, no change of Rh dispersion due to ion exchange
2.5wt% RhTiO <sub>2</sub>	DP method, calcined at 350°C in air for 1h followed by reduction at the same temperature for 1h	Rh agglomerates into predominantly metallic nanoparticles (Figure 4.4)
1.0wt% RhTiO <sub>2</sub>	DP method, calcined at 350°C in air for 1h followed by reduction at the same temperature for 1h	Rh agglomerates into predominantly metallic nanoparticles (Figure 4.4)
0.6wt% RhTiO <sub>2</sub>	UV irradiation in ethanol using 2.5wt% RhTiO <sub>2</sub> for 3h, 3M HCl leaching at RT for 3h	Rh single cations only
0.1Fe0.5RhZSM-5	Incipient wetness co-impregnation; 5% H <sub>2</sub> reduction at 550°C for 3h	Fe single cations only, Rh in mixed single cations and metallic nanoparticles

#### 4.2.2 Catalytic testing

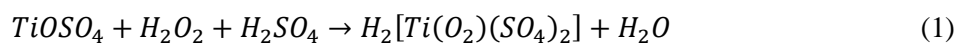
CH<sub>4</sub> oxidation reaction was conducted in a 50mL Parr reactor following the procedure described in Chapter 2. For high temperature (>100°C) reactions, deionized water was used as solvent. For reactions conducted under 100°C, diluted sulfuric acid solutions with concentrations of 0.01mol/L to 0.1mol/L were used. For a typical reaction, 560mg catalyst was suspended in 20mL of 0.1mol/L H<sub>2</sub>SO<sub>4</sub> aqueous solution. After sonicating to achieve a homogeneous suspension, the mixture was placed in the reactor and charged with 5bar O<sub>2</sub>, 5bar CO, 30bar CH<sub>4</sub>. The reaction was conducted at a temperature below 100°C for a certain reaction time and then cooled in ice bath to 10°C.

Isotope labeling experiments were conducted by substituting reactants with corresponding labeled molecules.  $^{13}\text{C}$ ,  $^{18}\text{O}$  and  $^2\text{H}$  labeling experiments were conducted using  $^{13}\text{CO}$ ,  $^{18}\text{O}_2$  and  $\text{D}_2\text{O}$ . All reactions were performed under the following conditions: 100mg catalyst, 2bar  $\text{O}_2$ , 5bar  $\text{CO}$ , 20bar  $\text{CH}_4$ , 20mL DI water,  $150^\circ\text{C}$ , 3h. For  $^{13}\text{C}$ -labeling experiments, the aqueous product was analyzed using  $^{13}\text{C}$ -NMR following the same sample preparation method.  $^{12}\text{C}$  nuclei has a spin state 0 and therefore is NMR silent. NMR spectra were recorded on Bruker Avance III 500MHz NMR spectrometer. A zgpg program was used which applies 90-degree pulse to the sample to maximize sensitivity. 5000 scans were recorded to achieve good signal to noise ratio. In the  $^{18}\text{O}$ -labelling experiment, air inside the reactor was carefully removed by purging with He, and 2 bar  $^{18}\text{O}_2$  was pressurized into the reactor. The gas phase products were analyzed with a Residual Gas Analyzer (RGA) by injecting a pulse of the gas mixture into a stream of helium at 10mL/min. Aqueous phase analysis was conducted by injecting 10 $\mu\text{L}$  of the filtered sample into a vaporization chamber at  $150^\circ\text{C}$  and carried by 30mL/min helium. The vaporized stream was analyzed by the RGA mass spectrometer. The incorporation of isotopically labeled oxygen into liquid oxygenates was monitored by  $^{13}\text{C}$ -NMR. The resonance feature of the carbon atom directly adjacent to labeled oxygen shows an upfield shift compared to unlabeled oxygen<sup>4</sup>. 50,000 scans were recorded to detect the natural abundance of  $^{13}\text{C}$  in the liquid oxygenates. For the deuterium labelling experiment, the aqueous sample containing  $\text{D}_2\text{O}$  was directly analyzed by H-NMR. Due to the constant exchange of protons in the carboxylic group of acetic acid with water, it is difficult to differentiate  $\text{CH}_3\text{COOD}$  with respect to  $\text{CH}_3\text{COOH}$  in the presence of  $\text{D}_2\text{O}$ .

The mechanistic investigation was conducted using  $\text{CH}_3\text{OH}$ ,  $\text{CO}$ , and  $\text{O}_2$  as the reactants. 3mM  $\text{CH}_3\text{OH}$  in 20 mL water, 2 bar  $\text{O}_2$ , 5 bar  $\text{CO}$ , and 20mg 0.5wt% RhZSM-5 were heated to  $150^\circ\text{C}$  for 1h. The liquid before and after reaction was analyzed by H-NMR to determine the conversion and product of methanol.

Initial rates were measured in the temperature region of 130°C to 170°C with 2bar O<sub>2</sub>, 5bar CO, 20bar CH<sub>4</sub> and 30min reaction. The catalyst amount was varied to maintain the conversion of limiting reactant (O<sub>2</sub>) below 15% to ensure the reaction was in the kinetically limited regime.

H<sub>2</sub>O<sub>2</sub> synthesis was conducted in a 50mL Parr reactor following the standard testing procedure. The gas mixture contained CO, O<sub>2</sub> and He as balancing gas. Solid catalysts were suspended in an aqueous solution containing 0.1mol/L H<sub>2</sub>SO<sub>4</sub> and 0.1mol/L TiOSO<sub>4</sub>. The acidic solvent is required to stabilize the H<sub>2</sub>O<sub>2</sub> generated<sup>5</sup> while TiOSO<sub>4</sub> is used as reagent to determine H<sub>2</sub>O<sub>2</sub> formation using colorimetric method<sup>6</sup>. Reaction of H<sub>2</sub>O<sub>2</sub> and TiOSO<sub>4</sub> forms peroxy titanate following equation (1)



The reaction is selective to H<sub>2</sub>O<sub>2</sub> and the formed peroxy titanate shows strong yellow color and absorption in the 380-430 nm region<sup>6</sup>. The liquid sample was periodically taken from the reactor and filtered. Analysis of the sample was conducted on an Agilent Cary 5000 UV-Vis-NIR spectrometer. Spectra were collected in double-beam mode from 200nm to 800nm with a Baseline collected using the initial aqueous solution containing 0.1mol/L H<sub>2</sub>SO<sub>4</sub> and 0.1mol/L TiOSO<sub>4</sub>.

#### 4.2.3 Catalyst characterization

The catalysts were characterized by CO-DRIFTS, EPR and XPS as detailed in Chapter 2. For FeRh bimetallic catalyst, XAS measurements were conducted at Argonne National Lab, BM 10B. Fe K-edge and Rh K-edge spectra were recorded *ex situ* with catalysts in fresh and used state. A gas mixture containing CO/O<sub>2</sub>/H<sub>2</sub>O (3% v/v each) balanced with He was used to simulate the hydrogen peroxide synthesis environment. Fresh catalysts were first treated in the gas mixture at 50°C for 30min and cooled down to RT before taking the measurement.

## 4.3 Results and Discussion

### 4.3.1 Identification of a two-pathway functionalization mechanism

The reaction conducted with methanol as the reactant using 0.5wt% RhZSM-5 showed no formation of acetic acid and only over-oxidation products (formic acid and CO<sub>2</sub>) were found, Figure 4.1. Although rhodium is the catalyst for methanol carbonylation with CO to form acetic acid in the Monsanto Process<sup>7</sup>, here methanol is not a precursor for acetic acid formation but an intermediate for C1 oxygenates like formic acid and CO<sub>2</sub>. Therefore, the reaction clearly demonstrates a two-pathway mechanism, with one being the formation of methanol which was then sequentially oxidized to formic acid and CO<sub>2</sub> (C1 pathway), and the other being the formation of acetic acid (C2 pathway). No other C2 molecules, e.g. ethane, ethylene, ethanol or acetaldehyde, were identified in the gas or aqueous phase product.

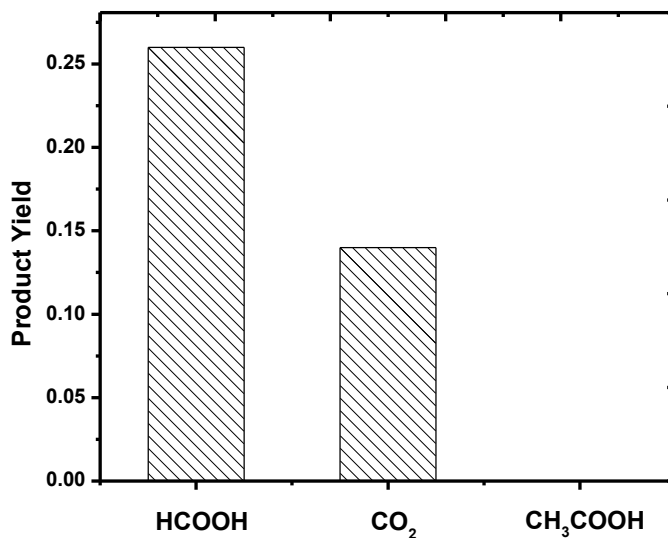


Figure 4.1 Product formation using methanol as reactant on 0.5wt% RhZSM-5. Conditions: 20mg catalyst, 3mM CH<sub>3</sub>OH solution, 2bar O<sub>2</sub>, 5bar CO, 20bar CH<sub>4</sub>, 150°C, 1h

The two-pathway mechanism raises a second question: what is the origin of carbon source in the product, especially for the case of acetic acid? One first attempt is to rule out CO as the sole carbon source of C1 products, as the reactions of CO leading to methanol or formic acid with just water has not yet been reported.



Overall



Reaction (5) has a Gibbs free energy of 12.9kJ/mol<sup>8</sup> which is highly unfavorable thermodynamically. Although reaction (4) has a standard Gibbs free energy of -69.6kJ/mol<sup>8</sup>, a control experiment without methane in the gas mixture was conducted and no carbon-based product could be found in the aqueous phase solution. One can thus conclude that methane is needed to generate liquid oxygenates.

To further verify the source of carbon in the different oxygenate species, <sup>13</sup>C-labelling experiment was conducted using <sup>13</sup>CO. H-NMR was used first to confirm the formation of aqueous oxygenates and the solution was further analyzed by <sup>13</sup>C-NMR. For 0.5wt.% Rh-ZSM-5 the solution contains a mixture of formic acid, methanol and acetic acid, same as the product obtained using unlabeled CO. Figure 4.2 shows the <sup>13</sup>C-NMR spectrum of the filtered liquid. Only CH<sub>3</sub><sup>13</sup>COOH (δ=177.2)<sup>9</sup> along with dissolved <sup>13</sup>CO<sub>2</sub> (δ=124.6)<sup>10</sup> were found in the liquid. No labeled <sup>13</sup>CH<sub>3</sub>OH (δ=49.5), <sup>13</sup>CH<sub>3</sub>COOH (δ=21.0) or H<sup>13</sup>COOH (δ=166.3) is formed.<sup>9-11</sup> The result further confirms that all carbons in C1 species are derived from methane instead of CO. Acetic acid, on the other hand, contains one carbon (methyl group) from methane and the other (carbonyl group) from CO.

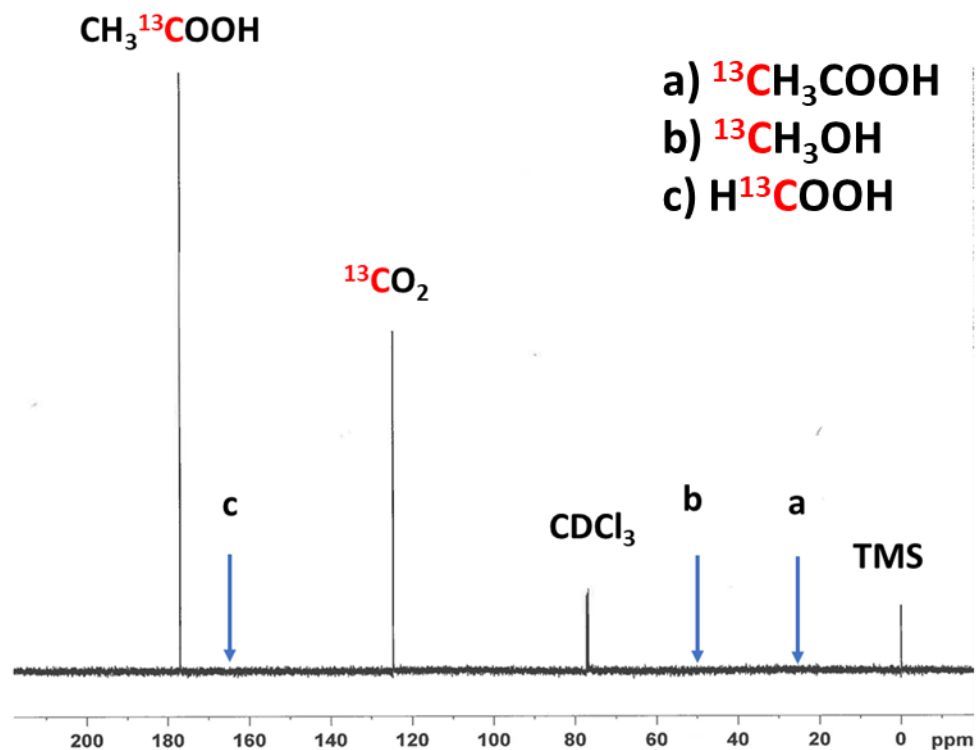
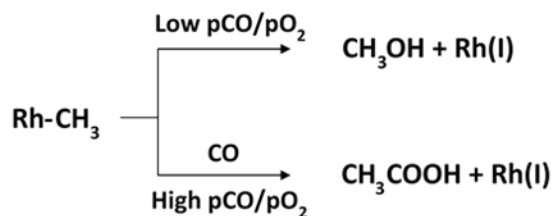


Figure 4.2  $^{13}\text{C}$ -NMR spectrum of the aqueous solution after reaction with  $^{13}\text{CO}$ . Conditions: 100mg 0.5wt% RhZSM-5, 2bar  $\text{O}_2$ , 5bar  $^{13}\text{CO}$ , 20bar  $\text{CH}_4$ , 150°C, 3h.

The  $^{13}\text{C}$ -labelling experiment suggests that formation of acetic acid involves the oxidative carbonylation of methane. While methanol carbonylation reaction was ruled out, its well-established homogeneous mechanism can still shed some light on the reaction steps here. The catalytic cycle of Monsanto process involves the oxidative addition of methyl iodide to the square planar complex  $[\text{RhI}_2(\text{CO})_2]^-$  followed by migratory insertion of CO into the Rh-CH<sub>3</sub> bond, forming Rh-COCH<sub>3</sub>. The Rh-acetyl complex further reacts with I<sup>-</sup> and water through reductive elimination and hydrolysis to generate acetic acid.<sup>12, 13</sup> At the same time, solid acid catalyzed carbonylation of methanol to acetic acid using HZSM-5 or H-MOR was also reported.<sup>14-16</sup> Although the same form of zeolite is used here as support, its carbonylation activity can be ruled out as the reaction using aqueous methanol as reactant does not show any acetic acid formation using HZSM-5 either.

The Rh-CH<sub>3</sub> complex is a necessary precursor for the next carbonylation step to generate acetic acid in the Monsanto process. Here the same Rh-CH<sub>3</sub> can be proposed as an intermediate, with the methyl species derived from methane activation. This intermediate is also proposed as the precursor for methanol formation, as methanol formation can either go through oxygen insertion followed by hydrolysis or direct hydroxylation from methyl species. Based on the previous discussion, a two-pathway mechanism, involving Rh-CH<sub>3</sub> as the precursor to either methanol or acetic acid can be proposed in Scheme 4.1



Scheme 4.1 Proposed two-pathway mechanism for functionalization of Rh-CH<sub>3</sub> on RhZSM-5

Initial reaction rates were measured using 0.5wt% RhZSM-5 at temperatures from 130-170°C. C1 and C2 product formation rates plotted separately in an Arrhenius-type plot shows that the two pathways have similar activation energy, close to 100 kJ/mol. The similar activation energy suggests a common rate limiting step for both C1 and C2 pathways, which can only be the generation of Rh-CH<sub>3</sub> complex through methane activation. Subsequent functionalization of this complex to either methanol or acetic acid is likely much faster compared to the initial methane activation. This is in line with reports that oxidative addition of methyl iodide is the rate limiting step in the Monsanto process compared to migratory insertion.<sup>17, 18</sup> Considering the much stronger C-H bond in methane compared to C-I bond in methyl iodide, the C-H activation step should be even slower compared to C-I bond breaking.

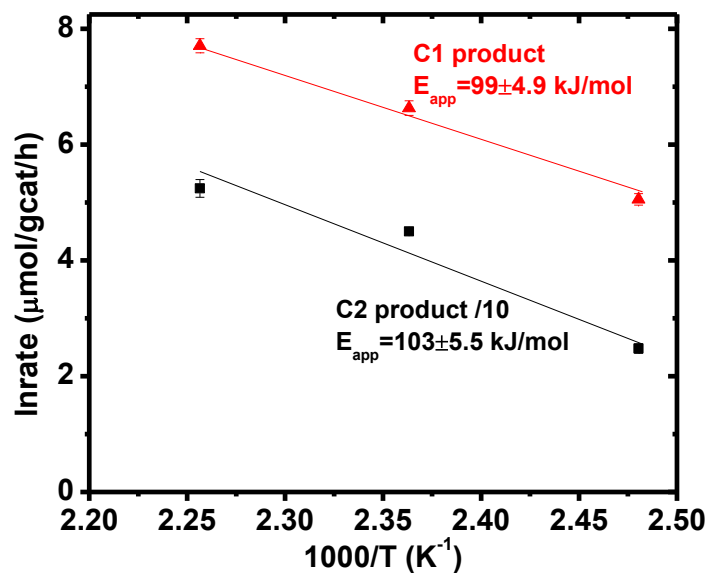


Figure 4.3 Arrhenius-type plot of the initial rate of reaction on 0.5wt% RhZSM-5. Conditions: 2bar O<sub>2</sub>, 5bar CO, 20bar CH<sub>4</sub>, 130-170°C, 30min, 9-83mg catalyst.

For the case of RhZSM-5, both C1 and C2 pathways take place in parallel at the isolated cationic rhodium center. However, reaction of aqueous phase rhodium cations clearly shows the suppression of C2 pathway when isolated rhodium cations are not coordinated with HZSM-5 (Figure 3.9). It is hypothesized that the coordination environment of rhodium on the solid support will also have a strong effect on the two reaction pathways. Therefore, rhodium single cations anchored on other supports were synthesized. The desired support should have ample sites for anchoring single atom cations. TiO<sub>2</sub> has rich surface hydroxyl species and its intermediate band gap provides the unique property to use UV irradiation to coordinate with metal single atoms through establishing M-O-Ti<sup>3+</sup> linkages.<sup>19-21</sup> Therefore, a UV-assisted deposition method that was previously developed for AuTiO<sub>2</sub><sup>19</sup> was adapted for rhodium. The specific steps involve first depositing Rh<sub>2</sub>O<sub>3</sub> through a Deposition-Precipitation (DP) method (adapted from literature<sup>22</sup>) followed by UV irradiation at 365nm in ethanol. During the irradiation step, UV light with wavelength lower than the titania bandgap excites the electrons from valence band to conduction band,

forming negatively charged electrons and positively charged holes. The electron-hole pair can either recombine or react with hole scavengers and surface metal species.<sup>23</sup> In this case the hole scavenger is ethanol which reacts with holes through reaction (6) and the electron reacts with surface OH group to form H<sub>2</sub>.



The Rh<sub>2</sub>O<sub>3</sub> deposited onto titania support is bound loosely and can readily agglomerate to form rhodium nanoparticles. Figure 4.4 shows the CO-DRIFT spectra of 1wt% and 2.5wt% RhTiO<sub>2</sub> prepared by DP method without irradiation. The sample was calcined in air at 350°C and reduced by 20% H<sub>2</sub> at 350°C for 1h and the formation of Rh nanoparticles from the CO atop and bridged binding features is clearly visible.<sup>24</sup>

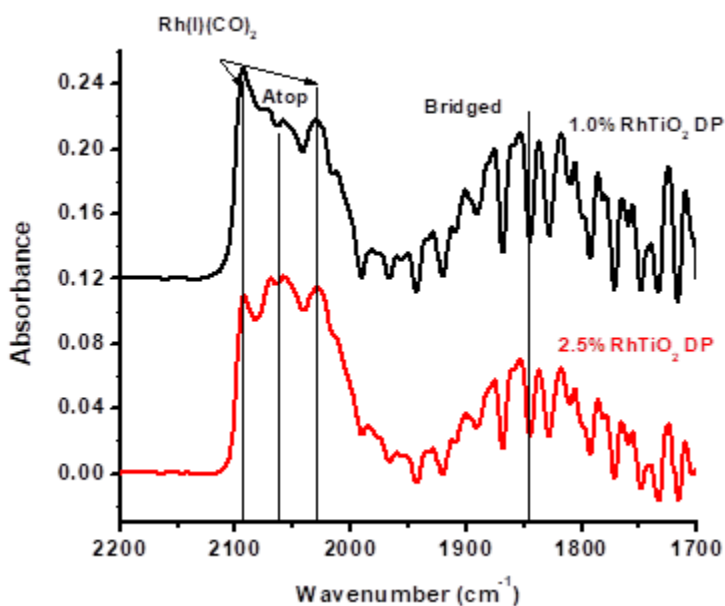


Figure 4.4 CO-DRIFT spectra of RhTiO<sub>2</sub> catalysts of different loadings prepared by DP method

A previous study on AuTiO<sub>2</sub> has shown that the optimum irradiation time is 5~20min using the same setup, while higher Au loading needs longer irradiation time<sup>23</sup>. However, for RhTiO<sub>2</sub> the irradiation time needs to be extended. It has been reported that the photo deposition rate of different metals onto TiO<sub>2</sub> follows the order of Ag > Pd > Au > Pt >> Rh >> Ir >> Cu = Ni = 0.<sup>25</sup> A series of samples with different irradiation time (30-180min) was prepared. To determine how much Rh is anchored stably onto TiO<sub>2</sub> after irradiation, a leaching step was used to remove the loosely bound Rh<sub>2</sub>O<sub>3</sub>. 100mg RhTiO<sub>2</sub> after UV irradiation was leached using 3M HCl at room temperature for 3h and ICP-AES was used to quantify the fraction of leachable rhodium (Figure 4.5). For the parent DP sample, 100% leaching of the loading was achieved which is as expected since no metal support interaction has been established and Rh is loosely bound on the surface in the form of Rh<sub>2</sub>O<sub>3</sub>. As the irradiation time increases, the amount of rhodium that can be leached decreases which shows that more rhodium species are now stabilized by titania. The sample irradiated for 180min shows around 78% leaching of the loading, which corresponds to residual loading of 0.6wt%.

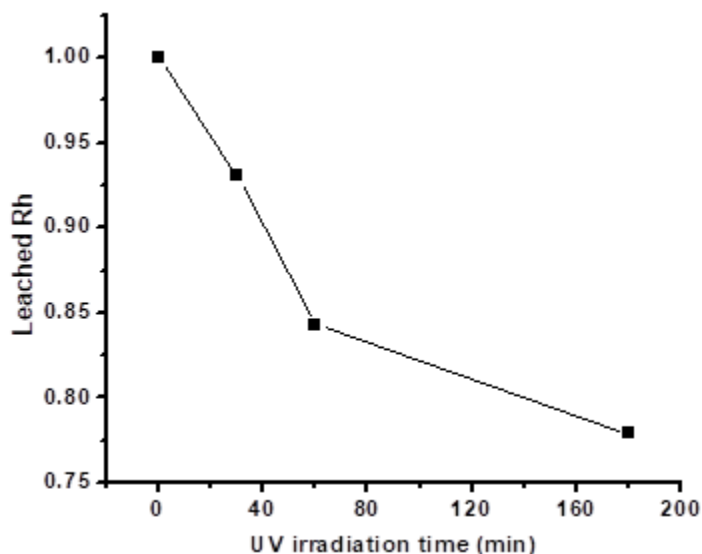


Figure 4.5 Amount of leachable rhodium after UV irradiation of RhTiO<sub>2</sub> in ethanol solution for different lengths of time.

The nature of interaction between the support and rhodium was investigated by EPR. Species with unpaired electrons from the sample will show a spin state split due to Figure 4.6(a) shows the EPR spectra of the parent  $\text{TiO}_2$  (calcined at  $350^\circ\text{C}$ ), 2.5wt%  $\text{RhTiO}_2$  prepared by DP method followed by UV irradiation for 180min and 0.6wt%  $\text{RhTiO}_2$  after HCl leaching. All three samples show resonance features at  $g=1.988$ , corresponding to bulk  $\text{Ti}^{3+}$  defects in anatase titania. UV irradiation of the sample in ethanol creates an additional feature at  $g=1.935$  which can be assigned to  $\text{Ti}^{3+}$  species associated with oxygen defects on the anatase surface<sup>26</sup>, as can be seen on both 2.5wt%  $\text{RhTiO}_2$  after UV irradiation and 0.6wt%  $\text{RhTiO}_2$  after HCl leaching. This feature is not visible on the parent  $\text{TiO}_2$  without irradiation. Therefore, UV irradiation has indeed created surface  $\text{Ti}^{3+}$  defect sites that can be used to anchor rhodium cations.

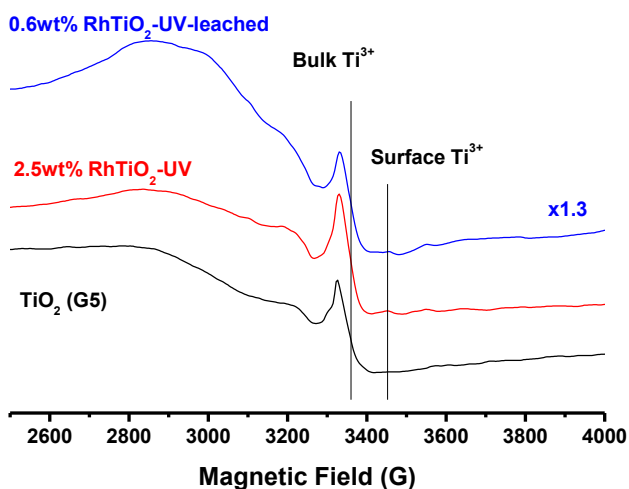


Figure 4.6 X-band EPR spectra of different  $\text{TiO}_2$  samples recorded at 120K.

The formation of surface  $\text{Ti}^{3+}$  species can be corroborated by XPS. Indeed, the Ti 2p scan on the 0.6wt%  $\text{RhTiO}_2$  catalyst clearly shows the formation of  $\text{Ti}^{3+}$  species as a shoulder at 456.6 eV. The same photoelectron peak is not visible on the parent  $\text{TiO}_2$  G5. The  $\text{Ti}^{3+}$  species is still observed after reaction at  $150^\circ\text{C}$  for 3h in the aqueous phase. The atomic ratio of  $\text{Ti}^{4+}$  to  $\text{Ti}^{3+}$  is 3.5 on the fresh catalyst and 4.8 on the used one. It has been reported that surface oxygen vacancies of  $\text{TiO}_2$  can be healed by reaction with

O<sub>2</sub>.<sup>27</sup> Here the Ti<sup>3+</sup> species are stabilized due to the interaction with rhodium and healing of the oxygen defects decreases the available anchoring site of rhodium. For Rh 3d, surface scan shows clear rhodium photoemission peaks, contrary to RhZSM-5 catalysts. The rhodium species is predominantly on the titania surface and no encapsulation of rhodium species is found.

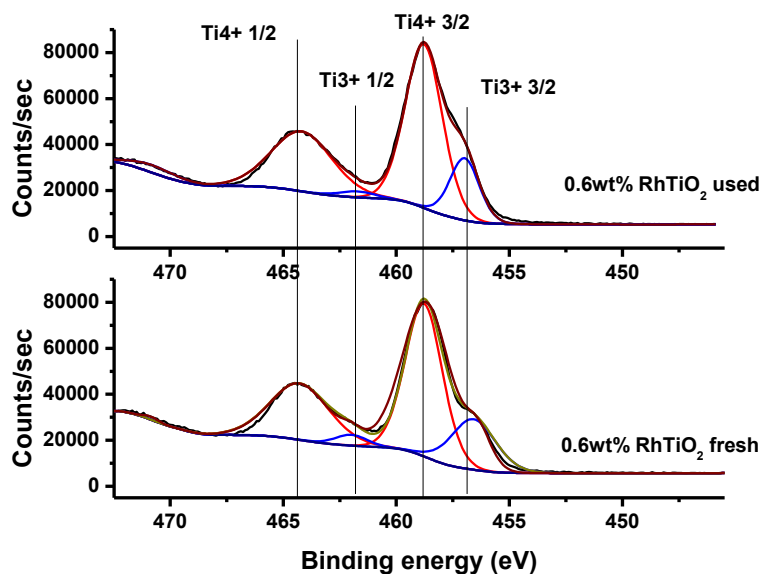


Figure 4.7 Ti 2p XP spectra of the fresh and used 0.6wt% RhTiO<sub>2</sub>.

Rh K-edge XANES and EXAFS was further used to probe the oxidation state and coordination environment of rhodium on 0.6wt% RhTiO<sub>2</sub>. Figure 4.8(a) shows the XANES spectra of 0.6wt% RhTiO<sub>2</sub> with metallic and cationic rhodium standards. The rhodium species in this case is highly cationic, and linear combination fitting shows that different from RhZSM-5 which is predominantly Rh<sup>+</sup> and metallic Rh<sup>0</sup>, 0.6wt% RhTiO<sub>2</sub> shows 88% Rh<sup>3+</sup> and 12% Rh<sup>2+</sup>. No Rh<sup>+</sup> or Rh<sup>0</sup> contribution can be included in the linear combination fitting. EXAFS fitting confirms that rhodium is evidently in single atom dispersion, with only Rh-O interaction and no Rh-Rh interaction. Corroborating with higher oxidation state, the fitted Rh-O coordination number is 6.6, much higher compared to that of 0.5wt% RhZSM-5\_washed which is only 4.

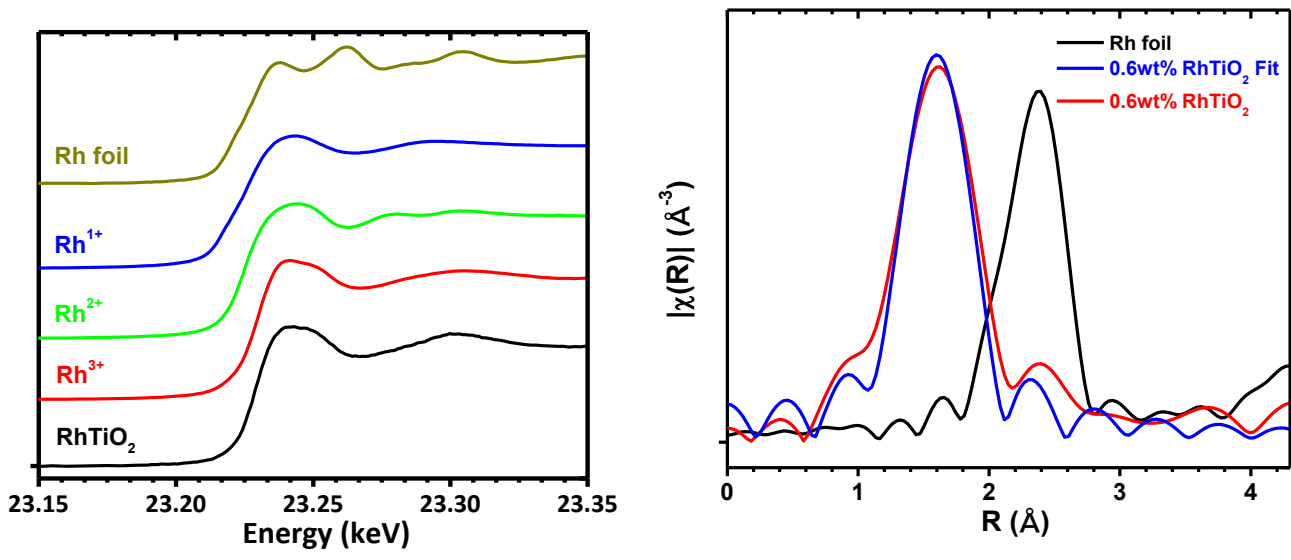


Figure 4.8 XANES and EXAFS spectra of 0.6wt% RhTiO<sub>2</sub> prepared by UV-assisted deposition. EXAFS fitting parameters are summarized here: Rh-O: CN 6.6±1.4, R(Å) 2.10±0.02, σ<sup>2</sup> (Å<sup>2</sup>) 0.003±0.0028; Rh-Rh: 0

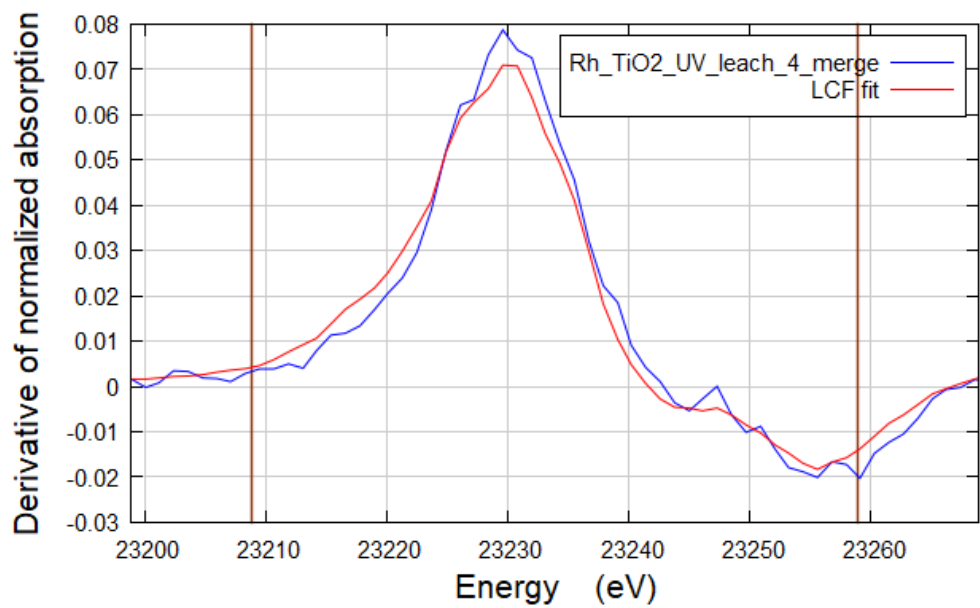


Figure 4.9 Linear Combination Fitting (LCF) of XANES spectrum for 0.6wt% RhTiO<sub>2</sub> prepared by UV-assisted deposition.

From the above characterization, it can be confirmed that 0.6wt% RhTiO<sub>2</sub> prepared by UV-assisted deposition contains solely isolated rhodium cations anchored through Rh-O-Ti<sup>3+</sup> linkages. Considering the high oxidation state of rhodium, additional coordination of OH<sup>-</sup> is also possible. To explore the catalytic activity of this kind of rhodium single site, the 0.6wt% RhTiO<sub>2</sub> was subjected to the same reaction conditions used by RhZSM-5. Figure 4.10 shows the catalytic activity of different catalysts with isolated rhodium species. The product distribution on RhZSM-5 and RhTiO<sub>2</sub> is very different, with RhZSM-5 forming selectively acetic acid and RhTiO<sub>2</sub> forming selectively methanol. The sharp contrast of selectivity in terms of reaction pathways raises another question: is the pathway dependent on the kind of metal oxo species (Al-O-Rh versus Ti-O-Rh) used to stabilize rhodium? To prove this, another catalyst prepared by back ion exchange of the 0.5wt% RhZSM-5 with sodium acetate was included in the test. The back ion exchange process converts excess Brønsted acid sites to non-acidic Si-NaO-Al structure while for rhodium, the coordination with aluminum oxygen is unchanged. 0.5wt% RhNaZSM-5 also shows almost complete suppression of the C2 pathway, which demonstrates that formation of acetic acid not only requires the coordination of rhodium to zeolite framework, but also the presence of Brønsted acid sites. The C1 pathway, on the other hand, does not require Brønsted acidity and can proceed on a non-acidic support like NaZSM-5 or TiO<sub>2</sub>.

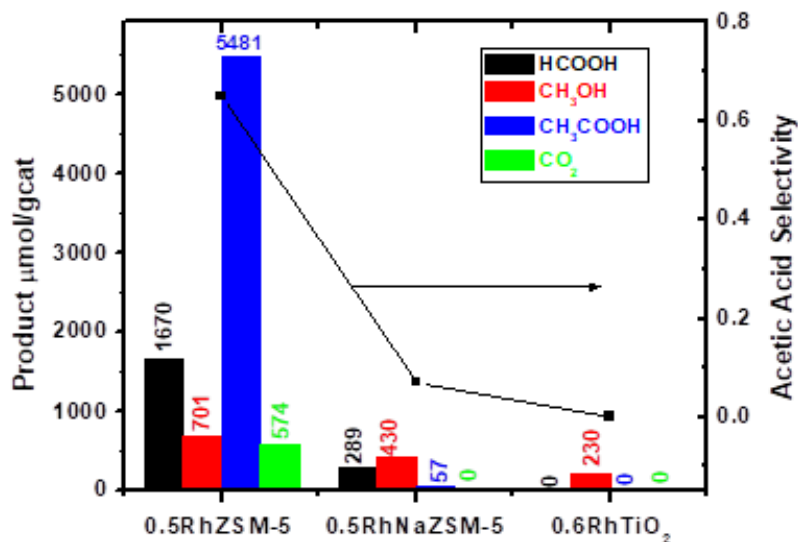


Figure 4.10 Catalytic activity of different rhodium catalysts with single atom dispersion. Conditions: 20mg catalyst, 20mL DI water, 2bar O<sub>2</sub>, 5bar CO, 20bar CH<sub>4</sub>, 150°C, 3h.

Although the as-synthesized RhTiO<sub>2</sub> has a higher oxidation state, the reduction to Rh(I) upon exposure to CO can readily occur at room temperature. The reduction does not change the isolated nature of rhodium on the catalyst, as evidenced by CO-DRIFTS characterization of the catalyst. The same kind of Rh(I) dicarbonyl features can be found on RhZSM-5, RhNaZSM-5 and RhTiO<sub>2</sub>. A shift of the dicarbonyl feature to lower wavenumber has been observed on RhTiO<sub>2</sub>.

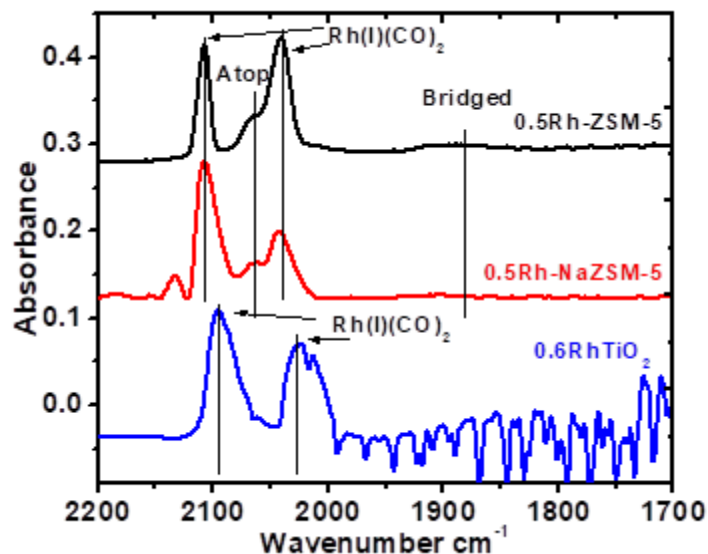


Figure 4.11 CO-DRIFT spectra of rhodium species anchored on different supports.

In summary, the results demonstrate that the oxidative conversion of methane to methanol and acetic acid follows two parallel pathways for functionalization while the initial activation of methane leads to the formation of a Rh-CH<sub>3</sub> complex as the common source of two pathways.

#### 4.3.2 Exploration of methane activation mechanism

In the previous section, the mechanism and structural dependence of Rh-CH<sub>3</sub> functionalization leading to C1 and C2 oxygenates was elucidated. The next step is to understand the mechanism leading to the generation of Rh-CH<sub>3</sub> complex. Such a step requires activation of methane on the rhodium site, for which the mechanism is still not clearly understood. To shed more light on the reaction mechanism, <sup>18</sup>O-labelling experiments were conducted to understand the origin of the oxygen species. After reaction using <sup>18</sup>O<sub>2</sub>, product analysis was first performed for the gas phase. A pulse of the gas phase product was injected into mass spectrometer and Figure 4.11 shows the response of different channels.

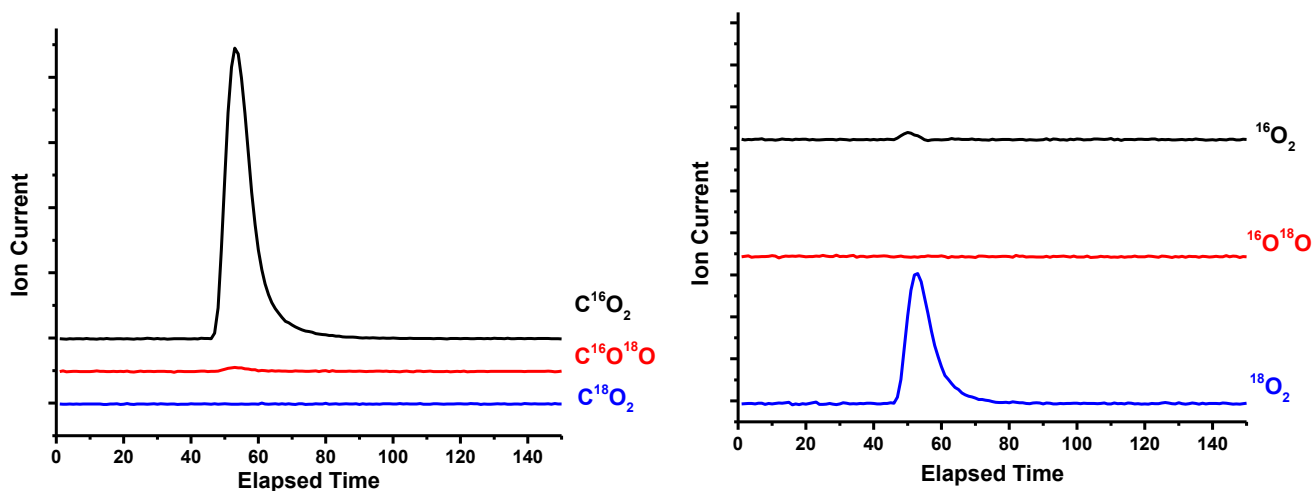


Figure 4.12 Mass spectrometry analysis of gas phase products after reaction with  $^{18}\text{O}_2$ . Conditions: 100mg 0.5wt% RhZSM-5, 2bar  $^{18}\text{O}_2$ , 5bar CO, 20bar  $\text{CH}_4$ , 150°C, 3h. Channels:  $\text{C}^{16}\text{O}_2$  ( $m/z=44$ ),  $\text{C}^{16}\text{O}^{18}\text{O}$  ( $m/z=46$ ),  $\text{C}^{18}\text{O}_2$  ( $m/z=48$ ),  $^{16}\text{O}_2$  ( $m/z=32$ ),  $^{16}\text{O}^{18}\text{O}$  ( $m/z=34$ ) and  $^{18}\text{O}_2$  ( $m/z=36$ )

Gas phase analysis shows that only a trace amount of mixed  $\text{C}^{16}\text{O}^{18}\text{O}$  ( $m/z=46$ ) was formed and  $\text{CO}_2$  is mostly unlabeled  $\text{C}^{16}\text{O}_2$  ( $m/z=44$ ). The source of the second oxygen therefore can only be from  $\text{H}_2\text{O}$ , which is used as solvent in the reaction mixture. Analysis of  $\text{O}_2$  species shows no formation of mixed labelled  $^{16}\text{O}^{18}\text{O}$  and only  $^{18}\text{O}_2$  is present in the gas phase. Since GC-TCD analysis clearly shows the consumption of  $\text{O}_2$ , the consumed  $^{18}\text{O}$  can therefore only be converted into species in the aqueous phase.

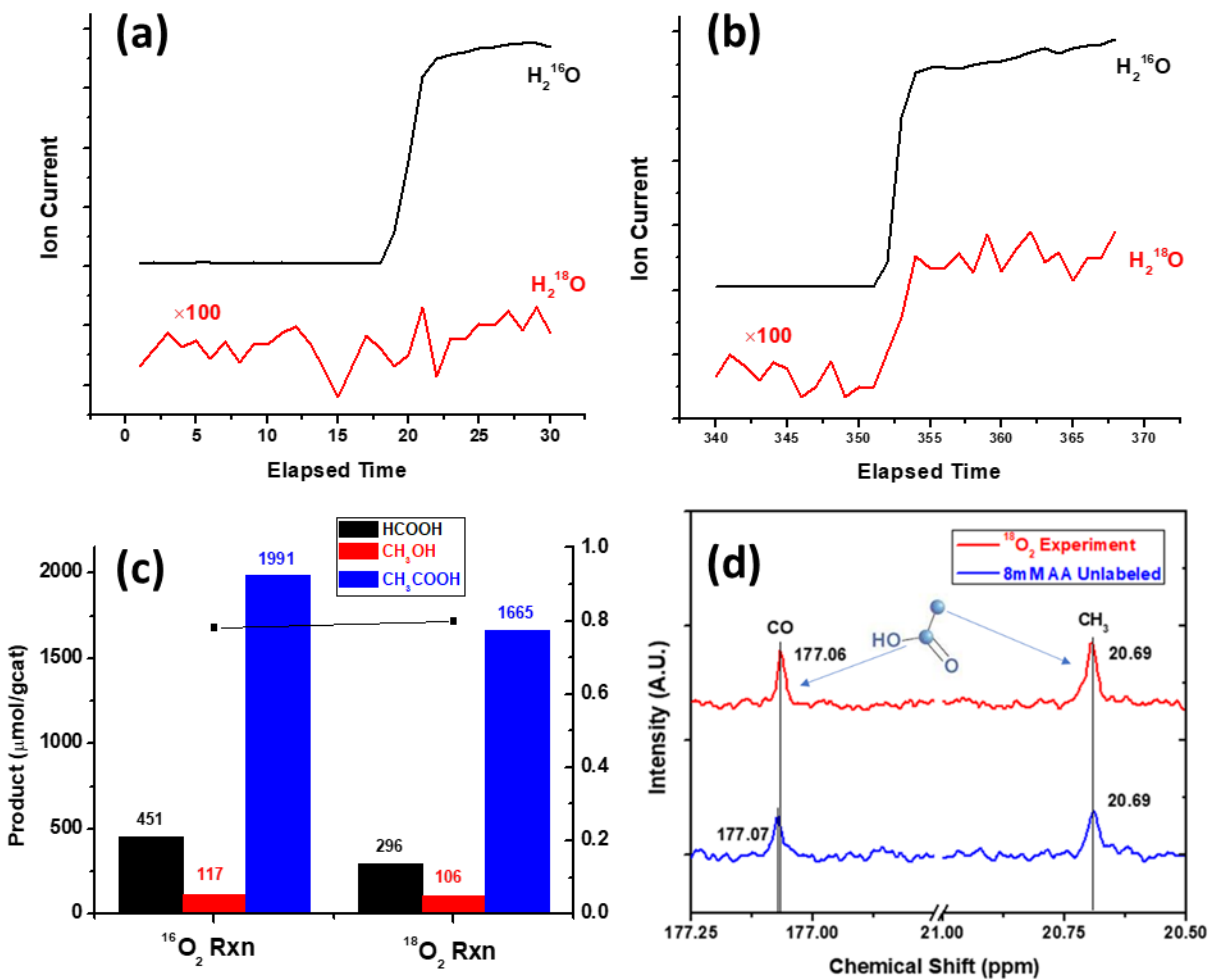


Figure 4.13 Mass spectrometry, H-NMR and  $^{13}\text{C}$ -NMR analysis of the aqueous phase product after reaction with  $^{18}\text{O}_2$ . (a)  $\text{H}_2\text{O}$  analysis in control experiments without  $^{18}\text{O}_2$ ; (b)  $\text{H}_2\text{O}$  analysis of aqueous phase in labeling experiment; (c) H-NMR analysis of aqueous phase from both labeling and control experiment; (d)  $^{13}\text{C}$ -NMR analysis of aqueous phase product of  $^{18}\text{O}_2$  experiment and control experiment. Conditions: 100mg 0.5wt% RhZSM-5, 2bar  $^{18}\text{O}_2$ , 5bar CO, 20bar  $\text{CH}_4$ , 150°C, 3h. Channels:  $\text{H}_2^{16}\text{O}$  ( $m/z=18$ ),  $\text{H}_2^{18}\text{O}$  ( $m/z=20$ ).

Figure 4.13(d) clearly shows that the carbonyl carbon of acetic acid shifted by 0.01ppm in the  $^{18}\text{O}_2$  experiment while methyl carbon did not change. Perturbation of chemical environment due to  $^{18}\text{O}$

substitution caused an upfield shift in  $^{13}\text{C}$ -NMR of the carbon atom directly attached to labeled oxygen<sup>4</sup>. The shift of carbonyl group carbon by 0.01ppm confirms that  $^{18}\text{O}$  was incorporated into the OH group of acetic acid, while the methyl group carbon chemical shift is unchanged. At the same time,  $^{18}\text{O}$  was present also in water in significant amounts, Figure 4.13(b). The scrambling of oxygen between gas phase  $\text{O}_2$  and liquid phase  $\text{H}_2\text{O}$  strongly suggest that water participates in the activation of  $\text{O}_2$  which has been reported in articles studying CO oxidation in the presence of water.<sup>28, 29</sup> Water assisted oxygen activation was reported to involve hydroperoxo species or  $\text{H}_2\text{O}_2$  production, reaction (8-9).<sup>30, 31</sup> However, redox titration using  $\text{Ce}(\text{SO}_4)_2$  did not detect residual  $\text{H}_2\text{O}_2$ . It is noted that at temperatures above  $100^\circ\text{C}$ , decomposition of  $\text{H}_2\text{O}_2$  is dominant and leads to  $\text{O}_2$  and  $\text{H}_2\text{O}$ , reaction (10).



The activation of  $\text{O}_2$  with water is not only needed for CO oxidation but also the formation of liquid oxygenates. In the liquid phase, water was substituted by another polar solvent and the reaction was conducted under the same conditions as when using water. Here ethylene glycol is chosen which is a protic solvent and is just slightly less polar than water (relative polarity 0.79 referenced to water).

Switching to ethylene glycol completely quenched the oxidation of methane (Figure 4.13) and no oxygenates derived from methane were formed. At the same time, the background CO oxidation was also retarded. Total  $\text{CO}_2$  formation measured in the gas phase product was reduced from  $1528\mu\text{mol}$  in water to  $69\mu\text{mol}$  in ethylene glycol. This observation is consistent with the results from labeling experiments that water is also involved in the oxidation of CO. It is important to note that the solubility of methane in these two solvents is of the same order ( $6.17 \times 10^{-3}$  M/atm in ethylene glycol vs.  $1.4 \times 10^{-3}$  M/atm in water).

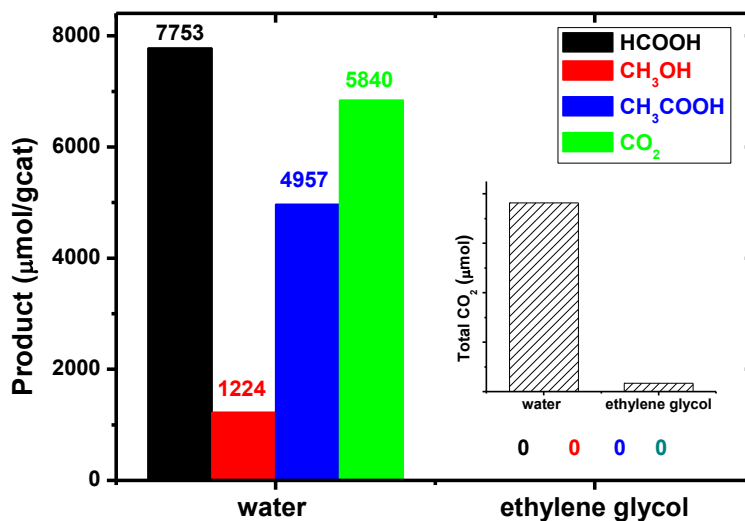


Figure 4.14 Effect of solvent on the catalytic activity of 0.5wt% RhZSM-5. Conditions: 20mg catalyst, 20mL DI water, 4bar O<sub>2</sub>, 5bar CO, 20bar CH<sub>4</sub>, 150°C, 1h.

Furthermore, a strong kinetic isotope effect is observed when H<sub>2</sub>O is substituted with D<sub>2</sub>O. The total amount of oxygenates formed decreased by 56% due to switching from H<sub>2</sub>O to D<sub>2</sub>O, which corresponds to a KIE of 2.3. Water not only participates in the formation of Rh-CH<sub>3</sub>, its H-O bond cleavage is also part of a kinetically relevant step. These results all point to a methane activation mechanism that involves first activation of O<sub>2</sub> by water to form a peroxide type species and then the peroxide species oxidize methane into the Rh-CH<sub>3</sub> complex. Furthermore, it should be noted that reaction (8) is not charge balanced. The right-hand side of the reaction contains two surface species both carrying one negative charge (a hydroperoxide OOH<sup>-</sup> and a hydroxyl OH<sup>-</sup>). Therefore, two electrons need to be supplied on the left-hand side to balance the charge.



The supply of electrons requires the reaction of a two-electron reductant. In this case we believe CO acts as the electron supplier and itself is oxidized into CO<sub>2</sub>.

The detection of residual  $\text{H}_2\text{O}_2$  in the product liquid is difficult due to the fast decomposition into  $\text{H}_2\text{O}$  and  $\text{O}_2$  at high temperature. Therefore, a  $\text{H}_2\text{O}_2$  synthesis experiment using RhZSM-5 is devised. To stabilize the formed  $\text{H}_2\text{O}_2$ , the reaction needs to be conducted at much lower temperature ( $<100^\circ\text{C}$ ), and an acidic media containing  $0.1\text{mol/L}$   $\text{H}_2\text{SO}_4$  was used. The detection of  $\text{H}_2\text{O}_2$  was realized using colorimetric method with  $\text{TiOSO}_4$ . Reaction of  $\text{H}_2\text{O}_2$  with  $\text{TiOSO}_4$  results in intense yellow color and an absorption band at  $380\text{-}430\text{nm}$ .<sup>6</sup> Figure 4.14 shows the UV-Vis spectra of the product liquid after conducting the  $\text{H}_2\text{O}_2$  synthesis reaction at  $50^\circ\text{C}$  for different reaction time. The spectra show the gradual development of an absorption band centered at  $410\text{nm}$ , indicating accumulation of  $\text{H}_2\text{O}_2$ . The final liquid also shows yellow color which is consistent with the formation of peroxy titanate. The successful capture of this reactive oxygen intermediate at lower temperature confirms that  $\text{H}_2\text{O}_2$  is the species activating methane and it leads to the generation of the  $\text{Rh-CH}_3$  complex.

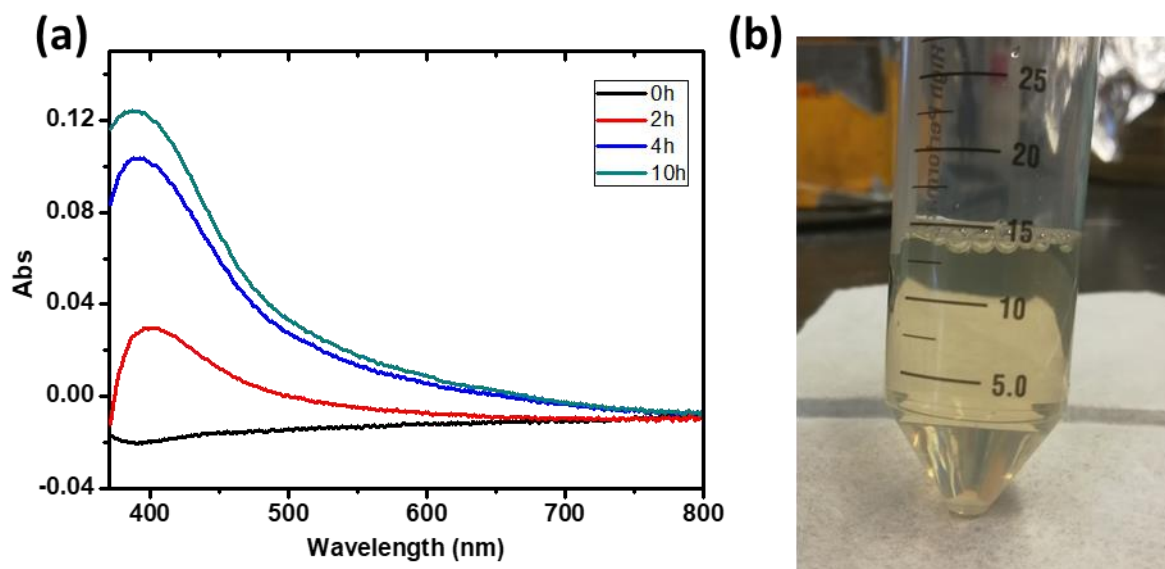
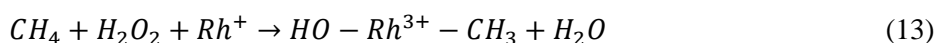


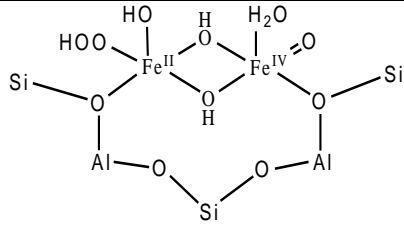
Figure 4.15 (a) UV-Vis spectra and (b) picture of the product liquid showing  $\text{H}_2\text{O}_2$  production on  $0.5\text{wt}\%$  RhZSM-5 determined by colorimetric method. Conditions:  $560\text{mg}$  catalyst,  $20\text{mL}$  aqueous solution containing  $0.1\text{mol/L}$   $\text{H}_2\text{SO}_4$  and  $0.1\text{mol/L}$   $\text{TiOSO}_4$ ,  $5\text{bar}$   $\text{O}_2$ ,  $5\text{bar}$   $\text{CO}$ ,  $50^\circ\text{C}$ .

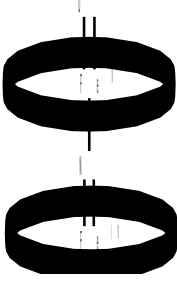
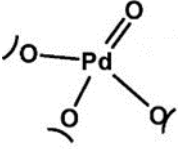
With the above knowledge, the detailed elementary steps leading to the formation of Rh-CH<sub>3</sub> can be put together. The first step is reaction of O<sub>2</sub>, H<sub>2</sub>O and CO to form H<sub>2</sub>O<sub>2</sub> and CO<sub>2</sub>. The oxygen that is incorporated into CO<sub>2</sub> stems from H<sub>2</sub>O while both oxygen atoms of O<sub>2</sub> are activated into H<sub>2</sub>O<sub>2</sub>, reaction (10). Since the O-H bond of water is split in order for the reaction to happen, this step shows the kinetic isotope effect for H-D. The same kinetic isotope effect is not observed for oxygen because the labeled and unlabeled oxygen only shows a mass difference of 12.5%. Observation of KIE on <sup>16</sup>O-<sup>18</sup>O is thus challenging. The H<sub>2</sub><sup>18</sup>O observed in the aqueous phase when using <sup>18</sup>O<sub>2</sub> is then from the decomposition of H<sub>2</sub><sup>18</sup>O<sub>2</sub>.



Subsequent reaction leading up to the formation of Rh-CH<sub>3</sub> accompanies the deposition of one reactive oxygen that splits the first C-H bond of methane. The oxygen deposition step likely induces the simultaneous oxidation of the metal center, as has been proposed in other studies using H<sub>2</sub>O<sub>2</sub> as oxidant.<sup>32-</sup>  
<sup>35</sup> Table 4.2 summarizes the different metal oxo structures proposed to activate methane using H<sub>2</sub>O<sub>2</sub>.

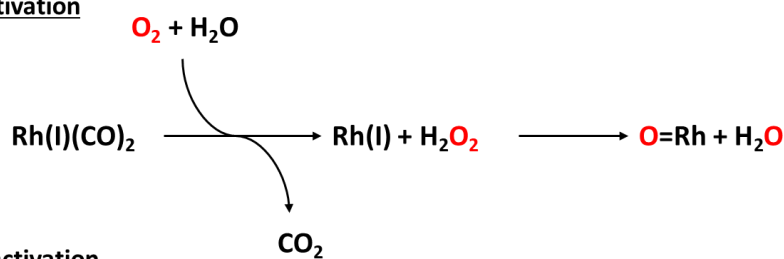
Table 4.2 Metal-oxo structures proposed after oxidation with peroxide species for C-H bond activation

Catalyst	Oxidized state	Redox couple	Reference
FeZSM-5		Fe(II)-Fe(II)/Fe(II)-Fe(IV)	32

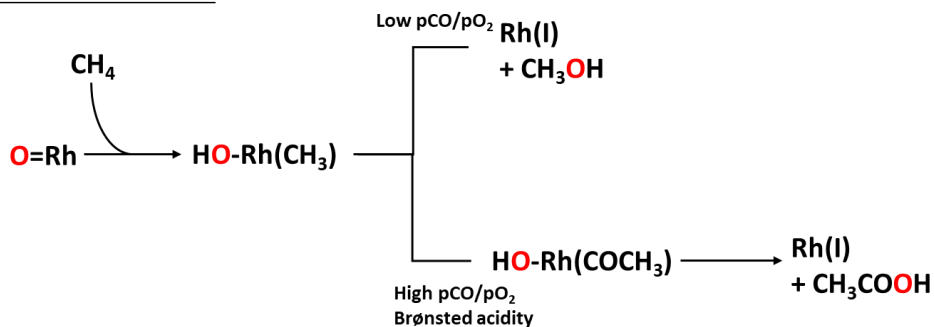
(FePc <sup>t</sup> Bu <sub>4</sub> ) <sub>2</sub> N		Fe(III)-Fe(IV)/Fe(V)-Fe(IV)	33
Pd-Al-MCM-41		Pd/[Pd=O] <sup>2+</sup>	34
RhCl <sub>3</sub>	Rh <sup>n</sup> + <sup>2</sup> =O	Rh <sup>n</sup> /[Rh=O] <sup>n+2</sup>	35

Here a Rh(III)-CH<sub>3</sub> is most likely as it is the center for the carbonylation reaction in the Monsanto catalyst.<sup>12</sup> Further release of the product through an elimination step with -OH can revert the metal center back to Rh(I), closing the catalytic cycle. The full mechanism proposed here is detailed in Scheme 4.2

**Oxygen activation**



**Methane activation and functionalization**



Scheme 4.2 Catalytic cycle of oxidative conversion of methane on RhZSM-5.

#### 4.3.3 Understanding the efficiency of CO

The mechanism identified in 4.3.2 placed a minimum amount of CO that needs to be consumed as sacrificial reagent to activate oxygen. For one molecule of methanol or acetic acid to be formed, one CO molecule will be converted to CO<sub>2</sub>. This is the maximum achievable CO efficiency. We can define the ratio of moles of CO oxidized to CO<sub>2</sub> over moles of liquid oxygenates formed as R which is used to characterize CO efficiency. Therefore, the lowest value of R is unity, and the closer to unity R value is, the higher the efficiency of the catalytic system.

$$R = \frac{\text{Number of CO molecules oxidized}}{\text{Number of liquid oxygenates formed}}$$

Reasons of R being higher than one can be attributed to low rate of methane activation which in turn favors H<sub>2</sub>O<sub>2</sub> decomposition. Combining reaction (10) and (12) together, the CO is only consumed for CO oxidation rather than H<sub>2</sub>O<sub>2</sub> synthesis.



To understand how reaction conditions and catalyst structures affect the efficiency of the system, R values corresponding to different reaction conditions were calculated. Figure 4.16 shows the R value at different reaction time corresponding to selective acetic acid formation condition (Figure 3.5(a)). At the onset of reaction, the efficiency of the system is very low. Every 6.2 molecules of CO consumed forms 1 molecules of liquid oxygenate. As the reaction proceeds the R values decreases, finally reaching 4.3 at 6h. As the reaction proceeds, H<sub>2</sub>O<sub>2</sub> becomes more stable which could be attributed to the decrease of pH of the aqueous phase. The formation of both CO<sub>2</sub> and acetic acid helps to stabilize H<sub>2</sub>O<sub>2</sub> which has been reported in the literature.<sup>36, 37</sup>

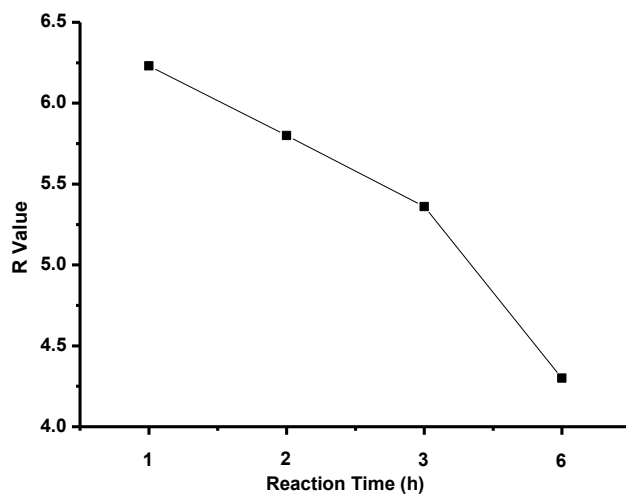


Figure 4.16 CO efficiency on 0.5wt% RhZSM-5 at different reaction time. Conditions: 20mg catalyst, 20mL DI water, 2bar O<sub>2</sub>, 5bar CO, 20bar CH<sub>4</sub>, 150°C.

Conditions that facilitate methane activation were found to increase CO efficiency. Higher methane pressure leads to higher concentration of dissolved methane in the aqueous phase. As shown in Figure 4.17, increasing the methane partial pressure from 20bar to 30bar leads to 1.5 times increase of the acetic acid formed, and the R value decreased from 4.3 to 3.4. However, further increasing the methane pressure to 40bar does not improve product formation, indicating that the reaction is no longer limited by dissolved methane.

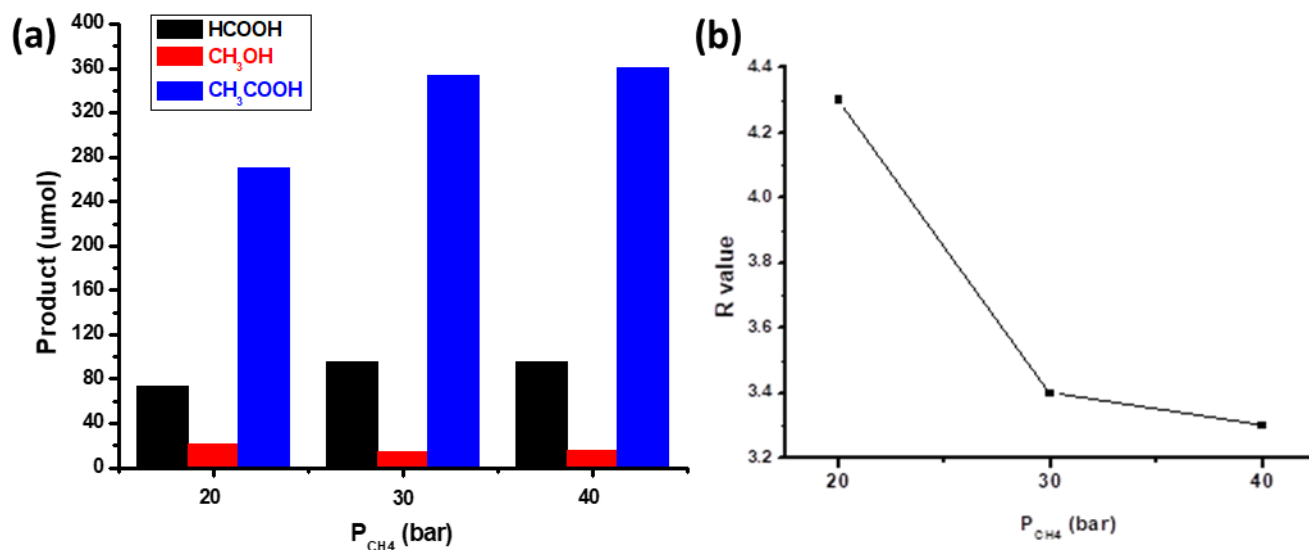


Figure 4.17 (a) Catalytic activity and (b) CO efficiency of 0.5wt% RhZSM-5 with different methane partial pressure. Conditions: 100mg catalyst, 20mL DI water, 2bar O<sub>2</sub>, 5bar CO, 150°C, 3h.

The dependence of CO efficiency on temperature is also investigated and the results are shown in Figure 4.18. The maximum amount of product formation at different temperature shows a volcano type plot and CO efficiency is low at both the high end of the temperature (190°C) and the low end (110°C). Although higher temperature facilitates the oxidation of methane, H<sub>2</sub>O<sub>2</sub> decomposition reaction is also facilitated and excessive H<sub>2</sub>O<sub>2</sub> decomposition leads to low CO efficiency and high R value. At lower temperature, the reaction with the lower activation energy is favored. Figure 4.19 shows the Arrhenius type plot of both the initial rate of CO consumption and CH<sub>4</sub> oxidation. The CO consumption accounts for the activation energy of H<sub>2</sub>O<sub>2</sub> formation (measured by CO<sub>2</sub> formed from CO) and the activation energy is

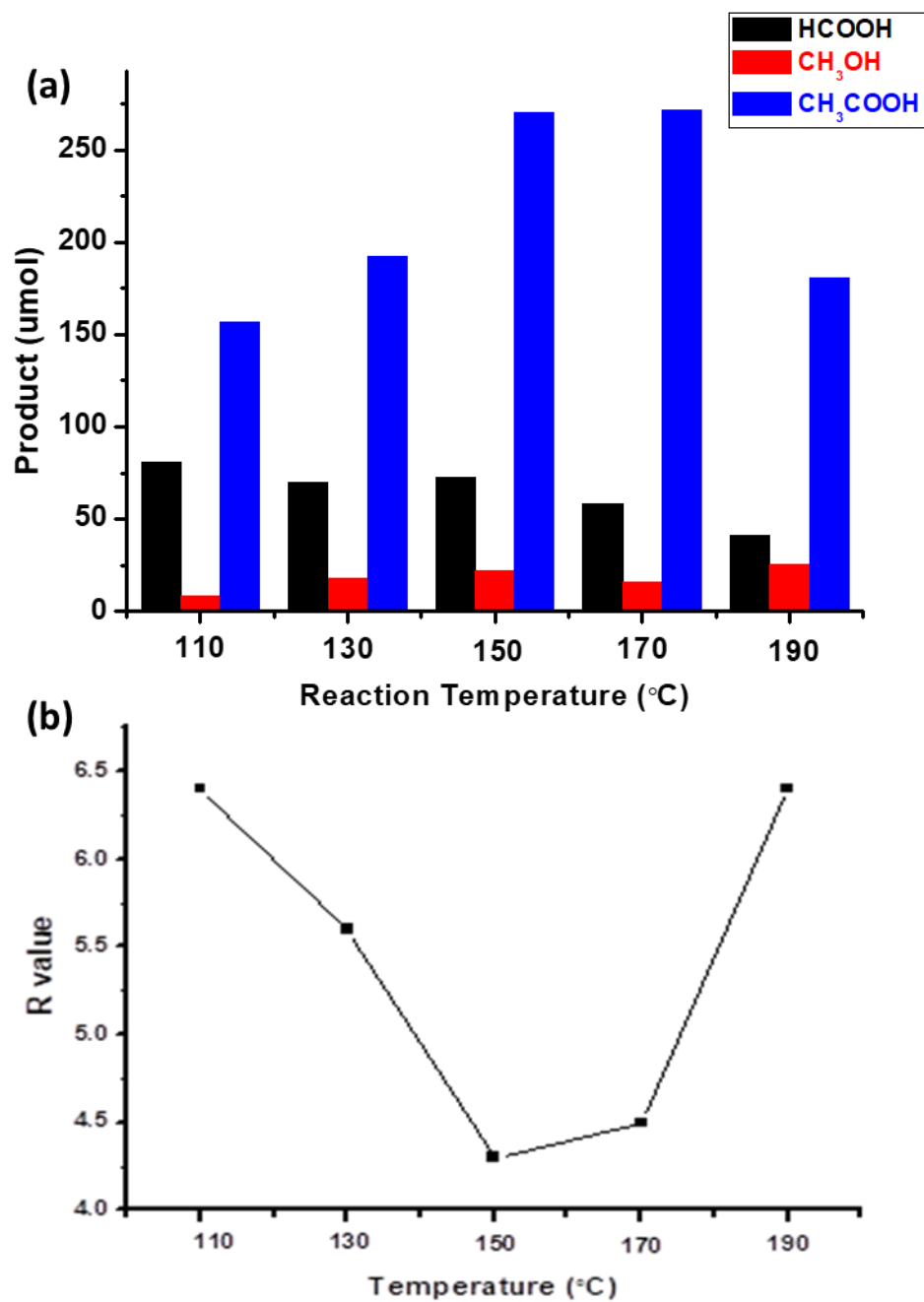


Figure 4.18 (a) Catalytic activity and (b) CO efficiency of 0.5wt% RhZSM-5 at different reaction temperature. Conditions: 10-300mg catalyst, 20mL DI water, 2bar  $\text{O}_2$ , 5bar  $\text{CO}$ , 20bar  $\text{CH}_4$ , 3h.

10 kJ/mol lower than that of CH<sub>4</sub> oxidation. Lower temperature favors the formation of H<sub>2</sub>O<sub>2</sub> but not subsequent CH<sub>4</sub> activation with H<sub>2</sub>O<sub>2</sub>. The accumulation of H<sub>2</sub>O<sub>2</sub> also leads to enhanced decomposition and lowers CO efficiency. Therefore, simply tuning the temperature does not lead to a more efficient catalytic system and to improve CO efficiency, the two steps need to be balanced to maximize CO utilization.

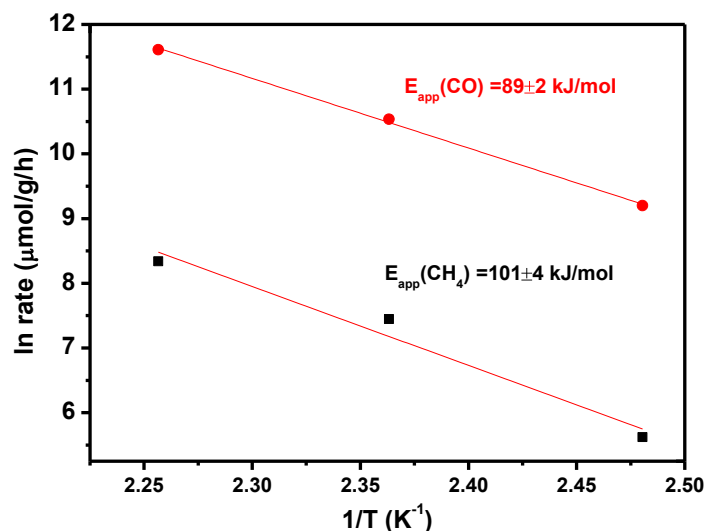


Figure 4.19 Arrhenius-type plot of initial rate of both CO consumption and CH<sub>4</sub> oxidation on 0.5wt% RhZSM-5. Conditions: 20mL DI water, 2bar O<sub>2</sub>, 5bar CO, 20bar CH<sub>4</sub>, 0.5h, 130-170°C.

The structural dependence of the two reactions is explored using a catalyst with only isolated Rh cations and a catalyst with mixed structure of cations and nanoparticles. The results in Figure 4.20 clearly demonstrate that at the same level of O<sub>2</sub> conversion, the catalyst with only isolated rhodium cations shows about 1.6 times higher formation of oxygenates compared to catalyst with mixed structure and the R value decreased from 4.3 to 3.3. The active site for CH<sub>4</sub> oxidation is proposed to be isolated rhodium atoms, but for H<sub>2</sub>O<sub>2</sub> formation the reaction can proceed on both nanoparticles (1-3nm) and sub-nanometer clusters.<sup>38</sup> Therefore, a catalyst with higher fraction of nanoparticles will contribute to the formation of H<sub>2</sub>O<sub>2</sub> only but not CH<sub>4</sub> oxidation, leading to lower CO efficiency.

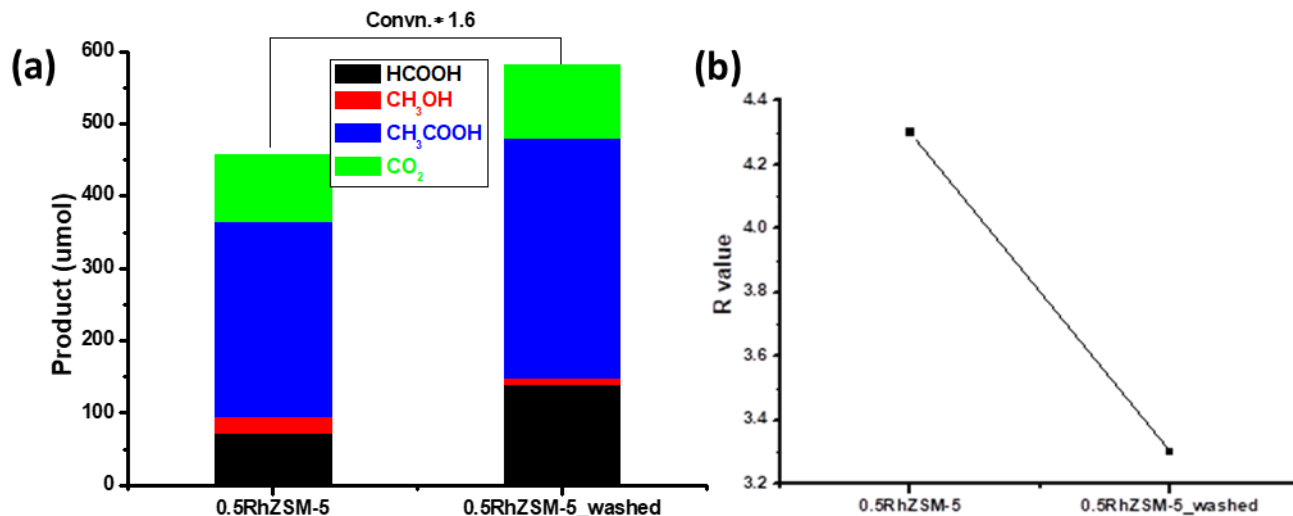
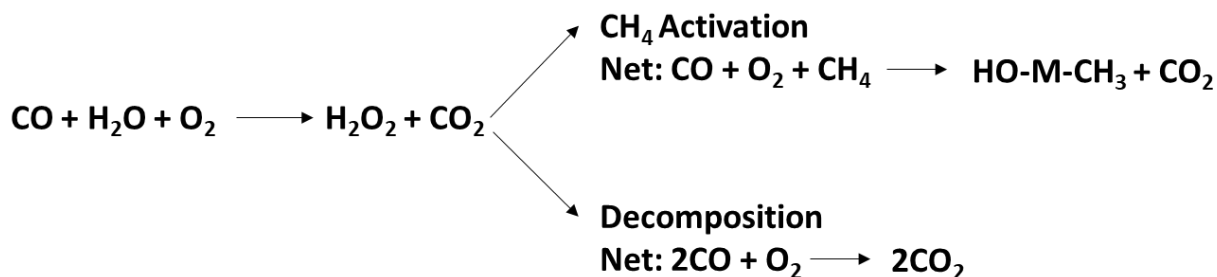


Figure 4.20 (a) Product formation and (b) CO efficiency on 0.5wt% RhZSM-5 and 0.5wt% RhZSM-5\_washed at full O<sub>2</sub> conversion. Conditions: 100mg 0.5wt% RhZSM-5 (or 500mg 0.5wt% RhZSM-5\_washed), 2bar O<sub>2</sub>, 5bar CO, 20bar CH<sub>4</sub>, 150°C, 3h.

From these experimental observations, one can generalize that the key for developing an efficient catalytic system for methane oxidation with molecular oxygen in the presence of CO is balancing the reaction of H<sub>2</sub>O<sub>2</sub> formation and CH<sub>4</sub> oxidation. Since the H<sub>2</sub>O<sub>2</sub> formation step is much faster compared to CH<sub>4</sub> oxidation, reaction conditions favoring CH<sub>4</sub> oxidation like higher CH<sub>4</sub> partial pressure should be used. Increasing the single atom concentration of rhodium leads to more sites for CH<sub>4</sub> activation and therefore increases the CO efficiency. The reaction is preferably conducted at temperatures that do not lead to strong decomposition of H<sub>2</sub>O<sub>2</sub> and coupling this step with a metal center that can efficiently activate CH<sub>4</sub> at such a temperature will be a viable catalyst design strategy.



Scheme 4.3 Reaction network accounting for pathways of CO consumption.

#### 4.3.4 Design of bimetallic FeRhZSM-5 catalyst for selective C1 formation

With the knowledge garnered from the mechanistic study, I further set out to explore possible catalyst systems for selective C1 oxygenates formation at temperatures below 100°C. Although the 0.5wt% RhNaZSM-5 and 0.6wt% RhTiO<sub>2</sub> catalysts both catalyze selective formation of methanol or formic acid, the amount of oxygenates obtained is low (below 10 μmol) and efficiency of CO is low (R>6). The most desirable catalyst for C1 product formation, as outlined in 4.3.3, should operate at temperatures below 100°C to minimize H<sub>2</sub>O<sub>2</sub> decomposition and over-oxidation of oxygenates. An initial attempt is to test the catalytic activity of RhZSM-5 at such a temperature regime. As demonstrated in the first entry of Table 4.3, RhZSM-5 is no longer active at such a low temperature to activate methane and the reaction does not light off even when the catalyst amount is increased 28 times. However, the formation of CO<sub>2</sub> from peroxide synthesis reaction can still be initiated, indicating that H<sub>2</sub>O<sub>2</sub> synthesis can happen at a much lower temperature on rhodium center compared to methane oxidation. As demonstrated in Figure 4.15, formation of H<sub>2</sub>O<sub>2</sub> is readily realized on 0.5wt% RhZSM-5 at 50°C. To utilize the formed H<sub>2</sub>O<sub>2</sub> at such a low temperature, a secondary metal center that catalyzes oxidation of methane with H<sub>2</sub>O<sub>2</sub> should be incorporated. Iron species stabilized inside ZSM-5 pores either as isolated ions<sup>36</sup> or diiron oxo centers<sup>29</sup> have been reported to activate C-H bond of lower alkanes with high activity. Therefore, iron species were introduced together with rhodium by co-impregnation and the same reduction procedure was used. The hydrogen reduction not only produces reduced rhodium species that allows for facile CO adsorption as

dicarbonyl, as demonstrated in Chapter 3, but also produces highly dispersed extra-framework iron species inside the zeolite pores. Addition of 0.1 wt% of iron leads to formation of oxygenates at 50°C, although the amount is limited, Table 4.3 entry 2. It has been reported that the formation of hydrogen peroxide with CO/O<sub>2</sub>/H<sub>2</sub>O mixture requires acidic promoters to desorb the OOH species from metal surface to form H<sub>2</sub>O<sub>2</sub>.<sup>40</sup> Here the need for an acidic environment is strongly demonstrated by reaction light-off in 0.1 mol/L H<sub>2</sub>SO<sub>4</sub> compared to neutral pH water, entry 3. It is hypothesized that the acidic environment stabilizes the peroxide intermediate and allows for its spillover to iron sites. Therefore, rhodium is only the H<sub>2</sub>O<sub>2</sub> synthesis site at this low temperature and methane activation happens on the peroxide activated iron center, presumably through an Fe<sup>IV</sup>=O site. Indeed, the absence of any C<sub>2</sub> product formation of this catalytic system is indicative that Rh-CH<sub>3</sub> complex is not formed, but rather a Fe-CH<sub>3</sub> complex is present. Cationic iron site is not active for carbonylation reactions, therefore eliminating the C<sub>2</sub> functionalization pathway.

Table 4.3 Catalytic activity of rhodium-based catalysts at 50°C in different solvents

Catalyst	Solvent	HCOOH ( $\mu\text{mol}$ )	CH <sub>3</sub> OH ( $\mu\text{mol}$ )	CH <sub>3</sub> COOH ( $\mu\text{mol}$ )	CH <sub>4</sub> Convsn.	R value
0.5RhZSM-5	DI water	0	0	0	0	-
0.1Fe0.5RhZSM-5	DI water	0	1.0	0	0.005%	850
0.1Fe0.5RhZSM-5	0.1mol/L H <sub>2</sub> SO <sub>4</sub>	325	0	0	1.8%	3.2
0.5Fe0.5RhZSM-5	0.1mol/L H <sub>2</sub> SO <sub>4</sub>	320	0	0	1.8%	3.3

0.1Fe0.5RhZSM-5*	0.1mol/L H <sub>2</sub> SO <sub>4</sub>	75	0	0	2.5%	11.8
------------------	--	----	---	---	------	------

Conditions: 560mg catalyst, 5bar O<sub>2</sub>, 5bar CO, 30bar CH<sub>4</sub>, 50°C, 3h.

\* 5bar CH<sub>4</sub> instead of 30bar.

The above hypothesis can be further confirmed through several spectroscopic studies. Figure 4.21 shows the UV-Vis spectra of the aqueous phase product of H<sub>2</sub>O<sub>2</sub> synthesis reaction carried out using 0.5wt% FeZSM-5. No formation of H<sub>2</sub>O<sub>2</sub> can be detected through the colorimetric method and the CO<sub>2</sub> formation in the gas phase is negligible. The iron site does not function as oxygen activation site to generate H<sub>2</sub>O<sub>2</sub>. Indeed, efficient heterogeneous metal species reported for H<sub>2</sub>O<sub>2</sub> synthesis using O<sub>2</sub>/CO/H<sub>2</sub>O mixtures are limited to palladium, ruthenium, copper and nickel. These metals readily adsorb CO and form carbonyl species at room temperature. Iron, on the other hand, adsorbs CO weakly if it is not in metallic state.

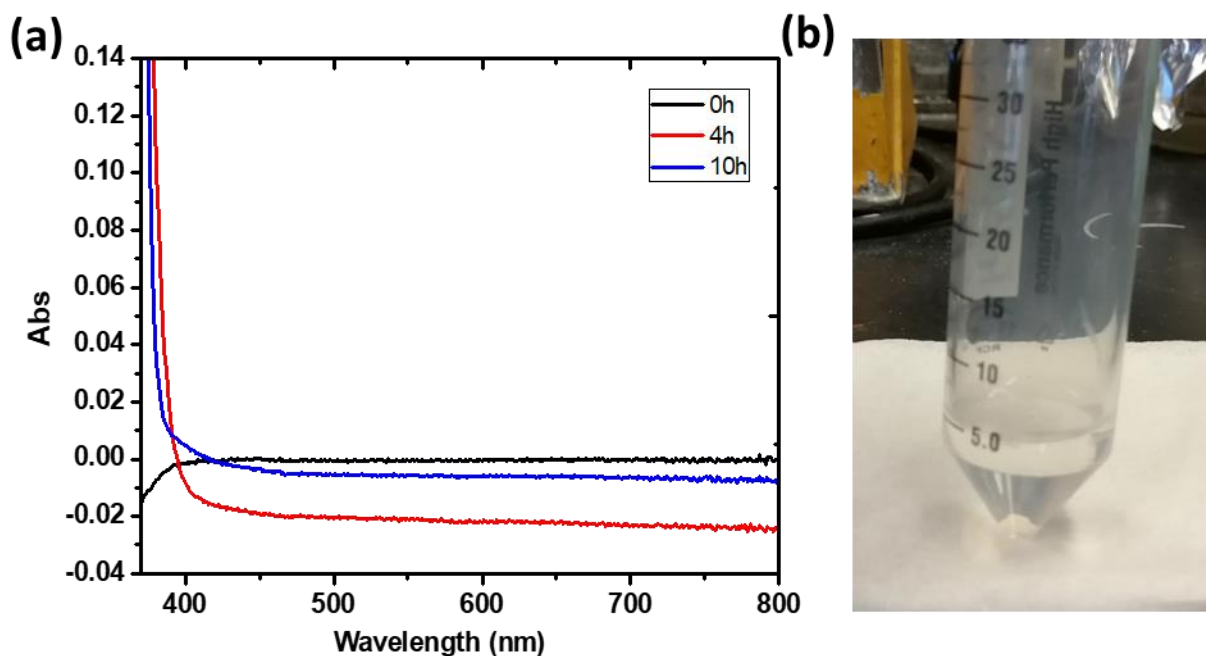
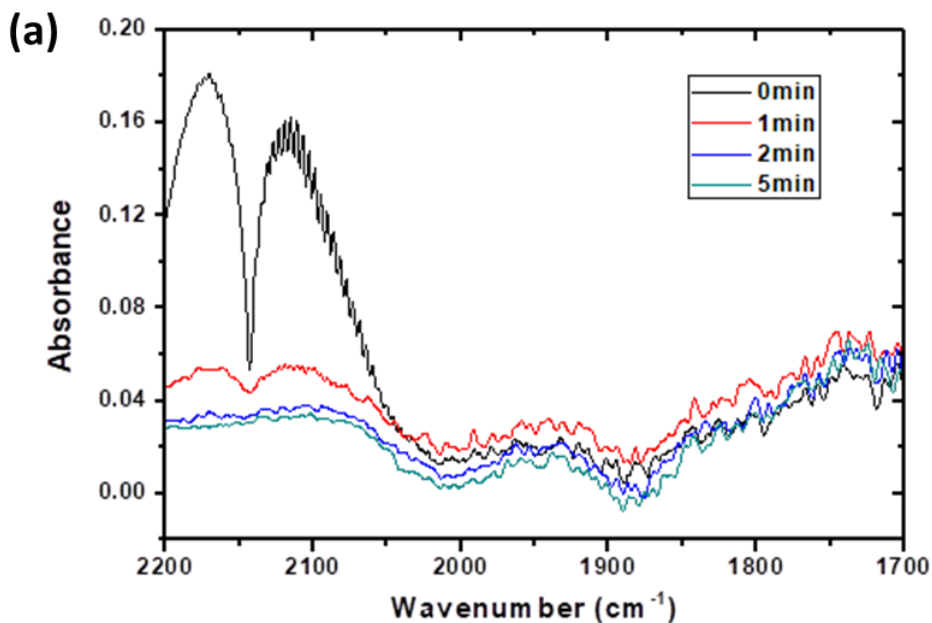


Figure 4.21 (a) UV-Vis spectra and (b) picture of the product liquid showing no  $\text{H}_2\text{O}_2$  production on 0.5wt% FeZSM-5 determined by colorimetric method. Conditions: 560mg catalyst, 20mL aqueous solution containing 0.1mol/L  $\text{H}_2\text{SO}_4$  and 0.1mol/L  $\text{TiOSO}_4$ , 5bar  $\text{O}_2$ , 5bar  $\text{CO}$ , 50°C.

To confirm the weak interaction of CO with iron, CO-DRIFTS of FeZSM-5 and FeRhZSM-5 was conducted. CO-DRIFT spectra of 0.1wt% FeZSM-5 show no adsorption of CO on the iron site at room temperature, even with gas phase CO present at pressure of 0.1 atm, Figure 4.22(a). On the other hand, only CO binding features on rhodium can be observed for the 0.1Fe0.5RhZSM-5 catalyst. The result is in line with carbonyl chemistry of iron species, as only metallic  $\text{Fe}(\text{CO})_5$  is reported for supported iron catalysts. Both the carbonylation reaction and  $\text{H}_2\text{O}_2$  synthesis reaction requires CO adsorption onto the metal center as the first step. From both UV-Vis and CO-DRIFTS findings, one can safely rule out the contribution of iron in activating  $\text{O}_2$ .



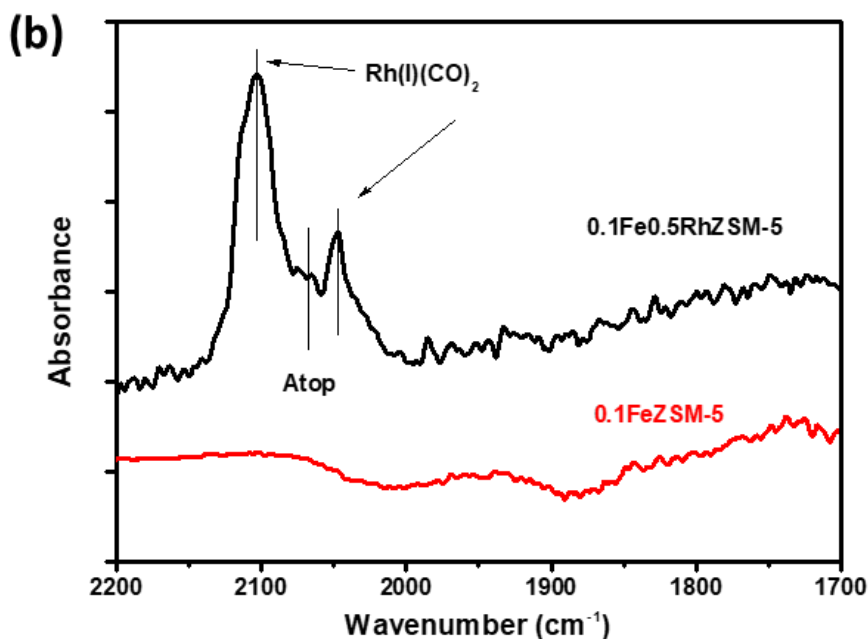


Figure 4.22 CO-DRIFT spectra of (a) 0.1wt% FeZSM-5 with CO desorption at room temperature at different time and (b) 0.1wt% FeZSM-5 and 0.1Fe0.5RhZSM-5 after desorption of 5min at room temperature.

The next step is to confirm the spillover of  $\text{H}_2\text{O}_2$  to iron site in acidic media. The interaction of  $\text{H}_2\text{O}_2$  with cationic iron site was reported to generate highly oxidized iron oxo species at low temperature. Fe K-edge XANES spectra were therefore recorded on 0.1Fe0.5RhZSM-5 catalyst in fresh and used state and in a gas mixture of  $\text{O}_2/\text{CO}/\text{H}_2\text{O}$  (1:1:1) at  $50^\circ\text{C}$ . Compared to the fresh catalyst, the used catalyst shows a shift of edge position to higher energy by 2eV and a higher white line intensity. The XANES spectra at Fe K-edge strongly suggests that iron species underwent oxidation during reaction. To check whether this oxidation is due to the interaction with  $\text{H}_2\text{O}_2$  or  $\text{O}_2$ , XANES spectra of the fresh catalyst treated in a mixture of  $\text{O}_2/\text{CO}/\text{H}_2\text{O}$  at  $50^\circ\text{C}$  was also recorded. Different from the used catalyst, the sample treated with the gas mixture at  $50^\circ\text{C}$  shows a shift of edge position to lower energy accompanied by a rise of the pre-edge feature at 7114eV. The rise of pre-edge corresponds to a change of coordination environment

from octahedral to tetrahedral, while extra-framework octahedral coordinated iron is considered to be the active site for alkane activation.<sup>39</sup> The XANES results demonstrate that interaction with the reaction gas mixture without acidic environment only leads to tetrahedral iron species that are not active for methane activation, while exposure to H<sub>2</sub>O<sub>2</sub> generated in-situ in the acidic media maintains the octahedral coordination environment and also leads to highly oxidized iron site.

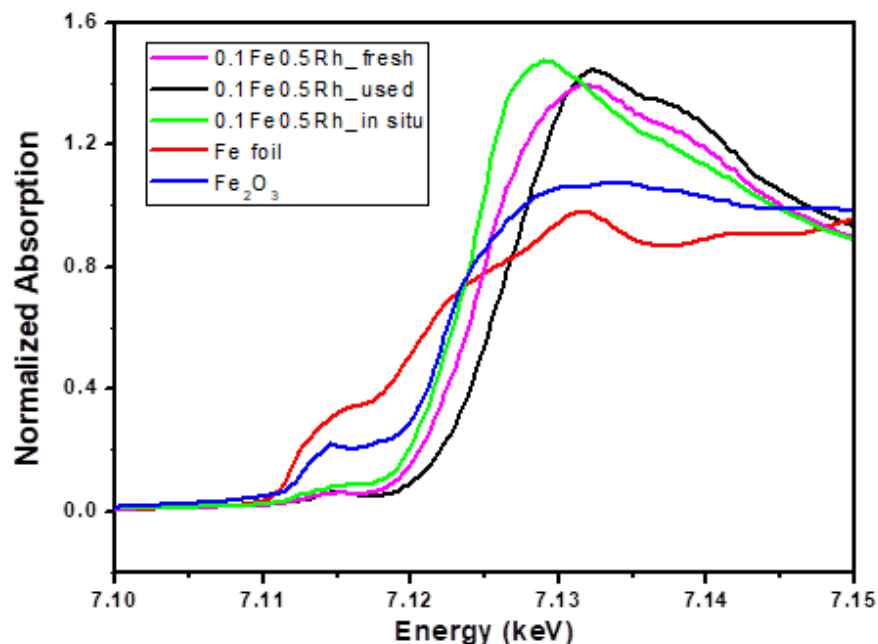


Figure 4.23 Fe K-edge XANES spectra of fresh, used and in-situ FeRhZSM-5 catalyst along with Fe foil and Fe<sub>2</sub>O<sub>3</sub> used as standards.

Another piece of evidence for the change in methane activation site is the decrease in apparent activation energy. The Arrhenius-type plot of the initial rate measured on 0.1Fe0.5RhZSM-5 is shown in Figure 4.24. The apparent activation energy of the reaction was measured on RhZSM-5 to be 101±4 kJ/mol while on 0.1Fe0.5RhZSM-5 the apparent activation energy decreased to 39±6 kJ/mol. Also, it is worth noting that the catalyst is active even at RT. Although experimental value of the apparent activation energy of methane oxidation on iron site was not reported, DFT calculations help shed some light.

Szécényi et al. calculated the activation barrier of C-H bond scission on zeolite supported iron sites and found that multiple mechanisms of C-H bond scission can account for methane activation, namely homolytic, heterolytic dissociation and Fenton-type reaction. The reaction barrier for homolytic dissociation of the first C-H bond of methane on Fe=O structures is 64 kJ/mol which is the closes to our experimental result.<sup>43</sup> Heterolytic dissociation has a much higher reaction barrier, 112 kJ/mol and Fenton-type reaction is lower, 20 kJ/mol. It is thus hypothesized methane activation takes place on iron sites following these three mechanisms simultaneously, resulting in an intermediate activation energy.

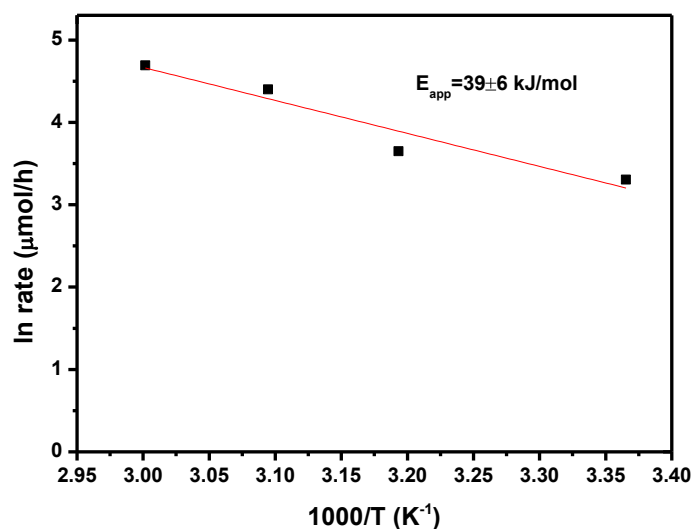


Figure 4.24 Arrhenius-type plot using 0.1Fe0.5RhZSM-5 in the temperature range of 24-60°C. Conditions: 5bar O<sub>2</sub>, 5bar CO, 30bar CH<sub>4</sub>, 357mg catalyst, 20mL 0.1mol/L H<sub>2</sub>SO<sub>4</sub>, 30min.

Figure 4.25 shows the Fe K-edge EXAFS data of 0.1Fe0.5RhZSM-5 catalyst plotted in Fourier Transform space. The EXAFS data clearly shows that most of iron species is in isolated ionic state, with Fe-O interaction and no Fe-Fe interaction. A separate Fe-Rh can be identified, which shows that on bimetallic catalyst, rhodium and iron species are in close proximity inside the zeolite pores. It is reported that reduction of iron species on zeolite by H<sub>2</sub> at high temperature leads to the formation of isolated iron species in ionic state instead of metallic particles or clusters.<sup>39</sup> Here it is demonstrated that this strategy

can also be applied to bimetallic FeRh catalyst. The close proximity of the two sites is crucial to catalyst activity at low temperature as spillover of peroxide intermediate is most effective.

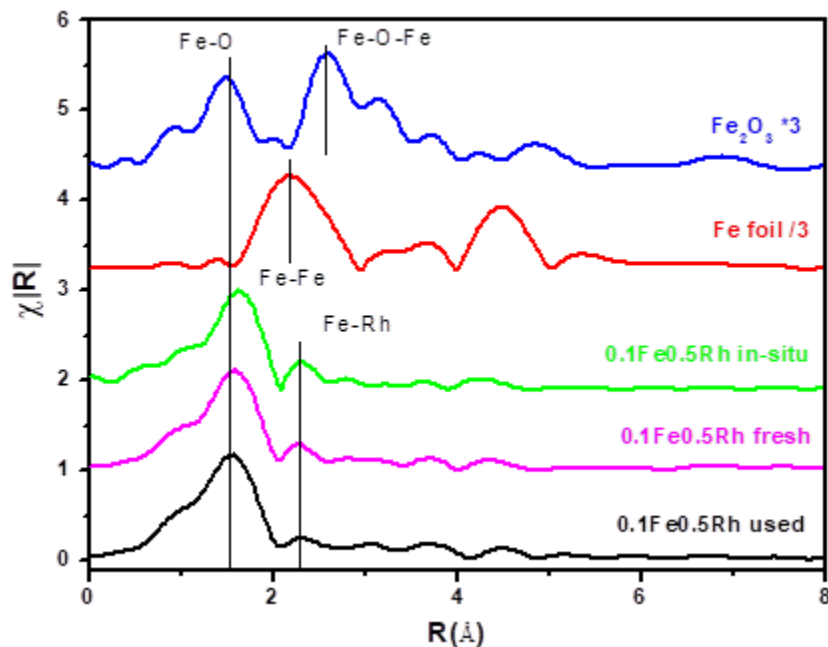


Figure 4.25 Fe K-edge EXAFS data of fresh, used and in-situ FeRhZSM-5 catalyst plotted in Fourier Transform space along with Fe foil and Fe<sub>2</sub>O<sub>3</sub> as standards.

The preservation of iron site in mostly atomically dispersed state after reaction prompts further study on the catalyst stability. Cyclic activity test of 0.1Fe0.5RhZSM-5 was performed by filtering out the catalyst after reaction and washing thoroughly with DI water to remove acid and oxygenate residuals. The washed catalyst was dried and suspended in 0.1mol/L H<sub>2</sub>SO<sub>4</sub> for the next cycle of test. The results shown in Figure 4.26 demonstrate that 0.1Fe0.5RhZSM-5 can be reused without deactivation for up to 4 cycles. Compared to monometallic RhZSM-5 which operates at 150°C, the bimetallic system catalyzes methane oxidation at much milder temperature and is therefore less susceptible to metal sintering. The stability of the catalyst is therefore another advantage of the bimetallic system.

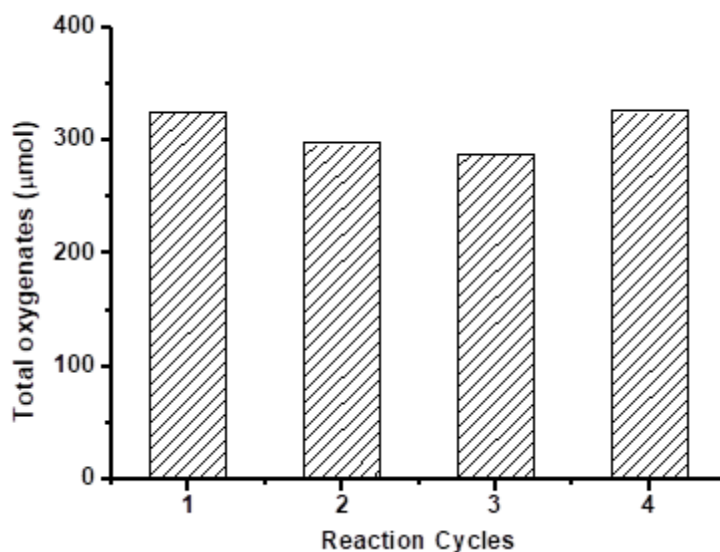


Figure 4.26 Cyclic stability of 0.1Fe0.5RhZSM-5 catalyst. Conditions: 5bar O<sub>2</sub>, 5bar CO, 30bar CH<sub>4</sub>, 560mg catalyst, 50°C, 20mL 0.1mol/L H<sub>2</sub>SO<sub>4</sub>.

In summary, by incorporating isolated iron species into zeolite pores together with rhodium, and using an acidic environment to facilitate peroxide spillover, an active and reusable bimetallic catalyst system was constructed that catalyzes selective oxidation of methane to formic acid at temperatures below 100°C. The catalyst shows comparable CO utilization efficiency with that of RhZSM-5 but with product selectivity to C1 oxygenates only.

#### 4.4 Conclusions

Functionalization pathways of a Rh-CH<sub>3</sub> complex was elucidated in this part of the work which involves CO carbonylation to acetic acid (C2 pathway) or direct hydroxylation to methanol (C1 pathway). The two pathways proceed in parallel and methanol is not an intermediate for acetic acid formation. The functionalization pathway also depends on the coordination environment of rhodium cations, with

Brønsted acidity of the zeolite needed for the C2 pathway. The C1 pathway does not require support acidity or zeolite porosity and is realized on open oxide supports like titania.

The detailed mechanism of methane activation and oxygen activation leading to a Rh-CH<sub>3</sub> complex was also demonstrated. The reaction of adsorbed CO with O<sub>2</sub> and H<sub>2</sub>O generates a peroxide intermediate that further oxidizes isolated rhodium center into a rhodium oxo complex. Of the two oxygen atoms from molecular oxygen, only one is incorporated onto rhodium and subsequently inserted into liquid oxygenates, which is consistent with the mechanism proposed for methane monooxygenase.<sup>42</sup>

With the knowledge of peroxide intermediate, a bimetallic catalyst that combines isolated iron and rhodium atoms as bi-functional system can be constructed. The catalyst catalyzes selective oxidation of methane at temperatures below 100°C, at which rhodium can no longer activate methane. The shift of methane activation site from rhodium to iron leads to a change in product selectivity to only C1 molecules and a drop in the apparent activation energy.

#### 4.5 References

- (1) Periana, R. A.; Mironov, O.; Taube, D.; Bhalla, G.; Jones, C. J. Catalytic, oxidative condensation of CH<sub>4</sub> to CH<sub>3</sub>COOH in one step via CH activation. *Science* **2003**, 301, 814-818.
- (2) Shilov, A. E.; Shul'pin, G. Activation of C-H bonds by metal complexes. *Chem. Rev.* **1997**, 97, 2879-2932.
- (3) Huang, X.; Groves, J. T. Beyond ferryl-mediated hydroxylation: 40 years of the rebound mechanism and C-H activation. *J. Biol. Inorg. Chem.* **2017**, 22, 185-207.
- (4) Moore, R. N.; Diakur, J.; Nakashima, T. T.; McLaren, S. L. Vederas, J. C. Isotopic shifts in <sup>13</sup>C-N.M.R. spectra of <sup>18</sup>O-labelled acetals; Multiple labelling effects at β-carbons. *J. Chem. Soc. Chem. Comm.* **1981**, 1, 501-502.
- (5) Lewis, R. J.; Hutchings, G. J. Recent advances in the direct synthesis of H<sub>2</sub>O<sub>2</sub>. *ChemCatChem* **2019**, 11, 298-308.
- (6) Eisenberg, G. M. Colorimetric determination of hydrogen peroxide, *Ind. Eng. Chem. Anal. Ed.* **1943**, 15, 5, 327-328.
- (7) Paulik, F. E.; Roth, J. F. Novel catalysts for the low-pressure carbonylation of methanol to acetic acid, *Chem. Comm.* **1968**, 0, 1578a.
- (8) *CRC handbook of chemistry and physics, Internet Version*; Lide, D. R. ed.; CRC Press: Boca Raton, FL, 2005.
- (9) Gottlieb, H. E.; Kotlyar, V.; Nudelman, A. NMR chemical shifts of common laboratory solvents as trace impurities. *J. Org. Chem.* **1997**, 62, 7512-7515.
- (10) Seravalli, J.; Ragsdale, S. W. <sup>13</sup>C NMR characterization of an exchange reaction between CO and CO<sub>2</sub> catalyzed by carbon monoxide dehydrogenase. *Biochemistry* **2008**, 47, 26, 6770-6781.

- (11) Babij, N. R.; McCusker, E. O.; Whiteker, G. T.; Canturk, B.; Choy, N.; Creemer, L. C.; De Amicis, C. V.; Hewlett, N. M.; Johnson, P. L.; Knobelsdorf, J. A.; Li, F.; Lorsbach, B. A.; Nugent, B. M.; Ryan, S. J.; Smith, M. R.; Yang, Q. NMR chemical shifts of trace impurities: industrially preferred solvents used in process and green chemistry. *Org. Proc. Res. Dev.* **2016**, *20*, 661-667.
- (12) Dekleva, T. W.; Forster, D. Mechanistic aspects of transition-metal-catalyzed alcohol carbonylations. *Adv. Catal.* **1986**, *34*, 81-130.
- (13) Howard, M. J.; Jones, M. D.; Roberts, M. S.; Taylor, S. A. C1 to acetyls: catalysis and process. *Catal. Today* **1993**, *18*, 325-354.
- (14) Stepanov, A. G.; Luzgin, M. V.; Romannikov, V. N.; Zamaraev, K. I. NMR observation of the Koch reaction in zeolite H-ZSM-5 under mild conditions. *J. Am. Chem. Soc.* **1995**, *117*, 3615-3616.
- (15) Ellis, B.; Howard, M. J.; Joyner, R. W.; Reddy, K. N.; Padley, M. B.; Smith, W. J. Heterogeneous catalysts for the direct, halide-free carbonylation of methanol. *Stud. Surf. Sci. Catal.* **1996**, *101*, 771-779.
- (16) Zhou, L.; Li, S.; Qi, G.; Su, Y.; Li, J.; Zheng, A.; Yi, X.; Wang, Q.; Deng, F. Methanol carbonylation over copper-modified mordenite zeolite: A solid-state NMR study. *Solid State Nucl. Mag.* **2016**, *80*, 1-6.
- (17) Kinnunen, T.; Laasonen, K. The oxidative addition and migratory 1,1-insertion in the Monsanto and Cativa processes. A density functional study of the catalytic carbonylation of methanol. *J. Mol. Struct. – THEOCHEM* **2001**, *542*, 273-288.
- (18) Jones, J. A. The Cativa™ process for the manufacture of acetic acid. *Platinum Metals Rev.* **2000**, *44*, 94-105.
- (19) Yang, M.; Allard, L. F.; Flytzani-Stephanopoulos, M. Atomically dispersed Au-(OH)<sub>x</sub> species bound on titania catalyze the low-temperature water-gas shift reaction. *J. Am. Chem. Soc.* **2013**, *135*, 3768-3771.

- (20) Liu, P.; Zhao, Y.; Qin, R.; Mo, S.; Chen, G.; Gu, L.; Chevrier, D. M.; Zhang, P.; Guo, Q.; Zang, D.; Wu, B.; Fu, G.; Zheng, N. Photochemical route for synthesizing atomically dispersed palladium catalysts. *Science* **2016**, 352, 797-800.
- (21) Liu, P.; Zhao, Y.; Qin, R.; Gu, L.; Zhang, P.; Fu, G.; Zheng, N. A vicinal effect for promoting catalysis of Pd<sub>1</sub>/TiO<sub>2</sub>: supports of atomically dispersed catalysts play more roles than simply serving as ligands. *Sci. Bull.* **2018**, 63, 675-682.
- (22) Guan, H.; Lin, J.; Qiao, B.; Yang, X.; Li, L.; Miao, S.; Liu, J.; Wang, A.; Wang, X.; Zhang, T. Catalytically Active Rh sub-nanoclusters on TiO<sub>2</sub> for CO oxidation at cryogenic temperatures. *Angew. Chem. Int. Ed.* **2016**, 55, 2820-2824.
- (23) Yang, M. Atomically dispersed gold and platinum species on various oxide support for catalytic low-temperature hydrogen generation. Ph.D. Thesis, Tufts University, Medford, MA, 2015.
- (24) Matsubu, J. C.; Yang, V. N.; Christopher, P. Isolated metal active site concentration and stability control catalytic CO<sub>2</sub> reduction selectivity. *J. Am. Chem. Soc.* **2015**, 137, 3076-3084.
- (25) Hermann, J. M.; Disdier, J.; Pichat, P.; Fernandez, A.; Gonzalez-Elipe, A.; Munuera, G.; Leclercq, C. Titania-supported bimetallic catalyst synthesis by photocatalytic codeposition at ambient temperature: preparation and characterization of Pt-Rh, Ag-Rh, and Pt-Pd couples. *J. Catal.* **1991**, 132, 490-497.
- (26) Xiong, L.; Li, J.; Yang, B.; Yu, Y. Ti<sup>3+</sup> in the surface of titanium dioxide: generation, properties and photocatalytic application. *J. Nanomater.* **2012**, 831524.
- (27) Setvín, M.; Aschauer, U.; Scheiber, P.; Li, Y.-F.; Hou, W.; Schmid, M.; Selloni, A.; Diebold, U. Reaction of O<sub>2</sub> with subsurface oxygen vacancies on TiO<sub>2</sub> anatase (101). *Science* **2013**, 341, 988-991.
- (28) Ojifinni, R. A.; Froemming, N. S.; Gong, J.; Pan, M.; Kim, T. S.; White, J. M.; Henkelman, G.; Mullins, C. B. Water-enhanced low-temperature CO oxidation and isotope effects on atomic oxygen-covered Au(111). *J. Am. Chem. Soc.* **2008**, 130, 6801-6812.

- (29) Jiang, J.; Oxford, S. M.; Fu, B.; Kung, M. C.; Kung, H. H.; Ma, J. Isotope labelling study of CO oxidation-assisted epoxidation of propene. Implications for oxygen activation on Au catalysts. *Chem. Commun.* **2010**, 46, 3791-3793.
- (30) Zope, B. N.; Hibbitts, D. D.; Neurock, M.; Davis, R. J. Reactivity of the gold/water interface during selective oxidation catalysis. *Science* **2010**, 330, 74-78.
- (31) Saavedra, J.; Doan, H. A.; Pursell, C. J.; Grabow, L. C.; Chandler, B. D. The critical role of water at the gold-titania interface in catalytic CO oxidation. *Science* **2014**, 26, 1599-1602.
- (32) Hammond, C.; Forde, M. M.; Ab Rahim, M. H.; Thetford, A.; He, Q.; Jenkins, R. L.; Dimitratos, N.; Lopez-Sanchez, J. A.; Dummer, N. F.; Murphy, D. M.; Carley, A. F.; Taylor, S. H.; Willock, D. J.; Stangland, E. E.; Kang, J.; Hagen, H.; Kiely, C. J.; Hutchings, G. J. Direct catalytic conversion of methane to methanol in an aqueous medium by using copper-promoted Fe-ZSM-5. *Angew. Chem. Int. Ed.* **2012**, 51, 5129-5133.
- (33) Sorokin, A. B.; Kudrik, E. V.; Alvarez, L. X.; Afanasiev, P.; Millet, J. M. M.; Bouchu, D. Oxidation of methane and ethylene in water at ambient conditions. *Catal. Today* **2010**, 157, 149-154.
- (34) Gannouni, A.; Delbecq, F.; Zina, M. S.; Sautet, P. Oxidation of methane to methanol over single site palladium oxide species on silica: A mechanistic view from DFT. *J. Phys. Chem. A* **2017**, 121, 5500-5508.
- (35) Chepaikin, E. G.; Bezruchenko, A. P.; Boiko, G. N.; Gekhman, A. E.; Moiseev, I. I. Isotope effects in the oxidative functionalization of methane in the presence of rhodium-containing homogeneous catalytic systems. *Kinet. Catal.* **2006**, 47, 12-19.
- (36) Scoville, J. R.; Novicova, I. A. Hydrogen peroxide disinfecting and sterilizing compositions. US5900256A, 1996.

- (37) Edwards, J. K.; Solsona, B.; Ntainjua, E. N.; Carley, A. F.; Kiely, C. J.; Hutchings, G. J. Switching off hydrogen peroxide hydrogenation in the direct synthesis process. *Science* **2009**, 323, 1037-1041.
- (38) Freakley, S. J.; He, Q.; Harrhy, J. H.; Lu, L.; Crole, D. A.; Morgan, D. J.; Ntainjua, E. N.; Edwards, J. K.; Carley, A. F.; Borisevich, A. Y.; Kiely, C. J.; Hutchings, G. J. Palladium-tin catalysts for the direct synthesis of H<sub>2</sub>O<sub>2</sub> with high selectivity. *Science* **2016**, 351, 965-968.
- (39) Forde, M. M.; Armstrong, R. D.; McVicker, R.; Wells, P. P.; Dimitratos, N.; He, Q.; Lu, L.; Jenkins, R. L.; Hammond, C.; Lopez-Sanchez, J. A.; Kiely, C. J.; Hutchings, G. J. Light alkane oxidation using catalysts prepared by chemical vapor impregnation: tuning alcohol selectivity through catalyst pre-treatment. *Chem. Sci.* **2014**, 5, 3603-3616.
- (40) Feng, W.-L.; Cao, Y.; Yi, N.; Dai, W.-L.; Fan, K.-N. Direct production of hydrogen peroxide from CO, O<sub>2</sub>, and H<sub>2</sub>O over a novel alumina supported Cu catalyst. *New J. Chem.* **2004**, 28, 1431-1433.
- (41) Campos-Martin, J. M.; Blanco-Brieva, G.; Fierro, J. L. G. Hydrogen peroxide synthesis: an outlook beyond the anthraquinone process. *Angew. Chem. Int. Ed.* **2006**, 45, 6962-6984.
- (42) Tinberg, C. E.; Lippard, S. J. Dioxygen activation in soluble methane monooxygenase. *Acc. Chem. Res.* **2011**, 44, 280-288.
- (43) Szécsényi, Á.; Li, G.; Gascon, J.; Pidko, E. A. Mechanistic complexity of methane oxidation with H<sub>2</sub>O<sub>2</sub> by single-site Fe/ZSM-5 catalyst. *ACS Catal.* **2018**, 8, 7961-7972.

# Chapter 5 Selective conversion of methane to methanol over Ir- based catalysts

## 5.1 Introduction

Since Rh single cations anchored inside the pores of ZSM-5 or on TiO<sub>2</sub> open support catalyze the oxidation of methane to methanol or acetic acid using molecular oxygen as the oxidant<sup>1</sup>, investigation of other metals that potentially catalyze the same chemistry is of interest.

Besides Rh, iridium cationic sites have been reported to activate the first C-H bond of methane at mild conditions. In homogeneous catalysis, Cp\*Ir(CO)<sub>2</sub> can cleave the C-H bond through oxidative addition to generating a Ir-CH<sub>3</sub> hydride complex photochemically at room temperature<sup>2</sup>. Recently, the IrO<sub>2</sub> (110) single crystal surface was reported to break the C-H bond of methane at 150K in Ultra High Vacuum conditions and generate surface CH<sub>x</sub> species. However, desorption shows only CO<sub>x</sub> and H<sub>2</sub>O<sup>3</sup>. Furthermore, studies in homogeneous systems have confirmed that catalytic turnover of methane to oxygenates or CO<sub>2</sub> can be achieved with Ir(III) metal complexes, but with strong oxidants like cerium ammonium nitrate or sodium periodate<sup>4</sup>. In this chapter, we demonstrate that IrZSM-5 catalyst promoted by copper and palladium can catalyze the direct oxidation of methane to methanol using molecular oxygen under moderate pressure and temperature in the presence of CO. The reaction is conducted in the aqueous phase. Isolated Ir(I)(CO)<sub>2</sub> is generated under the reaction conditions activating the C-H bond of methane via the generation of peroxide intermediate, following the similar mechanism as rhodium. Addition of palladium enables the spillover of peroxide to palladium site that is more active for methane oxidation, promoting the overall catalytic activity and forming primarily formic acid. Addition of copper selectively promotes the formation of methanol through both increasing peroxide intermediate formation and suppressing hydroxyl radical that over-oxidizes methanol.

## 5.2 Experimental Methods

### 5.2.1 Catalyst synthesis

The ammonium form of the zeolite ZSM-5 with Si/Al=15 was purchased from Alfa Aesar. Before depositing metal precursors, the zeolite was dried at 160°C for 2h to remove adsorbed water inside the micropores. All metal precursors were purchased from Alfa Aesar and were used as received. For Ir/ZSM-5 catalyst, the dehydrated zeolite was impregnated with an aqueous solution of IrCl<sub>3</sub> of the desired concentration to reach the designed metal loading. 0.6mL aqueous solution per 1g of dehydrated zeolite was used. The powder was further dried under vacuum at room temperature overnight. The dried powder was further reduced in 5% H<sub>2</sub> balanced with helium at 550°C (ramping rate=3°C/min) for 3h.

The 1.33wt% Ir<sub>1</sub>Cu<sub>1</sub>ZSM-5 catalyst was prepared by first impregnation of Cu(NO<sub>3</sub>)<sub>2</sub> following the same procedure described above. After drying in vacuum at room temperature, the copper containing catalyst was calcined in static air at 550°C for 3h to obtain 0.33wt% Cu/ZSM-5. IrCl<sub>3</sub> corresponding to 1wt% loading was impregnated on the calcined Cu/ZSM-5 and the catalyst was reduced with 5% H<sub>2</sub> at 550°C for 3h. The total metal weight loading is 1.33wt% and atomic ratio of Ir and Cu is 1:1.

The 1.06wt% Ir<sub>1</sub>Pd<sub>0.1</sub>ZSM-5 catalyst was prepared by a sequential impregnation method. First, the 1wt% IrZSM-5 was prepared by incipient wetness impregnation using an IrCl<sub>3</sub> solution and was dried in a vacuum oven at RT overnight. The dried IrZSM-5 was further dehydrated at 80 °C under vacuum for 2h before impregnating with Pd. The impregnation of 0.06wt% Pd to 1.0wt% IrZSM-5 was through an aqueous solution of Pd(NH<sub>3</sub>)<sub>4</sub>Cl<sub>2</sub>, followed by drying in a vacuum oven at RT overnight. The dried product was further reduced in 5% H<sub>2</sub> at 550°C for 3h to obtain the as-synthesized 1.06wt% Ir<sub>1</sub>Pd<sub>0.1</sub>ZSM-5 catalyst. Note that the molar ratio of Ir to Pd in the IrPdZSM-5 catalyst is 10:1.

The 1.39wt% Ir<sub>1</sub>Cu<sub>1</sub>Pd<sub>0.1</sub>ZSM-5 catalyst was prepared by a three-step synthesis. In the first step, 0.33wt% CuZSM-5 was synthesized by incipient wetness impregnation of dehydrated NH<sub>4</sub>-ZSM-5 with

an aqueous solution of  $\text{Cu}(\text{NO}_3)_2$ , followed by drying in a vacuum oven at RT overnight and calcination in air at 550 °C for 3h. In the second step, 1wt% Ir was impregnated to CuZSM-5 using the  $\text{IrCl}_3$  solution and then was dried in a vacuum oven at RT overnight. In the third step, the dried product was further dehydrated at 80 °C under vacuum for 2h and then 0.06wt% Pd was impregnated through an aqueous solution of  $\text{Pd}(\text{NH}_3)_4\text{Cl}_2$ , followed by drying in a vacuum oven at RT overnight. The dried product was further reduced in 5%  $\text{H}_2$  at 550°C for 3h to obtain the as-synthesized 1.36wt%  $\text{Ir}_1\text{Cu}_1\text{Pd}_{0.1}\text{ZSM-5}$  catalyst. Note that the molar ratio of Ir, Cu and Pd is 1:1:0.1.

### 5.2.2 Catalyst evaluation

Catalytic activity of different catalysts was evaluated in a pressurized 50mL Parr reactor. The solid catalysts were suspended in deionized water inside the reactor body with a glass liner. The suspension was sonicated for 2-10 min to ensure a uniform dispersion. A type J thermocouple is inserted into the liquid phase to measure the temperature of the aqueous suspension during reaction. The reactor was charged with 4bar  $\text{O}_2$ , 5bar  $\text{CO}$  and 20bar  $\text{CH}_4$  at room temperature and heated to the desired reaction temperature in an oil bath. A magnetic stirrer bar was used to agitate the aqueous suspension during reaction. After the desired reaction time was reached, the reactor was cooled with an ice bath to 12°C. The gas phase product was collected with a gas bag which was evacuated with a vacuum pump prior to releasing the pressurized gas from reactor. The gas mixture was analyzed using an SRI model 310 GC equipped with a TCD detector and by a Residual Gas Analyzer mass spectrometer. Liquid phase product was collected by removing solid catalyst with a syringe filter and the clear solution was stored in a refrigerator.

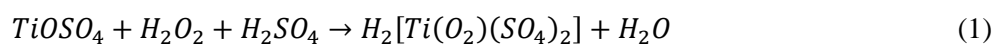
Analysis of the liquid phase product was conducted on a Bruker AVANCE III 500MHz NMR instrument. 100 $\mu\text{L}$  of  $\text{D}_2\text{O}$  was mixed with 600 $\mu\text{L}$  aqueous sample inside the NMR tube and  $\text{CDCl}_3$  with

1% TMS was placed in a coaxial insert inside the NMR tube as an internal standard. H-NMR was recorded with a presaturation program to suppress water peak. Oxygenate identified by H-NMR includes formic acid ( $\delta=8.34$ , singlet), methanol ( $\delta=3.36$ , singlet) and acetic acid ( $\delta=2.08$ , singlet). For each of the three oxygenates, a calibration curve was constructed by analyzing standard samples and plotting concentration versus the respective peak area relative to TMS ( $A_{oxygenate}/A_{TMS}$ )

Isotope labeling experiments were performed with  $^{13}\text{C}$  to identify the origin of carbon in liquid oxygenates. Reaction was conducted with 4bar  $\text{O}_2$ , 5bar  $^{13}\text{C}$  and 20bar  $\text{CH}_4$  on 1.39wt%  $\text{Ir}_1\text{Cu}_1\text{Pd}_{0.1}\text{ZSM-5}$  to achieve high product concentration.  $^{13}\text{C}$ -NMR analysis of the product was performed on Bruker Avance III 500MHz NMR instrument with the same sample preparation method for H-NMR. To maximize  $^{13}\text{C}$  sensitivity a zgpg pulse program was used which applies 90-degree pulse to the sample. 5000 scans were recorded to achieve good signal to noise ratio.

Initial rates of methane oxidation on different Ir-based catalysts were measured in the temperature range of 110-170°C. The conditions used were 4bar  $\text{O}_2$ , 5bar  $\text{CO}$ , 20bar  $\text{CH}_4$ , 20mL DI water, 30min reaction time. The amount of catalyst was varied at different temperature to maintain the same level of conversion of limiting reactant  $\text{O}_2$  (<15%). Rates were calculated as moles of C1 oxygenates formed per gram of catalyst used per hour of reaction.

$\text{H}_2\text{O}_2$  synthesis experiments were conducted in the same reactor. 300mg catalyst was suspended in an aqueous solution containing 0.1mol/L  $\text{H}_2\text{SO}_4$  and 0.1mol/L  $\text{TiOSO}_4$ . 5bar  $\text{O}_2$  and 5bar  $\text{CO}$  was pressurized into the reaction and the reaction was conducted at 50°C for 3h. The aqueous phase was filtered and analyzed by UV-Vis spectroscopy on an Agilent Cary 5000 UV-Vis-NIR spectrometer. Spectra were recorded from 350nm to 800nm with 1nm interval. Baseline was recorded with the aqueous solution before reaction.  $\text{TiOSO}_4$  reacts with  $\text{H}_2\text{O}_2$  via reaction (1) to form pertitanic acid which shows intense yellow color and absorption in 380-430nm region.<sup>5</sup>



### 5.2.3 Catalyst characterization

The catalysts were characterized by X-ray Diffraction (XRD), X-ray Photoelectron Spectroscopy (XPS), High Angle Annular Dark Field Transmission Electron Microscopy (HAADF-TEM), Diffuse Reflectance Infrared Fourier Transform Spectroscopy (DRIFTS), X-ray Absorption Near Edge Spectroscopy (XANES) and Extended X-ray Absorption Fine Structure (EXAFS).

XRD patterns of fresh and used catalysts were collected on a PANalytical X'Pert Pro instrument with nickel-filtered Cu K $\alpha$  X-ray source. The measurements were taken at 45kV and 40mA in continuous mode and 2 $\theta$  range from 10 $^\circ$  to 60 $^\circ$ . Aberration-corrected HAADF STEM imaging of Ir/ZSM-5 were conducted at Oak Ridge National Laboratory using a JEOL 2200FS-AC STEM/TEM system. XPS spectra were recorded on a PHI VersaProbe II system with Al K $\alpha$  source and a double focusing hemispherical analyzer. An argon ion sputtering gun was also used to sputter off zeolite surface layers to reveal structures inside zeolite pores. The samples were loaded on copper foil attached to a carbon tape.

DRIFTS measurements were conducted on a Thermo Scientific Nicolet iS50 FTIR fitted with a high temperature Praying Mantis chamber from Harrick. The spectra were recorded with 4cm $^{-1}$  resolution on a DTGS KBr detector and processing was carried out using OMNIC Spectra software. For CO-DRIFTS experiment, the sample was pre-treated in He at 170 $^\circ$ C for 1h and the background spectrum was recorded after sample was cooled down to room temperature. CO was introduced using 10% CO/He at different temperature and after cooling down to room temperature, the sample was purged with He for 10 min before recording the spectra. For in-situ DRIFTS experiment, the sample was also pre-treated in He at 170 $^\circ$ C for 1h and cooled down to room temperature to record background spectra. A gas mixture containing CH $_4$ , CO and O $_2$  simulating reaction gas was introduced via mass flow controllers. The sample was treated with the gas mixture at 150 $^\circ$ C for 1h and cooled down to room temperature. After He purge

for 15 min, spectra were recorded both in the CO and CH stretching region. Finally, a stream of He saturated with H<sub>2</sub>O vapor was introduced via a bubbler and the sample was treated at 150°C for 1h. The bubbler was switched off at 150°C for 15 min and sample was cooled down to room temperature to record the spectra. This cycle of treatment simulates a complete catalytic cycle of the reaction.

XAS measurements were performed at the Advanced Photon Source beamline 12BM at Argonne National Laboratory. Absorption data of different Ir samples at the Ir LIII edge were acquired in the fluorescence mode with Ir or Pt foil measured simultaneously to calibrate the energy. At least 5 consecutive scans were obtained with each sample to improve the signal to noise ratio. High resolution EXAFS of 0.05wt% IrZSM-5 was conducted at Stanford Synchrotron Radiation Lightsource. XANES and EXAFS data processing was conducted using the Demeter software package.

## 5.3 Results and discussion

### 5.3.1 Catalytic activity of IrZSM-5 promoted by copper and palladium

Catalyst activity testing is conducted in a batch reactor with the catalyst in powder form suspended in water and a gas mixture containing O<sub>2</sub>, CO and CH<sub>4</sub> pressurized into the headspace. Oxidation of methane is realized directly on 1.0wt% IrZSM-5 and the aqueous phase product contains formic acid, methanol and acetic acid. Reaction with pre-added methanol in the aqueous phase, in the absence of methane, shows that formic acid is produced from over-oxidation of methanol. Similar to RhZSM-5, IrZSM-5 does not catalyze the methanol carbonylation reaction under the conditions studied, as shown in the first entry of Figure 5.1 by the absence of any acetic acid formation. The origin of acetic acid is therefore the result of direct oxidative carbonylation of methane. Nevertheless, this pathway only contributes a small fraction of the activity. From the above, we surmise that the functionalization pathway on iridium is thus the same as that of rhodium catalysts.

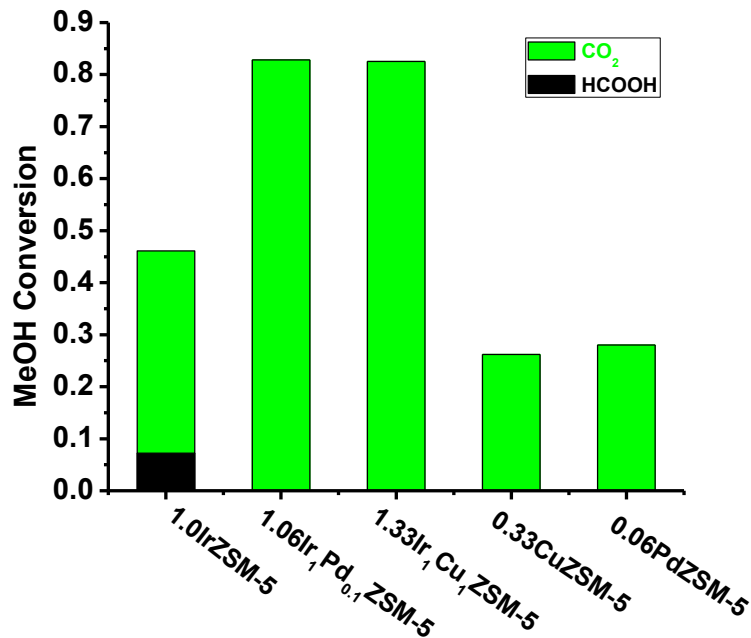


Figure 5.1 Oxidation of methanol over iridium-based catalysts. Conditions: 4bar O<sub>2</sub>, 5bar CO, 20bar He, 20mL 3mM methanol, 150°C, 1h.

Figure 5.2 shows the <sup>13</sup>C-NMR spectrum of product liquid obtained in <sup>13</sup>CO labeling experiments. The absence of liquid oxygenates peaks in <sup>13</sup>C-NMR spectrum confirms that all the liquid oxygenates carbon derives from CH<sub>4</sub> instead of CO. The absence of C2 functionalization product is intriguing, as both iridium and rhodium have been reported as active site for CO insertion into the metal carbon bond.<sup>6</sup> Industrially, iridium is used as the catalyst for methanol carbonylation reaction in the Cativa process.<sup>7</sup> The low activity for the C2 pathway may be attributed to the lower affinity of iridium to CO. CO as a soft Lewis base binds stronger to soft Lewis acids. Iridium has a chemical hardness higher than rhodium by 0.64eV.<sup>8</sup>

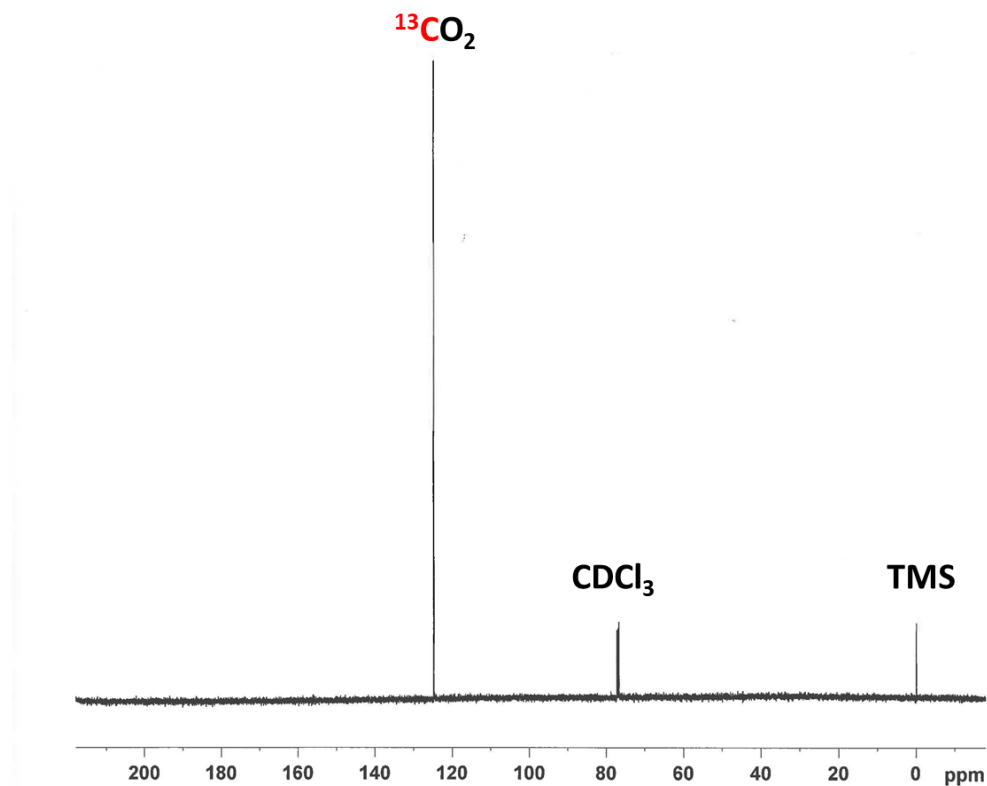


Figure 5.2  $^{13}\text{C}$ -NMR spectrum of the aqueous solution after reaction with  $^{13}\text{CO}$ . Conditions: 100mg 1.39wt%  $\text{Ir}_1\text{Cu}_1\text{Pd}_{0.1}\text{ZSM-5}$ , 4bar  $\text{O}_2$ , 5bar  $^{13}\text{CO}$ , 20bar  $\text{CH}_4$ , 150°C, 3h.

Figure 5.3 shows the catalytic performance of iridium monometallic catalyst together with iridium copper and iridium palladium catalyst. The monometallic iridium catalyst shows inferior activity compared to rhodium. Addition of a small amount of palladium (Ir:Pd=10:1 in atomic ratio) onto 1.0wt% IrZSM-5 by impregnation significantly promotes the activity. However, formic acid is now the main product. Methanol selectivity on 1.06wt%  $\text{Ir}_1\text{Pd}_{0.1}\text{ZSM-5}$  drops to 14% compared to 37% on 1.0wt% Ir/ZSM-5. Addition of copper, on the other hand, promotes the selective formation of methanol with methanol reaching 606  $\mu\text{mol/g-cat}$  and selectivity increasing to 62% on 1.33wt%  $\text{Ir}_1\text{Cu}_1\text{ZSM-5}$ .

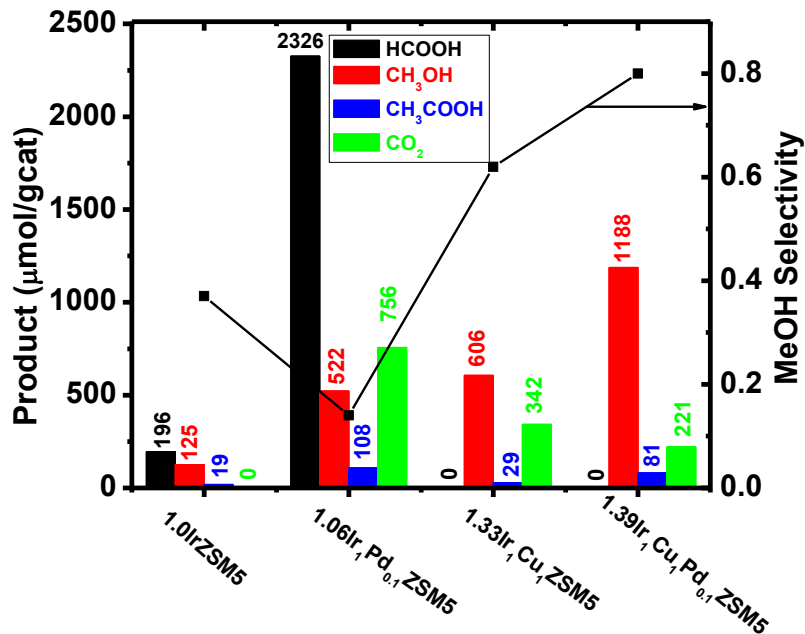


Figure 5.3 Product formation and methanol selectivity on copper and palladium promoted 1.0wt% IrZSM-5. Reaction conditions: 30mg catalyst (40mg for IrCuPdZSM-5), 4bar O<sub>2</sub>, 5bar CO, 20bar CH<sub>4</sub>, 20mL water, 150°C, 1h.

The high selectivity towards methanol on 1.33wt% Ir<sub>1</sub>Cu<sub>1</sub>ZSM-5 catalyst led us to examine it at different reaction conditions. The product formation and methanol selectivity (over all oxygenated products) using this catalyst at different reaction temperatures and reaction times is shown in Figure 5.4. Although formic acid is no longer formed as an over-oxidation product, the conversion of methanol to deeply oxidized oxygenate CO<sub>2</sub> is still dominant at high reaction temperature or long reaction time. A direct pathway of methanol oxidation to CO<sub>2</sub> is still present, and it is not suppressed by the addition of copper.

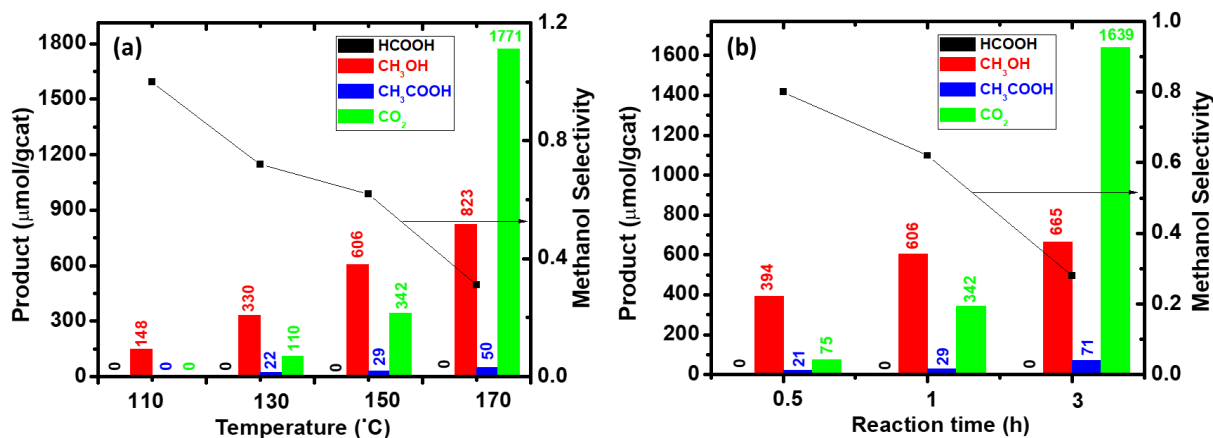


Figure 5.4 Product formation and methanol selectivity (over both liquid and gaseous oxygenates) on 1.33wt% Ir<sub>1</sub>Cu<sub>1</sub>ZSM-5 at (a) different temperatures and (b) different reaction times. Reaction conditions: 30mg catalyst, 4bar O<sub>2</sub>, 5bar CO, 20bar CH<sub>4</sub>, 20mL water, 110-170°C, 0.5-3h.

The stability of the catalyst was checked by filtering out the catalyst at the end of 1h reaction cycle and washing it with DI water. The washed catalyst after drying was suspended in DI water for the next cycle of activity test. The copper promoted Ir catalyst can be reused for multiple cycles, with no reduction of catalyst activity after the catalyst was used for 4 times, Figure 5.5(a). The stability of the catalyst is also confirmed by the absence of metal leaching into the aqueous phase monitored by ICP-AES. Furthermore, X-ray Diffraction (XRD) patterns of the catalyst before and after reaction shows ZSM-5 diffraction peaks with high crystallinity, and no degradation of the support was observed. Zhang, et. al reported that zeolite Y and zeolite β undergo severe loss of crystallinity in hot water treatment due to hydrolysis of silanol defects.<sup>9</sup> Here it is confirmed that the crystal framework of ZSM-5 does not collapse and is stable in hot water treatment, in agreement with previous reports.<sup>10, 11</sup>

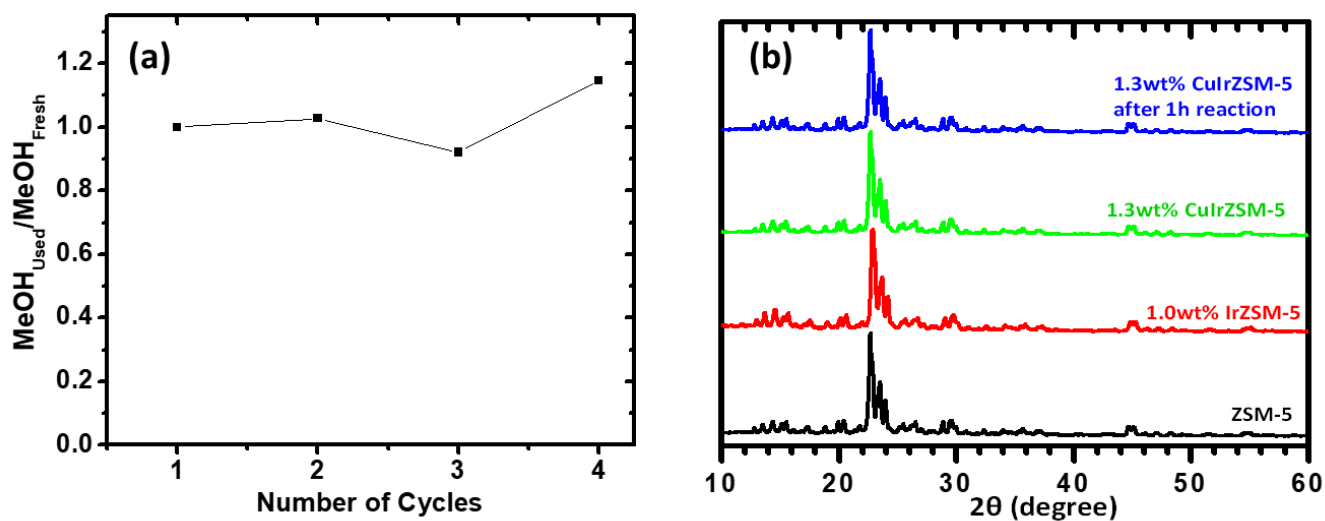


Figure 5.5 Catalyst stability as shown in (a) Methanol formation of 1.33wt%  $\text{Ir}_1\text{Cu}_1\text{ZSM-5}$  catalyst after multiple reaction cycles and (b) XRD patterns of parent ZSM-5, 1.0wt% IrZSM-5 and 1.33wt%  $\text{Ir}_1\text{Cu}_1\text{ZSM-5}$  after reaction.

Finally, the selective promotional effect of copper can also be applied on the IrPd catalyst and the trimetallic 1.39wt%  $\text{Ir}_1\text{Cu}_1\text{Pd}_{0.1}\text{ZSM-5}$  shows remarkable activity for methanol production with selectivity of 80%. Production of methanol can be further improved by extending the reaction time on this catalyst, Figure 5.6. The methanol production is increased to  $1600\mu\text{mol/g-cat}$  at 3h of reaction but accompanied by a drop in selectivity. Further extending the reaction time to 5h does not improve methanol production and  $\text{CO}_2$  become the dominant product. Similar to IrCuZSM-5, a separate pathway for methanol over-oxidation directly to  $\text{CO}_2$  leads to low methanol selectivity at long reaction time.

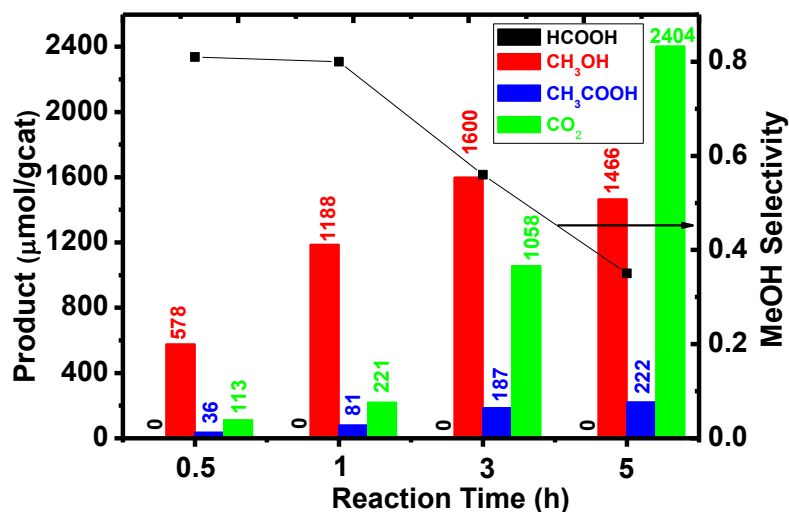


Figure 5.6 Product formation and methanol selectivity on 1.39wt% Ir<sub>1</sub>Cu<sub>1</sub>Pd<sub>0.1</sub>ZSM-5 at different reaction times. Reaction conditions: 40mg catalyst, 4bar O<sub>2</sub>, 5bar CO, 20bar CH<sub>4</sub>, 20mL water, 150°C.

### 5.3.2 Elucidating the role of metal promoters

Although the trimetallic catalyst is the most active and selective for the oxidation of methane to methanol, the complex system makes it difficult to delineate the contribution of each component. Therefore, we first set out to study the bimetallic catalysts to elucidate the role of Cu and Pd. The promotional effect of Cu on the selective formation of methanol during methane oxidation has been reported in several different articles. Hammond et al. reported that addition of Cu onto FeZSM-5 improves only the selectivity to methanol without affecting the overall reaction rate when using H<sub>2</sub>O<sub>2</sub> as the oxidant<sup>12</sup>. The improved selectivity is attributed to the suppression of hydroxyl radical formation which would over-oxidize methanol to formic acid and CO<sub>2</sub>. In strongly acidic media, both RhCl<sub>3</sub> and Pd/C catalysts can be promoted by addition of CuCl<sub>2</sub> in CF<sub>3</sub>COOH and both a higher rate of product formation and higher methanol selectivity can be achieved<sup>13, 14</sup>. This is also the case for the heterogeneous Ir- based catalysts examined here. On IrZSM-5 catalyst, addition of Cu either as second metal on the

support or as  $\text{Cu}(\text{NO}_3)_2$  in the solution shows the same promotional effect, as shown in Figure 5.7. Post reaction analysis of 1% IrZSM-5 used with aqueous  $\text{Cu}(\text{NO}_3)_2$  reveals that a significant amount of copper had been deposited on the ZSM-5 support, due to reduction of cupric ions to cuprous species ( $\text{Cu}_2\text{O}$ ,  $\text{Cu}(\text{OH})$ ) and deposition onto the zeolite during reaction. The reduction of copper at pH higher than 4 favors the formation of cuprous species. As the starting pH of the aqueous phase is 7, the deposition of copper as cuprous species is highly likely.

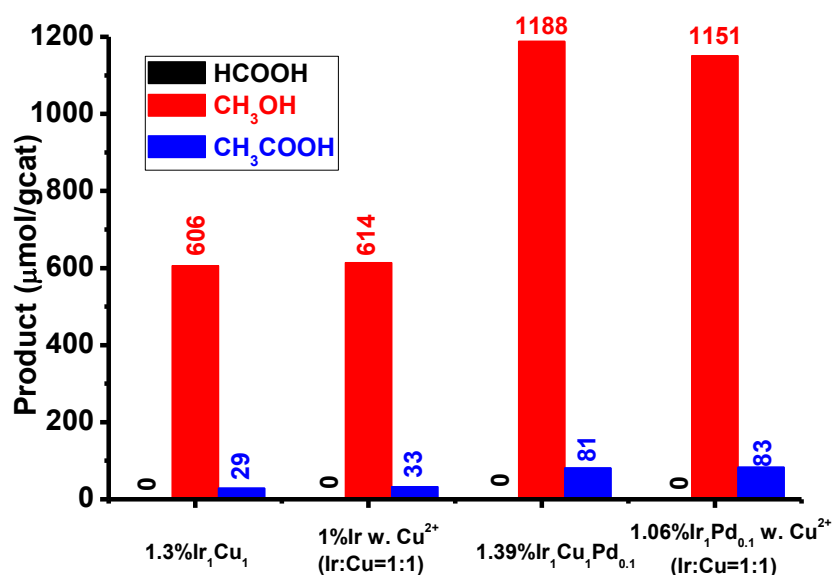


Figure 5.7 Promotional effect of Cu on 1.0wt% IrZSM-5 and 1.06wt% Ir<sub>1</sub>Pd<sub>0.1</sub>ZSM-5 as either heterogeneous metal species or aqueous  $\text{Cu}^{2+}$  ions. Conditions: 4bar  $\text{O}_2$ , 5bar  $\text{CO}$ , 20bar  $\text{CH}_4$ , 150°C, 1h, 20mL DI water or aqueous solution of  $\text{Cu}(\text{NO}_3)_2$ .

Although copper promotes both the amount of total product formed and methanol selectivity for IrZSM-5, as shown in Figure 5.3, it does not significantly decrease the apparent activation energy. On 1.0wt% IrZSM-5, an apparent activation energy of  $63 \pm 3$  kJ/mol is measured, while on 1.33wt% Ir<sub>1</sub>Cu<sub>1</sub>ZSM-5 the apparent activation energy is  $56 \pm 2$  kJ/mol, Figure 5.6. We postulate that copper

promotion does not affect the rate limiting step and methane activation still takes place on the Ir center. On the other hand, promotion by Pd shows a significant reduction of activation energy by 17 kJ/mol which indicates that Pd species participate in the rate limiting C-H activation step. Indeed, reports from both homogeneous and heterogeneous systems have shown that Pd is capable of activating the C-H bond at temperatures below 200°C<sup>15, 16</sup>. However, PdZSM-5 alone shows negligible activity under the same reaction conditions, and the presence of Ir is required to yield an active catalyst, which suggests a synergistic effect between Pd and Ir.

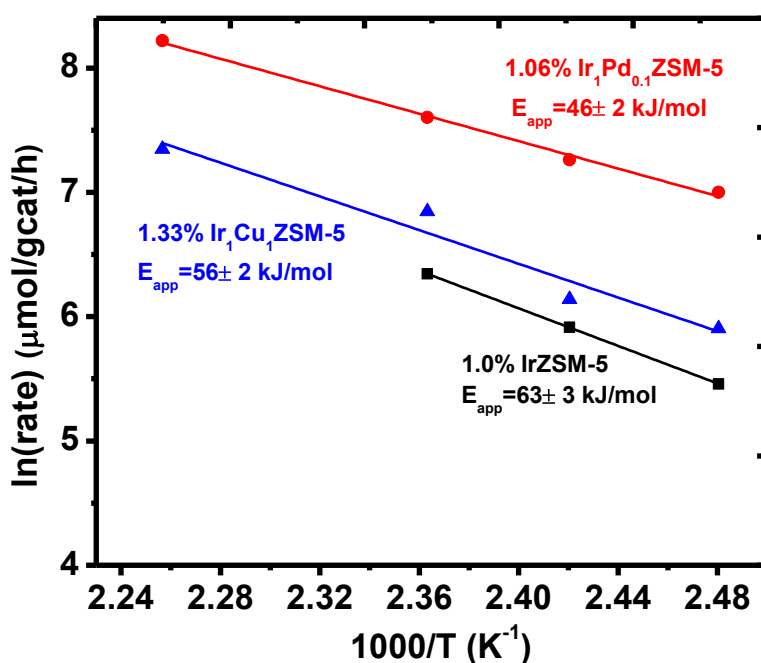
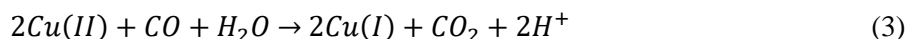
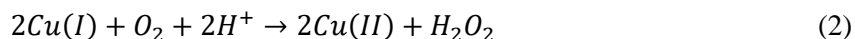


Figure 5.8 Arrhenius-type plot of 1.0wt% IrZSM-5, 1.33wt% Ir<sub>1</sub>Cu<sub>1</sub>ZSM-5 and 1.06wt% Ir<sub>1</sub>Pd<sub>0.1</sub>ZSM-5.

Conditions: 4bar O<sub>2</sub>, 5bar CO, 20bar CH<sub>4</sub>, 20mL DI water, 30min.

Considering the similar chemistry of iridium and rhodium, we assume the oxidation of methane by molecular oxygen in the presence of CO on the two metals shares the same kind of peroxide intermediate, as shown in Chapter 4. To confirm the existence of hydrogen peroxide in the reaction mixture, low temperature H<sub>2</sub>O<sub>2</sub> synthesis experiment on IrZSM-5 and IrCuZSM-5 was conducted. Colorimetric detection of H<sub>2</sub>O<sub>2</sub> using TiOSO<sub>4</sub> shows indeed production of H<sub>2</sub>O<sub>2</sub> at 50°C. The capture of such an

intermediate at high temperature is not possible due to its rapid decomposition. Figure 5.9 shows the UV-Vis monitoring of peroxy titanate formation on both IrZSM-5 and IrCuZSM-5. The same kind of peroxide intermediate can be captured on iridium-based catalyst, which confirms the activation of O<sub>2</sub> into H<sub>2</sub>O<sub>2</sub> in the presence of CO and H<sub>2</sub>O. The higher rate of oxygenate formation observed on 1.33wt% Ir<sub>1</sub>Cu<sub>1</sub>ZSM-5 can be explained by another promotional effect of copper, namely that copper increases the formation of peroxide intermediate that is responsible for methane activation. Such a catalytic effect of copper was proposed by Chepaikin, et. al, where Cu(I) reacts with O<sub>2</sub> and H<sub>2</sub>O to form Cu(II) and peroxide species, and Cu(II) is reduced by CO to Cu(I) which closes the catalytic cycle.<sup>13</sup> On the solid copper catalysts, reaction (2) and (3) can be proposed accordingly:



In Figure 5.9, stronger absorption band of peroxy titanate was observed when reaction was conducted using 1.33wt% Ir<sub>1</sub>Cu<sub>1</sub>ZSM-5, confirming the hypothesis that addition of copper leads to increased H<sub>2</sub>O<sub>2</sub> formation.

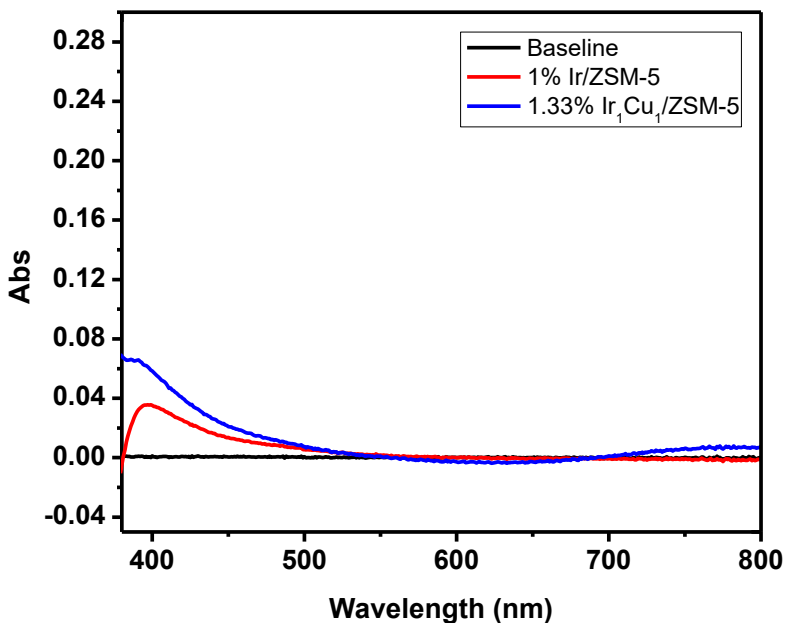


Figure 5.9 UV-Vis spectra of liquid product after H<sub>2</sub>O<sub>2</sub> synthesis reaction with 1.0wt% IrZSM-5 and 1.33wt% Ir<sub>1</sub>Cu<sub>1</sub>ZSM-5. Conditions: 300mg catalyst, 20mL 0.1mol/L H<sub>2</sub>SO<sub>4</sub>, 0.1mol/L TiOSO<sub>4</sub>, 5bar O<sub>2</sub>, 5bar CO, 50°C, 3h. Absorption band centered at 400nm clearly indicated formation of H<sub>2</sub>O<sub>2</sub> on both IrZSM-5 and IrCuZSM-5. The higher intensity on IrCuZSM-5 confirms the promoted formation of H<sub>2</sub>O<sub>2</sub> due to addition of copper.

With the peroxide as an intermediate in mind, understanding of the synergistic effect between iridium and palladium becomes straightforward. Peroxide intermediates formed on iridium surfaces spillover to palladium in a similar way as FeRhZSM-5 catalyst, as discussed in Chapter 4. Table 5.1 demonstrates the catalytic activity of 0.06wt% PdZSM-5 and 1.06wt% Ir<sub>1</sub>Pd<sub>0.1</sub>ZSM-5 catalysts with different oxidants. Catalyst containing only palladium species catalyzes methane oxidation effectively with H<sub>2</sub>O<sub>2</sub> but not with O<sub>2</sub>. Using O<sub>2</sub> as oxidant, only the combination of iridium with palladium leads to high activity of methane oxidation. Iridium supplies the peroxide intermediate to palladium that activates methane as Pd-CH<sub>3</sub> species. One difference between rhodium and iridium system is that iridium does not require acidic environment for the peroxide to spillover.

Table 5.1 Product formation on 0.06wt% PdZSM-5 and 1.06wt% Ir<sub>1</sub>Pd<sub>0.1</sub>ZSM-5 catalyst with different oxidants

Oxidant	Catalyst	Liquid Oxygenates (μmol/gcat)		
		HCOOH	CH <sub>3</sub> OH	CH <sub>3</sub> COOH
H <sub>2</sub> O <sub>2</sub> <sup>a</sup>	0.06wt% PdZSM-5	4427	428	89
O <sub>2</sub> <sup>b</sup>	0.06wt% PdZSM-5	0	53	0
O <sub>2</sub> <sup>b</sup>	1.06wt% Ir <sub>1</sub> Pd <sub>0.1</sub> ZSM-5	2326	522	108

a: 30mg catalyst, 0.5M H<sub>2</sub>O<sub>2</sub>, 5bar CO, 20bar CH<sub>4</sub>, 70°C, 1h

b: 30mg catalyst, 4bar O<sub>2</sub>, 5bar CO, 20bar CH<sub>4</sub>, 150°C, 1h

Catalysts with different Pd to Ir ratio and Cu to Ir ratio were investigated. Table 5.2 shows product formation on IrPd catalyst with Pd to Ir ratio from 0.1:1 to 1:1. Whereas a small amount of palladium with ratio of 0.1:1 can drastically promote catalyst activity, further increasing the palladium loading showed little improvement. Copper species, on the other hand, shows the radical scavenging effect through suppressing HCOOH formation. A ratio of 1:1 Ir to Cu fully suppresses HCOOH formation, but further increasing the Cu content leads to a decrease in methanol formation.

Table 5.2 Product formation on IrPdZSM-5 catalysts with different metal atomic ratio

Pd to Ir ratio	HCOOH	CH <sub>3</sub> OH	CH <sub>3</sub> COOH
0:1	196	125	19
0.1:1	2326	522	108
0.5:1	2119	629	105
1:1	1875	435	90

Conditions: 30mg catalyst, 4bar O<sub>2</sub>, 5bar CO, 20bar CH<sub>4</sub>, 150°C, 1h

Table 5.3 Product formation on IrCuZSM-5 catalysts with different metal atomic ratio

Cu to Ir ratio	HCOOH	CH <sub>3</sub> OH	CH <sub>3</sub> COOH
0	196	125	19
0.5:1	70	244	21
1:1	0	606	29
3:1	0	153	11

Conditions: 30mg catalyst, 4bar O<sub>2</sub>, 5bar CO, 20bar CH<sub>4</sub>, 150°C, 1h

### 5.3.3 Characterization of iridium- based catalysts

The palladium species on the 1:0.1 Ir:Pd catalyst shows cationic features, as revealed from Pd K edge XANES spectra of the higher white line intensity compared to palladium foil, Figure 5.8. EXAFS analysis confirms that Pd species is a mixture of oxygen bonded Pd cations and small Pd clusters, evidenced by Pd-O and Pd-Pd interaction, Figure 5.9. The Pd-O interaction arises from isolated palladium cations inside zeolite pores, with coordination number of three (two from framework oxygen and one from OH). The Pd-Pd interaction shows coordination number of 5. Kodre et al. studied EXAFS data obtained on different sizes of palladium clusters and reported that Pd-Pd coordination number lower than 6 corresponds to clusters with less than 12 atoms.<sup>17</sup> The formation of metallic clusters at low loading of palladium demonstrates that palladium tends to agglomerate into metallic ensembles as a result of hydrogen reduction. Higher loading of palladium only contributes to further aggregation of clusters into particles that are not active in promoting methane activation.

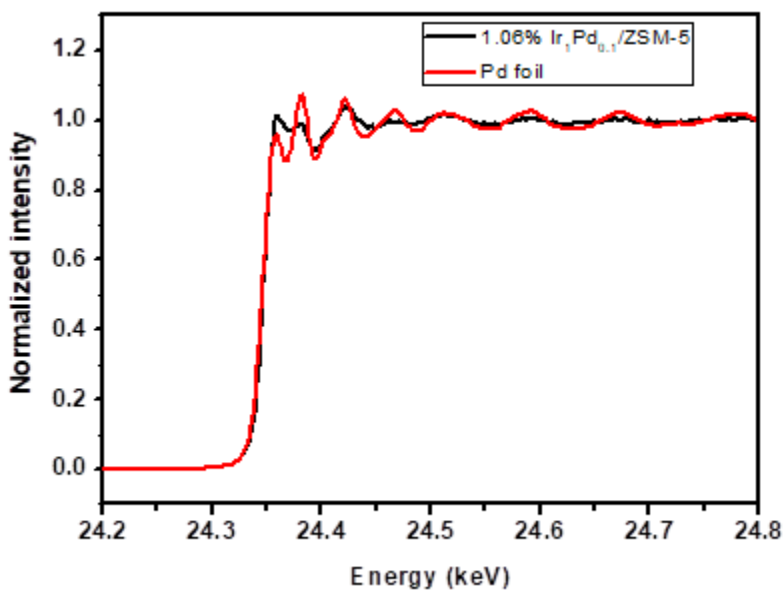


Figure 5.10 Normalized Pd K edge XANES spectra of 1.06wt% Ir<sub>1</sub>Pd<sub>0.1</sub>ZSM-5 and Pd foil. The higher absorption edge position and white line intensity clearly demonstrate the presence of cationic Pd species.

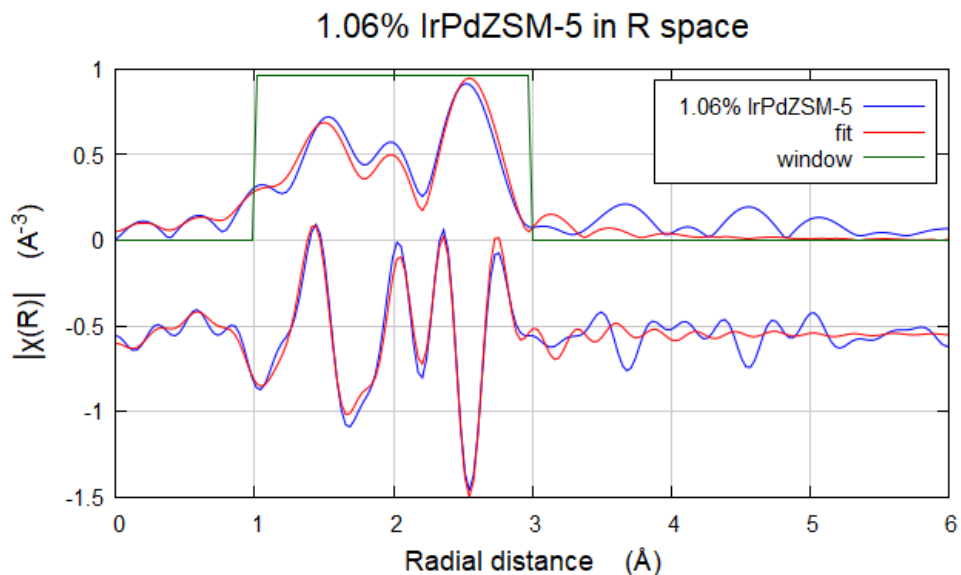


Figure 5.11 Pd K edge EXAFS data and fitting of 1.06wt% IrPd<sub>0.1</sub>ZSM-5. Detailed fitting parameters Pd-O: CN 3.02±1.08, R(Å) 2.00±0.02,  $\sigma^2$  (Å<sup>2</sup>) 0.008±0.006; Pd-Pd: CN 4.92±1.19, R(Å) 2.76±0.01,  $\sigma^2$  (Å<sup>2</sup>) 0.007±0.002.

X-ray Photoelectron Spectroscopy (XPS) was also conducted to probe the catalyst surface and the spectra of 1.0wt% IrZSM-5, 1.33wt% Ir<sub>1</sub>Cu<sub>1</sub>ZSM-5 and 1.06wt% Ir<sub>1</sub>Pd<sub>0.1</sub>ZSM-5 are shown in Figure 5.12. Ar<sup>+</sup> sputtering was used to remove a few of the surface layers of the zeolite framework to reveal Ir species inside the pore channels. XP spectra of the Ir 4f region before and after Ar<sup>+</sup> sputtering (Figure 5.12(a)) shows that iridium species are present both on the external surface and inside the zeolite micropores. The maximum cavity size inside the ZSM-5 cages is 6.4Å.<sup>18</sup> Therefore, it can be concluded that 1.0wt% IrZSM-5 consists a mixture of intrazeolite iridium atoms or clusters inside the micropores, while the larger iridium nanoparticles reside on the external surface. The atomic ratio of Ir to Si was found to be 0.0016 from the XP spectra while the design loading corresponds to a bulk ratio of 0.0034 which further confirms that the majority of Ir is inside the pores rather than on the external surface of the zeolite. Copper species was found to reside on the external surface of zeolite, as indicated by Cu 2p

spectra (Figure 5.12(b)). The absence of strong satellite peak indicates that copper is mostly in +1 or metallic state. Palladium species on the external surface of zeolite are negligible, below the detection limit of XPS and are most likely all anchored inside the zeolite pore channels.

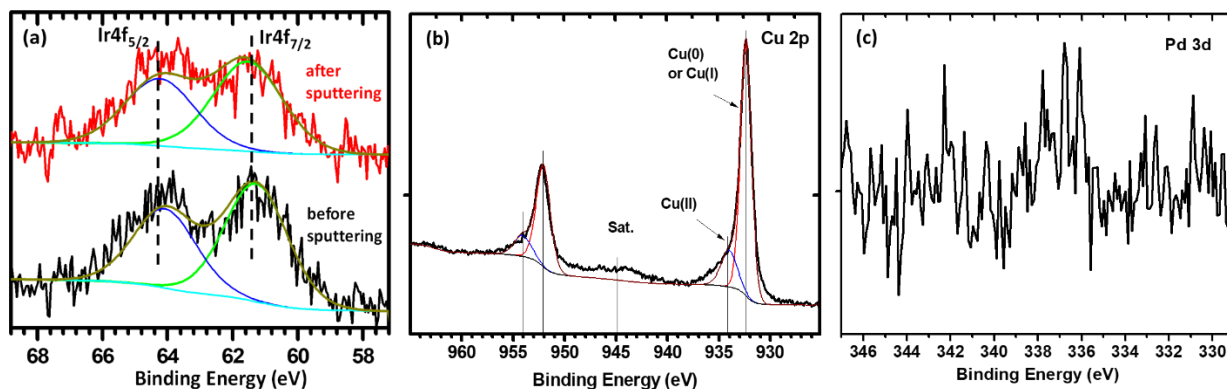


Figure 5.12 Ir 4f, Cu 2p and Pd 3d XPS spectra of catalyst 1.0wt% IrZSM-5, 1.33wt% Ir<sub>1</sub>Cu<sub>1</sub>ZSM-5 and 1.06wt% Ir<sub>1</sub>Pd<sub>0.1</sub>ZSM-5.

To further understand the nature of active iridium species, Diffuse Reflectance Infrared Fourier Transform Spectroscopy (DRIFTS) is performed on different Ir-based catalysts using CO as probe molecule (Figure 5.13). Three types of CO binding mode can be identified on 1.0 wt% IrZSM-5. The two peaks at 2102cm<sup>-1</sup> and 2033cm<sup>-1</sup> correspond to the symmetric and anti-symmetric stretching of the Ir(I)(CO)<sub>2</sub> species<sup>19,20</sup>. The single peak at 2071cm<sup>-1</sup> can be assigned to CO binding atop Ir<sup>0</sup> while the broad band centered at 1875cm<sup>-1</sup> can be assigned to CO binding in the bridged mode on extended Ir surfaces<sup>21</sup>. Previous reports have demonstrated that iridium atoms are highly electron deficient and readily undergo oxidative carbonylation with CO to form Ir(I)(CO)<sub>2</sub> at room temperature<sup>22</sup>. This transformation, however, does not occur on extended iridium surfaces at room temperature and CO adsorbed on Ir nanoparticles shows atop and bridged binding features only. The addition of Cu or Pd does not change the nature of Ir species, as can be observed from the similar CO binding features of Ir in Figure 5.13(a). For 1.06wt% Ir<sub>1</sub>Pd<sub>0.1</sub>ZSM-5, a shoulder at 2080 cm<sup>-1</sup> can be attributed to CO binding linearly to Pd<sup>23, 24</sup> and

two new peaks at  $2137\text{ cm}^{-1}$  and  $2159\text{ cm}^{-1}$  appear on 1.33wt%  $\text{Ir}_1\text{Cu}_1\text{ZSM-5}$ , which can be assigned to linearly bound CO on  $\text{Cu}^+$  species anchored on different zeolite sites<sup>25, 26</sup>. Furthermore, treating the 1.0wt% IrZSM-5 in 10% CO at elevated temperatures leads to an increase in the  $\text{Ir(I)(CO)}_2$  feature and a decrease in atop and bridged binding peaks, Figure 5.11(b). This phenomenon is well documented in the literature as CO can disaggregate metallic iridium nanoparticles into isolated iridium sites in the presence of hydroxyl species or water<sup>22</sup>. From these measurements, one can conclude that at reaction temperature, Ir species can readily undergo restructuring to form mononuclear Ir sites due to the presence of CO.

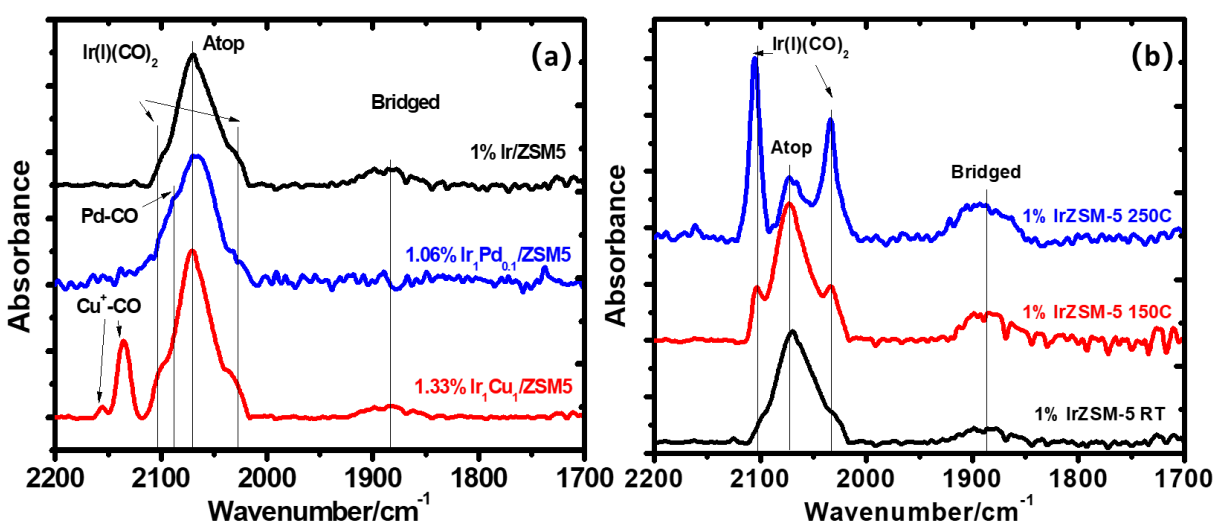


Figure 5.13 CO-DRIFTS spectra of (a) 1.0wt% IrZSM-5, 1.33wt%  $\text{Ir}_1\text{Cu}_1\text{ZSM-5}$  and 1.06wt%  $\text{Ir}_1\text{Pd}_{0.1}\text{ZSM-5}$  exposed to CO at room temperature and (b) 1.0wt% IrZSM-5 exposed to CO at 25-250°C.

CO-DRIFTS of the used iridium catalyst was also conducted. Spectra of used 1.0wt% IrZSM-5 and 1.33wt%  $\text{Ir}_1\text{Cu}_1\text{ZSM-5}$  before and after CO reduction are detailed in Figure 5.14. The used catalyst after drying in vacuum shows bridged binding of CO which demonstrates that metallic nanoparticles did not undergo restructuring after reaction. However, both the features corresponding to  $\text{Ir(I)(CO)}_2$  and atop binding have changed into a broad band ( $2070\text{-}2100\text{ cm}^{-1}$ ). Reduction of the used catalyst with 10% CO at 150°C regenerates the  $\text{Ir(I)(CO)}_2$  and atop feature. The redox cycling of these iridium carbonyl species is

directly correlated with the reusability of the catalyst. The active iridium species can be regenerated by reduction with CO at reaction temperature.

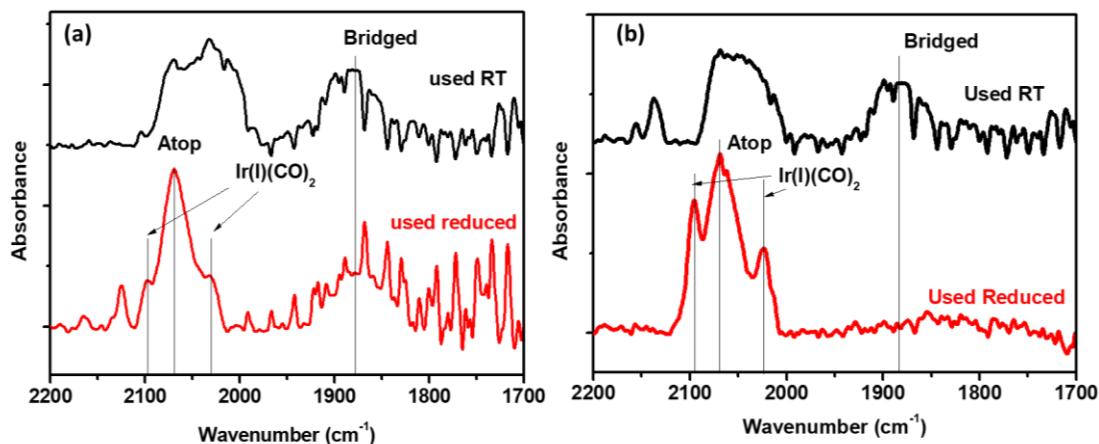


Figure 5.14 CO-DRIFTS spectra of (a) 1.0wt% IrZSM-5 and (b) 1.33wt% Ir<sub>1</sub>Cu<sub>1</sub>ZSM-5 catalyst after reaction exposed to CO at RT and after 10% CO reduction at 150°C.

The as-synthesized 1.0wt% IrZSM-5 was characterized by ac HAADF-STEM imaging. The presence of iridium nanoparticles with a size of 1-2 nm on the external surface is clearly visible, Figure 5.15(a-f). It is noted that the existence of nanoparticles on the external surface makes imaging of the iridium atoms inside the zeolite pores challenging.

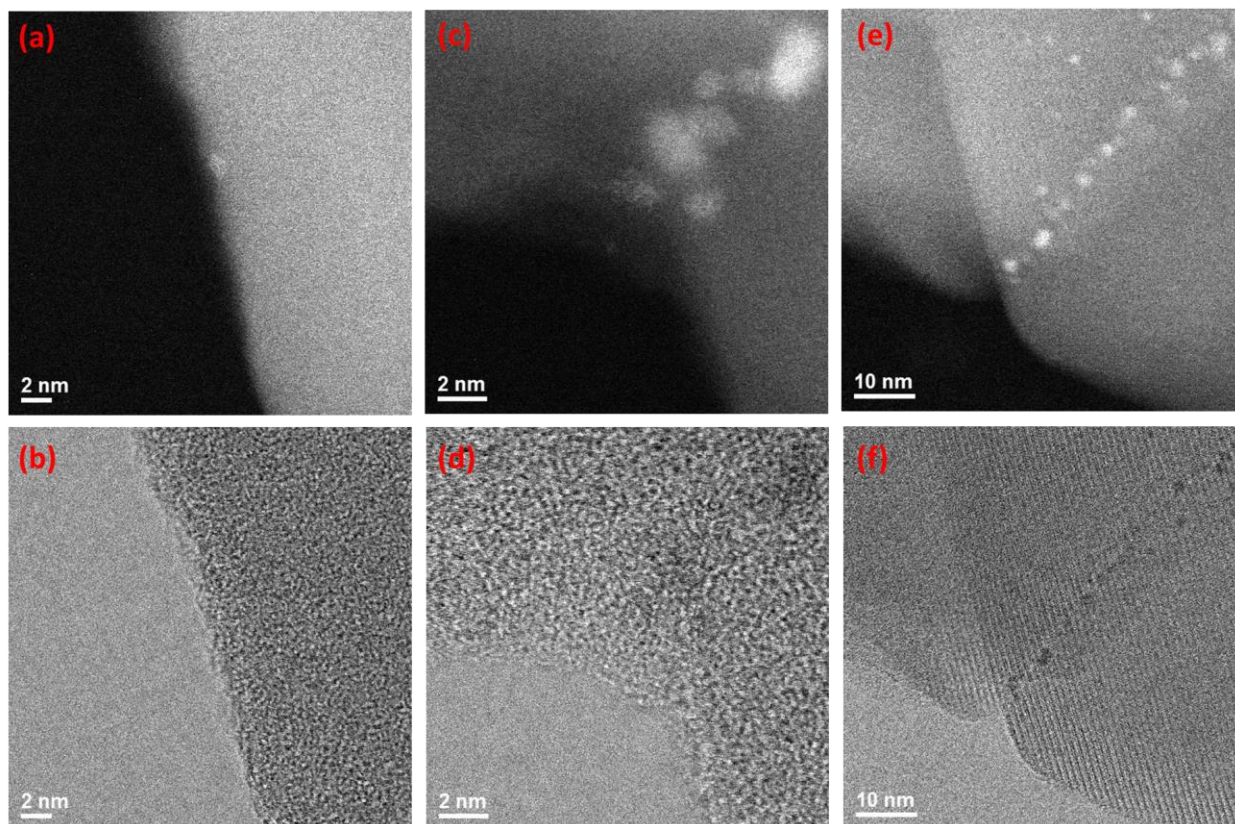


Figure 5.15 HAADF and BF image pairs of as-prepared 1.0wt% IrZSM-5 from STEM imaging.

Nanoparticles of size up to 2nm are clearly visible on the external surface of zeolite.

Figure 5.16 shows normalized XANES spectra at Ir LIII edge for 1.0wt% IrZSM-5, 1.33wt% Ir<sub>1</sub>Cu<sub>1</sub>ZSM-5 and 1.06wt% Ir<sub>1</sub>Pd<sub>0.1</sub>ZSM-5 along with standard samples of Ir foil and IrO<sub>2</sub>-ZSM-5. The spectra were recorded ex-situ in the fluorescence mode. The white line intensity of ZSM-5 supported Ir catalysts clearly indicates that Ir is in a mixed oxidation state consisting of both metallic and cationic components. The metallic state is attributed to Ir nanoparticles on the external surface, while Ir atoms anchored inside the zeolite pore channels are more cationic due to the stronger interaction with the zeolite lattice even if the sample is reduced with H<sub>2</sub><sup>22</sup>. Similar to the result of CO-DRIFTS, addition of Pd or Cu does not change the electronic state of Ir species.

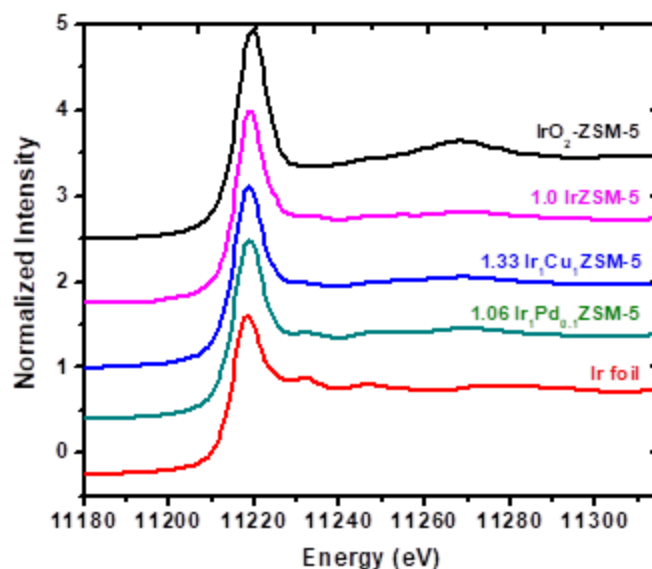
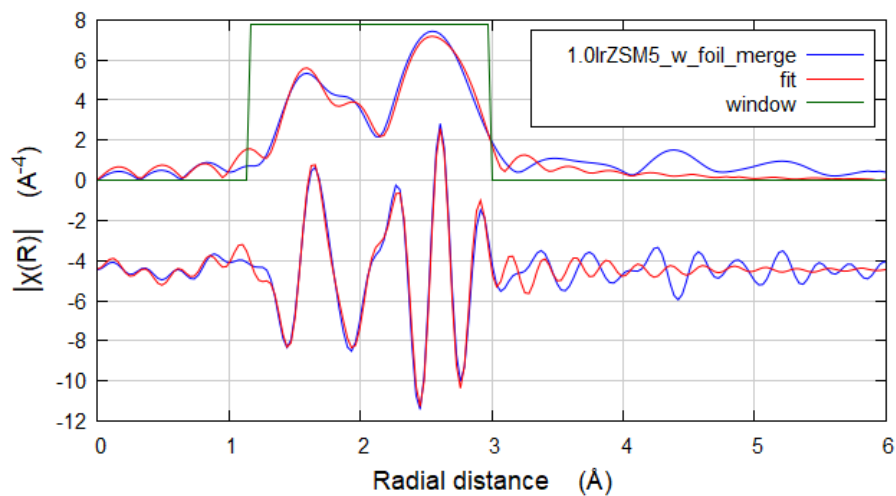


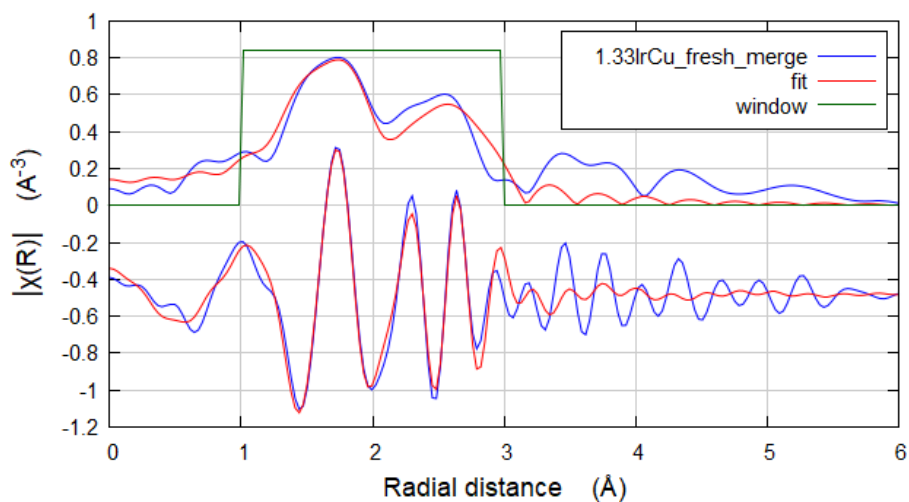
Figure 5.16 Normalized XANES spectra of 1.0wt% IrZSM-5, 1.33wt% Ir<sub>1</sub>Cu<sub>1</sub>ZSM-5 and 1.06wt% Ir<sub>1</sub>Pd<sub>0.1</sub>ZSM-5 with Ir foil and IrO<sub>2</sub>-ZSM-5 at Ir LIII edge.

EXAFS data of 1.0wt% IrZSM-5, 1.33wt% Ir<sub>1</sub>Cu<sub>1</sub>ZSM-5 and 1.06wt% Ir<sub>1</sub>Pd<sub>0.1</sub>ZSM-5 catalysts were collected at the Ir LIII edge and the corresponding EXAFS plots in the Fourier Transform space are shown in Figure 5.17. Table 5.4 summarizes the fitting parameters of the three catalysts. Both Ir-O and Ir-Ir interactions can be observed on all the samples. Ir-O interaction arises from single Ir species coordinated with the bridging oxygen on zeolite framework, which corresponds to the Ir(I)(CO)<sub>2</sub> structure identified by CO-DRIFTS, Figure 5.15. The bond length of Ir-O is shorter than the value reported for Ir<sub>6</sub> clusters confined in zeolite cages<sup>27</sup>. Also, the coordination number is much higher compared to the value reported for Ir<sub>6</sub> cluster. Therefore, we can exclude the contribution from clusters for Ir-O interaction. Ir-Ir interaction contains contribution of metallic Ir nanoparticles, as evidenced by the STEM images of particles on the external surface of the zeolite, Figure 5.15. The addition of Cu and Pd leads to an increase in Ir-O coordination number and a decrease in Ir-Ir coordination number. This is likely due to pore opening effect of adding a second metal during synthesis, which results in more Ir entering the pores.<sup>28</sup>

1.0IrZSM5\_w\_foil\_merge in R space



1.33IrCu\_fresh\_merge in R space



1.06IrPd\_fresh\_merge in R space

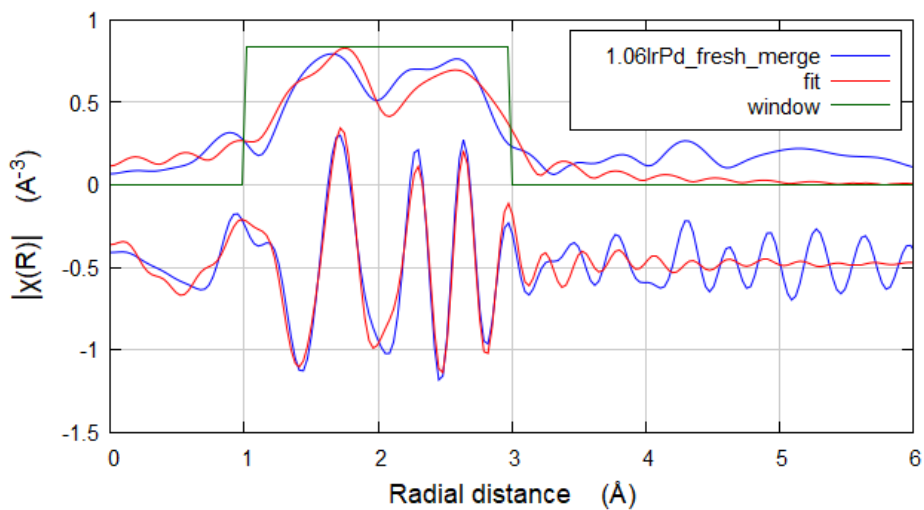


Figure 5.17 EXAFS fitting of 1.0wt% IrZSM-5, 1.33wt% Ir<sub>1</sub>Cu<sub>1</sub>ZSM-5 and 1.06wt% Ir<sub>1</sub>Pd<sub>0.1</sub>ZSM-5 plotted in R space. XAS spectra were recorded at Ir LIII edge ex-situ in fluorescence mode.

Table 5.4 EXAFS fitting parameters for iridium catalysts at Ir LIII edge

Sample	Path	CN <sup>[a]</sup>	R(Å) <sup>[b]</sup>	σ <sup>2</sup> (Å <sup>2</sup> )
1.0% IrZSM-5	Ir-O	3.36±0.5	2.00±0.01	0.005±0.002
	Ir-Ir	8.56±1.4	2.69±0.01	0.007±0.001
1.33% Ir <sub>1</sub> Cu <sub>1</sub> ZSM-5	Ir-O	4.82±1.2	2.04±0.01	0.010±0.004
	Ir-Ir	5.60±1.9	2.71±0.01	0.006±0.002
1.06% Ir <sub>1</sub> Pd <sub>0.1</sub> ZSM-5	Ir-O	5.03±1.4	2.03±0.01	0.011±0.005
	Ir-Ir	5.51±1.5	2.71±0.01	0.004±0.001

[a] CN, coordination number; [b] R, distance between absorber and backscattered atoms

To understand how Ir structure evolves in the reaction atmosphere, a DRIFTS study was conducted in a gas mixture mimicking the composition of reaction gas. A gas stream containing CH<sub>4</sub>, CO and O<sub>2</sub> with a ratio of 4:5:20 in flow rate was used to treat IrZSM-5 at 150°C for 1h and a He stream saturated with water vapor was applied at the same temperature. This two-step treatment simulates a full catalytic cycle. Figure 6 shows the DRIFT spectra both in the CO stretching and C-H stretching regions. After contacting with reaction gas at 150°C for 1h, the dicarbonyl features originally observed on IrZSM-5 disappears and were replaced with two new peaks at 2114 cm<sup>-1</sup> and 2159 cm<sup>-1</sup>. The peak at 2159 cm<sup>-1</sup> corresponds to Ir<sup>2+</sup>-CO<sup>29</sup> while the peak at 2114 cm<sup>-1</sup> was only reported in literature without assignment of structure<sup>19, 30</sup>. Here it is tentatively assigned as a (CO)IrO structure from oxidation of Ir(I)(CO)<sub>2</sub><sup>31</sup>. It is important to note that the atop and bridged binding features remain unchanged. Concurrently, two peaks centered at around 2948 cm<sup>-1</sup> and 2870 cm<sup>-1</sup> arise which can be assigned as asymmetric and symmetric stretching of surface methyl species<sup>32</sup>. This strongly suggests that CH<sub>4</sub> was activated into methyl species

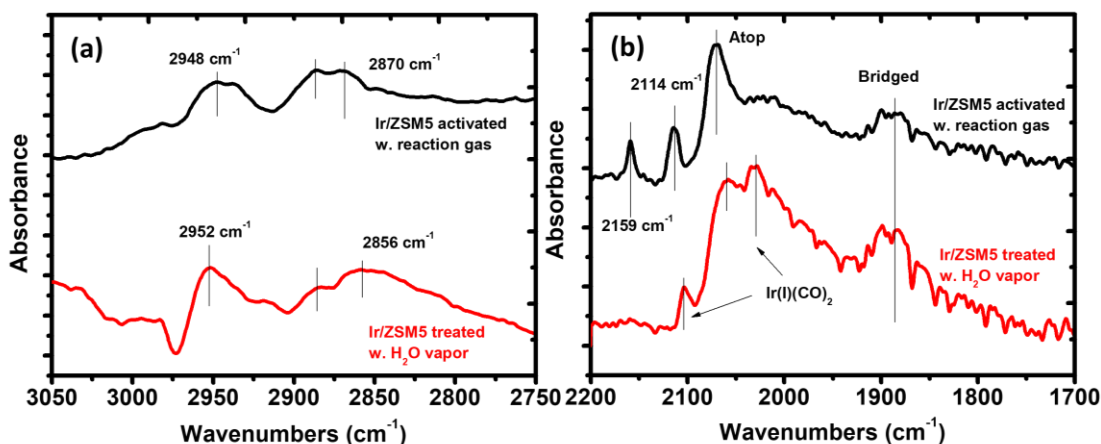


Figure 5.18 DRIFT spectra of IrZSM-5 in (a) C-H stretching region and (b) CO stretching region after activation with reaction gas (black) followed by H<sub>2</sub>O vapor treatment (red) at 150°C.

accompanied by conversion of Ir(I)(CO)<sub>2</sub>. Subsequent reaction with water restores the dicarbonyl structure in the CO region and the peaks in the C-H stretching region shift to 2952 cm<sup>-1</sup> and 2856 cm<sup>-1</sup>. These two peaks correspond to C-H stretching of methoxy species attached to zeolite framework<sup>33, 34</sup>. The surface-bound methoxy species likely arise from methanol formed on Ir center and then re-adsorbing on the zeolite acid sites. Based on these experimental results, we conclude that Ir(I)(CO)<sub>2</sub> is the active center for methane activation to form a surface bound methyl species and subsequent reaction with water leads to methanol formation. Activation of CH<sub>4</sub> without CO was also conducted, using either aqueous batch reactor or gas phase flow reactor. The IrZSM-5 catalyst was activated by O<sub>2</sub> at 400°C and reacted with CH<sub>4</sub> at 200°C following the similar procedure of gas phase oxidation on CuZSM-5 catalyst. No liquid oxygenates could be detected when extraction with deionized water was used. Similarly, without CO present in the batch reactor, no formation of liquid oxygenates was detected.

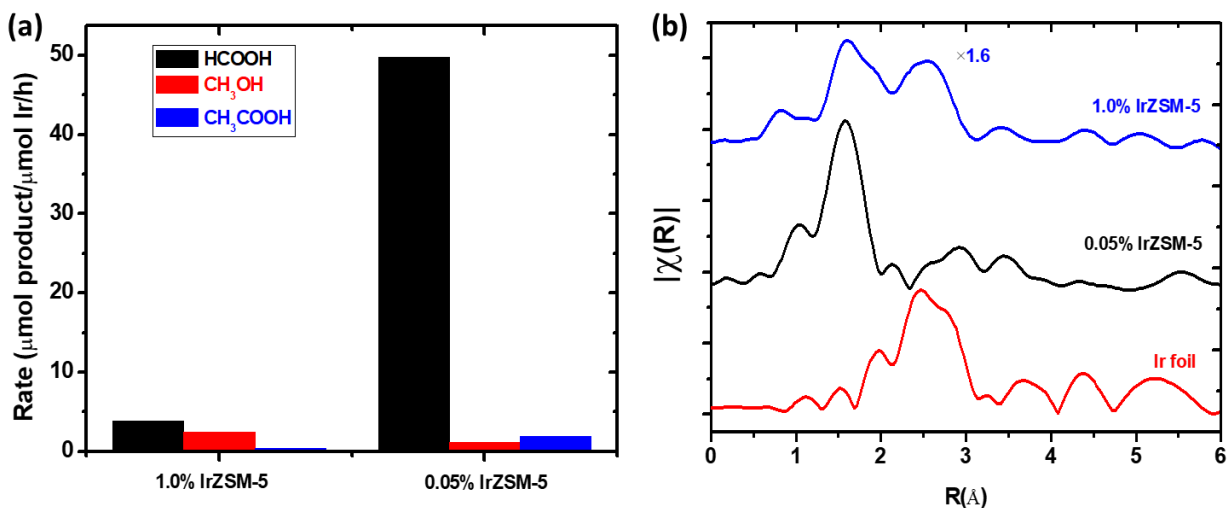


Figure 5.19 (a) Product formation rate of 1.0wt% IrZSM-5 and 0.05wt% IrZSM-5, conditions: 4bar O<sub>2</sub>, 5bar CO, 20bar CH<sub>4</sub>, 150°C, 1.6 $\mu\text{mol Ir}$ , 20mL DI water, 1h; (b) EXAFS data of 1.0wt% IrZSM-5, 0.05wt% IrZSM-5 and Ir foil in R space.

Further verification of Ir single atom as the site to activate the C-H bond of CH<sub>4</sub> can be obtained by synthesizing the catalyst with only iridium single atom species. From the Ir LIII edge EXAFS data, the 0.05wt% IrZSM-5 prepared by impregnation followed by heat treatment in helium at 450°C showed only Ir-O interaction (Figure 5.19(b) and Figure 5.20). The absence of Ir-Ir interaction indicated no formation of metallic iridium clusters or nanoparticles. The activity of the catalyst containing only Ir single atoms was compared to the catalyst with mixed structure, 1.0wt% IrZSM-5 (Figure 5.19(a)). The rate of product formation normalized by amount of iridium is ten times higher on the single atom Ir catalyst. Of course, in this calculation the rate on the particle containing catalyst is underestimated since not all of the Ir atoms are exposed, but the trend is clear.

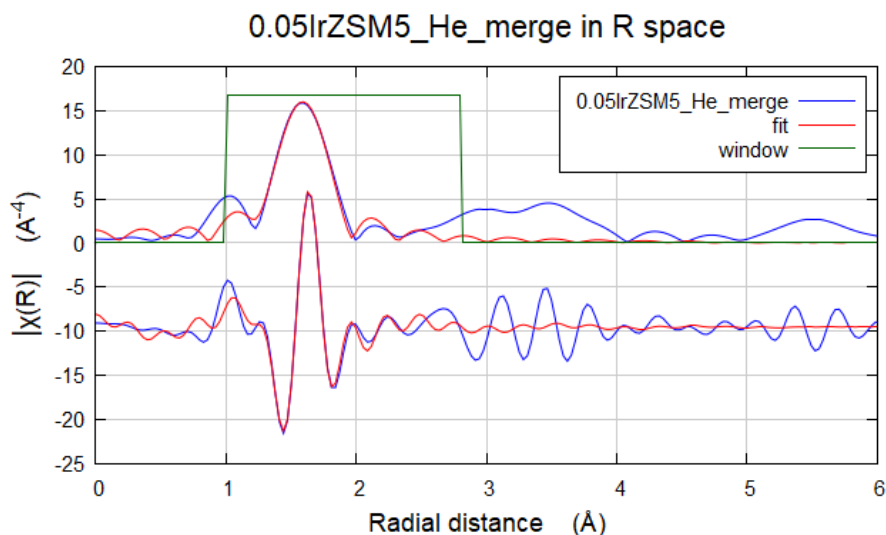


Figure 5.20 EXAFS fitting of 0.05wt% IrZSM-5 plotted in R space. XAS spectra were recorded at the Ir LIII edge ex-situ in fluorescence mode. Detailed fitting parameters Ir-O: CN  $6.00 \pm 0.7$ ,  $R(\text{\AA})$   $1.97 \pm 0.01$ ,  $\sigma^2$  ( $\text{\AA}^2$ )  $0.002 \pm 0.001$ ; Ir-Ir: 0.

#### 5.4 Conclusions

We have demonstrated the catalytic oxidation of methane to methanol on heterogeneous iridium-based catalysts using molecular oxygen as the oxidant in the presence of CO in aqueous solution under mild conditions. The monometallic IrZSM-5 was found to activate methane on the isolated  $\text{Ir(I)(CO)}_2$  sites and the formation of a peroxide intermediate is the possible reactive oxygen species to break the C-H bond of methane. The catalytic performance of IrZSM-5 is promoted by addition of palladium or copper. The promotional effect of each metal is identified. Pd participates synergistically with Ir to lower the activation barrier of C-H bond scission. The result is to increase the overall activity. Cu on the other hand promotes the peroxide intermediate formation and suppresses methanol over oxidation by scavenging hydroxyl radicals, boosting the selectivity to methanol. Both promotional effects are clearly shown on the IrCuPdZSM-5 catalyst. The good stability in cyclic operation is an additional attribute, rendering this type catalyst a “front-runner” in future catalyst development.

At the same time, the experimental results indicate that reaction at high temperature eventually leads to over-oxidation of methanol to CO<sub>2</sub>, even with the addition of copper. Therefore, accumulation of methanol in the aqueous phase is limited. Further investigation of the iridium-based catalysts at close-to-ambient temperatures to achieve high concentration of methanol is desired. To operate at such low temperatures, the desired catalyst should possess ample amount of active iridium and palladium single cations. Maximizing single cation loading of the metal species should be the next direction for catalyst development.

## 5.5 References

- (1) Shan, J.; Li, M.; Allard, L. F.; Lee, S.; Flytzani-Stephanopoulos, M. Mild oxidation of methane to methanol or acetic acid on supported isolated rhodium catalysts. *Nature* **2017**, 551, 605-608.
- (2) Hoyano, J. K.; McMaster, A. D.; Graham, W. A. G. Activation of methane by iridium complexes. *J. Am. Chem. Soc.* **1983**, 105, 7190-7191
- (3) Liang, Z.; Li, T.; Kim, M.; Asthagiri, A.; Weaver, J. F. Low-temperature activation of methane on the IrO<sub>2</sub> (110) surface. *Science*, **2017**, 356, 299-303
- (4) Zhou, M.; Hintermair, U.; Hashiguchi, B. G.; Parent, A. R.; Hashimi, S. M.; Elimelech, M.; Periana, R. A.; Brudvig G. W.; Crabtree, R. H. Cp\* iridium precatalysts for selective C-H oxidation with sodium periodate as the terminal oxidant. *Organometallics* **2013**, 32, 957-965
- (5) Eisenberg, G. M. Colorimetric determination of hydrogen peroxide. *Ind. Eng. Chem. Anal. Ed.* **1943**, 15, 5, 327-328.
- (6) Foster, D. Mechanistic pathways in the catalytic carbonylation of methanol by rhodium and iridium complexes. *Adv. Organomet. Chem.* **1979**, 17, 255-267.

- (7) Jones, J. A. The Cativa<sup>TM</sup> process for the manufacture of acetic acid. *Platinum Metals Rev.* **2000**, 44, 94-105.
- (8) Pearson, R. G. Absolute electronegativity and hardness: application to inorganic chemistry. *Inorg. Chem.* **1988**, 27, 734-740.
- (9) Zhang, L.; Chen, K.; Chen, B.; White, J. L.; Resasco, D. E. Factors that determine zeolite stability in hot water. *J. Am. Chem. Soc.* **2015**, 137, 11810-11819.
- (10) Ravenelle, R. M.; Schüßler, F.; D'Amico, A.; Danilina, N.; van Bokhoven, J. A.; Lercher, J. A.; Jones, C. W.; Sievers, C. Stability of zeolites in hot liquid water. *J. Phys. Chem. C* **2010**, 114, 19582-19595.
- (11) Zaker, A.; Guerra, P.; Wang, Y.; Tompsett, G. A.; Huang, X.; Bond, J. Q.; Timko, M. T. Evidence of heterogeneous catalytic activity of ZSM-5 in supercritical water for dodecane cracking. *Catal. Today* **2018**, 317, 2-11.
- (12) Hammond, C.; Forde, M. M.; Ab Raim, M. H.; Thetford, A.; He, Q.; Jenkins, R. L.; Dimitratos, N.; Lopez-Sanchez, J. A.; Dummer, N. F.; Murphy, D. M.; Carley, A. F.; Taylor, S. H.; Willock, D. J.; Stangland, E. E.; Kang, J.; Hagen, H.; Kiely, C. J.; Hutchings, G. J. Direct catalytic conversion of methane to methanol in an aqueous medium by using copper-promoted Fe-ZSM-5. *Angew. Chem. Int. Ed.* **2012**, 51, 5129-5133.
- (13) Chepaikin, E. G.; Bezruchenko, A. P.; Leshcheva, A. A. Homogeneous rhodium-copper-halide catalytic systems for the oxidation and oxidative carbonylation of methane. *Kinet. Catal.* **2002**, 43, 507-513.
- (14) Lin, M.; Hogan, T.; Sen, A. A highly catalytic bimetallic system for the low-temperature selective oxidation of methane and lower alkanes with dioxygen as the oxidant. *J. Am. Chem. Soc.* **1997**, 119, 6048-6053.

- (15) Periana, R. A.; Mironov, O.; Taube, D.; Bhalla, G.; Jones, C. J. Catalytic, oxidative condensation of CH<sub>4</sub> to CH<sub>3</sub>COOH in one step via CH activation. *Science* **2003**, 301, 814-818.
- (16) Huang, W.; Zhang, S.; Tang, Y.; Li, Y.; Nguyen, L.; Li, Y.; Shan, J.; Xiao, D.; Gagne, R.; Frenkel, A. I.; Tao, F. Low-temperature transformation of methane to methanol on Pd<sub>1</sub>O<sub>4</sub> single sites anchored on the internal surface of microporous silicate. *Angew. Chem. Int. Ed.* **2016**, 55, 13441-13445.
- (17) Kodre, A.; Arçon, I.; Batista, J.; Pintar, A. EXAFS analysis of Pd atomic clusters. *J. Synchrotron Rad.* **1999**, 6, 458-459.
- (18) Foster, M. D.; Rivin, I.; Treacy, M. M.; Delgado-Friedrichs, O. A geometric solution to the largest-free-sphere problem in zeolite frameworks. *Micopor. Mesopor. Mat.* **2006**, 90, 32-38.
- (19) Mihaylov, M.; Ivanova, E.; Thibault-Starzyk, F.; Daturi, M.; Dimitrov, L.; Hadjiivanov, K. New types of nonclassical iridium carbonyls formed in Ir-ZSM-5: a fourier transform infrared spectroscopy investigation. *J. Phys. Chem. B* **2006**, 110, 10383-10389.
- (20) Martinez-Macias, C.; Xu, P.; Hwang, S.-J.; Lu, J.; Chen, C.-Y.; Browning, N. D.; Gates, B. C. Iridium complexes and clusters in dealuminated zeolite HY: distribution between crystalline and impurity amorphous regions. *ACS Catal.* **2014**, 4, 2662-2666.
- (21) Gelin, P.; Coudurier, G.; Taarit, Y. B.; Naccache, C. Formation of iridium carbonyl complex in NaY zeolite. *J. Catal.* **1981**, 70, 32-40.
- (22) Voskobojnikov, T. V.; Shpiro, E. S.; Landmesser, H.; Jaeger, N. I.; Schulz-Ekloff, G. Redox and carbonylation chemistry of iridium species in the channels of H-ZSM-5 zeolite. *J. Mol. Catal. A: Chem.* **1996**, 104, 299-309.
- (23) Dann, E. K.; Gibson, E. K.; Catlow, R. A.; Collier, P.; Erden, T. E.; Giannolio, D.; Hardacre, C.; Kroner, A.; Raj, A.; Goguet, A.; Wells, P. P. Combined in situ XAFS/DRIFTS studies of the evolution of nanoparticle structures from molecular precursors. *Chem. Mater.* **2017**, 29, 7515-7523.

- (24) Chakarova, K.; Ivanova, E.; Hadjiivanov, K.; Klissurski, D.; Knözinger, H. Co-ordination chemistry of palladium cations in Pd-H-ZSM-5 as revealed by FTIR spectra of adsorbed and co-adsorbed probe molecules (CO and NO). *Phys. Chem. Chem. Phys.* **2004**, *6*, 3702-3709.
- (25) Hadjiivanov, K. I.; Kantcheva, M. M.; Klissurski, D. G. IR study of CO adsorbed on Cu-ZSM-5 and CuO/SiO<sub>2</sub> catalysts:  $\sigma$  and  $\pi$  components of the Cu<sup>+</sup>-CO bond. *J. Chem. Soc., Faraday Trans.* **1996**, *92*, 4595-4600.
- (26) Hwang, I. C.; Kim, D. H.; Woo, S. I. The existence of dual Cu site involved in the selective catalytic reduction of NO with propene on Cu/ZSM-5. *Catal. Lett.* **1996**, *42*, 177-184.
- (27) Martinez-Macias, C.; Chen, M.; Dixon, D. A.; Gates, B. C. Single-site zeolite-anchored organoiridium carbonyl complexes: characterization of structure and reactivity by spectroscopy and computational chemistry. *Chem. Eu. J.* **2015**, *21*, 11825-11835.
- (28) Kim, J.-H.; Ikoma, Y.; Niwa, M. Control of the pore-opening size of HY zeolite by CVD of silicon alkoxide. *Micropor. Mesopor. Mat.* **1999**, *32*, 37-44.
- (29) Aydin, C.; Lu, J.; Shirai, M.; Browning, N. D.; Gates, B. C. Ir<sub>6</sub> clusters compartmentalized in the supercages of zeolite NaY: direct imaging of a catalyst with aberration-corrected scanning transmission electron microscopy. *ACS Catal.* **2011**, *1*, 1613-1620.
- (30) Voskoboinikov, T. V.; Shpiro, E. S. Iridium in pentasil: redox behavior and reactivity. *Stud. Surf. Sci. Catal.* **1997**, *105*, 2027-2034.
- (31) Lu, Y.; Wang, J.; Yu, L.; Kovarik, L.; Zhang, X.; Hoffman, A. S.; Gallo, A.; Bare, S. R.; Sokaras, D.; Kroll, T.; Dagle, V.; Xin, H.; Karim, A. M. Identification of the active complex for CO oxidation over single-atom Ir-on-MgAl<sub>2</sub>O<sub>4</sub> catalysts. *Nat. Catal.* **2019**, *2*, 149-156.

(32) Okolie, C.; Belhseine, Y. F.; Lyu, Y.; Yung, M. M.; Engelhard, M. H.; Kovarik, L. K.; Stavitski, E.; Sievers, C. Conversion of methane into methanol and ethanol over nickel oxide on ceria-zirconia catalysts in a single reactor. *Angew. Chem. Int. Ed.* 2017, 56, 13876-13881.

(33) Forester, T. R.; Howe, R. F.; In situ FTIR studies of methanol and dimethyl ether in ZSM-5. *J. Am. Chem. Soc.* **1987**, 109, 5076-5082.

(34) Sepurahman; Visur, M.; Olsbye, U.; Bjørgen, M.; Svelle, S. In situ FT-IR mechanistic investigations of the zeolite catalyzed methylation of benzene with methanol: H-ZSM-5 versus H-beta. *Top. Catal.* **2011**, 54, 1293-1301.

# Chapter 6 Conclusions and Recommendations

## 6.1 Conclusions

The abundant supply of natural gas calls for alternative methods of methane upgrading compared to the conventional syngas route in industry, and direct oxidation of methane to C1 and C2 oxygenates with molecular oxygen is the most attractive process. The success of such a process depends on the design of a highly active and selective catalyst to bring down cost of downstream separation. The focus of this Ph.D. thesis was to understand how catalyst structure and operating conditions affect the C-H bond activation, what intermediate is needed for methane activation and the specific elementary reactions leading to product formation. The beneficial effect of single atom catalyst – catalyst with metal species in atomic dispersion, was illustrated and the strategy to combine different metal components to construct efficient bifunctional catalysts was also explored. Specifically, the main findings of this thesis are summarized below:

- (1) RhZSM-5 catalysts prepared by impregnation method followed by high temperature reduction in 5% H<sub>2</sub> are highly active for selective oxidation of methane to methanol and acetic acid. The active form of metal species is cationic rhodium in lower oxidation state generated during the reduction step followed by exposure to ambient environment. Rhodium oxide clusters, on the other hand, are not active for this reaction. The rhodium cations are coordinated directly to the zeolite framework through electrostatic interactions and such a coordination is crucial to product selectivity to acetic acid. In addition, the cations are atomically dispersed inside the micropores of the zeolite, as evidenced by XPS, CO-DRIFTS, XANES/EXAFS and ac HAADF-STEM characterizations.
- (2) Parametric studies on the reaction conditions show that the reaction light-off on RhZSM-5 is at temperatures above 110°C and methane oxidation products comprise of formic acid, methanol, acetic acid and carbon dioxide. Whereas C1 products are prone to over-oxidation and high

temperature or long reaction time eventually lead to decrease in C1 liquid oxygenates formation, C2 product of acetic acid is accumulated to higher concentration. The reactions conducted at lower  $pO_2$  show high selectivity to acetic acid but decreased reaction rate. At  $pO_2=2\text{bar}$ , which provides balanced selectivity and reaction rate, batch reaction on 0.5wt% RhZSM-5 leads to 4% conversion of methane and selectivity to acetic acid was maintained at ~60%. Further tests with different reactor setups demonstrate that the catalyst is stable in 12 h-on-stream and concentration of acetic acid continues to build up. Eventual deactivation of the catalyst is a result of both coke formation and rhodium sintering to metallic particles.

- (3) The reaction mechanism involves multiple reaction steps. First CO coordinated with rhodium activates  $O_2$  in the aqueous phase, forming  $H_2O_2$  intermediate. The peroxide intermediate is proposed to activate isolated rhodium sites into rhodium oxo species that split the first C-H bond of methane, forming the Rh- $CH_3$  complex. Subsequent functionalization of Rh- $CH_3$  follows two separate reaction pathways: C1 pathway involves direct hydroxylation of the methyl species yielding methanol, and C2 pathway involves carbonylation of the methyl species into acetyl first, and final hydroxylation forms acetic acid. The two reaction pathways proceed in parallel rather than in sequence and methanol is not an intermediate for acetic acid formation. The selectivity between the two pathways is governed by the operating conditions, with low  $pO_2$  favoring the formation of acetic acid.
- (4) CO plays an important role in the catalytic system. First CO stabilizes isolated rhodium cations into  $Rh(I)(CO)_2$  and the ability of CO to split metallic rhodium particles into  $Rh(I)(CO)_2$  further increases the number of these active sites. Similar chemistry is realized on iridium catalyst to generate  $Ir(I)(CO)_2$ . Furthermore, CO acts as the two-electron reductant to activate molecular oxygen into  $H_2O_2$ , and both rhodium and iridium catalyze this  $O_2$  activation step. The transient stability of  $H_2O_2$  intermediate demands fast methane activation to utilize this species effectively. Decomposition of the  $H_2O_2$  intermediate lowers CO efficiency, which contributes to the side

reaction of direct CO oxidation. Increasing methane activation site or methane partial pressure remedy the efficiency.

- (5) The  $\text{H}_2\text{O}_2$  intermediate can be utilized by a more active methane activation center, and the combination of one metal species highly active for methane oxidation and the other active for  $\text{H}_2\text{O}_2$  synthesis generates a bifunctional catalyst with optimized efficiency. The FeRh bimetallic catalyst in acidic environment catalyzes the reaction sequence of  $\text{H}_2\text{O}_2$  synthesis, spillover and methane oxidation at temperatures as low as room temperature.
- (6) Both the oxygen activation step and methane oxidation step are catalyzed on iridium- based catalysts in the same way, with oxygen activated to  $\text{H}_2\text{O}_2$  and splitting C-H bond of methane into Ir- $\text{CH}_3$  on isolated iridium cations. The low activity of C2 pathway of iridium catalyst is attributed to iridium being a harder Lewis acid compared to rhodium with a lower affinity to CO which is a soft Lewis base. Addition of copper improves both catalyst activity and selectivity to methanol. Its role is two-fold: copper improves the  $\text{H}_2\text{O}_2$  synthesis activity of the catalyst which leads to higher activity and at the same time suppresses hydroxyl radical formation that oxidizes methanol to formic acid and  $\text{CO}_2$ . Addition of palladium improves the overall activity and decreases the apparent activation energy. The promotional effect involves first formation of  $\text{H}_2\text{O}_2$  intermediate at the iridium sites followed by its spillover to more active palladium cations. The measured apparent activation energy on IrPd catalysts corroborates the DFT calculations of methane activation barrier on palladium single site, 35-84 kJ/mol.<sup>1</sup> The spillover of  $\text{H}_2\text{O}_2$  intermediate leads to a shift of methane activation site from iridium to more active palladium cations, resulting in higher activity and a decrease in apparent activation energy.

## 6.2 Recommendations

An extensive effort of this thesis was directed towards understanding the chemistry of methane activation with molecular oxygen. The identification of a mechanism that involves first oxygen activation

into peroxide followed by methane activation and the introduction of the concept of designing a bifunctional catalyst have opened new doors for rational catalyst design. At the same time, future research on both catalyst design and process development based the knowledge obtained in this thesis should continue to bring forth successful methane upgrading technology. The following recommendations are made to provide guidelines for further study:

- (1) It is demonstrated in this thesis that rhodium and iridium catalyze peroxide synthesis at low temperature in O<sub>2</sub>/CO/H<sub>2</sub>O mixture and that isolated rhodium, iridium, iron and palladium cations are effective methane activation sites, albeit at different temperatures. The exploration other possible metal and metal combinations should be conducted to further expand the scope of catalyst design. Notably, metal species that coordinate with CO and form isolated cationic carbonyls are likely to catalyze both peroxide synthesis and methane activation. Ruthenium for example, forms a range of +1 and +2 carbonyl complexes with CO and can be the next subject to study. Catalytic H<sub>2</sub>O<sub>2</sub> synthesis and methane oxidation on ruthenium catalysts have been reported separately<sup>2,3</sup> and demonstrate that the same kind of chemistry as rhodium and iridium takes place on ruthenium. Therefore, single atom ruthenium<sup>4</sup> catalyst should be evaluated for methane oxidation using O<sub>2</sub> and CO.
- (2) On the development of a catalytic process to make acetic acid from methane, I recommend continuing the testing of continuous reactors at a lower temperature to avoid metal sintering and carbon deposition. The ultimate goal of the process is not to produce acetic acid as a commercial product, but to couple it with the acetic acid-to-lipids bioprocess developed at MIT.<sup>5</sup> This would realize the methane-to-biodiesel process, which is under intense investigation by the catalysis and biocatalysis communities. The minimum acetic acid concentration for *Y. lipolytica* yeast to metabolize is on the scale of 10-30 g/L and process conditions to continuously condense methane into acetic acid at this concentration would make a methane-to-biofuel process viable.

(3) Iridium-based catalysts have been demonstrated to be promising candidate for selective production of methanol from methane. As indicated in Chapter 5, further investigation should focus on increasing the amount of methane activation sites, namely iridium and palladium single cations on the catalyst. Such a catalyst with ample methane activation sites would allow one to perform the reaction at close-to-ambient temperatures to limit methanol over-oxidation and maximize methanol concentration. I would also recommend conducting the reaction in a bubbler reactor at the said temperatures and developing a continuous process to convert methane to methanol using the iridium-based catalysts.

### 6.3 References

- (1) Gannouni, A.; Delbecq, F.; Zina, M. S.; Sautet, P. Oxidation of methane to methanol over single site palladium oxide species on silica: A mechanistic view from DFT. *J. Phys. Chem. A* **2017**, 121, 5500-5508.
- (2) Brill, W. F. Preparation of hydrogen peroxide. US Patent 4462978A, 1984 (Linde Inc.)
- (3) Khokhar, M. D.; Shukla, R. S.; Jasra, R. V. Selective oxidation of methane by molecular oxygen catalyzed by a bridged binuclear ruthenium complex at moderate pressures and ambient temperature. *J. Mol. Catal. A: Chem.* **2009**, 299, 108-116.
- (4) Zhang, C.; Sha, J.; Fei, H.; Liu, M.; Yazdi, S.; Zhang, J.; Zhong, Q.; Zou, X.; Zhao, N.; Yu, H.; Jiang, Z.; Ringe, E.; Yakobson, B. I.; Dong, J.; Chen, D.; Tour, J. M. Single-atomic ruthenium catalytic sites on nitrogen-doped graphene for oxygen reduction reaction in acidic medium. *ACS Nano* **2017**, 11, 6930-6941.
- (5) Hu, P.; Chakraborty, S.; Kumar, A.; Woolston, B.; Liu, H.; Emerson, D.; Stephanopoulos, G. Integrated bioprocess for conversion of gaseous substrates to liquids. *Proc. Natl. Acad. Sci. USA* **2016**, 113, 3773-3778.